Numerical simulation and experimental study of horizontal wave slamming on offshore platforms

By

Lei Li

A thesis presented in fulfilment of the requirements for
the degree of Doctor of Philosophy

Department of Naval Architecture, ocean and Marine
Engineering

University of Strathclyde, Glasgow

2025

This thesis is the result of the author's original research. It has been composed by the author and has not been previously submitted for examination which has led to the award of a degree.

Signed: Date:

Acknowledgements

First and foremost, I would like to express my deepest gratitude to my supervisors, Professor Atilla Incecik, Professor Huajun Li, and Professor Zhiming Yuan, for their invaluable guidance, continuous encouragement, and steadfast support throughout the course of my Ph.D studies. Their profound expertise in marine hydrodynamics and unwavering dedication to academic excellence have been a constant source of inspiration. I feel truly privileged to have conducted my research and development work under their supervision at the University of Strathclyde.

To my family—my late father, Mr Jian Li, and my mother, Ms Faying Wang—thank you for your enduring strength, unwavering love, and unconditional support throughout the years. You have shaped my character and nurtured my perseverance without ever asking for anything in return. To my beloved wife, Ms Dong Li, and my lovely children, Yishan Li and Pucheng Li, thank you for your unwavering love, patience, and belief in me, even during the most challenging times. Your support has been the cornerstone of my journey.

I am also sincerely grateful to the staff and colleagues at the Department of Naval Architecture, Ocean and Marine Engineering, including Ms Susan Pawson and others, for their generous support and for fostering such a stimulating research environment.

Special thanks are due to the R&D and technical teams for their dedicated support throughout the experimental phases of this work, as well as to my fellow researchers and friends, whose insightful advice and enduring camaraderie have greatly enriched this academic journey. I wish to express my heartfelt appreciation to the collaborators from Shanghai Jiao Tong University—Professor Xin Li and Dr Yinghao Guo—for their critical contributions to the design and execution of wave slamming pool tests, and to experts from Harbin Engineering University, Sun Yat-Sen University, Dalian University of Technolgy and China Ocean University, including Professor Kangping Liao and Professor Yong Ma, Professor Shuqing Wang, Professor Bing Ren, Professor Liang Li, Dr Yuanyao Zhu, Dr Zhi Yao, Dr Chao Hu, Mr Ducheng Li and others for their invaluable support with numerical analysis and tool development. Their collaboration laid a strong foundation for this research.

Finally, I would like to thank my colleagues at the company, including Mr Ya Yu, Mr Yao Teng, Mr Ronggui Han, Ms Yuan Xiao, Mr Hao Li, Mr Qiutong Tan, Mr Fangjie Zhai and others. Thank you all for your teamwork and dedication in advancing R&D efforts on floating platform design and wave slamming. Your contributions have been integral to this work.

TABLE OF CONTENTS

LIST OF FIGURES

LIST OF TABLES

ABSTRACT

The development of offshore oil and gas resources has long been a fundamental pillar of global energy supply and has driven continuous advances in large-scale marine engineering equipment such as floating platforms. Deep-sea mining is recognised as the next strategic frontier in marine resource development, and its development likewise relies heavily on semi-submersible platforms or mining vessels. Under extreme sea conditions, platforms are prone to wave run-up, overtopping, and slamming, which impose short-duration, high-intensity impact loads on the column and deck structures, posing significant safety risks. Wave slamming is strongly nonlinear, transient, and characterized by coupled air – water – structure interactions, all of which are influenced by platform geometry. Existing research approaches have notable limitations: experimental methods often lack the precision to capture transient peaks; simplified analytical models such as OTG13/14, though efficient, have limited accuracy and applicability under complex geometries and extreme conditions. Conventional CFD tools can describe detailed flow phenomena but are computationally expensive, limiting their practicality during design stages.

This study conducts a comprehensive experimental and numerical investigation into wave slamming on the columns of semi-submersible platforms. A scaled physical testing system was established, employing regular, focused, and freak wave conditions to measure column load responses under varying sea states. Meanwhile, a Cartesian-grid numerical wave flume was developed and applied to the wave slamming problem. By combining high-resolution free-surface capturing with finite-difference algorithms, the method achieves a favorable balance between computational accuracy and efficiency.

More than 180 experimental cases were conducted, systematically revealing the effects of air gap, wave steepness, period, and incident angle on slamming loads. Signal processing techniques were applied to extract peak loads and representative events. The numerical results showed strong agreement with experimental data, verifying the reliability of CGNT-CFD in wave reproduction, pressure prediction, and total force estimation. Furthermore, 153 numerical sensitivity analyses quantified how parameters such as column diameter, shape, deck elevation, and column spacing influence the distribution and characteristics of slamming loads.

This research establishes a complete experimental methodology and proposes a fast numerical prediction technique for slamming loads based on the CGNT-CFD approach. The developed experimental and numerical frameworks can be effectively applied to the impact-resistance design and performance evaluation of floating platforms, offering both theoretical significance and broad engineering applicability.

EXECUTIVE SUMMARY

Oil and gas resources have long served as fundamental energy resources supporting the sustainable development of human society. The abundant oil and gas reserved in deep and ultra-deep waters are increasingly becoming a central focus of global energy strategies and the development of the marine industry. Meanwhile, the strategic value of deep-sea mineral resources is also rising rapidly. Critical resources such as polymetallic nodules, cobalt-rich crusts, and seafloor massive sulfides are widely distributed across deep-sea basins, offering high economic value, limited global supply, and significant development potential. Deep-sea mining is thus regarded as the next strategic frontier in marine resource exploitation, following oil and gas. Similar to hydrocarbon extraction, the development of deep-sea mineral resources relies heavily on large-scale offshore equipment, particularly floating platforms. These platforms are frequently subjected to complex wave-structure interactions such as wave run-up, wave overtopping, and wave slamming during operation. As a result, the platform's columns, topside structures, and production facilities on the main deck are exposed to significant impact loads, posing substantial safety risks to the structural integrity, onboard equipment, and personnel. Wave slamming is characterized by strong gas-liquid-solid coupling, pronounced nonlinearity, and short-duration high-intensity impacts. The process is strongly influenced by the platform's geometric features, including columns, braces, and pontoons, and is often accompanied by highly nonlinear local hydrodynamic phenomena such as wave climbing, near-field interference, and wave focusing. Existing experimental and numerical approaches still face key challenges in

addressing such problems. On the one hand, experimental measurements are limited in accuracy, making it difficult to capture instantaneous peak responses. On the other hand, although simplified methods such as OTG13/14 offer rapid evaluation capabilities, they suffer from limited accuracy and narrow applicability, making them insufficient for engineering applications involving complex structures and extreme conditions. Furthermore, while high-fidelity CFD methods (e.g., STAR-CCM+) can provide detailed representations of slamming phenomena, their high computational cost makes them unsuitable for multi-condition and batch analyses during the design phase.

Given the complexity of wave slamming phenomena, it is essential to elucidate the initiation and evolution processes of slamming, as well as the underlying mechanisms, patterns, and phenomena. This requires overcoming current technical bottlenecks such as limited experimental measurement accuracy and low efficiency in numerical prediction. This study focuses on the key characteristics of wave slamming loads acting on platform columns. A dedicated experimental setup was developed, and a physical testing system for column slamming was constructed in a numerical wave tank environment. Experimental methodologies were established to investigate the slamming behavior of platform columns and to process long-duration, high-frequency measurement data. Through laboratory experiments, the characteristics and mechanisms of slamming loads on platform columns were systematically analyzed. This study develops a Regular Fixed Cartesian Grid Numerical Tank CFD solver (referred to as CGNT-CFD), which integrates a high-resolution free surface capturing algorithm with a three-dimensional Cartesian finite difference method. While maintaining high agreement between the simulated wave slamming responses and experimental results, the solver significantly enhances computational efficiency, achieving a balance between accuracy and speed. This overcomes the high computational cost and limited suitability for iterative design posed by conventional CFD tools such as STAR-CCM+. Furthermore, by incorporating multiple parameters—including platform scale, column geometry, and air gap—the CGNT-CFD method enables a systematic parametric sensitivity analysis, providing quantitative guidance for the structural optimization of offshore platforms.

Firstly, this study establishes an experimental procedure based on a small numerical wave tank to investigate the hydrodynamic properties of semi-submersible platforms. It creates a single-column horizontal wave slamming experiment platform and uses pressure transducers and force plates to quantify wave slamming loads on platform columns under waves. A total of 184 experimental cases were conducted to systematically investigate the wave slamming characteristics on columns under regular waves, focused waves, and freak waves. For regular waves, the peak slamming load, pressure distribution, and pressure-time history are analyzed in relation to variations in air gap, wave incidence angle, and wave period. For focused waves, the study compares slamming effects within wave period ranges of 6.0–14 s and 8.0–12 s. Additionally, it evaluates differences in slamming loads induced by freak waves generated from S-type and J-type spectra under identical wave height conditions. To mitigate the interference from power amplification in the measured slamming loads, wavelet analysis and frequency transfer function (FRF) approaches are applied.

Subsequently, this study presents an innovative CGNT-CFD wave slamming load prediction method, developed by integrating Cartesian-grid finite difference techniques with high-accuracy free surface capturing algorithms. The proposed method achieves both high fidelity in wave reproduction, wave run-up simulation, and structural parameter sensitivity analysis, and significantly improves computational efficiency. It is particularly suitable for rapid prediction of platform load responses under representative wave conditions during the engineering design stage. A convergence analysis was conducted to determine appropriate grid resolution and time step settings. Numerical simulations of 9 regular wave cases were performed, showing excellent agreement with physical experiments, thereby validating the accuracy and robustness of the CGNT-CFD method in wave generation, pressure time history reproduction, and total load prediction. Moreover, the method effectively captured the influence of wave steepness and period on slamming loads under regular wave conditions and accurately reproduced the localized pressure evolution during wave run-up events.

Building upon the preceding research, a multi-parameter sensitivity analysis model was established by incorporating platform parameters such as column shape, scale, and relative position. Using the CGNT-CFD method, a total of 153 simulation cases were conducted to systematically investigate the effects of wave parameters, column air gap, shape, diameter, and deck position on slamming loads acting on platform columns under regular wave conditions. Additionally, the influence mechanism of column spacing on platform wave slamming loads is explored. Under a regular wave condition, it examined the variation in wave loads on the front columns, rear columns, and deck structure for multiple column spacings. The research shows that when the column spacing increases, the wave slamming load on the rear columns increases significantly, even nearly twentyfold. The load changes on the front columns are relatively moderate. Meanwhile, wave slamming loads on the deck structure show a decreasing trend.

This study focuses on the problem of wave slamming on the columns of floating platforms. A scaled model of a platform column and its auxiliary support structure was designed, and a wave-flume-based experimental setup was constructed to establish a comprehensive testing and measurement methodology. Systematic slamming experiments were conducted under regular waves, focused waves, and freakwave conditions to investigate the fundamental characteristics, acting mechanisms, and evolution patterns of wave slamming loads. The findings offer important insights for further research on similar problems. Furthermore, a rapid numerical prediction technique for slamming loads based on the CGNT-CFD method was proposed, which significantly improves computational efficiency while

maintaining high accuracy. This method enables fast assessment of column slamming responses under typical wave conditions. The developed experimental procedures and numerical model provide effective tools for the impact-resistance design and performance evaluation of floating platforms, demonstrating strong theoretical significance and promising engineering applicability.

1 BASIC INTRODUCTION OF HORIZONTAL WAVE SLAMMING

1.1 Background

Maritime resources are gaining increasing attention in the 21st century due to scientific and technological advancements, leading countries to focus on exploiting the vast resources found in the deep sea. As a result, many countries have developed strategies for marine development, moving away from traditional land-based competition. International organizations have also released strategic research reports and planning programs for marine science and technology, with a focus on the period from 2025 to 2030. In 2017, the United Nations Educational, Scientific, and Cultural Organization (UNESCO) released a report titled “Global Ocean Science Report: The Current Status of Ocean Science around the World” at the United Nations Ocean Conference, urging greater investment in marine scientific research and international scientific cooperation. Additionally, the United States and the European Union have released their own ocean development plans, including the “An Ocean Blueprint for the 21st Century” and “U.S. Ocean Action Plan” from the United States and the “European Offshore Renewable Energy Roadmap” which highlights the synergistic growth of offshore wind energy, wave energy, and tidal energy and their associated benefits and development opportunities and challenges.

Oil and gas resources have become crucial energy sources for humanity. Preliminary estimates suggest that global ocean oil reserves have reached 100 billion tons, while natural gas reserves have reached 140 trillion cubic meters. In the past decade, over

100 significant oil and gas deposits have been discovered, with over 60% located in the deep sea. China’s submarine oil and gas resources are primarily situated in the northern parts of the South China Sea, the East China Sea, the Yellow Sea, and the Bohai Sea. Current estimates suggest that these reserves have reached 27.5 billion tons of oil and 10.6 trillion cubic meters of natural gas. Developing and using these resources hold great potential.

Offshore oil and gas resources are now being explored and developed in deep-sea environments, resulting in the emergence of several ultra-deepwater drilling platforms. Floating platforms, in particular, have represented over 100 billion yuan of offshore engineering equipment. Advancements in science and technology continue to increase the scientific and technological content of marine engineering equipment, resulting in the cost of subsea oilfield exploitation decreasing. The use of deep-sea floating equipment, such as floating drilling platforms, production platforms, pipe-laying ships, supply ships, and offshore cranes, is becoming increasingly widespread. In the future, marine engineering equipment will become the core industrial chain of marine resource development and exploration. Although the development of marine engineering equipment and technology in China is still in its infancy and rising stage, there is massive potential for improvement.

Beyond conventional offshore oil and gas development, the mineral resources located in deep-sea regions—particularly at depths ranging from 4,000 to 6,000 meters—are receiving increasing global strategic attention. These resources, including polymetallic nodules, cobalt-rich crusts, and seafloor massive sulfides, are primarily distributed in international waters far from coastal zones, where oceanic conditions are significantly more complex and severe than those found in traditional offshore oil and gas fields. With the rapid rise of advanced manufacturing and the renewable energy sector, the strategic value of these critical minerals continues to grow, positioning deep-sea mining as the next major frontier in marine resource development following oil and gas exploitation.

Unlike operations in nearshore or conventional offshore oil and gas regions, deep-sea mining faces extreme environmental challenges in remote ocean areas, where abnormal waves, long-period swells, and strongly nonlinear wave interactions are frequently encountered. These conditions lead to more intense and complex wave slamming phenomena. The slamming pressure induced by such extreme waves (e.g., rogue waves) is significantly greater than that of conventional random waves with the same significant wave height. A distinct double-peak slamming phenomenon is observed, and the impact periods at different structural locations are out of sync, which further compounds the safety risks for deep-sea structures(Huo et al., 2023). The strength and impact of such nonlinear hydrodynamic effects far exceed those observed in traditional offshore environments, posing significant threats to platform structures. Moreover, due to the lack of long-term observational data, our understanding of sea state patterns in deep and ultra-deep waters remains limited, creating greater uncertainty and design challenges for the hydrodynamic performance and structural safety of mining platforms.

At present, surface support for deep-sea mining still relies primarily on traditional mining vessels. However, these platforms are increasingly unable to meet the demands of multi-location, long-duration operations in severe ocean conditions due to high energy consumption, limited motion stability, and poor wave resistance. In contrast to conventional platforms—which focus on structural stability for drilling and production—deep-sea mining platforms must manage highly coupled systems, including remotely operated mining arms, multi-DOF tracked vehicles, and dynamically loaded lifting pipes. Furthermore, the design of deepwater floating platforms must consider how operational water depth affects the dynamics of structural components like the mooring system(Lin et al., 2021).The platform’s response to wave-induced loads is significantly more sensitive, and the presence of strong nonlinearities—such as wave run-up, green water, and slamming—poses critical risks to structural integrity.

Despite the growing importance of this field, systematic studies on the hydrodynamic performance of deep-sea mining platforms under extreme environmental conditions remain scarce. Both the physical understanding of wave-platform interactions and the availability of accurate, efficient numerical simulation tools are insufficient. In response, this study addresses both oil and gas and deep-sea mining contexts, and for the first time, systematically incorporates the wave slamming phenomenon into the structural analysis of deep-sea floating mining platforms. Through extensive model tests and numerical simulations, it investigates transient hydrodynamic loads and structural responses in sensitive areas such as columns and bottom deck regions under extreme wave conditions.

To address the limitations of conventional approaches, this study further develops a high-efficiency numerical wave tank-A Regular Fixed Cartesian Grid Numerical Tank CFD (referred to as CGNT-CFD), which effectively overcomes challenges in mesh generation and free surface tracking. The proposed method significantly enhances computational efficiency and stability in wave impact simulations. Additionally, a fast wave load estimation model and correction algorithm is introduced, tailored to the structural complexity and coupling characteristics of mining platforms, offering a practical and robust tool for design and risk assessment in extreme sea states.

1.1.1 Development and application of typical floating platforms

Floating offshore platforms have emerged as the primary equipment for developing oil and gas resources. These platforms come in four primary forms based on their structural design, including Tension Leg Platform (TLP)(Yang et al., 2009; Hayat, 2012), single-column Spar(Gu, 2008), semi-submersible(Qiang, 2013), and floating production storage and transportation units (FPSOs)(Zhao, 2006). This section will introduce TLP and semi-submersible.

Fig 1.1. Various forms of floating platforms, adapted from Cui (2018)

A TLP is a vertically moored compliant deepwater platform that consists of three primary parts: the main platform body, the tension leg system, and the structural foundation. The main body of the platform supports the load on the upper part of the deck and provides pre-tensioning to the structure. The tension leg system connects the main body of the platform to the seabed to provide support, while the structural foundation provides the pull-out force of the tension leg system to ensure the platform's overall stability.

The main structure of a TLP typically consists of columns and buoys, and the tension legs connect the main body and the seabed foundation. The buoyancy of the main structure puts the tension legs in a tensioned state, while the seabed foundation uses a gravity foundation or a pile foundation.

The TLP was conceived by American engineer R.O. Marsh in the 1950s(Dong, 2005), using tension in the heaving direction to vertically moor the platform's tension leg system on the seabed. This method offers an advantage in that the natural period of each movement direction of the platform is far from the energy concentration period range of waves in the ocean. As a result, the TLP has good movement performance and is suitable for the exploitation of deepwater oil and gas resources(Gie and de Boom, 1981; McIver, 1981; Oran, 1983; Datta and Jain, 1988). Its structural design is relatively diverse and can be selected based on the specific marine environment and seabed geological conditions. The TLP has been widely used in recent decades.

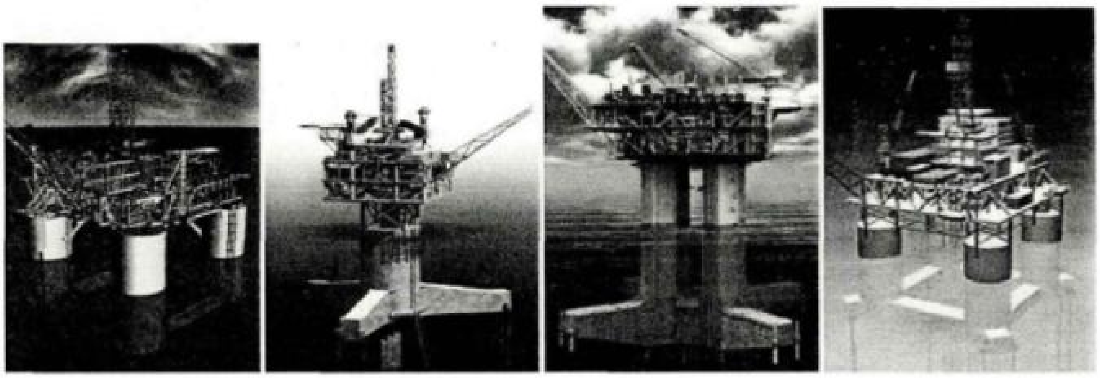

(a)CTLP (b)Seastar (c)MOSES (d)ETLP

Fig 1.2. Different tension leg platforms, adapted from Wu (2014)

There are four types of TLPs. Firstly, the traditional TLP consists of 3 or 4 columns and pontoons connecting them. Secondly, the Starfish TLP, similar in design concept to the mini-TLP, is a single-column TLP. Designed and patented by Atlantia in 1992, it is mainly used in the exploration and development of oil and gas fields with small reserves. Thirdly, the Minimize Deep-sea Surface Equipment Structural Tension Leg Platform (MOSES-TLP), proposed by Peter Wybro, not only improves the effective bearing efficiency of the platform but also reduces the difficulty and cost of installation and construction. It inherits the main advantages of traditional TLPs, including better heaving motion performance, and improves the motion performance to some extent. Lastly, the Extended Tension Leg Platform (ETLP), proposed by ABB, expands the mooring range and reduces the distance between the columns, thus improving the main structure of the traditional TLP. The obvious advantages of this type of platform over traditional TLPs are better motion performance and greater carrying capacity(Yan and Ou, 2012).

Semi-submersible platform, also known as a column-stabilized platform, is a type of mobile platform with most of its floating body located below the waterline. This design, featuring a low waterline area, was developed in the late 19th century primarily for the purpose of studying the wave resistance of high-speed vessels. Over time, with advancements in technology, it has evolved into semi-submersible drilling platforms and other floating marine equipment. The emergence of semi-submersible platforms can be traced back to the 1960s. Initially, they were often used for bottom-seated operations. However, as the water depths increased, semi-submersible platforms abandoned the bottom-seated drilling approach starting from the 1970s.

Table 1.1. Parameters of typical semisubmersible platforms in China

Name	Year of Construction	Classification society	Max working depth(m)	Main dimension(m)	Number of columns
Nanhai No.2	1974	ABS	304	108.2×67.36	8+2
Nanhai No.6	1982	DNV	457	95.11×71.14	6+2
Nanhai No.5	1983	ABS	457	92.35×68	6
Pioneer	2011	DNV	750	104.5×65	4
Innovator	2011	DNV	750	104.5×65	4
HYSY-981	2012	CCS+ABS	3000	114×89	4
Promoter	2012	DNV	750	104.5×65	4

A semi-submersible platform is mainly composed of a double-deck structure, multiple columns, lower pontoons, and other support structures. The deck supports operational and living facilities for personnel, while the columns connect the lower pontoons and the deck. During operation, the lower pontoons are submerged below the free surface to provide sufficient buoyancy, while the deck maintains a certain air gap to minimize the impact of wave slamming. The columns maintain a certain height of submersion below the water surface. Compared to other types of floating platforms, semi-submersibles exhibit smaller pitch and roll motions but larger heave motions. In deepwater operations, they rely on an anchoring system for positioning.

Benefiting from its structural form, the semi-submersible platform is more resistant to wind and wave and has a greater deck space, can operate in sea depths of up to 3,000 meters, and is capable of drilling and production, lifting, pipelaying, among other operations.

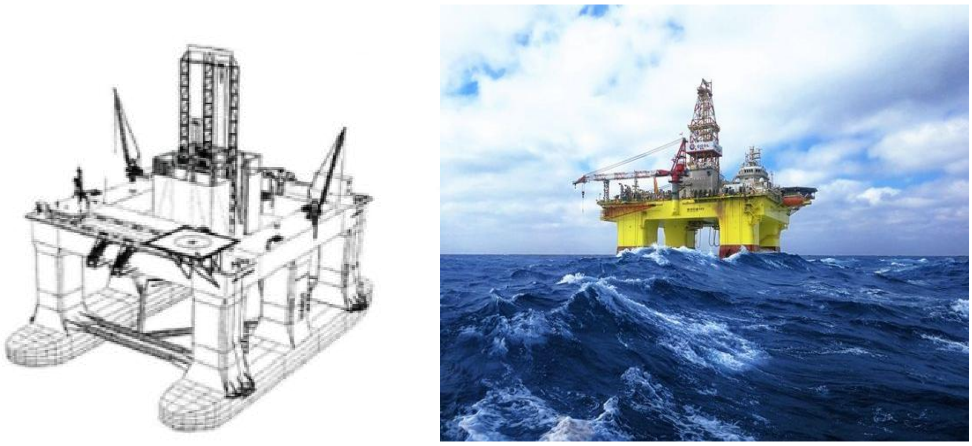

Fig 1.3. Schematic diagram of a typical semi-submersible offshore platform, adapted from Shaanxi United Mechanical Co., Ltd. (2024)

The semi-submersible platform has undergone significant changes from the first to the current sixth generation. In the sixth generation, the platform can operate at a depth of 3000m, a significant improvement from the initial depth of 200m.

1.1.2 Typical cases of horizontal slamming accidents of floating structure

Due to inadequate understanding of the deep-sea marine environment and its complexity, marine platforms are vulnerable to extreme marine conditions such as high winds and huge waves, leading to damage during service. Between 1954 and 1982, more than 30 oil platforms worldwide sank due to bad storms(Zhao, 2009). For instance, Norway’s Ekofisk Petroleum Drilling Platform sank due to large waves(Kaplan and Silbert, 1976). In 2004, Hurricane Ivan caused the American drilling platform ENSCO64 to drift 60 kilometers away from its working waters(Veldman et al., 2011). In 2005, Hurricane Katrina caused extensive damage to 47 platforms, including the American Shell Mars and Ocean Warwick(Kaiser et al., 2009). Despite the advanced design of the MARS TLP platform, which had a wind resistance capacity of 62.5m/s and a wave resistance of 22.86m, the maximum wind speed caused by Hurricane Katrina was 64.7m/s, and the maximum wave height was 25.9m. As a result, the MARS TLP platform suffered severe damage under such conditions, and over 1 million working hours were required to repair it. Fig 1.4 shows the damage caused to the ENSCO platform by waves.

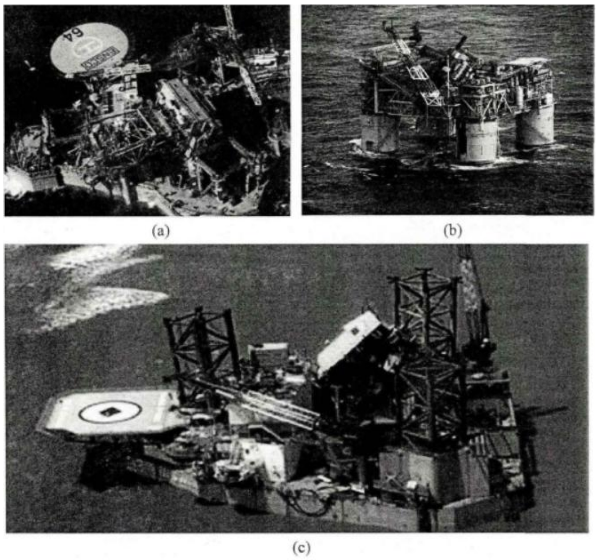
(a) (b)
(c)

Fig 1.4. Damage to platforms due to extreme sea conditions (a) Ensco 64 platform (b) Shell Mars platform (c) Ocean Warwick platform, adapted from Fu (2020)

On September 28, 1994, the Estonia passenger ship (shown in Fig 1.5) was en route from Tallinnia, Estonia to Stockholm, Sweden, carrying 964 passengers and crew members, of which only 141 survived(PC 2001). This incident remains the worst maritime accident in Europe since World War II. The accident investigation report revealed that the passenger ship suffered damage under the action of wave shock loads. Additionally, the ship’s large and flat tail caused tail-knocking phenomena under extreme wave conditions, leading to overall hull structure resonance, reducing passenger comfort, and causing severe damage to the hull structure.

Fig 1.5. Estonia passenger ship, adapted from The Sun (2020)

Fig 1.6. Wave slamming in actual marine environment, adapted from Webb (2009) and Marine Public (2020)

Fig 1.7. Damage sustained in the COSL Innovator wave slamming incident, adapted from Petroleum Safety Authority Norway (PSA) (2016)

On December 30, 2015, during operations at the Troll oil field in the Norwegian North Sea, the semi-submersible drilling platform COSL Innovator encountered severe wave slamming under harsh sea conditions, resulting in a major safety incident. The accident caused one fatality, two serious injuries, and extensive structural damage to the forward accommodation area of the platform. The deceased crew member was located in a lower deck cabin, where the porthole was shattered by wave impact, leading to instantaneous death. The slamming event severely damaged a total of 17 cabins and corridors across two accommodation decks on the forward port side of the platform. On the lower deck, six windows were broken, while the mezzanine deck suffered damage to eleven windows, resulting in significant water ingress. Figure 1.7 illustrates the structural damage sustained by COSL Innovator due to wave slamming in the extreme sea state, showing clear signs of typical horizontal wave impact on the upper structure. This incident revealed a lack of consideration for horizontal slamming loads on the platform's upper structure during the design phase and highlighted the serious safety risks floating platforms may face in real sea conditions.

1.2 Research challenges of wave slamming on floating structure

The phenomenon of wave slamming is expected in both natural and engineering applications, such as the interaction between floating marine structures and waves, the process of wavy surge to the coast, and the collapse of the coast. This process involves the coupling of gas, liquid, and solid, and has highly nonlinear characteristics. For typical semi-submersible platforms, the slamming process is complicated by the impact of columns and horizontal support on the transmission of waves passing through columns. When the structure contacts wave peaks, it experiences not only solid dynamic pressure with relatively slow changes, but also a short but intense shock pressure that can cause partial or overall destruction of the platform’s stability.

The moment the structure is in contact with the peaks, in addition to the solid dynamic pressure of the relatively slow changes, it will also receive a very short but intense shock pressure. In addition to the partial shock load that can lead to partial parts of the structure, the destruction will also cause the overall stability of the platform.

The physical processes of slamming waves have the following six characteristics: very short duration of action; strong non-linearity of the instantaneous fluid; severe changes in the wet surface of the structure; broken splashes and wave rolls at the free water surface; instant pressure and acceleration; existence of high-speed firing and air cushion effects. Due to the presence of intense free surface breaking and transient high-pressure processes, conventional CFD methods struggle to achieve efficient simulations without compromising accuracy, making the rapid prediction of slamming loads a major bottleneck in current engineering design. In addition to the aforementioned characteristics, floating platforms are typically subjected to the effects of hurricanes, waves, and ocean currents in the working environment. The structural motion responses occurring in the complex environmental conditions act in coupling with each other. Furthermore, various physical quantities undergo rapid variations in time and space during the slamming process, further complicating the research on wave slamming phenomena. Additionally, in addition to conventional waves, the load effects of special wave types, such as internal solitary waves, on semi-submersible platforms must also be incorporated into complex environmental analyses. Their nonlinear load characteristics further increase the research complexity of the wave-structure coupling response, necessitating in-depth investigation through an integrated approach of numerical simulation and experimental testing(Wang et al., 2018).Particularly noteworthy is that the nonlinear impact mechanisms of extreme waves (e.g., rogue waves) are considerably more challenging to capture. During their interaction with a fixed horizontal deck, both the abrupt changes in the wave surface profile and the highly concentrated energy transfer exhibit strongly nonlinear characteristics. Conventional linear theories prove inadequate for accurately describing these phenomena, necessitating the use of targeted numerical simulation methods to elucidate the underlying impact physics(Qin et al., 2017).

The wave slamming phenomenon is closely related to the platform’s air-gap response. According to the definition in DNV-RP-C205, the initial air gap refers to the vertical distance between the lower deck of the platform and the still water level, while the dynamic air gap denotes the vertical distance between the deck and the instantaneous wave surface under wave action, as expressed in the following equation. A negative air gap indicates that the wave has impacted the deck, i.e., a slamming event has occurred. Research on wave slamming loads is therefore inseparable from the study of air-gap response, which is inherently challenging to predict. This difficulty arises because the multiple columns and bracing members of a floating platform cause wave interactions, superposition, and disturbances as waves propagate beneath the deck. In certain local regions, this can lead to wave amplification, greatly increasing the complexity of slamming analysis.

$$a(x,y,t) = a_0 + z(x,y,t) - \eta(x,y,t) \tag{1.1}$$

A significant coupling effect exists between wave slamming and structural vibration. The dynamic amplification induced by the structural vibration itself can further exacerbate the impact loads from breaking waves on the structure. Consequently, load prediction must simultaneously account for both fluid nonlinearities and structural dynamic response, which substantially increases the complexity of the analysis(Choi et al., 2015). Furthermore, scale effects are a key concern that must be considered in both numerical modeling and physical experiments. Failure to account for them may result in inaccurate load forecasts, which complicates the load scaling process for design purposes(Chen et al., 2024).

1.3 Research objectives, content and meaning of horizontal wave slamming

The mechanical equipment for production operations and staff accommodation are on the upper deck of floating offshore platforms. When the wave slamming accident occurs, the main deck and the column structure are the first to bear the brunt. In order to ensure the safety of personnel and equipment, it is necessary to conduct research on the location of wave slamming and the magnitude of slamming pressure acting on floating platforms under different environmental conditions. Strengthening measures should be implemented for vulnerable structures, while also making rational arrangements for the placement of machinery and personnel on the deck, avoiding areas where wave slamming is likely to occur, and minimizing the hazards associated with wave slamming.

With the increase of operating water depth, offshore drilling or Deep-sea mining semi-submersible platform will face more severe marine environments, such as rapids, gales and huge waves. Meanwhile, due to the lack of deep-sea hydrographic data, it is also difficult to forecast the hydrographic conditions in the working area of floating platforms. Therefore, in order to minimize the potential losses of personnel and property when floating platforms experience wave slamming, it is necessary to consider the interaction between wave slamming and the structural integrity of the platform during the design phase. Further investigation into the underlying mechanisms of the wave slamming process is highly warranted.

On the other hand, the wave slamming process is characterized by strong nonlinearity and intense locality, with its effects significantly influenced by wave parameters (such as period and steepness) and platform geometry (such as column spacing and air gap). Traditional potential flow theory fails to accurately capture strongly nonlinear phenomena like breaking waves and free surface overturning. While general-purpose CFD tools (e.g., STAR-CCM+) can deliver high-accuracy simulation results, they come with extremely high computational costs, making them unsuitable for rapid evaluation of numerous cases during the engineering design phase. Existing simplified methods, such as OTG13/14, offer computational efficiency but suffer from clear limitations in accuracy and applicability.

This study adopts a combined experimental and numerical simulation approach to systematically reveal the mechanisms, response characteristics, and key influencing factors of wave slamming on the columns of floating platforms. Particular emphasis is placed on beam sea (transverse wave) conditions, as they are more likely to induce intense, transient nonlinear impacts on the wave-facing surfaces and corner regions of the structure, making them highly representative and technically challenging. The proposed CGNT-CFD method, integrating structured Cartesian grids with an efficient free surface capturing algorithm, improves simulation efficiency while ensuring accuracy, enabling rapid prediction of slamming loads under typical wave conditions. This method provides strong support for establishing quantitative relationships between slamming loads and platform geometric parameters, laying a solid foundation for future parametric design in engineering applications.

1.4 Review of the method and development of horizontal wave slamming research

1.4.1 Theoretical methods and progress on wave slamming research

In general, the wave slamming phenomenon on marine structures can be simplified as the impact of waves on flat plates and cylinders. The deck of a floating platform can be considered as a larger-scale flat plate. However, due to the presence of multiple columns and submerged bodies, complex interactions occur between the platform and the waves, making the mechanism of wave slamming even more intricate.

For decades, the early research on wave slamming was simplified to columns covered with platforms or box structures. However, as the study progresses, the non-linear processes, such as the crushing and rolls of waves, are also considered. In the case of slamming on asymmetric structures, such as angled wedges, conventional simplified models are often inadequate in representing the variations in load distribution, necessitating the use of comprehensive numerical approaches for analysis(Krastev et al., 2018).

The simplified calculation method based on momentum theory and the estimation method based on statistical theory is often used by the engineering community to quickly forecast the platform’s maximum horizontal and vertical slamming load. In the simplified calculation method for wave slamming loads on platforms, the slamming pressure coefficient C_S is an essential parameter used to predict the maximum slamming load. Its expression is defined as follows:

$$C_S = \frac{2F_S}{\rho A U^2} \tag{1.1}$$

F_S is the wave slamming load measured in the model experiment. ρ is the density of the seawater. A is the wet area of the wavy hit area. U is the velocity of the water quality point in contact with the platform structure during the wave slamming process. The slamming pressure coefficient determines the relationship between the water quality point velocity and the slamming load. Generally speaking, the value of the slamming pressure coefficient is selected between π and 2π(Roos et al., 2009). Baarholm proposed a simplified calculation formula for determining the vertical slamming load on offshore platform decks, which is applicable to three-dimensional complex structures and holds certain significance(Baarholm, 2005). The core of this method lies in approximating the additional mass of the slamming region during wave slamming on the deck using thin rectangular plates and thin elliptical plates as additional masses.

According to the constant theorem of momentum, the vertical wave slamming load received by the deck can be expressed as:

$$F_3 = \left(\frac{d}{dt}(A_{(t)}V_{(t)}) \right) = \frac{dA_{(t)}}{dt}V_{(t)} + A_{(t)}\dot{V}_{(t)} \tag{1.2}$$

Among them, *A(t)* is the wet surface area of the immediate deck slamming area. *V(t)* is an average relative wave slamming velocity. The first item on the right represents the contact force of the water quality point and the deck. The latter item is the inertial force on the fluid mass. This formula was previously used to study water ingress as well as egress from structures(Wagner, 2006).

In addition, the fluctuating pressure from diffracted wave fields and the hydrostatic pressure also have a significant impact on the slamming load of the entire platform. Therefore, the total load on the platform deck can be expressed as:

$$F_3 = \frac{dA_{(t)}}{dt}V_{(t)} + A_{(t)}\dot{V}_{(t)} + \rho\Omega(g + \overline{a}) \tag{1.4}$$

Among them, ρ is the density of seawater, ω is the volume of seawater instantly above the lower deck surface, and $\overline{\alpha}$ is the average acceleration of water particles in the slamming region beneath the deck during wave slamming. It is worth noting that the vertical momentum transfer is considered only during the stages of submergence and emergence of the structure.

Arbitrary-shaped deck slamming regions can be approximated using rectangular or elliptical plates. The additional mass of a three-dimensional rectangular plate located at the free water surface can be expressed as:

$$A_{(t),rect} = J(k)\frac{\pi}{8}\rho l^2 b \tag{1.5}$$

Among them, *l* and *b* represent respectively the length and width of the plate, while *k=b/l* is the length-width ratio coefficient. The formula *J(k)* reflects the three-dimensional effect, and its expression is:

$$J(k) = \frac{1}{\sqrt{1+k^2}}(1-\frac{0.425k}{1+k^2}) \tag{1.6}$$

Similarly, the additional quality of the three-dimensional oval plate (long shaft is *b*/2, and short shaft is *a*/2) at the surface of the free liquid can be expressed as:

$$A_{(t),ellipse} = C_s\rho\frac{\pi}{12}a^2 b \tag{1.7}$$

Among them, C_S is the additional quality coefficient of the plate, which depends on the length and width of the oval plate aspect ratio *b/a*. It should be noted that b must be equal to or greater than a. For platform slamming events with a wave incidence angle of 45°, the shape of the slamming region closely resembles an isosceles triangle. The additional mass of the slamming region in the form of an isosceles triangle can also be approximated using the formulas for rectangular or elliptical plates. In this case, the aspect ratio is defined as the ratio between the base length *b* of the triangle and its height *h*.

In the end, Baarholm applied this simplified calculation formula to estimate the wave slamming load on a gravity platform and compared verification with the corresponding model experiment results. This method can well forecast the wave slamming load. However, when considering high-order effects, Stansberg and Suyuthi(Stansberg et al., 2004; Suyuthi and Haver, 2009)believe that for the problem of wave slamming on the multi-column platform, particularly in severe sea conditions with large wave steepness parameters, the application of simplified calculation methods based on momentum theorem and potential flow theory to estimate platform slamming loads still fails to meet the requirements.

In addition, the current research hotspot is the method of obtaining the statistical model of platform wave slamming loads based on the wave statistical model of regional sea conditions, which is closer to real sea conditions and has significant implications for the engineering field. In the early stages, Haver proposed a Gumbel distribution model to predict platform wave slamming loads under extreme sea conditions(Haver, 2013). Subsequently, Dalane also established a Cumulative Frechet distribution model to estimate platform wave slamming loads under design sea conditions(Dalane, 2011).

For multi-platform column events of wave slamming, the occurrence of peak slamming loads is both spatially and temporally a local phenomenon(Iwanowski et al., 2009). There is still debate on how to select representative wave groups or sea conditions when selecting design wave slamming loads. Different regions, regulations, and requirements of different organizations vary. Currently, most numerical simulations use regular waves to study wave slamming loads.

1.4.2 Numerical simulation methods and progress on wave slamming problems

Currently, the more conventional numerical simulation uses the numerical research method based on the theory of potential flow. Due to the short time of the slamming process, the viscosity of the fluid can be ignored, so the inviscid assumption of the potential flow theory can be well accepted. Furthermore, during the wave slamming event, the acceleration of fluid particles is significantly greater than the acceleration of gravity. If the duration of the structure's submergence phase to emergence phase during the slamming process is relatively small compared to the wave period, the gravitational term can be neglected when calculating the wave slamming load. However, the existing research shows that the second-order item must be considered when using the potential flow theory to solve the problem of waves of the platform.

From the perspective of research status, the study of air gap in offshore platforms has predominantly employed potential flow theory and combined model experiments with numerical calculations to analyze air gap responses. In the past two decades, significant progress has been made in the research on solving the free water surface using the second-order diffraction-radiation method, which has laid a solid foundation for solving wave slamming problems using potential flow theory. Among them, the interaction of small amplitude rules and simple structures can predict wave power through approximate interaction and dynamic relationships. However, under conditions of freak waves and extreme wave actions, potential flow theory struggles to accurately simulate the effects of radiation, diffraction, and wave generation on the wave surface. The simulation accuracy of the wave surface is insufficient, making it challenging to use potential flow theory for predicting wave slamming loads. In such cases, the use of computational fluid dynamics (CFD) offers significant advantages in predicting wave slamming loads. CFD methods typically employ the Navier-Stokes equations to describe the unsteady motion of viscous fluids over time, allowing for more accurate simulation of wave surface variations. In the context of water entry and slamming for three-dimensional solids (e.g., platform columns, ship bows), traditional two-dimensional simulations fail to capture three-dimensional effects such as lateral wave propagation and local impacts at structural corners. By employing the Finite Volume Method to discretize the Navier-Stokes equations, coupled with the Volume of Fluid method for simulating the gas-liquid two-phase flow, the intricate details of the three-dimensional slamming flow field can be effectively reconstructed(Facci et al., 2016).The numerical wave tank is central to CFD simulations of wave slamming, as the accuracy of its wave generation directly governs the reliability of slamming load predictions. Conventional wave-generating methods are often prone to issues such as wave surface distortion and reflected wave interference. In contrast, some advanced numerical wave-making techniques, which incorporate optimized algorithms, can enhance wave stability and fidelity, adapt to complex wave conditions, and thereby provide reliable incident wave conditions for load simulation(Martínez-Ferrer et al., 2018). Alternatively, some researchers have turned to improved density interpolation schemes to effectively mitigate numerical diffusion at the gas-liquid interface. This approach allows for a more accurate resolution of highly nonlinear phenomena such as wave breaking and overturning, thereby providing a superior tool for simulating the interaction between breaking waves and structures(Bihs et al., 2016).

Iwanowski and Matsumoto conducted nonlinear calculations of the air gap response of multi-column semi-submersible platforms using the commercial software ComFlow(Iwanowski et al., 2009). Zhu performed two-dimensional flow simulation and calculated the radiation damping coefficient and added mass of a specific model of container ship using Fluent(Zhu and Guo, 2009). Yang used CFD methods to investigate the effect of wave length variation on the roll motion of a frigate under regular waves, and the numerical results demonstrated that CFD can be an effective tool for studying nonlinear roll motion of ships(Yang and Shi, 2015). Zheng et al.. conducted resistance prediction analysis of ships based on potential flow theory and viscous theory, and proposed a numerical prediction method for ship resistance using CFD(Zheng and Huang, 2014). Terziev et al.. integrated posteriori error and uncertainty estimation methodologies into their CFD simulations of ship hydrodynamics. They verified the numerical accuracy against local parameters, including free-surface elevation and surface friction, thus providing a methodology for identifying regions of high error within the computational domain(Terziev et al., 2020). Kim et al.. conducted two preliminary simulations to predict the VIM of a

TLP design, and the validation against model experiments showed good agreement at low speeds(Kim et al., 2011). Du et al.. calculated the wind, wave, and current loads on a semi-submersible platform during towing motion using empirical formulas, CFD software, and numerical integration methods(Du and Liu, 2014). Wang implemented various hydrodynamic performance calculations related to the design of deepwater floating offshore platforms based on CFD and boundary element methods(Wang, 2011). Gu and Yang studied the motion response, particularly vortex-induced vibration phenomena, of a TLP using a combination of CFD methods and panel theory(Gu and Yang, 2015). Huo et al.. modified the computational fluid dynamics method based on potential flow theory to develop an air gap prediction method for a deepwater semi-submersible platform, and found that the effects of radiation, diffraction, and wave excitation resistance around the platform on air gap prediction were significant(Huo and Zhang, 2015). Bilandi et al.. supplemented the body of numerical research on asymmetric structure slamming by conducting simulations of a vertical water-entry asymmetric wedge using the Finite Volume Method(Bilandi et al., 2018).

The utilization of CFD method for the analysis of wave slamming on floating platforms enables the simulation of non-linear flow phenomena such as wave breaking, which cannot be accurately captured by the potential flow theory. CFD can also obtain detailed data of the flow field, laying the foundation for analyzing the slamming pressure distribution and the improvement of the mechanism and platform structure laid the foundation. However, there are certain defects in the CFD method. Due to its requirement for a high-resolution mesh, accurate results necessitate the generation of millions of computational grids. Consequently, this places significant demands on computing resources and results in low computational efficiency. Presently, hydrodynamic software packages such as Fluent and STAR-CCM+ offer solutions for simulating wave slamming on floating platforms. These software packages employ the Volume of Fluid (VOF) method to effectively handle the complex changes in the free water surface.

It is worth mentioning that Lucy and Monaghan proposed an SPH (smooth particle method) in 1977, which is also used to solve non-linear free water surfaces. The core idea of the SPH method is to describe continuous fluid with interactive particles combination(Gingold and Monaghan, 1977; Lucy, 1977). Each particle contains a set of corresponding physical quantities, including speed, mass, and other information. By solving the dynamic equations of particles and tracking the motion trajectories of each particle, the mechanical characteristics of the entire flow field can be obtained. In theory, as long as the number of particles is sufficient, this method can accurately describe the hydrodynamic process. Later, many scholars used this method to study the problem and obtained better results. Oger investigated the water entry problem of wedge-shaped objects using the Smoothed Particle Hydrodynamics (SPH) method, and proposed a particle search method and a pressure treatment method for curved boundaries(Oger et al., 2006). Zheng et al.. established a CGNT-CFD method based on the incompressible SPH (ISPH) method and made a preliminary numerical simulation of two-dimensional and three-dimensional horizontal panel wave slamming problems(Zheng and Sun, 2009). Lind et al.. employed an incompressible-compressible SPH approach to simulate water-air wave slamming, thereby extending the application of SPH methodology to multi-phase impact problems(Lind et al., 2015).

1.4.2.1 Influence of platform air gap height on slamming

The air gap height is an important parameter that must be considered when designing the marine platform. It determines the survivability of the platform under extreme sea conditions. The earliest studies of platform air gap heights originated from flat plate wave slamming. Ren Bing et al.. used the PIV (Particle Image Velocimetry) method to observe wave slamming on the flat plates(Ren et al., 2007). Their statistical patterns were obtained by measuring the velocities of the water particle points contacting the flat plate at different hydrostatic air gaps and their corresponding generated slamming loads.

Sweetman et al.. researched the minimum air gap distribution near a semi-submersible marine platform(Sweetman and Winterstein, 2003). Through the extreme statistical model of the two fluid software, the effects of the numerical calculation and model experiment were compared. Stansberg et al.., based on the WIMIT potential flow software, conducted a simulation calculation of wave height and air gap response near the semi-submersible platform column(Stansberg et al., 2004). Kazemi et al.. analyzed their air gap response for a semi- submersible platform(Kazemi and Incecik, 2005). The relevant effects of mixed boundary element method and weighted residual method were considered during the calculation process. From the results, it can be found that wave steepness and air gap values are closely connected. The results of the two are not much different when the wave steepness is small, but when the wave steepness is large, there is a significant difference between the calculation results of the two. Kazemi et al.. conducted model experiment research on a semi-submersible platform(Kazemi and Incecik, 2006). The study showed that the air gap was minimal when the platform was near the column area, and the extreme value of the wave height appeared at the junction of the front column facing the waves and the pontoon. Simos et al.. modeled a semi-submersible platform in a pool and found that the wave climbing phenomenon near the column was often ignored in previous research, and this has an important impact on the air gap response(Simos et al., 2008).

Iwanowski et al.. conducted a study using ComFLOW software to analyze the air gap variations on the marine platform and compare the theoretical study with the experimental results(Iwanowski et al., 2009). Li et al.., taking the semi-submersible platform with double-pontoon and multi-columns as the research object, analyzed the relative distance between the deck's focus and the wave surface, and also the air gap value under extreme sea conditions(Li et al., 2010). Macaymoto et al.. have proposed a complete non-linear method for calculating its air gap response and distribution for a large water line surface column semi-submersible platform(Matsumoto et al., 2013). Naess et al.., for the semi-submersible platform working in the North Atlantic region, designed a pool experiment model and conducted water power analysis tests(Naess et al., 2008). This platform's hydrodynamic performance under extreme sea conditions was obtained and their focus were the air gap response value and wave slamming load at different structures of the platform. Kim et al.. conducted numerical simulations of the air gap response of a floating platform equipped with a lifesaving device under various environmental loads such as waves, wind, and currents, taking into account the effect of the air gap of the lifesaving boat, for a floating platform under complex environmental loads(Kim et al., 2016).

Zeng et al.. used numerical simulation to study the distribution of air gaps in different environmental conditions and compared the calculation results with the model experiment(Zeng and Yang, 2009). Jiang et al.. used the method of three-dimensional source-sink distribution, carefully considered the six-degree-of-freedom motion response function and free water surface change function, and obtained the response spectral function through wave spectral computation to carry out the research of forecasting methods for the air-gap response of semi-submersible platforms(Jiang and Cui, 2014). Wang et al.. studied the air gap response of the semi-submersible platform based on the theory of potential flow and analyzed the effects of different periods, wave directions, and wave height on the air gap value(Wang and Liu, 2015). Huo et al.. explored how the changes in environmental conditions such as depth, quality rotation radius, and wave currents in the working waters are related to air gap response and wave slamming load of the platform(Huo et al., 2016).

In order to analyze the air gap distribution of the platform under the influence of various wave steepness, Simos performed a pool test with a semi-submersible platform model with relatively large downsizing(Simos et al., 2008). The results revealed that the wave climbing phenomenon around the columns has a non-negligible impact on the air gap value under smaller wave steepness. Liang et al.. used the DeepC commercial software of potential flow theory, combined with the VOF method, which can set the wavefront as a free water surface, and obtained the air gap response prediction of the moored positioning platform(Liang et al., 2010). The accuracy of the model calculations was higher than the results from linear theoretical calculations when the wave height was significant, according to research by Sweetman et al.. into the air gap response prediction of ocean platforms using WAMIT software for the second-order nonlinear component of waves(Sweetman et al., 2001). Kazemi et al.. used a model test method to conduct a pool experiment and analyzed the air gap on a type of semi-submersible platform(Kazemi and Incecik, 2006). They found that the negative air gap of the platform mainly appeared near the column and a wave height maximum occurs in the middle region of the column above the pontoon.

1.4.2.2 Effect of wave climbing on slamming

During the interaction between waves and platform columns, prominent waves bypass and amplitude effects will occur around the column, and the waves will rise rapidly upward along the surface of the column. The free water surface presents strong non-linear characteristics on the surface of the column, and the wave climbing significantly increases the slamming and the risk of wave crossing, which will cause damage to localized components of the semi-submersible platform and related equipment. Therefore, the study of wave climbing effect is essential for the prediction of the semi-submersible platform wave slamming load.

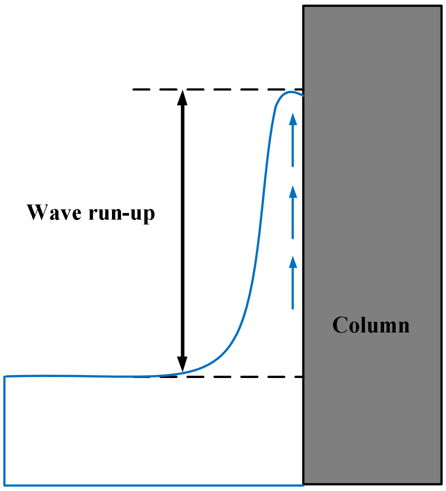

Fig 1.8. Wave climbing phenomenon

Iwanowski used ComFLOW, acommercial fluid computing software, to simulate the wave climbing phenomenon around a semi-submersible platform and compared it with the results of a simplified semi-submarine platform experimental model(Iwanowski et al., 2009). The research results show that with ComFLOW, the platform, when in the fixed mode, can accurately simulate the deformation and rolling phenomenon that appears after the waves climbed along the columns to the lower deck. However, not considering nonlinear coupling movement between the waves and the platform, this method cannot truly reflect the wave surface distribution around the platform.

Apart from the wave parameters, the research of Shang Tiebing et al.. shows that the inherent attributes of the platform, such as the scale and horizontal section shape of the platform column, the platform air gap, the shape and scale of the underwater sinking box, the distance between the columns, the form of platform mooring system, etc., have influenced wave climbing effect around the opposite column(Shan et al., 2012). P. Teigen et al.., based on the second-order scattering theory, researched the wave surface distribution characteristics near the platform, and compared and analyzed the numerical forecast of the platform in stationary and moored states(Teigen and Niedzwecki, 2003). The results show that the platform motion response has a large impact on the wave surface distribution around the four columns of the platform as well as in the middle position of the platform infield; especially when the wave steepness parameter is large and the radiation effect is enhanced, a large wave surface elevation in the local area will occur due to more obvious coupling between the wave and the platform,

Shan also conducted the wave climbing test research in three models (single column, double-standing columns, and four-standing column forms)(Shan and Yang, 2014). The results reveal that the wave climbing level reached the maximum value at the front column windward surface and gradually decreased as the spread of the waves gradually decreased. It is found from the test of the double-standing column and the four columns that as the spacing of the column increases, the wave climbing level gradually decreases, which shows that column spacing has a significant influence on the interaction between the waves and the columns. For the first time, Nielsen conducted a regular wave experiment on the column-like cylinder with the guidance angle and studied the effects of the horizontal section of the column on the wave climbing effect and its surrounding wave surface distribution(Nielsen, 2003).

1.4.2.3 Influence of wave parameters on slamming

Studying the effect of wave direction on wave slamming on multi-column platforms, especially on load distribution, can guide the arrangement of platform equipment. This is especially significant for semi-submersible platforms using dynamic positioning systems. To show the difference, relevant codes such as API and DNV have defined the wave slamming load estimation formulas for 0° wave angle and 45° wave angle, respectively.

Brodtkorb conducted wave slamming research on a catenary platform at 0° wave angle and 45° wave angle by using CFD numerical simulation method and the formula based on API specification(Brodtkorb, 2008). The results show that the maximum horizontal slamming pressure coefficient at 0° wave angle is larger than that at 45° wave angle. However, the maximum vertical slamming pressure coefficient appears at 45° wave angle. At the same time, the degree of dispersion of the spatial distribution of the load is greater at a wave angle of 45° than at a wave angle of 0°. Sonneville studied the wave-slamming load characteristics of a gravity platform at 0° wave angle and 45° wave angle through model experiments(de Sonneville et al., 2015). The research results also show that the maximum horizontal slamming load occurs at a wave angle of 0°.

Using model experiments, Stansberg studied the wave-slamming problem of a gravity platform at different wave angles(Stansberg et al., 2004). The results show that the horizontal slamming load and vertical slamming load on the platform deck are close when the wave angle is 0°. Nevertheless, at a wave angle of 30°, the vertical slamming load on the deck is greater than the horizontal slamming load.

However, when the wave angle is 45° , the horizontal wave slamming load acting on the deck is weakened due to the interference of the upstream column on the incident wave. However, for a multi-column platform such as a semi-submersible platform, due to the interference of the columns, it becomes difficult to study the influence of the wave angle on the slamming load of the platform.

Liu et al.. studied the wave slamming load and its spatial distribution of the semi-submersible platform in different wave directions through the method of model experiments(Liu and Guo, 2018) and found that the wave slamming load is the most serious under the condition of transverse waves, followed by head waves and under the condition of oblique waves the lower slamming load and frequency are relatively moderate. In terms of spatial distribution, the slamming load on the column is greater than that on the deck, and the wave slamming on the deck is more severe under 180-degree transverse waves. The slamming presents a certain degree of random distribution in space. The wave slamming load has solid nonlinear characteristics, and there is no clear linear relationship with the wave height. In the horizontal direction, the wave slamming load shows three-dimensional characteristics; even the measurement results of different slamming units at the same height will have considerable differences.

The wave steepness parameter *KA* is also an essential factor affecting the wave slamming load of the platform. Waves with larger wave steepness are more likely to cause large slamming loads, and small changes in wave steepness will cause changes in the maximum water particle velocity during wave slamming.

Generally speaking, waves with a large steepness parameter *KA*, show strong nonlinear characteristics before they come into contact with the platform. Entezam and Kazemi et al. used the commercial CFD software Flow3D to study the wave slamming load on a semi-submersible platform under different wave steepness parameters(Entezam and Kazemi, 2015). At the same time, the mooring system was considered in the numerical simulation process to make a better comparation with the model's experimental results. The results show that the Flow3D fluid analysis software can reasonably simulate the wave slamming event when the wave steepness parameter $KA \leq 0.04$. The wave slamming load, free water surface wave height change, and platform motion response calculated by numerical simulation is very close to the experimental results. However, with the increase of the steepness parameter KA, the numerical simulation and the experimental results are no longer in good agreement, and large deviations begin to appear. At present, it must be recognized that existing numerical simulation methods have difficulty in accurately simulating events where a steep wave hitting the platform.

1.4.2.4 Effect of wave breaking on slamming

When a wave collides with a multi-column platform, energy is often dissipated in turbulence, resulting in wave breaking. Wave period and wave steepness parameters are the main factors affecting wave breaking. In addition, wave breaking is also affected by the joint action of wind and wave, the joint action of wave and current, and the mutual interference between waves. In the process of breaking wave slamming multi-column platform, the air component entrained in the wave greatly influences the slamming load.

The study by Bredmose et al.. showed that when the breaking wave entrains a small amount of air and interacts with the structure, the slamming load will increase significantly(Bredmose et al., 2009). At the same time, their research also shows that when the breaking wave entrains a large amount of air, the slamming load will decrease, but the slamming action time will increase significantly. However, there is no systematic and quantitative analysis of the gas volume fraction and slamming load in breaking waves. Another view is that the gas-liquid mixing in the breaking wave will lead to changes in fluid density, which will lead to changes in the mass, momentum, and energy of water particles during the slamming process. Based on this point of view, Ariyarathne studied the influence of fluid density changes on the slamming pressure coefficient through advanced and reliable experimental measurement methods to monitor fluid density and obtained related calculation formulas(Ariyarathne et al., 2012). As shown in Fig 1.9, there are two main modes of contact between the incident wave and the structure: one is the Wagner type, which is characterized by no entrained air; the other is the Bagnold type, which is characterized by entrained air.

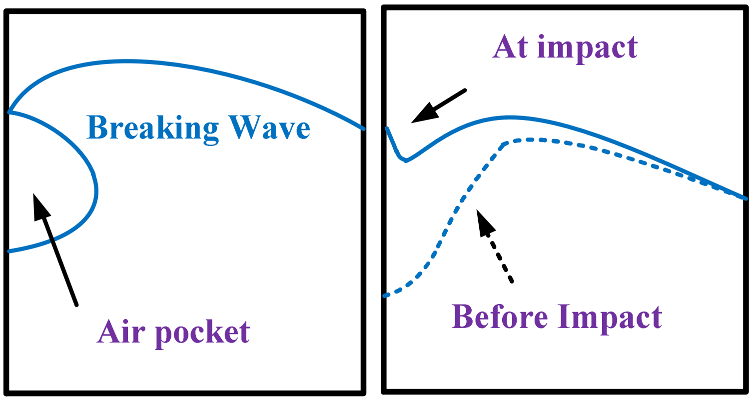

Fig 1.9. Two kinds of wave slamming contact processes

In addition, Lugni described the “flip-through” phenomenon that occurs during the slamming process(Lugni et al., 2006). The “flip-through” phenomenon often occurs when waves slam vertical structures such as columns and straight walls. This phenomenon is characterized by vertical solid jets. The presence of air pockets will increase the velocity of water particles in the jet process. The interaction between the deck and the waves will lead to the generation of horizontal jets. As shown in Fig 1.10, the velocity of the horizontal jets is often remarkably high. Therefore, the impact of the jets must be considered during the slamming process of the structure above the column and below the deck and the waves. It is noteworthy that in the interaction between breaking waves and vertical structures (e.g., platform columns), the breaking position plays a critical role in determining the structural load. Different breaking locations lead to marked differences in the impact loads exerted on the structure, further highlighting the complexity of the breaking wave slamming mechanism. Therefore, close attention must be paid to the dynamic variation of the breaking position in both experimental and numerical studies(Kamath et al., 2016).

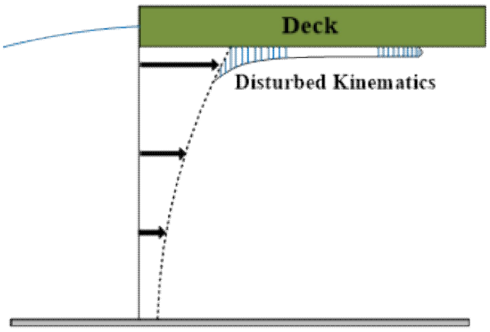

Fig 1.10. Horizontal jet produced by wave slamming process

It should be noted that, in the present study, the classification of slamming events into Wagner-type and Bagnold-type impacts is based on the characteristics of the measured pressure–time histories, rather than on direct visual observation of air entrainment. Due to the absence of high-speed imaging or PIV measurements, air entrainment and cavity formation could not be directly identified. Therefore, the classification adopted here should be regarded as a phenomenological interpretation, following commonly used pressure-based criteria such as peak sharpness and impact duration.

1.4.3 The method and development of horizontal wave slamming experimental research

For the study of wave slamming, the wave slamming of simple structures such as wedge-shaped objects into water and flat plates became the focus of early research. Zou Li et al.. conducted a detailed experiment on the wave slamming of a wedge-shaped object entering the water. They found that the wedge-shaped object with a convex profile was subjected to greater wave slamming pressure than a wedge-shaped object with a recurved profile. Moreover, the faster the wedge-shaped object enters the water, the greater the wave slamming pressure on the wedge-shaped object will be.

Engle and Lewis used wedges with two angles of 10° and 20° to conducted the experimental research of the falling body model, and compared with the simulation data(Engle and Lewis, 2003), they found that the results at the angle of 20°were in good agreement. Chuang once performed a systematic study on the problem of water impact(Chuang et al., 2017). Based on the experimental research of the model, an empirical formula for the relationship between the slamming pressure coefficient and the bottom slope angle is extracted by interpolation approximation. Sun et al.. manufactured an approximate V-shaped section derived from an ABS board to simulate a two-dimensional wedge structure(Sun and Lu, 2003). The physical quantities of acceleration and strain in the impacting water surface were dynamically measured, and a series of bottom surface inclination angles, falling heights, etc., that had a greater impact were investigated. The characteristics of the dynamic response of the structure under the action of fluid-solid coupling are studied.

With the complexity of the structure of the research objects, the experimental research methods of small-scale structures are only partially suitable for the experimental research of large-scale structures. Therefore, Kazemi et al.. conducted a model experiment on a semi-submersible platform (GVA4000 class), and the scale ratio of the model was 1/100(Kazemi and Incecik, 2006). A similar conclusion was obtained to the gravity platform slamming event: the wave climbing phenomenon is more evident on the upstream column. The maximum vertical wave slamming load occurs at the centre of the lower surface of the deck, and the magnitude of the slamming load has a great relationship with the wave steepness parameter. In order to better measure the wave slamming load, Liu et.al (2018) designed a high-precision measurement unit and studied the variation pattern of the wave slamming load of the semi-submersible platform under the influence of different wave directions. Also, with a model experiment, Abdussamie studied the kinematic response of a TLP when waves slam it(Abdussamie et al., 2017). First, a simplified setup of the tension leg is carried out, and the response of wave slamming to the platform motion is studied by monitoring the acceleration of the platform model. The study found that when the wave slammings the platform deck’s leading edge, the platform’s movement direction is basically the same as the wave propagation direction. Therefore, as the velocity of the platform surge movement increases, the relative velocity at which the wave touches the leading edge of the platform deck will decrease. Compared with the previous fixed platform test, it can be reduced to a maximum of 50%, which shows that the platform movement may also reduce the slamming load. In order to study the influence of the platform air gap on the floating platform, Simos et al.. conducted model experiments(Simos et al., 2008) and found that, in addition to low wave steepness, the standard first-order numerical analysis severely underestimated the run-up effect in the area near the column. Ding took the four-pontoon offshore platform as the test object, focusing on the influence of different towing speeds on towing conditions(Ding and Liu, 2012). In the final test, the acceleration in X, Y and Z directions of the floating cylinder platform was measured, and the air pressure and the water pressure at the bottom of the floating cylinder were studied. By benchmarking against a synthetic numerical dataset, Facci et al.. ssessed the application of PIV in water-entry problems and confirmed its reliability for velocity and pressure field quantification, offering robust support for experimental methodologies (Facci et al., 2015).

Model tests and numerical studies have further demonstrated that mooring compliance and platform motion can significantly influence air gap characteristics and wave slamming responses of floating platforms, although the degree of influence is highly condition-dependent. Under regular wave conditions, the restrained – floating comparison tests conducted by Kazemi and Incecik (2006) showed that, when platform motions were allowed, the measured air gap values were consistently higher and the peak vertical impact forces beneath the deck were significantly lower than those obtained under fully restrained conditions, indicating that fixed configurations tend to overestimate slamming loads. Under irregular wave conditions, Liang et al. (2010) reported similar trends, showing that the inclusion of platform motion and mooring effects reduced the extreme negative air gaps and the associated impact responses compared with fixed assumptions, although the spatial distribution of local responses became more scattered. In contrast, under focused and freak wave conditions, Huo and Yuan’s group (2021) reported substantially amplified local slamming pressures on a moored floating platform, with a maximum value of 137.2 kPa, which was 287.68% higher than the normal slamming value observed under conventional wave conditions, and a pronounced double-peak slamming phenomenon was observed. It should be noted, however, that this amplification was primarily associated with the extreme wave event itself rather than a direct consequence of mooring compliance, as the study did not include a fixed-platform reference or a systematic variation of mooring stiffness. These results collectively indicate that allowing platform motions and mooring compliance generally mitigates extreme slamming loads under moderate wave conditions, whereas under extreme and transient wave events, motion-induced relative velocities may lead to severe local slamming responses that cannot be solely attributed to mooring effects.

1.5 The originality and Innovation points

To briefly describe the major originality and present the innovations of this thesis which are threefold:

a. A single-column impact experimental platform with a deck was constructed based on a numerical wave tank, and the experiment was conducted under the action of regular waves, focused waves, and freak waves. For the first time, the relationship between the frequency range of focused waves and the intensity of wave slamming was explored. It was discovered that the slamming load caused by freak waves generated by the J-spectrum can reach up to 6 times the S-spectrum, providing a short-period and low-cost solution for wave slamming test research on offshore platforms.

b. A CGNT-CFD numerical wave tank method, based on Cartesian grids and high-precision free surface capturing, is proposed by combining the orthogonal grid finite difference scheme with an advanced interface tracking technique. This method significantly enhances computational efficiency while maintaining high accuracy, enabling fast and reliable prediction of slamming loads on platform columns.

c. A platform parameter sensitivity analysis model was established by incorporating variables such as column shape, size, and relative position. The study clearly demonstrates that the shape, scale, and spatial arrangement of columns and deck structures have a significant impact on the upper wave slamming loads, with variations reaching up to 166.7%, while their influence on lower loads is relatively limited (<10%). Under head-sea conditions (180°), upper column loads exhibit low sensitivity to these parameters (<10%), whereas the lower loads are significantly amplified, with differences up to 98.6%. These findings provide valuable references for the protection of lower platform components and the design of connections between upper and lower hull structures.Regarding column spacing, the effect on the wave load of the front-row columns is limited, while the slamming response of the rear-row columns shows a typical nonlinear trend: as spacing increases, the load transitions from being reduced due to shielding to being enhanced by wave interference. Notably, under the 3D spacing condition, the slamming peak on the rear columns can exceed 20 times that of the 1D spacing case. This phenomenon identifies a "characteristic spacing scale" in platform structural arrangement, where the platform is subject to significantly intensified slamming loads under certain spacing conditions. This should be avoided in engineering design and carries important practical significance.

1.6 Structure of this thesis

This thesis is organized into seven chapters and revolves around two main research threads. On one hand, a typical single-column physical model was constructed, and a series of systematic hydrodynamic experiments were conducted to innovatively reveal the response characteristics and governing patterns of column structures under wave slamming, thereby establishing a new experimental paradigm for complex offshore conditions. On the other hand, a novel numerical wave tank method based on three-dimensional Cartesian grids was developed to simulate the fully nonlinear fluid–structure interactions throughout the wave slamming process, addressing the limitations of conventional methods in terms of accuracy and applicability. Building upon this numerical framework, the study further investigates the influence of key platform parameters on wave slamming loads.

The detailed chapter arrangement is as follows:

Chapter 1 outlines the research background, discusses the challenges in studying wave slamming problems, and reviews mainstream research methodologies. The research progress in wave slamming on offshore platforms is summarized in three aspects: theoretical studies, experimental investigations, and numerical simulations. The chapter concludes with a summary of the innovations and research scope of this study.

Chapter 2 provides an overview of the theoretical foundations of the STAR-CCM+ solver, including control equations, grid generation methods, turbulence models, and free surface treatment. It then focuses on the in-house Cartesian-grid-based CFD solver, or numerical wave tank, detailing its solution modules such as the convection module, turbulence module, free surface tracking module, and floating body motion module. This chapter lays the theoretical groundwork for the subsequent numerical analysis.

Chapter 3 presents the experimental design and setup for transverse wave slamming. A deck-supported platform column model was designed based on a prototype, and the test setup, including the numerical wave tank and associated equipment, is described in detail. Special attention is given to the layout of pressure monitoring points on the platform model. The experimental conditions for regular waves, focused waves, and freak waves are then introduced, establishing a comprehensive experimental methodology for column slamming load analysis.

Chapter 4 analyzes the slamming test results under three wave types: regular waves, focused waves, and freak waves. First, the peak pressures recorded by the sensors under regular waves are compared and examined, followed by an analysis of pressure distribution and time-history characteristics. For focused and freak waves, wave run-up behavior, air gap, and wave incidence angles are discussed, and their effects on slamming loads are analyzed. The pressure time histories at various sensor locations are compared, and the relationship between slamming force and time-history features is summarized.

Chapter 5 focuses on the regular wave experimental conditions discussed in Chapter 4, comparing them with simulation results from the CGNT-CFD method to validate its accuracy in predicting slamming loads under regular wave conditions. Additionally, the method's computational efficiency is assessed through a comparative analysis with STAR-CCM+.

Chapter 6 investigates the influence of key parameters on slamming loads based on the validated numerical model. This includes both wave characteristics (e.g., wave type, wave height, and period) and platform parameters (e.g., geometric configurations). The wave slamming process under regular waves and the variation of slamming loads with wave period, column geometry, and wave heading are systematically studied.

Chapter 7 summarizes the main research findings of this study and discusses future directions for deeper investigation into wave loads on floating platforms.

2 BASIC SIMULATION APPROACH TO HORIZONTAL WAVE SLAMMING PROBLEM

With the advancement of computer hardware and algorithms, computational fluid dynamics (CFD)-based numerical simulation techniques have been widely applied in the study of wave-structure interaction problems. By constructing a numerical wave tank, CFD methods have, to a certain extent, replaced physical wave tank experiments, reducing dependence on experimental facilities and sensor arrangements.

However, despite the high accuracy of traditional CFD approaches, several critical engineering bottlenecks remain. On one hand, they are highly resource-intensive, involve complex mesh generation, and are inefficient for simulating multiple parametric conditions within a limited timeframe. On the other hand, when dealing with strongly nonlinear processes involving violent free surface variations, such as wave slamming, traditional methods suffer from low computational efficiency and poor convergence. Consequently, in the design phase of engineering projects, conventional CFD methods fall short of meeting the practical demands for rapid and stable prediction of load responses. Although simplified approaches such as OTG13/14 offer advantages in efficiency, they are limited in accuracy and applicability, making them insufficient as comprehensive and reliable design tools.

This chapter provides a brief overview of two representative CFD approaches: the commercial software STAR-CCM+ and the efficient solver CGNT-CFD proposed in this study. The CGNT-CFD method is developed based on a three-dimensional

Cartesian grid finite difference framework, employing a stepwise velocity–pressure coupling scheme and a high-resolution THINC/SW free surface capturing technique. An immersed boundary method is also introduced to handle structural motions, thereby avoiding the need for complex mesh generation and overlapping grid operations. The chapter details the structural simplicity, algorithmic efficiency, and engineering applicability of CGNT-CFD in simulating wave slamming scenarios.

2.1 General commercial CFD theoretical method for wave slamming

STAR-CCM+ is a relatively mature computing fluid dynamics business software with an extremely friendly interactive interface. Compared with other fluid mechanics software, STAR-CCM+ can perform pre-processing of fluid calculation (three-dimensional modeling, grid division) and post-processing (parameter image drawing, flow field analysis). It has many advantages and is widely used in ship hydrodynamic calculations. And in this numerical simulation study, STAR-CCM+ based on the finite volume method for spatial discretization of the Navier-Stokes equations, and the overlapping mesh technique, are applied to the slamming load prediction.

2.1.1 Control equation

The slamming process is a physical phenomenon of the three-phase (gas-liquid-solid). As a physical phenomenon, it is necessary to meet the three major patterns of physics, namely, the conservation of mass, momentum and energy. However, as this study does not involve heat transfer and other related issues, thermodynamic problems are ignored and the pattern of conservation of energy is not taken into account.

For fluids, the pattern of conservation of mass means that the mass added or subtracted in a fluid microcosm per unit time is equal to the mass flowing into or out of that microcosm. In this thesis, the compressibility of the gas and liquid phases under study is not considered, so the fluid density ρ in all the equations used in this thesis is constant and does not change with time, which greatly simplifies some of the equations and improves the computational efficiency of the numerical simulations.

Quality conservation equation (i.e. continuous equation) can be simplified into：

$$\frac{\partial u}{\partial x}+\frac{\partial v}{\partial y}+\frac{\partial w}{\partial z}=0 \tag{2.1}$$

Momentum conservation equation (i.e. motion equation, Navier-Stokes equation) can be simplified into：

$$\rho\frac{\partial u}{\partial t}+div\left(\rho u\vec{u}\right)=-\frac{\partial p}{\partial x}+\frac{\partial \tau_{xx}}{\partial x}+\frac{\partial \tau_{xy}}{\partial y}+\frac{\partial \tau_{xz}}{\partial z}+F_x \tag{2.2}$$

$$\rho\frac{\partial v}{\partial t}+div\left(\rho v\vec{u}\right)=-\frac{\partial p}{\partial y}+\frac{\partial \tau_{yx}}{\partial x}+\frac{\partial \tau_{yy}}{\partial y}+\frac{\partial \tau_{yz}}{\partial z}+F_y \tag{2.3}$$

$$\rho\frac{\partial w}{\partial t}+div\left(\rho w\vec{u}\right)=-\frac{\partial p}{\partial z}+\frac{\partial \tau_{zx}}{\partial x}+\frac{\partial \tau_{zy}}{\partial y}+\frac{\partial \tau_{zz}}{\partial z}+F_z \tag{2.4}$$

In the formula, p is the pressure distributed over the fluid microelement, F_x is the unit mass force acting on the fluid microelement in the x direction, and the same is for the y and z directions, τ is the viscous stress acting on the surface of the fluid microelement, ρ is the fluid density.

2.1.2 Focused wave and freak wave

Focused waves are generally considered as extreme waves formed by the superposition of several wave components with different frequencies at a specific time and position. At present, theoretical methods are used to generate focused waves, including linear wave superposition method and nonlinear focusing method. Linear wave superposition method is to superimpose cosine waves with different frequencies and random phases, and generate focused waves with specific amplitude at a specified time position by adjusting the initial phase of cosine waves. According to the linear superposition theory proposed by Longuet-Higgins (Longuet-Higgins and Cokelet, 1976), the free surface equation of focused wave is：

$$\eta = (x,t) = \sum_{n=1}^{N} \alpha_n \cos(k_n x - \omega_n t + \varepsilon_n) \quad (2.5)$$

Where η is the height of the wave surface relative to still water, α_n, k_n and ω_n are the wave surface amplitude (m) of the nth superimposed wave, the wave number of the nth component wave and the circular frequency (rad/s) of the nth component wave respectively, n is the number of component waves, and ε_n is the initial phase of the nth component wave.

Freak wave is an external manifestation of the temporal and spatial focus of wave energy. In a certain sea area, when the energy in waves is highly concentrated somewhere for some reason, the freak wave with wave height much higher than other waves is formed. In different marine environments, the causes of wave energy focusing are often different. At present, there is no unified conclusion about the mechanism of freak wave, but it can be divided into two categories: internal factors and external factors: internal factors mainly refer to the linearity and nonlinearity of waves themselves; External factors mainly refer to environmental factors such as seabed topography, ocean current and wind. In STAR-CCM+, the generation of freakwaves also relies on the linear superposition method (see Equation 2.5), where multiple wave components with different frequencies and phases are synchronously superimposed at specific spatial and temporal points, resulting in a concentrated energy peak that produces a “freakwave” significantly higher than the surrounding waves.

2.1.3 Grid construction method

In STAR-CCM+, there are many grid construction methods, such as motion grids and overlapping grids. As the motion response of the cylindrical FPSO studied in this thesis occurs when it is subjected to wave action, the overlapping grid method, which describes the motion of the object more accurately, is chosen for numerical simulation in this thesis.

The principle of the overlapping grid method is to add a new overlapping grid based on the external flow field grid. The moving object is located in the overlapping grid.

The moving object is located in the overlapping grid, and the boundary of the overlapping grid is in contact with the external flow field mesh. During the numerical simulation process, the external flow field grid does not follow the movement of the object, while the overlapping grid follows the movement of the object and exchanges data with the external flow field grid through the boundary surfaces of the overlapping grid to realize the numerical simulation. This method enables the effective simulation of large-scale object motion. However, during the numerical simulation process, it is necessary to constantly update the positions of overlapping grids and exchange data between the overlapping grids and external flow field grids. Therefore, compared to other methods, the overlapping grid method with an equal number of grids incurs higher computational costs. However, it can achieve more accurate results in numerical simulations of ship motion problems. In this study, the cylindrical FPSO exhibits significant motion ranges, and the use of overlapping grids can provide more precise results.

2.1.4 Turbulence model

Turbulence is a very complicated non-regular random vortex movement. There is a severe quality, momentum and energy exchange between fluid micro-groups due to the random collision of the molecule . At present, the direct numerical simulation method and the non-direct numerical simulation method are the main methods to deal with turbulence problems. The former not only has very high requirements on grids and time steps, but its calculation efficiency is also lower than the indirect numerical simulation method. In engineering, this approach is typically not utilized to cope with turbulence and non-direct numerical simulation method is applied instead. This study uses the $\mathrm{k}\text{-}\varepsilon$ model of the Renault average method in the non-direct numerical simulation method to handle the wave movement response and impact numerical load simulation of the cylindrical FPSO. RANS regards turbulent flow as a superposition of time average flow and instantaneous pulse flow. Its numerical simulation is accurate and highly calculated in actual applications. The k-ε models can solve the power (k) and turbulent scattering (ε), and have good numerical simulation accuracy and fast calculation efficiency.

2.1.5 Free water surface treatment

The method employed by STAR-CCM+ to capture the free water surface attitude is the Volume of Fluid (VOF) method. This method captures the free water surface by evaluating the magnitude of the function F, which represents the proportion of fluid occupied within each cell of the computational grid.

If F=1, it indicates that the specified phase fluid completely fills the current grid cell, while the non-specified phase fluid is not present.

If F=0, it indicates that the non-specified phase fluid completely fills the current grid cell, while the specified phase fluid is not present.

If $0<F<1$, it indicates that both the specified phase fluid and the non-specified phase fluid are present within the current grid cell, making it an interface cell.

The VOF method enables the capture of free water surfaces between immiscible fluids. It is based on solving a set of momentum equations for both fluids and combining the volume fractions of each fluid to describe multiphase flow. STAR-CCM+ software utilizes the High-Resolution Interface Capturing (HRIC) format, which offers relatively lower computational costs and higher accuracy, meeting the requirements of the calculations.

2.2 Theoretical Foundation of the Novel Three-Dimensional Rectangular Grid Numerical Wave Flume Method

The CGNT-CFD solver is a CFD solver based on rectangular grids. This method is based on the Cartesian coordinate system and adopts the finite difference method to discretize the Navier-Stokes equations. Following a step-by-step method, the entire computation process is divided into three stages, and then the decoupling calculation of velocity and pressure is realized.

2.2.1 Solving the governing equations step by step

When solving wave slamming problems using a Cartesian grid, the governing equations are the Navier-Stokes equations. The specific expression of the governing equations is as follows:

$$\frac{\partial u}{\partial x}+\frac{\partial v}{\partial y}+\frac{\partial w}{\partial z}=0 \tag{2.6}$$

$$\frac{\partial u}{\partial t}+u\frac{\partial u}{\partial x}+v\frac{\partial u}{\partial y}+w\frac{\partial u}{\partial z}=f_x-\frac{1}{\rho}\frac{\partial p}{\partial x}+\frac{\mu}{\rho}\left(\frac{\partial^2 u}{\partial x^2}+\frac{\partial^2 u}{\partial y^2}+\frac{\partial^2 u}{\partial z^2}\right) \tag{2.7}$$

$$\frac{\partial v}{\partial t}+u\frac{\partial v}{\partial x}+v\frac{\partial v}{\partial y}+w\frac{\partial v}{\partial z}=f_y-\frac{1}{\rho}\frac{\partial p}{\partial y}+\frac{\mu}{\rho}\left(\frac{\partial^2 v}{\partial x^2}+\frac{\partial^2 v}{\partial y^2}+\frac{\partial^2 v}{\partial z^2}\right) \tag{2.8}$$

$$\frac{\partial w}{\partial t}+u\frac{\partial w}{\partial x}+v\frac{\partial w}{\partial y}+w\frac{\partial w}{\partial z}=f_z-\frac{1}{\rho}\frac{\partial p}{\partial z}+\frac{\mu}{\rho}\left(\frac{\partial^2 w}{\partial x^2}+\frac{\partial^2 w}{\partial y^2}+\frac{\partial^2 w}{\partial z^2}\right) \tag{2.9}$$

In these formula, ρ is the fluid density, u, v and w are the velocity components in the x, y and z directions respectively, μ is the dynamic viscosity coefficient, p is the pressure and t is the time.

The above equation reveals that the governing equations involve numerous parameters, and the coupling of these parameters makes direct solutions challenging. To address this, this study employs the CGNT-CFD solver to solve the equations using a step-by-step approach, decoupling the velocity and pressure for numerical computation. The specific procedure for decoupling the velocity and pressure based on the step-by-step approach is as follows.

The time stepping of the Navier-Stokes equations is decomposed into three stages: the convection stage, the non-convection stage I, and the non-convection stage II. In the following equations, *n* and *n+1* represent the current and next time steps' physical quantities, while * and ** indicate intermediate states of the physical quantities.

Convection stage：

$$\frac{u_i^n-u_i^*}{\Delta t}+u_j^n\frac{\partial u_i^n}{\partial x_j}=0 \tag{2.10}$$

In the convection stage, only the convection items of the N-S equation can be used to solve the various convection formats during this stage.

Non-convection stage I：

$$\frac{u_i^{**}-u_i^{*}}{\Delta t}=f_i+\frac{\mu}{\rho}\left(\frac{\partial^2 u_i}{\partial x^2}+\frac{\partial^2 u_i}{\partial y^2}+\frac{\partial^2 u_i}{\partial z^2}\right) \tag{2.11}$$

The speed field calculated at this stage does not necessarily meet the dynamic equation. This is the intermediate state of the physical quantity. It also needs to introduce the pressure item of the dynamic equation to correct it.

$$\frac{u_i^{n+1}-u_i^{**}}{\Delta t}=-\frac{1}{\rho}\frac{\partial p^{n+1}}{\partial x_i} \tag{2.12}$$

$$\frac{\partial u_i^{n+1}}{\partial x_i}=0 \tag{2.13}$$

Because the obtained speed field needs to meet the requirements of the continuity equation, therefore, the pressure Poisson equation for p(n+1) can be obtained by taking the divergence.

$$\frac{1}{\Delta t}\frac{\partial u_i^{**}}{\partial x_i}=\frac{\partial}{\partial x_i}\left(\frac{1}{\rho}\frac{\partial p^{n+1}}{\partial x_i}\right) \tag{2.13}$$

In the above formula：i=1,2,3.

In summary, the procedure involves first calculating the intermediate velocity field, followed by determining the pressure field, and finally correcting the velocity field to obtain accurate computational results.

Based on the principles of the step-by-step approach, and considering modular development, the viscous flow Cartesian grid CFD solver (CGNT-CFD solver) is decomposed into five modules: convection equation solving module, velocity-pressure decoupling solving module, turbulence model solving module, free water surface tracking model solving module, and immersed boundary algorithm module.

2.2.2 Convection equation solving module

The purpose of solving the module of the streaming equations is to solve the non-linear convection items in the N-S equations. The essence is to solve the following convection equation.

$$\frac{u_i^n - u_i^*}{\Delta t} + u_j^n \frac{\partial u_i^n}{\partial x_j} = 0 \tag{2.15}$$

The convection equation belongs to the class of typical hyperbolic equations, where the actual flow direction of the fluid during the solution process must be considered. In other words, the flow field information at downstream grid nodes is primarily influenced by the upstream information. Taking into account this physical characteristic, a commonly adopted approach is to use upwind discretization schemes.

2.2.3 Speed and pressure decoupling solution module

The focus of this module is to achieve the decoupling of the speed-pressure field, simplifying the solution of the N-S equation, which involves sub-modules such as speed prediction, pressure Poisson equation solution, speed correction and other sub-modules.

The fundamental theoretical model for the velocity-pressure decoupling solving module is the staggered approach, which involves a step-by-step process. During the time advancement, the first step is to predict the flow field (initial flow field generally does not satisfy the continuity equation). Based on this predicted flow field, the source term for the pressure Poisson equation is obtained. Next, the pressure Poisson equation is solved to obtain a new pressure field. Finally, the predicted velocity field is corrected using the obtained pressure field to obtain a velocity field that satisfies the continuity equation.

The first step is to solve the convection equation, namely：

$$\frac{\partial u_i}{\partial t}+u_j\frac{\partial u_i}{\partial x_j}=0 \tag{2.16}$$

Here, according to the speed field of the n-time step, the estimated speed field is calculated.

The second step is to solve the viscous term and the volume force term, namely：

$$\frac{\partial u_i}{\partial t}=\frac{1}{\rho}\frac{\partial}{\partial x_j}\left(2\mu S_{ij}\right)+f_i\frac{\partial u_i}{\partial t}+u_j\frac{\partial u_i}{\partial x_j}=0 \tag{2.17}$$

Here, according to the estimated speed field, the estimated speed field is calculated.

The third step is to solve the pressure term, namely：

$$\frac{\partial u_i}{\partial t}=-\frac{1}{\rho}\frac{\partial p}{\partial x_j} \tag{2.18}$$

Here, based on the estimated velocity field and use the continuity equation,

$$\left(\frac{\partial u_i}{\partial x_i}\right)^{n+1}=0 \tag{2.19}$$

the pressure Poisson equation is constructed to obtain the pressure values at the next time step.

The fourth step is to correct the estimated speed field to get the velocity field at the next time step.

2.2.4 Turbulence model module

In the Cartesian grid CFD common solving module, the turbulence model module is primarily developed based on the Large Eddy Simulation (LES) approach, and a constant-coefficient Sub-Grid Scale (SGS) model has been developed.

The Large Eddy Simulation (LES) method is a transient approach that directly solves the large-scale eddies in the fluid domain while modeling the small-scale eddies. Unlike the Reynolds-Averaged Navier-Stokes (RANS) method, the LES method filters out the higher-frequency small-scale eddies through spatial filtering, reducing the computational domain. Each solved variable is decomposed into filtered values and sub-grid values. The LES method calculates turbulence through partial modeling, ensuring a certain level of accuracy. However, it comes with a high computational cost and may not meet the computational requirements of high Reynolds number flows.

In this study, the constant-coefficient Smagorinsky model is employed as a typical sub-grid-scale (SGS) model. This model assumes that small-scale vortices primarily contribute to energy dissipation and do not significantly affect large-scale dynamics, thereby enabling stable simulation of large-scale flow phenomena. Since slamming problems are usually dominated by large-scale free-surface motions and large-scale vortex structures, the Smagorinsky model can effectively capture such behaviors while saving computational resources by avoiding full high-resolution direct simulation across all scales. Moreover, the constant-coefficient Smagorinsky model adopted in this work has been widely used in slamming studies. For example, Chen and Yu (2009) successfully applied an LES framework with a Smagorinsky model to simulate green water and wet-deck slamming on offshore structures and ships. More recently, Xie et al. (2020) employed a Cartesian cut-cell based multiphase LES model with a Smagorinsky-type subgrid-scale closure to investigate three-dimensional wave－structure interactions. These studies support the suitability of the Smagorinsky model for the present investigation, where the focus is on capturing global slamming load characteristics rather than detailed near-wall turbulence resolution.

2.2.5 Free water surface tracking module

This thesis uses the Thinc/SW method of the VOF method to simulate the change of the free water surface. The volume score of different phases in the free water surface is expressed. Among them, the i = 1 era is the liquid phase. Where i = 2 represents the gas phase. Among them, the $i = 3$ era is a solid phase, and the liquid phase Φ_1 control equation is as follows.

$$\frac{\partial \phi_1}{\partial t} + \nabla \cdot \left(u \phi_1 \right) = 0 \tag{2.20}$$

The liquid phase Φ_1 is solved through the Thinc/SW format. The Thinc/SW method can accurately handle the severe changes in the free water surface and capture vital non-linear phenomena such as wave rolling and splashing. The volume fraction of the solid Φ_3 is calculated in the immersed boundary method step, and the volume fraction of the gas Φ_2 can be calculated by the following formula：

$$\phi_1 + \phi_2 + \phi_3 = 1 \tag{2.21}$$

By accurately solving Φ_i, it is possible to precisely capture the free water surface.

2.2.6 Immersion boundary module

In Cartesian grid systems, due to the imperfect alignment between the grid and the surface of geometric objects, the immersed boundary method is commonly employed to numerically simulate fluid-structure interaction problems. The main approach involves updating the grid information on the object surface, determining the position of boundary points, reconstructing the velocity of boundary points, solving the momentum forces at the boundary points, thus achieving the solution of fluid-structure coupling motion.

The fundamental idea of the immersed boundary method is to supplement the source terms in the flow equations when solving the flow equations in a Cartesian grid. These source terms reflect both the interaction between the flow and the fluid and the properties of the moving boundaries (refer to Fig 2.1). In this study, the effect of the solid body on the entire flow field is represented by adding a volume force source term to the Navier-Stokes equations. The velocity in the flow field is interpolated using the volume fraction of the solid domain within a single grid.

The velocity in the flow field is obtained through interpolation based on the volume fraction occupied by the solid domain within a single grid. The specific expression is as follows:

$$u_i^{n+1} = u_{Bi}^{n+1} \cdot \phi_B + u_{Fi}^{n+1} \cdot \left(1 - \phi_B\right) \tag{2.22}$$

In the formula: u_{Bi}^{n+1} and u_{Fi}^{n+1} denotes the velocity of the solid and fluid in the grid node at the next time step and $\Phi_B$denotes the volume fraction of the solid domain in a single grid. The volume force f_{Bi} can be obtained from the non-slip boundary conditions of the two solid-liquid phases：

$$f_{Bi} = \phi_B \frac{u_{Bi}^{n+1} - u_{Fi}^{n+1}}{\Delta t} \tag{2.23}$$

This kind of immersed boundary method can effectively capture the movement of objects and does not need to deform and reconstruct the grid during the numerical simulation process, which greatly simplifies the calculations and enhances computational efficiency.

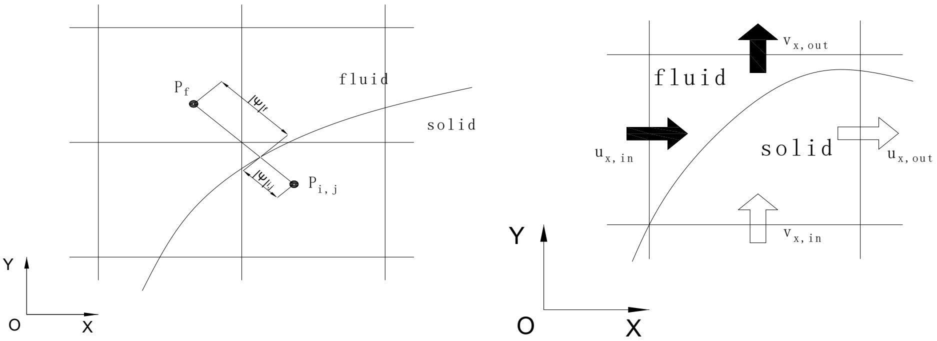

Fig 2.1. Volume force-solving schematic diagram (left)；Schematic diagram of the mass source term-solving grid (right)

2.2.7 Floating body motion solution module

Under the action of fluid, the six-degree-of-freedom motion equation for a floating structure on the water surface are as follows：

$$[M]\left\{\frac{\mathrm{d}U}{dt}\right\}=\left\{\mathrm{F}_{\mathrm{I}}+\mathrm{F}_{i,e}\right\} \tag{2.24}$$

$$[I]\left\{\frac{\mathrm{d}\Omega}{dt}\right\}_{B,r}+\Omega\times[I]\{\Omega\}=\left\{M_{B}+M_{B,\ell}\right\} \tag{2.25}$$

The hydrodynamic forces and moments acting on the floating structure can be obtained by integrating the forces of the surface of the object, that is,

$$\mathrm{F}=\oiint \vec{\mathrm{f}}\cdot \mathrm{d}\vec{\mathrm{s}} \tag{2.26}$$

$$\mathrm{M}=\oiint \vec{\mathrm{f}}\cdot\vec{\mathrm{r}}\,\mathrm{ds} \tag{2.27}$$

The force for calculating the force component in a certain direction on an individual surface element is as follows:

$$f_i=[-p\delta_{ij}+\mu(\frac{\partial u_i}{\partial x_i}+\frac{\partial u_j}{\partial x_j})]n_j \tag{2.28}$$

Based on the idea of the overlapping grid and the immersed boundary method, the solution of the flow field information and the solution of the 6DOF movement of the rigid body are calculated, and the model of the fluid-solid coupling algorithm is obtained.

2.3 Comparative Analysis of STAR-CCM+ and CGNT-CFD solver numerical simulation method

In the current numerical simulation of wave slamming problems, general-purpose commercial CFD software (such as STAR-CCM+) is widely used for wave load prediction and free surface modeling, offering advantages such as a well-established modeling workflow and user-friendly interface. However, due to its use of the finite volume method and body-fitted meshing strategy, challenges arise in mesh generation and computational efficiency when dealing with complex geometries. In contrast, the CGNT-CFD method proposed in this study is based on a three-dimensional Cartesian grid finite difference approach, which offers advantages such as simplified mesh generation and structured grid layout. While maintaining computational accuracy, it significantly enhances simulation efficiency, making it well-suited for large-scale parametric analyses and rapid engineering predictions.

This study proposes a novel numerical wave tank method based on three-dimensional Cartesian grids (i.e. CGNT-CFD). By integrating a custom high-resolution free-surface tracking algorithm with a modular solver architecture, the method enables efficient and accurate simulation of nonlinear wave–structure interaction processes. Table 2.1 summarizes the main differences between the two numerical methods. While both solvers solve the incompressible Navier-Stokes equations, STAR-CCM+ adopts a finite volume formulation, whereas CGNT-CFD uses a finite difference scheme on a structured Cartesian grid.

Table 2.1 Comparison between the CGNT-CFD Method and STAR-CCM+

Term	**STAR-CCM+**	**CGNT-CFD**
Control equation	Navier-Stokes equations $\partial u/\partial x + \partial v/\partial y + \partial w/\partial z = 0$ $\rho\partial V/\partial t + \mathrm{div}(\rho VV) = -\nabla p + \nabla \cdot \tau + F$	
Spatial discreteness	FVM $\int_{\Omega} \frac{\partial V}{\partial t} dV + \int_{\partial\Omega} \Gamma \cdot n dS = \int_{\Omega} F\, dV$	FDM $\frac{\partial}{\partial t}\int_{\Omega} \phi V\, dV - \int_{\Omega} \Gamma \cdot \nabla\phi dV + \int_{\partial\Omega} \Gamma \cdot n\phi dS = \int_{\Omega} F\, \phi dV$
Speed/Pressure decoupling	SIMPLE/PISO	Step-by-step method
Turbulence model	k-ω model	constant-coefficient Sub-Grid Scale (SGS) model
Grid type	overlapping grids, moving/dynamic grids, and so on	Cartesian grid

Free water surface treatment	HRIC in VOF	THINC/SW in VOF
Floating body motion	DFBI for body motion	immersed boundary method for six DOF/body motion

Compared to general CFD approaches, the proposed method offers the following advantages:

1. High accuracy in wave reproduction: Equipped with embedded wave generation boundary modules, the solver can accurately reconstruct various representative wave types, including regular, focused, and freak waves;
2. Improved computational efficiency: The use of structured Cartesian grids and a segregated solution scheme significantly reduces solver coupling complexity and enhances computation speed;
3. Robust free-surface tracking: The method incorporates high-resolution interface reconstruction algorithms capable of capturing complex interface phenomena such as wave breaking, run-up, and overturning with high fidelity;
4. Suitability for engineering multi-parameter analysis and parametric design: enables rapid construction of comparative models under varying platform geometries, wave parameters, and operating conditions, supports batch simulations across multiple parameters, and thereby facilitates multi-parametric design.

One of the significant advantages of the novel three-dimensional Cartesian Grid-based Numerical Tank (CGNT-CFD) method is its notably improved computational efficiency while maintaining calculation accuracy, making it highly suitable for engineering applications. For instance, in a typical ship-wave interaction validation case, the CGNT-CFD method achieved a parallel computation speed more than six times faster than STAR-CCM+, while ensuring comparable computational accuracy, substantially reducing the total computational time for multi-condition simulation analyses (Liu, 2024). A comparison of computational efficiency between CGNT-CFD and STAR-CCM+ for ship-wave interaction cases is provided in Table 2.2. This performance advantage is of great significance for the in-depth investigation of wave slamming problems, providing an efficient and reliable numerical approach for the rapid optimization of platform structures.

Table 2.2 Comparison of computational efficiency between CGNT-CFD and STAR-CCM+

Numerical Solver	Grid Size (Million)	Time Step (s)	Simulation Duration (s)	Computational Time×CPU cores
CGNT-CFD	6.35	0.0005	20s	226 core•hour
Star CCM+	5.98	0.003	20s	1467 core•hour

This numerical approach has been applied in subsequent chapters to simulate wave slamming on typical platform columns and has been validated through comparison with physical model test results, demonstrating strong accuracy and practical engineering applicability.

2.4 Summary of this chapter

In this chapter, the theory behind STAR-CCM+ solver, including control equations, grid generation methods, turbulence models, and treatment of free water surfaces, is briefly introduced, and then CGNT-CFD is explained. This method adopts a velocity–pressure stepwise decoupling strategy, effectively improving solution convergence and stability. The CGNT-CFD solver integrates multiple modular subsystems, including convection term solvers, turbulence modeling, THINC/SW free surface tracking, immersed boundary treatment, and floating body motion response simulation, offering strong scalability and engineering adaptability.

Leveraging its streamlined structure and high computational efficiency, CGNT-CFD significantly reduces the time required for wave load prediction while maintaining simulation accuracy, making it particularly suitable for engineering design scenarios where response time is critical, such as wave slamming. In the following chapters, a comparative study of wave slamming on platforms using both methods will be conducted to further validate the efficiency and accuracy of CGNT-CFD.

3 EXPERIMENTAL METHODOLOGY AND TEST SCHEME DESIGN FOR WAVE SLAMMING ON SQUARE COLUMNS WITH DECK STRUCTURES

Large offshore structures such as semi-submersible platforms operating in deepwater environments are subjected to various environmental loads, among which wave forces are the most significant. Among the different types of wave-induced loads, wave slamming caused by extreme wave events (such as freak waves and breaking waves) is one of the most critical and hazardous scenarios. Therefore, a thorough understanding and accurate assessment of wave slamming loads on semi-submersible platforms is of great importance for the structural design of such offshore systems.

A typical semi-submersible platform consists of pontoons, a topside deck, and vertical columns connecting the two. The deck and columns exposed above the free surface are the primary regions impacted directly by wave slamming. In this chapter, a square column with an attached partial deck section is selected as the test subject. A series of physical model experiments are conducted to investigate wave slamming loads on this representative configuration. The study focuses on the wave slamming processes and load characteristics induced by regular waves, focused waves, and freak waves, as well as the influence of wave parameters such as wave period, wave steepness, focusing period, and freak wave type on the resulting slamming loads.

The findings from this chapter provide a fundamental basis for further investigation into wave slamming loads acting on more complex semi-submersible structures under irregular wave conditions.

3.1 Similarity conditions and assumptions for numerical wave tank experiment

Wave slamming on an offshore platform operating at sea involves complex free-surface effects and unsteady wave–structure interactions. The associated hydrodynamic phenomena require consideration of gravitational forces, inertial effects, and time-varying unsteady fluid forces.. During the experiment, it is necessary to satisfy geometric similarity, ,Froude similarity, namely:

$$\frac{L_{1s}}{L_{1m}}=\frac{L_{2s}}{L_{2m}}=\cdots\cdots=\frac{L_{is}}{L_{im}}=\ldots=\lambda \tag{3.1}$$

$$\alpha_{1s}=\alpha_{1m};\ \alpha_{2s}=\alpha_{2m};\ \ldots\alpha_{is}=\alpha_{im};,\ldots \tag{3.2}$$

Here, L_{1s}、L_{2s}、L_{3s} are the characteristic lengths of the actual prototype; L_{1m}、L_{2m}、L_{3m} are the characteristic lengths of the model; λ is the scale ratio. α_{1s}、α_{2s}、α_{3s} are the characteristic angles of the actual prototype; α_{1m}、α_{2m}、α_{3m} are the characteristic angles of the model.

- Froude number

$$\frac{V_s}{\sqrt{gL_s}}=\frac{V_m}{\sqrt{gL_m}} \tag{3.3}$$

- Strouhal number

$$\frac{V_sT_s}{L_s}=\frac{V_mT_m}{L_m} \tag{3.4}$$

In formulas (3-3) and (3-4), V represents the characteristic velocity; L represents the characteristic length; T represents the characteristic period; the subscripts m and s denote the actual prototype and the model, respectively.

- The Reynolds number and the Weber number

$$\mathrm{Re}=\frac{\rho\ \mathrm{UD}}{\mu} \tag{3.5}$$

$We=\frac{\rho U^2 D}{\sigma}$ (3.6)

where ρ is the fluid density, U is the characteristic velocity, D is the characteristic length, μ is the dynamic viscosity, and σ is the surface tension coefficient of the fluid.

Table 3.1. Conversion between model and real body

Physical quantity	Entity symbols	Model symbol	Conversion coefficient
Linear scale	L_s	L_m	$\frac{L_s}{L_m}=\lambda$
Area	A_s	A_m	$\frac{A_s}{A_m}=\lambda^2$
Volume	∇_s	∇_m	$\frac{\nabla_s}{\nabla_m}=\lambda^3$
Period	T_s	T_m	$\frac{T_s}{T_m}=\lambda^{1/2}$
Frequency	f_s	f_m	$\frac{f_s}{f_m}=\lambda^{-1/2}$
Density	ρ_s	ρ_m	$\frac{\rho_s}{\rho_m}=\gamma$
Linear velocity	V_s	V_m	$\frac{V_s}{V_m}=\lambda^{1/2}$
Linear Acceleration	a_s	a_m	$\frac{a_s}{a_m}=1$
Angle	ϕ_s	ϕ_m	$\frac{\phi_s}{\phi_m}=1$
Quality (displacement)	Δ_s	Δ_m	$\frac{\Delta_s}{\Delta_m}=\gamma\lambda^3$
Force	F_s	F_m	$\frac{F_s}{F_m}=\gamma\lambda^3$
Rotational inertia	J_s	J_m	$\frac{J_s}{J_m}=\gamma\lambda^5$
Wind force coefficient	C_s	C_m	$\frac{C_s}{C_m}=1$

In principle, it is necessary to ensure that the initial and boundary conditions are similar in the experiment. However, in practice, due to the limitations of the experimental conditions and the different research points, the experiments in this thesis mainly study the mechanism, pattern and phenomenon of the model slamming and rising waves, such as phenomena that are more inclined to qualitative research. In terms of quantitative analysis, there is no special precision requirement.

3.2 Wave environment generation in the physical wave tank

An essential part of conducting experimental studies on wave slamming loads is the preparation of the wave environment. Currently, a variety of wave generation methods are available, most of which rely on mechanical motion of wave makers to produce specific surface wave patterns. In laboratory settings, the most commonly used methods are piston-type wave making and flap-type wave making. In this study, a flap-type wave maker was used to generate various regular and irregular waves required for the experiments. Accordingly, a brief introduction to the theory of flap-type wave making is first provided, followed by explanations of the procedures used to generate steep regular waves and focused waves in the laboratory.

Fig 3.1 illustrates the principle of flap-type wave generators. In a wave flume of water depth h, the flap oscillates sinusoidally about a hinge point o with angular frequency ω. The stroke of the flap (i.e., the maximum horizontal displacement at the still water level) is denoted as S, and it generates a regular wave with a wave height H.

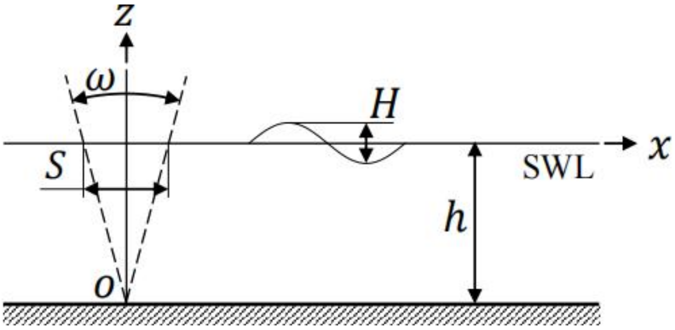

Fig 3.1 Schematic of flap-type wavemaker theory

The hydrodynamic transfer function between the target wave height H and the flap stroke S is given by:

$$T(\omega,h)=\frac{H}{S}=4\left(\frac{\sinh k_p h}{k_p h}\right)\frac{k_p h\sinh k_p h-\cosh k_p h+1}{\sinh 2k_p h+2k_p h} \tag{3.5}$$

Based on this transfer function, the motion control signal of the flap can be determined from the target wave parameters. Although the above theory is derived for regular waves, irregular waves, focused waves, and freak waves can also be generated by superimposing component waves of different frequencies, according to the principle of linear superposition.

3.3 Experimental model and constrained fixation scheme

The research object of this thesis is an fixed offshore drilling platform, a column-stabilized platform. The main dimensions and parameters of the platform prototype are shown in Table 3.2. The prototype is simplified into a square column with a deck for testing. Considering the scale and capability of the experimental equipment, the range and precision of the measuring instrument, the scale ratio between the prototype and the model is set at 100: 1.

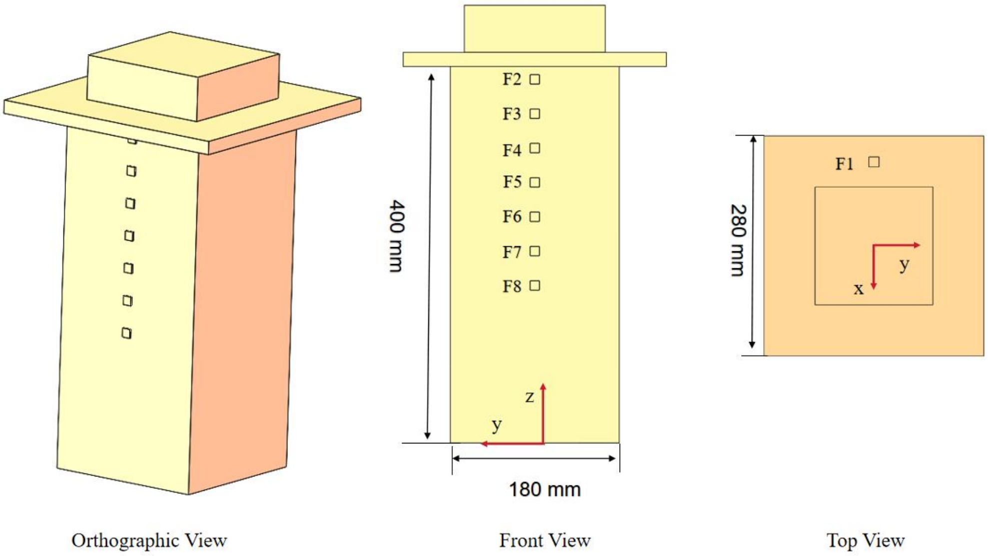

Fig 3.2. Model structure

The principles for model construction are as follows:

1. The geometry below the deck surface of the fixed platform is strictly similar to the prototype to ensure that the model of the fixed platform has the same hydrodynamic characteristics as the prototype;

2. For the superstructure above the deck surface, since the elevation and windward projected area fall within the normal range, the wind load is relatively small compared to the hydrodynamic load, and thus the aerodynamic effect of the superstructure is ignored during model design and fabrication;

3. The connection between the fixed platform column and the deck is rigid, and the connection strength and rigidity need to be ensured;

4. This design facilitates model connection and transducer installation, ensuring that neither interferes with the overall hydrodynamic performance of the model

A fixed platform experiment model was designed and manufactured according to the above principles. The model consists of square columns, overhanging decks, and part of the superstructure (extension of square columns). The model is constructed of aluminum, which has sufficient strength and rigidity, and the shape is smooth and flat, meeting the watertight requirements. Fig 3.2 shows the model's configuration.

At the model scale, the Reynolds and Weber numbers for the regular wave conditions are approximately $Re\_m=1.3\times10^4 - 1.0\times10^5$; $We\_m=6.5\times10 - 1.0\times10^3$, respectively. Except for the smallest wave amplitude case (R10), most (We_m) values fall within the range of ($10^2 - 10^3$), indicating that the capillary effects associated with surface tension are secondary compared to inertial effects. Under a 1:100 Froude scaling, the prototype Reynolds and Weber numbers are about 10^3 and 10^4 times larger than those of the model, further placing the flow in an inertia-dominated regime. Therefore, for the wave slamming peak pressures considered in this study, the effects of viscosity and surface tension are limited (refer to ITTC 7.5-02-07-04.5, 2017).

Table 3.2. Main dimensions and parameters of the fixed platform prototype

Number	Object name	Value	Unit
1	Column length	18	m
2	Column width	18	m
3	Column height	40	m
4	Deck length	28	m
5	Deck width	28	m

3.4 Experimental instruments and equipment and arrangement scheme

The fixed platform operates in a marine environment and is subject to the combined effects of the wind, wave and current environment. In pratice, both wind and current loads are small; at the same time, the direct impact of wind current on platform load, slamming and rising waves is also tiny. For this reason, the research focuses on the issues of platform load, slamming and green water in the wave environment. Creating a realistic wave environment is a key aspect of the experimental research in this thesis and taking into account the experimental cost, period, and convenience of systematic research, this study uses a numerical wave tank to simulate sea waves. The wave-induced loading,slamming and green water problems of the fixed platform model in the flume are investigated.

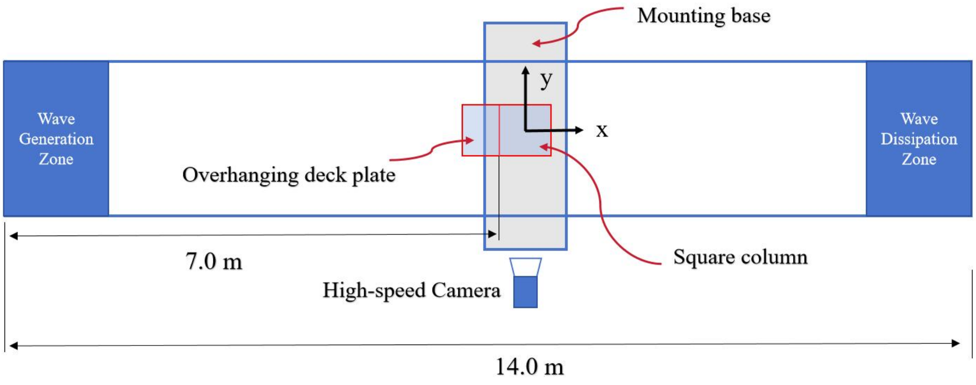

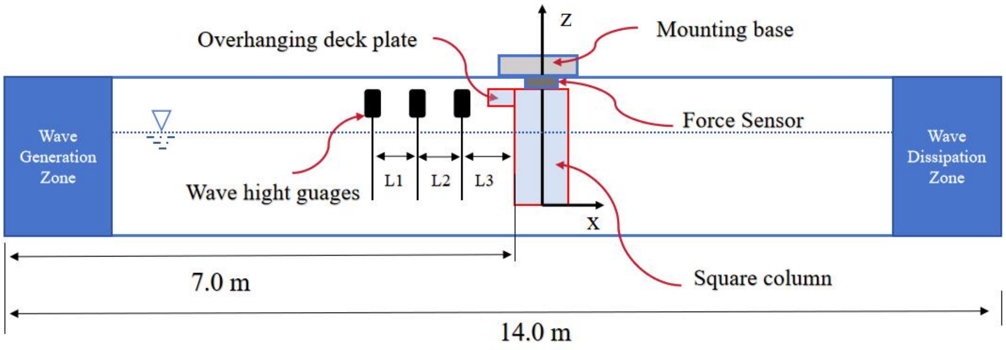

Fig 3.3. Coordinates and layout of the measurement system

The experimental model is positioned between the wave-generation and the wave-absorbing zones, and is fixed on the water flume through a mounting base. A three-component load cell is installed between the base and the water flume to measure the total load on the model. There are seven pressure monitoring points in the model, which are used to measure the pressure load at different column heights. The coordinates and layout of the test measurement system are shown in Fig 3.3. In the coordinate system, the positive direction of the ox axis is from the wave-generation area to the wave-dissipating area, and the positive direction of oy is from the right side of the water flume to the left side of the water flume. According to the right-hand rule, the positive direction of the oz axis is from the bottom to the top of the flume, and the origin of the coordinate axis is located at the center of the base of the column.. Comprehensively considering factors such as the variation range of platform air gap and wave height variation, when monitoring multi-point slamming loads, the distance between monitoring points is considered as 36.5mm, which is 9.125% of relative moulded depth. Seven monitoring points are distributed continuously from below the deck, respectively defined as F2, F3, F4, F5, F6, F7, and F8. In addition, there is also a slamming load monitoring point at the lower edge of the deck. The monitoring point uses a single-component pressure transducer to measure the slamming load.

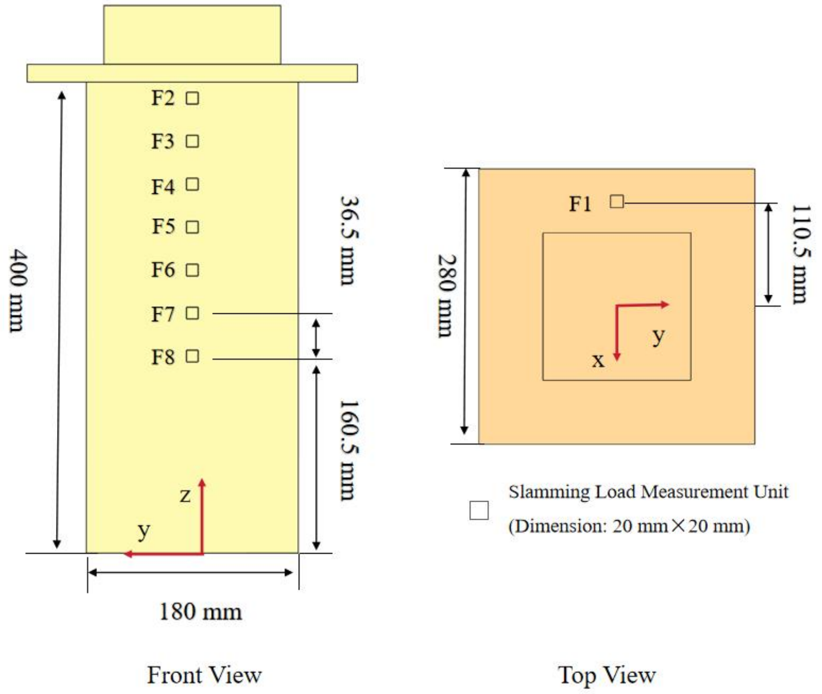

Fig 3.4. Layout of monitoring points

When the fixed platform is deployed in a specific water area, its motion response and deformation are relatively small compared to the significant scale and waves of the model. For this reason, the platform model is set to a fully constrained state in the experiment. The top of the model is rigidly connected to the fixed base above the wave tank. and there is no movement in the direction of six degrees of freedom. The test also involved capturing the motion characteristics of the test model. In this thesis, the acceleration transducer is used to record the vertical load distribution and change characteristics of the model under the wave action.

In this thesis's measurement scheme, the layout and coordinates of the slamming load monitoring points are provided in Fig 3.4 and Table 3.3.

Table 3.3. Coordinates of slamming load monitoring points

Number	x(mm)	y(mm)	z(mm)
F1	-110.5	0	400.0
F2	-90.0	0	379.5

F3	-90.0	0	343.0
F4	-90.0	0	306.5
F5	-90.0	0	270.0
F6	-90.0	0	233.5
F7	-90.0	0	197.0
F8	-90.0	0	160.5

In the experiment, the key input is the wave simulated by the wave-generation plate of the flume. In the water flume, three wave height gauges are arranged at positions L1, L2, and L3 in front of the model to monitor the quality of waves generated in the water flume.

During the experiment, waves are generated by the flume wave generator and act on the fixed platform model. Single-component force measurement units were installed at points F1 through F8 along the vertical distribution of the model to measure the slamming loads acting on the column in the horizontal direction. The high-speed camera set up in the model area records the process and phenomenon of wave slamming and climbing to grasp the mechanism, pattern and unique phenomenon of fixed platform wave slamming and climbing waves. While verifying the results of theoretical analysis and numerical simulation, it provides reference for the study of offshore platform slamming and green water problems.

The model experiments in this study primarily investigate the slamming and wave-induced phenomena, mechanisms, and patterns of a fixed platform. These experiments were conducted in the numerical wave tank at Shanghai Jiao Tong University. The selection and configuration of experimental instruments and equipment were based on the structural characteristics, scale, and output requirements of the model, as well as the scale and wave generation capabilities of the flume. The experiments involved various instruments and devices, including wave simulation equipment, instruments for monitoring wave generation quality, load measurement instruments for the model, as well as instruments for recording slamming and wave data. The specific details are as follows:

(1) numerical wave tank

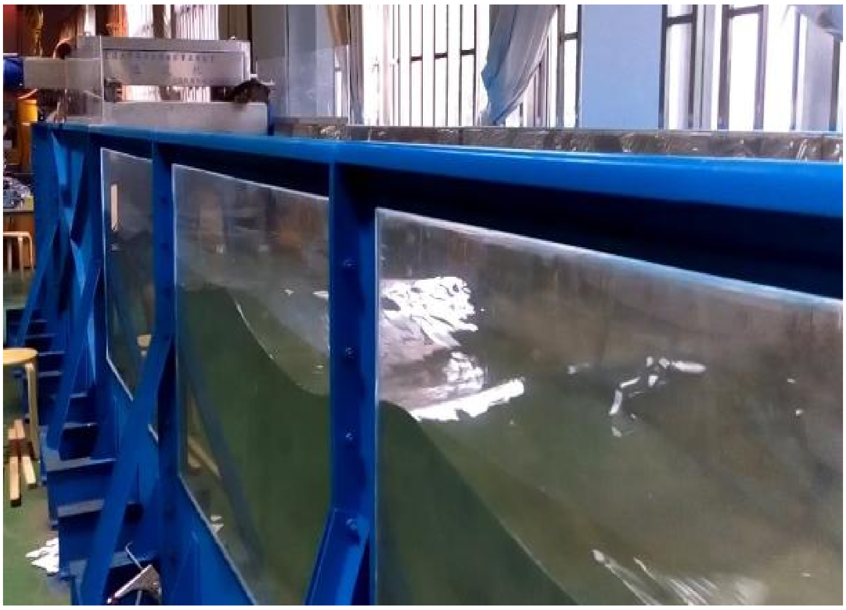

Fig 3.5. Wave channel

Fig 3.6. The wavemaking for Wave channel

The water flume used in this study is a steel frame glass flume, in which the power end is an all-steel structure, the test section is a steel frame glass wall, and the wave absorbing end uses damping wave absorbing. The numerical wave tank has a length of 14m, a width of 1m, a height of 1.2m, the water depth in this experiment is 0.9 m. and a water capacity of 30 tons. The trough uses a motor to drive a rocking plate to generate waves. The rocking plate is 1.5m high, 0.85m wide, and 0.05m thick. It is made of glass fiber reinforced plastics and can generate regular, freak, and singular waves. Among them, the maximum wave generation ability of regular waves: wave height 0.1~1m, period 0.5~6.5S. The numerical wave tank and its wave generation are shown in Fig 3.5 and 3.6.

(2) Wave gauge

A resistive wave height gauge was used in the experiment. The wave gauge has a measurement range of 0 to 0.5 meters for wave height, with an accuracy of ±1 millimeter. The measurement range for wave period is 0 to 15 seconds, with an accuracy of ±0.05 seconds. The wave gauge is powered by a voltage of 220 volts. The configuration of the resistive wave height gauge is shown Fig 3.7. Three wave gauges were positioned directly in front of the column to monitor the wave elevation. The specific installation positions are illustrated in Fig 3.7.

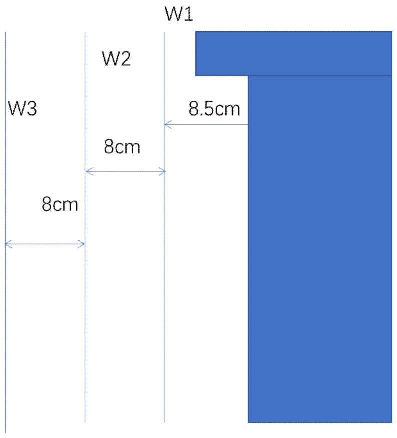

Fig 3.7. Installation location of wave height gauge

(3) Slamming load measurement unit

To accurately measure wave slamming loads acting on localized areas of a structure, this study independently developed a slamming load measurement unit. This unit adopts a force-sensor-based measurement approach, in which the combination of a sensing plate and force transducers directly captures the total slamming load over a target area. As shown in Fig. 3.8, the slamming unit mainly consists of force transducers, a load-sensing plate, a fixed mounting base, and an outer waterproof membrane. The transducers are tightly fitted into the mounting holes pre-machined in the base, while the sensing plate is supported from below by the transducers and remains flush with the base's cover plate. A 1 mm gap is reserved between the two to prevent mechanical interference under external loads. To minimize the influence of structural deformation on the measurement results, a base plate is embedded in the test model, and the entire unit is firmly fixed onto it via bolts through the mounting holes at the bottom of the base. After installation, a waterproof membrane with a thickness of only 0.02 mm is applied over the sensing surface to prevent water ingress into the transducers and model interior, without affecting the measurement accuracy.

Based on requirements for measurement area size and installation space, a force plate measuring 2 cm × 2 cm with a single sensor was designed in this study, with one single-axis force sensor placed at the center beneath the plate. Unless otherwise specified, the term "pressure" as measured by the slamming unit in the following sections refers to the area-averaged pressure. The single-axis force sensor has a measurement range of 100 N, with a linearity error of less than 1%. The slamming load measurement units used in this study were statically calibrated prior to installation. The calibration results showed good linearity of sensor output, with correlation coefficients (R^2) meeting the experimental requirements. All data channels were filtered during post-processing, with a low-pass cutoff frequency of 3.0 rad/s, corresponding to a physical period of 2.09 s. Signals with periods shorter than 2.09 s were treated as noise and removed. The overall measurement uncertainty is estimated to be less than 1 % FS.

Compared with the two commonly used methods for measuring slamming loads—those based on pressure sensors and those based on force transducers—the slamming unit developed in this study offers clear advantages in terms of engineering applicability and result representativeness. Pressure sensors, while small in size and highly sensitive—making them suitable for recording time-resolved pressure histories at specific points—are limited by the highly uneven spatial distribution of slamming loads. A small number of sensors may miss critical impacts, and capturing distributed loads over an area requires dense sensor arrays, leading to substantial data volume and increased processing complexity. Moreover, wave slamming is highly random, with local pressure readings significantly influenced by variations in slamming angle, entrained air, and other factors. These localized high peaks often lack broader representativeness, and using them directly in design may result in unnecessary conservatism.

Fig 3.8. Slamming Load Measurement Unit

In engineering practice, it is more meaningful to obtain area-averaged slamming pressure over a specified structural panel (e.g., 3 m × 3 m). Compared to traditional methods, the slamming unit designed in this study enables direct measurement of the total load over a defined area and calculation of the corresponding average pressure. This not only provides a more realistic representation of the structural impact intensity but also offers strong practical potential for engineering application and design optimization.

(4) Three-component force transducer

The total load on the fixed platform model is measured using a strain-based three-component load transducer, which records the wave direction force *X*, lateral force *Y*, and the ending moment *M* of the model. The measurement range of wave force *X* is 0~30N, and the accuracy is 0.01~0.05N. The lateral force *Y* measurement range is 0~30N, and the accuracy is 0.01~0.05N. The measurement range of bending moment *M* is 0~50N • m, and the precision is 0.05~0.1N • m. The working temperature of the transducer is -20~40℃, the working humidity is 0~100%, the power supply voltage is 220V, and the output sensitivity is 2mV/V.

(5) Data acquisition system

The Donghua DH5920 dynamic signal test and analysis system is adopted. The system comprises of a data acquisition software and a data collector powered by a DC stabilized power supply with 16 working channels; the working frequency during sampling is between 10 and 100kHz, the accuracy is 0.5%, and the stability is 0.05%/h. The system is capable of collecting frequency and time domain signals and perform spectrum analysis and real-time data processing. Fig 3.9 is the data acquisition software interface and the data collector.

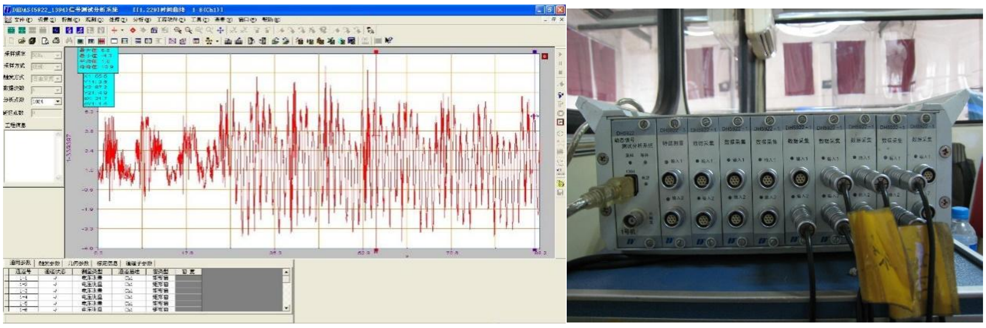

Fig 3.9. Software interface of data acquisition & Data collector

(6) Power supply

According to the hardware requirements of the data acquisition system, a JC series DC regulated power supply is used for power supply, dual-channel. The voltage output range is 0~30V which is continuously adjustable, and the current output range is 0~3A which is also continuously adjustable. Fig 3.10 is the power supply for the JC series dc stabilized power supply.

(7) high-speed camera

A high-speed camera captures the changes in the flow field during the interaction between the wave and the column. The resolution of the camera is 1280×1024.

Fig 3.10. Power supply & Interface force measuring transducer

The experimental measurements presented in this study are subject to several sources of uncertainty. These include sensor accuracy and calibration errors of the pressure transducers, signal noise and resolution limitations of the data acquisition system, and small variations in wave generation and repeatability. In addition, scale effects associated with the 1:100 physical model may influence the measured pressure amplitudes, particularly under highly nonlinear slamming conditions.

Although these uncertainties may affect the absolute values of local peak pressures, their influence on the comparative trends discussed in this study is considered limited. The analysis primarily focuses on relative variations in slamming loads under different wave conditions and geometrical configurations, for which the measurement uncertainty is expected to be consistent across test cases.

3.5 Introduction of the experimental wave load conditions

In this study, three types of wave conditions, namely regular waves, focused waves, and freak waves, are employed in the model experiments. This section will provide a detailed description of each wave condition. All test conditions can be found in Section 4.1 and Table 0.3 of Appendix A.3.

3.5.1 Regular wave experiment

The wave parameters for the regular wave conditions are presented in Table 3.4. Fourteen different load conditions were set up for the regular waves, focusing on the investigation of the effects of wave period and wave steepness on the wave loads on the platform columns. The wave steepness in the experiments was not less than 0.095. A higher wave steepness increases the probability of wave slamming events occurring during the model experiments.

Table 3.4. Regular wave parameters (model values)

Wave No.	H (cm)	T (s)	L (m)
R1	10.22	0.8	1.0754
R2	11.48	0.8	1.0934
R3	12.81	0.8	1.1135
R4	15.81	1	1.6637
R5	17.73	1	1.6882
R6	19.74	1	1.7160
R7	22.28	1.2	2.3456
R8	24.95	1.2	2.3759
R9	27.73	1.2	2.4106
R10	7.00	0.60	0.56
R11	12.00	0.80	1.00
R12	19.00	1.00	1.56
R13	23.00	1.10	1.89
R14	27.00	1.20	2.25

3.5.2 Focused wave experiment

The focused wave load conditions were set up with two different wave environments, and the parameters are listed in Table 3.5. The wave period and wave height were scaled based on the model experiments. The actual wave period ranges were 6.0 to 14 seconds and 8.0 to 12 seconds, respectively. These ranges were chosen to investigate the impact of focused waves on the slamming loads on the platform. Each focused wave test was conducted only once.

Table 3.5. Focused wave parameters (each wave duration is 60s)

No.	Prototype			Model Scale		
	Period(s)	Wave crest(m)	Remark	Period(s)	Wave crest(m)	Remark
1.	6.0～14	10	TAH5	0.6～1.4	0.10	TAH5
2.	8.0～12	10	TBH5	0.8～1.2	0.10	TBH5

3.5.3 Freak wave experiment

To investigate the extreme slamming effects of typical freakwaves on offshore platform structures, this study conducted physical model tests using two types of freak wave sequences, namely the S-type and J-type spectra. The detailed wave parameters are listed in Table 3.6.

The S-type freak waves are reconstructed based on actual sea state time series and offer greater representativeness and engineering applicability. The prototype is the well-known Draupner's abnormal "New Year" wave. a typical freak wave measured in the North Sea. This wave is characterized by a single peak, high steepness, and rapid variation, and is frequently cited in marine engineering as a real-world extreme wave case. In this study, the "New Year" wave was selected as the prototype, and five target wave sequences were generated using Froude similarity scaling with scale ratios of 100, 150, 200, 250, and 300. These test conditions are labeled as S100M10, S150M10, S200M10, S250M10, and S300M10.

The J-type freak wave spectrum was generated using Kriebel's bichromatic wave focusing theory. It is a synthetic bimodal freak wave sequence, where wave superposition leads to a distinct double-peak profile. This type is well-suited for comparative and sensitivity analyses of structural impact responses. Two representative test conditions were selected: JonM06 and JonM10. Among them, JonM10 closely matches the "New Year" wave in both timing and overall waveform, and thus serves as a comparative counterpart to the S-type spectrum in this study.

Table 3.6. Freak wave parameters (each wave duration is 60s)

No.	Prototype			Model Scale			Remark
	Period (s)	Wave height (m)	Wave crest(m)	Period (s)	Wave height (m)	Wave crest(m)	
1.	11.50	25.29	18.23	1.150	0.253	0.182	S100M10
2.	9.39	16.86	12.15	0.939	0.169	0.122	S150M10
3.	8.13	12.65	9.12	0.813	0.126	0.091	S200M10
4.	7.27	10.12	7.29	0.727	0.101	0.073	S250M10
5.	6.64	8.43	6.08	0.664	0.084	0.061	S300M10
7.	14.60	25.77	18.00	1.460	0.258	0.18	JonM10
8.	14.60	15.46	10.80	1.460	0.155	0.11	JonM06

3.6 Experimental Results and Validation

Partial experimental results were used to verify the accuracy and reliability of generating the three wave environments in the model tests. Taking condition B4 shown in Figure 3.11 as an example, it is observed that the heave, pitch, and roll motions of the floating body vary periodically and stably over time under wave excitation. The oscillation period of the motion curves corresponds to that of the regular waves, and the peak values show no significant discrepancies, indicating good convergence. These results demonstrate that the wave environments generated in the regular wave tests are accurate and reliable.

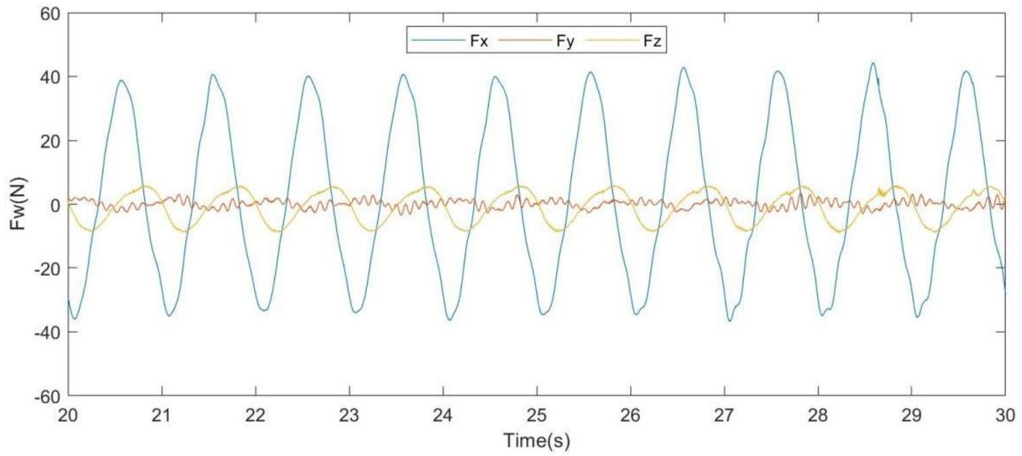

Fig 3.11. Time history curve of the total wave force under condition B4

As shown in Figure 3.12, the time history of the focused wave in the experiment—scaled by a 1:10 ratio—has a period of 0.6–1.4 s and a wave crest height of 0.1 m. From the time-history curve of the focused wave elevation, it is observed that the wave profile remains stable in the early stage and gradually evolves over time. A distinct peak appears between 30 s and 35 s, clearly illustrating the focusing process of “energy convergence and wave height amplification.” During the focusing interval, the wave height rises sharply, and the wave shapes before and after the peak transition smoothly, consistent with the physical characteristics of focused waves. These results indicate that the model experiment can stably generate a focused-wave environment, demonstrating good accuracy and reliability in producing focused waves.

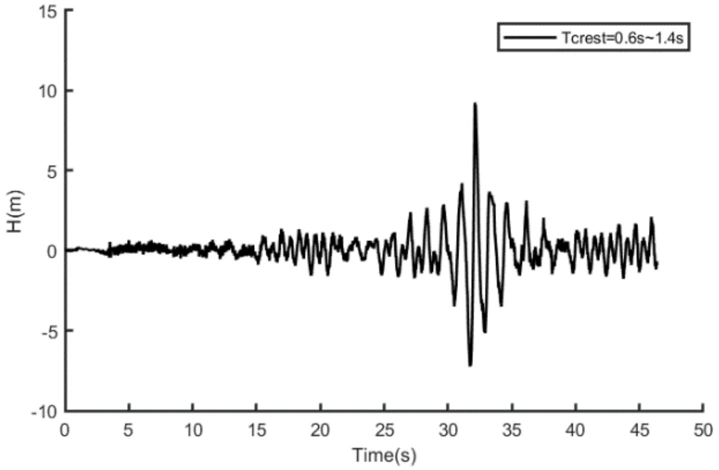

(a) Time history of focused waves

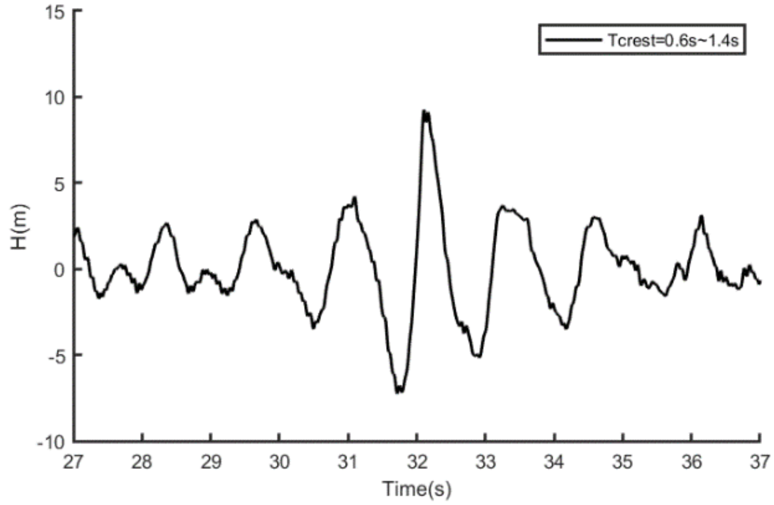

(b) Local magnified time history of focused waves (wide-band wave)

Fig 3.12. Wave time history of focused waves

As shown in Figure 3.13, the freak wave condition corresponds to a 1:100 scale ratio. From the time-history curve of wave elevation for the S100M10 freak wave, the waveform remains stable at the initial stage and then exhibits regular fluctuations as time progresses. A distinct peak appears during the evolution, clearly demonstrating the typical characteristics of a freak wave — “sharp wave-height variation with a pronounced single crest.” The waveform shape matches well with the prototype’s steepness and rapid variation features, indicating that the experiment can stably reproduce the physical process of a typical freak wave. This strongly demonstrates the accuracy and reliability of the model experiment in generating a realistic freak-wave environment.

From the time-history curve of the J-type freak wave (JonM10), the waveform shows a smooth transition in the early stage and evolves into regular oscillations with a prominent double-crest peak over time. The waveform exhibits a clear bimodal characteristic, consistent with the expected shape of the synthesized double-crest freak wave series generated based on Kriebel’s dual-wave-group focusing theory. This process aligns with the physical generation mechanism of the synthetic J-type freak wave, confirming the good accuracy and reliability of the experiment in reproducing such waves, and providing effective experimental conditions for studying the impact responses of typical structures.

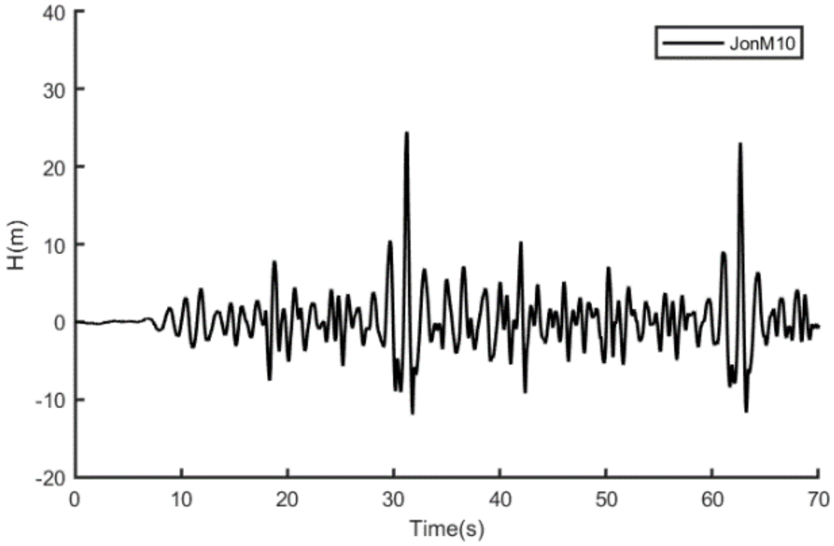

(a)JonM10, Period=1.46, Hight=0.258m

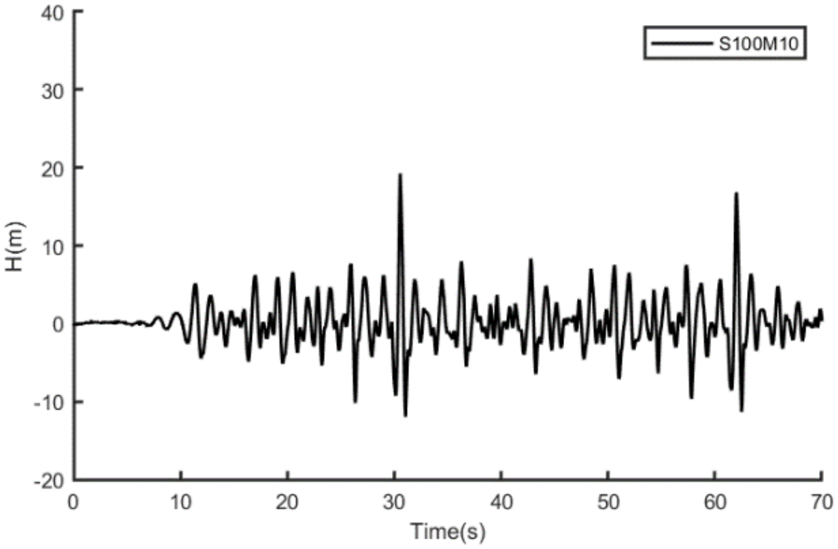

(b)S100M10, Period=1.15s, Hight=0.253m

Fig 3.13. Time-history curves of freak wave profiles (two wave types)

3.7 Summary of this chapter

This chapter focuses on the mechanisms and characteristics of extreme wave slamming loads acting on critical components of semi-submersible platforms, specifically the columns and attached deck structures. It systematically presents the experimental design rationale and its targeted configurations. The design adheres to two principles: concentrating on key structural elements and replicating core physical processes. The prototype is thus simplified into a representative square - column model with an overhanging deck, excluding secondary structural effects. The experiment is primarily governed by geometric similarity and Froude number similarity, ensuring accurate reproduction of wave motions dominated by gravity and inertial forces, while accepting limited quantitative precision in favor of qualitatively revealing the underlying slamming mechanisms. A fully constrained, rigid model setup is adopted to accurately represent the restrained condition of the actual platform under extreme wave loads.

All experimental settings agdheres to the research objectives: a 1:100 scale ratio is applied to ensure strict geometric fidelity and sufficient structural strength; sensors are purposefully arranged—with seven pressure sensors (F2–F8) distributed vertically along the column and one under the deck edge (F1)—to capture the spatial distribution and transient peaks of slamming loads. A three-axis load cell is used to measure the total force response, and a high-speed camera records transient flow phenomena such as slamming and wave overtopping. The wave conditions are designed to isolate the effects of critical parameters: regular waves are used to examine the influence of wave period and steepness (with deliberately high steepness, ≥0.095, to trigger slamming); focused waves simulate transient events with extreme crests; and freak waves are used to study the slamming characteristics of the highly hazardous S-type and J-type waveforms. Additionally, wave gauges placed upstream ensure the accuracy of wave generation. All experiments are conducted in a specially selected flume that satisfies the requirements for slamming studies.This highly targeted experimental design lays a solid foundation for subsequent research on wave slamming loads in irregular sea states. Partial experimental results were used to verify the accuracy and reliability of generating the three wave environments in the model tests, providing effective experimental conditions for studying the impact responses of typical structures and the characteristics of wave slamming under different types of waves.

4 EXPERIMENTAL RESULTS AND ANALYSIS OF HORIZONTAL WAVE SLAMMING

During the operation of floating platforms, a small air gap often requires the structure to withstand significant combined wind, wave, and current loads under harsh sea conditions to ensure adequate survivability. Compared to conventional operating conditions, variations in displacement, inertial properties, and natural periods lead to complex nonlinear interactions between the platform and incoming waves. Phenomena such as wave-current-wind coupling, mooring-induced interactions, wave run-up, and wave breaking all contribute to the complexity of the load response and increase the difficulty of numerical simulation. Therefore, model testing remains a crucial approach for investigating wave slamming behavior.

To gain deeper insight into the slamming ~~response~~ load characteristics of platform columns under various representative wave conditions, this chapter systematically analyzes experimental data on slamming loads, using the numerical wave tank setup established in Chapter 3 and the previously collected high-frequency pressure measurements. Through detailed observations and measurements, the study identifies pressure distribution patterns, time histories of impact loads, and their governing factors under different wave scenarios. The results provide essential physical insight for validating numerical models and supporting structural optimization in platform design.

4.1 Experimental conditions and data processing methodology

In Chapter 3, a series of combined tests were conducted under regular, focused, and freak wave conditions, considering four air gaps (135 mm, 185 mm, 235 mm, and 285 mm) and two wave headings (180° and 135°). The four air gaps are illustrated in Fig. 4.1. A total of 140 test conditions were designed, as listed in Table 0.2 of Appendix A.3. These include 56 regular wave cases (4 air gaps × 14 regular wave types × 180° wave heading), 8 focused wave cases (4 air gaps × 2 focused wave types × 180° wave heading), and 28 freak wave cases (4 air gaps × 2 wave angles × 180° wave heading). 25 oblique wave cases ((14 regular waves + 2 focused waves + 7 rogue waves + R1 + R2) × 185 mm air gap); 23 repeated tests (S100M10 × 185 mm air gap × head seas).

For each pressure sensor unit, all pressure data within the simulation time window were extracted under the regular wave conditions and ranked in descending order. The top one-third of the peak pressure values were selected, and their arithmetic mean was computed. This mean value is defined as the slamming pressure peak at the corresponding monitoring point.

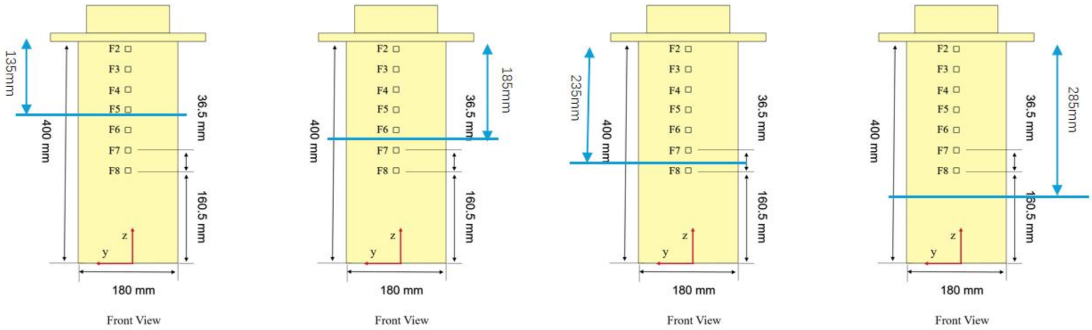

Fig 4.1 Relative positions of pressure sensor units and free surface under four air gap conditions (Blue horizontal lines represent the still water levels for different air gap scenarios)

In fact, the raw pressure data obtained from wave slamming experiments cannot be directly used for analysis without appropriate preprocessing, primarily due to the following reasons:

a. The raw signals contain significant high-frequency noise components, manifesting as strong interference;

b. The high sampling rate, extended recording duration, and large number of measurement channels lead to noisy datasets. It is thus necessary to first detect valid wave slamming events and extract characteristic parameters (e.g., peak loads) prior to further analysis.

Therefore, post-processing of the raw wave slamming data is essential. Due to the intermittent nature of wave slamming events in the long-duration measurements, the resulting signals are highly non-stationary, characterized by sporadic high peaks. Traditional filtering methods (such as Fourier transform-based techniques), which rely on the assumption of signal stationarity, are not well suited for such data. These methods often result in the loss of temporal resolution and may attenuate peak load values if the cutoff frequency is improperly chosen.To address this, Wavelet Transform (WT), a time-frequency analysis tool capable of resolving both temporal and spectral features with high precision, is adopted in this study. WT has been successfully applied in signal denoising and is increasingly utilized in the fields of ocean engineering and oceanography. Thus, this method is employed here to effectively remove noise from the measured wave slamming pressure signals.

During the entire wave test process, slamming events occur intermittently and unpredictably. Therefore, to avoid missing any slamming occurrences, the high-speed data acquisition system must operate continuously, resulting in massive datasets. During post-processing, it is necessary to identify individual wave slamming events for each test case to eliminate redundant data. Specifically, a slamming event is detected when the measured pressure from any slamming unit exceeds a predefined threshold, denoted as Eq.4.1.

$$\max\left(p_1, p_2, p_3, \cdots, p_i, \cdots\right) > p_{threshold} \tag{4.1}$$

Here, pi represent the slamming pressure measured by the i-th unit, and the threshold pressure pthreshold is selected based on the specific test condition. The peak pressure recorded by a unit during a single slamming event is denoted as ppeak , and among all slamming units and events, the highest peak pressure is defined as pmax, which is used in subsequent analyses.

4.2 Experimental results and horizontal wave slamming characteristics under regular waves

4.2.1 Distribution characteristics of horizontal wave slamming based on experimental results

Under the condition of a 180° wave heading and 14 regular wave cases, the peak slamming pressures measured at eight points (F1–F8) on the column surface were analyzed to examine their distribution patterns for four air gaps of 135 mm, 185 mm, 235 mm, and 285 mm. The spatial distribution of peak slamming pressures with respect to the measurement point locations is shown in Fig 4.2 to Fig 4.5. Under the condition of 135mm air gap, 10 of the 14 groups of wave load conditions show that the peak value of slamming pressure increases as the position of the measuring point increases, among which the pressure peak measured at F1 point is the largest, and the maximum value at F1 point under B108 load condition is 64.3kPa. The impact of wave slamming is more obvious at points F1 to F4, while the impact of wave slamming is weaker at points F5 to F8.

Generally speaking, when the wave conditions are conducive to the occurrence of slamming, the slamming pressure is closely related to the location of the measuring point. The farther the measuring point is from the free water surface, the stronger the wave slamming it experiences, but the frequency of slamming decreases. Taking the B108 load condition as an example, as the vertical distance decreases, the slamming pressure values from points F1 to F8 decrease in sequence by 17.03%, 51.36%, 58.84%, 39.71%, 23.70%, 62.09%, and 11.56%, which indicate very obvious change.

However, the pressure values of all measuring points under load conditions B1, B2, B106 and B107 are between 0-2kPa, and the wave slamming phenomenon is relatively weak, which cannot reflect the relationship between slamming pressure and the position of the measuring points.

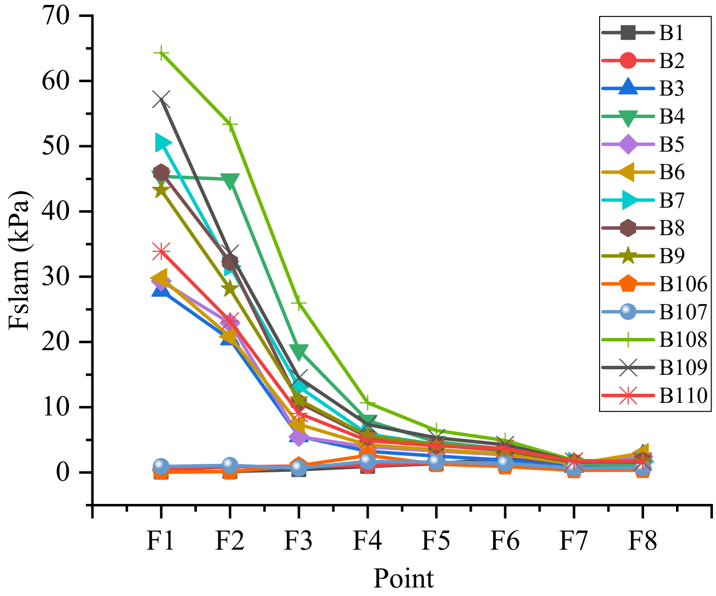

Fig 4.2. Peak value of slamming pressure at F1 to F8 points under 135mm air gap and 180° wave heading

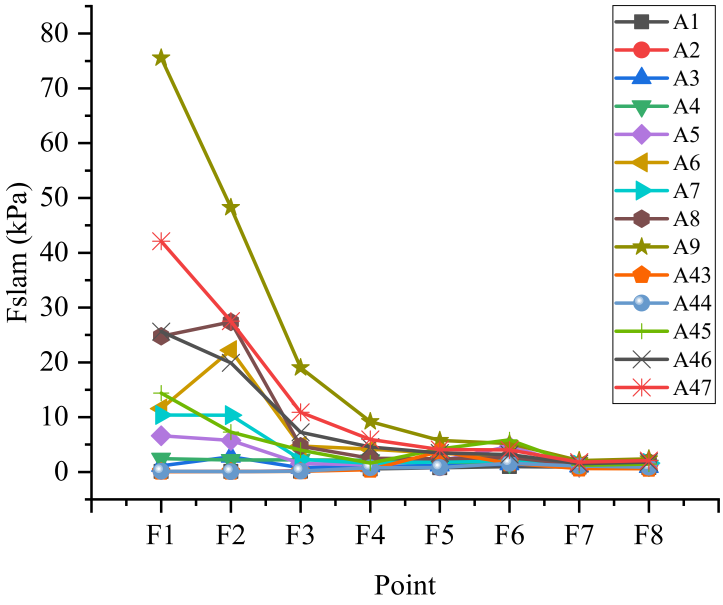

Fig 4.3. Peak value of slamming pressure at points F1 to F8 under 185mm air gap and 180° wave heading

Under an air gap of 185mm, compared with an air gap of 135mm, most wave conditions that have the potential for slamming still exhibit a clear trend of increasing slamming pressure peaks with higher measurement point positions. Among them, under the load conditions A9, A47, and A46, the slamming value gradually decreases as the position of the measuring point decreases; under the load conditions A6 and A8, the slamming value first increases and then decreases as the position of the measuring point decreases. When measured at point F2 the maximum pressure peak is obtained. Under the B44 load condition, the maximum value at point F1 is 38.48kPa. The impact of wave slamming is more obvious at points F1 to F4, while the impact of wave slamming is weaker at points F5 to F8.

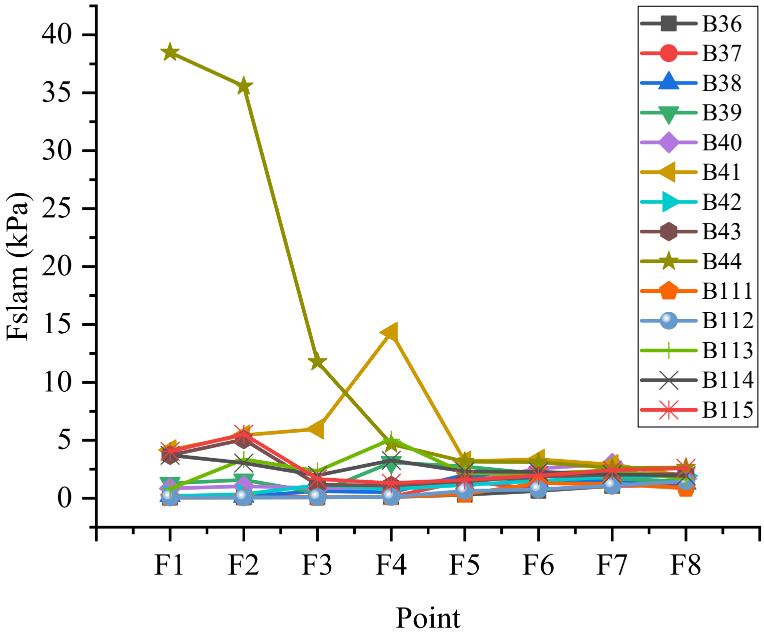

Fig 4.4. Peak value of slamming pressure at F1 to F8 points under 235mm air gap and 180° wave heading

Generally speaking, when wave conditions are favorable for the onset of slamming, the slamming pressure is closely related to the location of the measuring point. The farther the measuring point is from the free water surface,the stronger the effect of wave slamming it experiences, but the frequency of slamming is relatively small. Compared with the air gap of 135mm, the frequency of slamming is significantly reduced, and the number of slamming above 20kPa is reduced by 60%. Taking A9 load condition as an example, as the vertical distance decreases, the change rate of slamming pressure value from F1 to F8 is -36.13%, -60.59%, -51.57%, -37.32%, -10.27%, -59.55%, 15.22 %, and the change rate is more obvious. However, the pressure values of all measuring points under load conditions A1, A2, A3, A4, A43 and A44 are between 0-2kPa, and the wave slamming phenomenon is relatively weak. At this time, its relationship with the position of the measuring points cannot be further analyzed.

Under the air gap condition of 235mm, compared with the air gap values of 135mm and 185mm, fewer load conditions show a clear and consistent increase or decrease trends in the slamming pressure peak value with the change of the measuring point position. Observed from the distribution pattern, under the B44 load condition, the slamming value gradually decreases with the decrease of the measuring point position, and the slamming value at the F1 to F3 points is more obvious; under the B41 load condition, the slamming value at the F4 point has the peak value of 14.30kPa, while it fluctuates steadily around 5kPa at other measuring points. The peak pressure measured at point F2 is the largest.

The maximum value of point F1 under B44 load condition is 38.48kPa. The wave slamming effect is more obvious at points F1 to F3, and the wave slamming effect is weaker at points F4 to F8. Generally speaking, when wave conditions support the occurrence of slamming phenomenon, the slamming pressure is closely related to the location of the measuring point. Measurement points located farther from the free surface are subjected to stronger wave slamming effects, but the frequency of slamming is relatively small. It decreases more rapidly than when the air gap is 135mm and 185mm. Only the F1 and F2 points under the B44 load condition have a slamming of more than 20kPa. Taking the B44 load condition as an example, as the vertical distance decreases, the slamming pressure change rates from F1 to F8 are -7.61%, -66.93%, -60.37%, -32.16%, -1.67%, -16.01%, -1.34 %, and the change rate of many measuring points is obvious. Except for the B41 and B44 load conditions, the pressure values are all less than 6kPa, and the slamming phenomenon is not obvious.

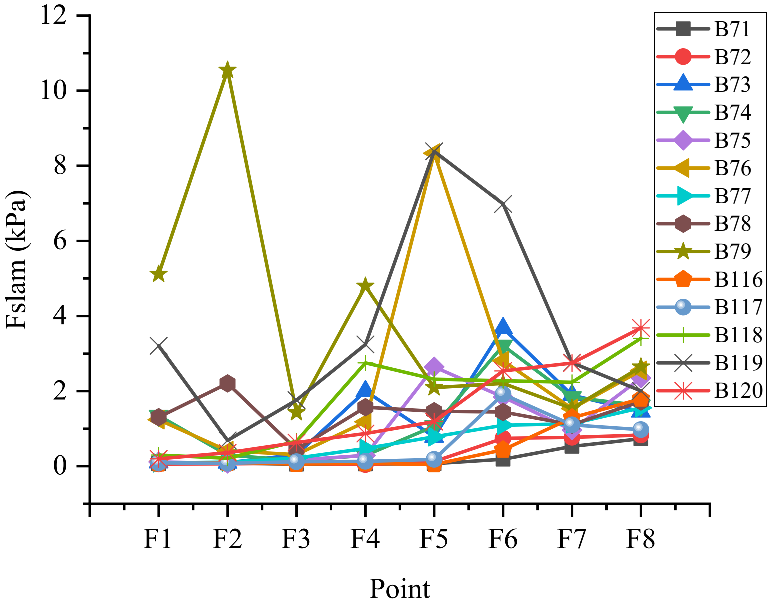

Fig 4.5. Peak value of slamming pressure at F1 to F8 points under 285mm air gap and 180° wave heading

Under the air gap of 285mm, compared with the air gap value of 135mm, 185mm, and 235mm, only a few wave conditions exhibit a clear and consistent variation in peak slamming pressure with measuring point location. The peak value of slamming pressure is the maximum at F2 points under load condition B79 and the maximum value is 10.55kPa. The fluctuation range of the slamming value is located in the 0 to 10.55kPa range, and the pressure value between 0 and 4kPa accounts for 94.6%, which means that only the effect of wave power occurs at most measuring points under 285mm air gap, and no slamming occurs and the relationship between slamming and the position of the measurement point cannot be further analyzed.

In summary, first, regarding slamming intensity and frequency: under the four air gap conditions, smaller air gaps (135 mm and 185 mm) result in a greater number of wave conditions producing more prevalent wave slamming phenomena, and when slamming occurs, the intensity is generally higher than that under larger air gap conditions. Second, in low air gap conditions with slamming potential (135 mm and

185 mm), the higher the measuring point position, the greater the slamming intensity, but the lower the slamming frequency—this trend is particularly evident from F4 to F1. Third, under the other two large air gap conditions (235 mm and 285 mm), except for a few special cases, the relationship between slamming intensity and measuring point height is less clear, with fewer regular wave cases showing a distinct pattern in peak slamming pressure variation with measuring point height (either increasing or decreasing), as most conditions exhibit only wave force effects without slamming. Based on this, the present study proceeds from the measuring points, conditions, and air gap values that exhibit relatively sensitive slamming pressure variations to further analyze the relationship between wave slamming and wave parameters.

4.2.2 Analysis of the development process of horizontal wave slamming based on experimental results

The total wave force reflects the magnitude of the six-degree-of-freedom motion amplitude of the floating body caused by the waves, such as pitching, rolling, and heaving. Taking the B4-B6 load conditions shown in Fig 4.6 to Fig 4.8 as an example, it is observed that at a wave direction angle of 180 degrees, the wave force is mainly reflected in the periodic changes of Fx, while both Fy and Fz fluctuate around 0. When the wave period is 1s and the air gap is 135mm, as the wave steepness increases, peak values of Fx increases by 39.9% and 75.4%. At the same time, the change curve of Fx develops from smooth to a sharp and steep wave peak. When the wave peak rises rapidly, the trough value changes slightly. This reflects that under the B6 load condition, an instantaneous wave slamming phenomenon with extremely high pressure occurs between the waves and the structure, and the change of wave force in this extremely short period of time to a certain extent lays the foundation for the analysis of the pattern for the change of wave slamming value.

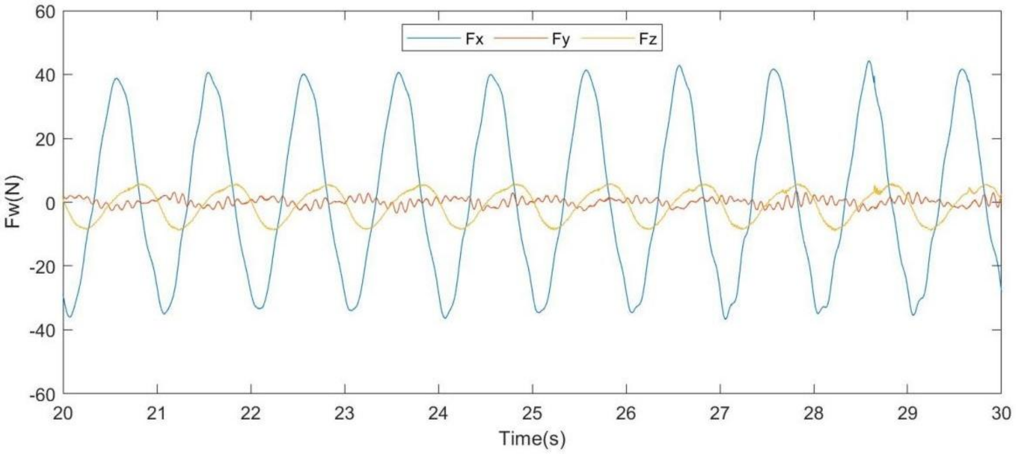

Fig 4.6. Total force time history curve of the wave under B4 load condition

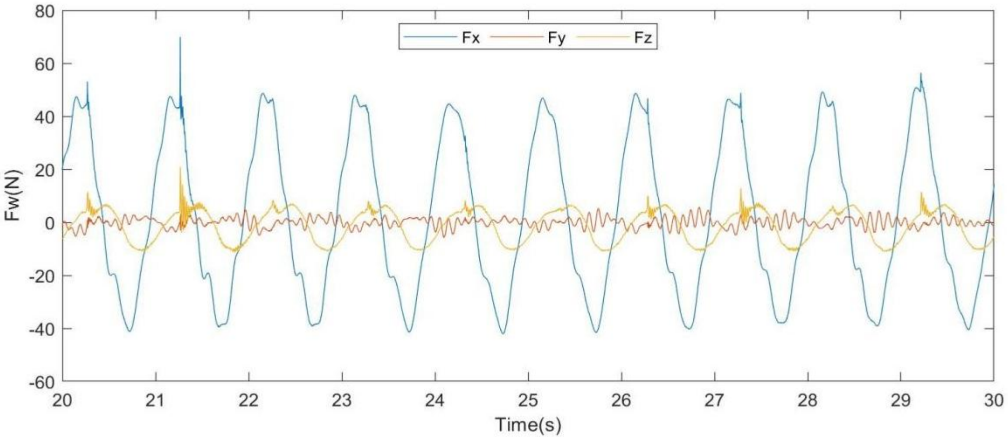

Fig 4.7. Wave total force time history curve under B5 load condition

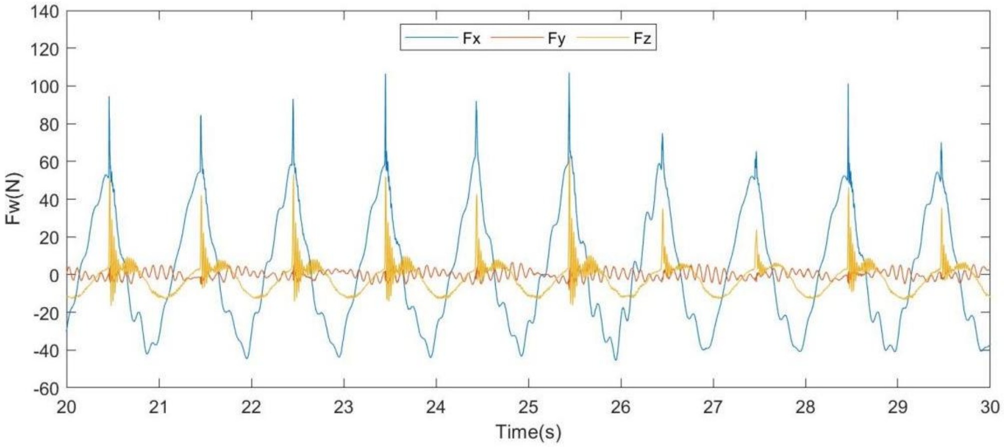

Fig 4.8. Total force time history curve of the wave under B6 load condition

4.3 Experimental results and horizontal wave slamming characteristics under focused waves

4.3.1 Characteristics of focused waves and wave climbing effect

For the two focused wave types, under four air gap conditions (135 mm, 185 mm, 235 mm, and 285 mm) and two wave headings (180° and 135°), the analysis covers: wave time histories for a single wave type, a single air gap, and a single wave heading; wave crest heights for two wave types, four air gaps, and a single wave heading at location W1; and wave time histories at three measuring locations for two wave types, two air gaps, and two wave headings. The results are shown in Figures 4.9 to 4.11.

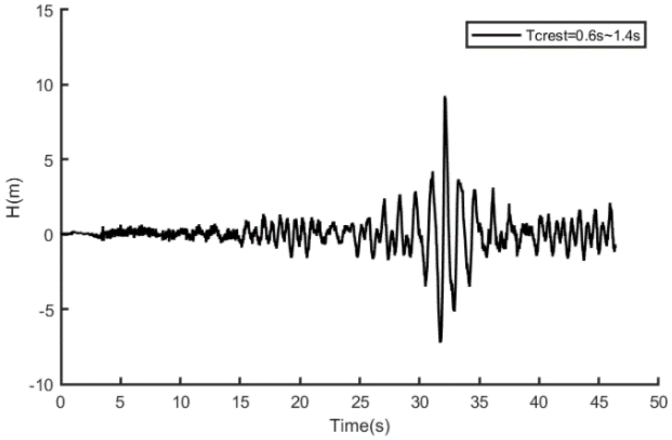

(a) Time history of focused waves

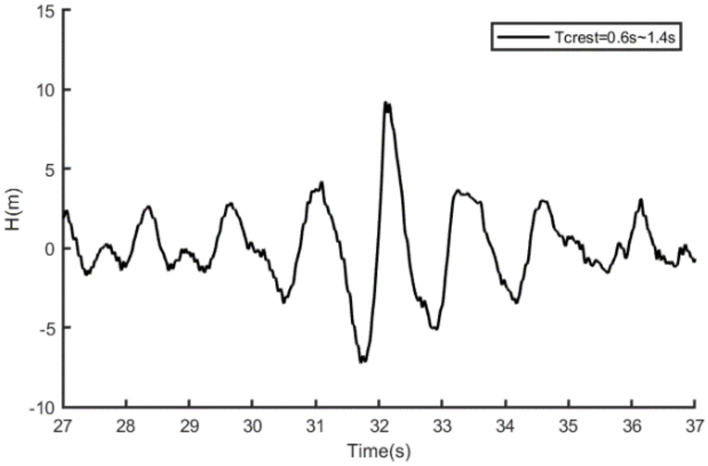

(b) Local magnified time history of focused waves (wide-band wave)

Fig 4.9. Wave time history of focused waves

The focused wave cycle is 6.0 ~ 14s and 8 ~ 12s, and the peak is 10m. After the 1:10 scaling ratio of the experiment, with the periods of 0.6 ~ 1.4S and 0.8 ~ 1.2s, the waves with 0.1m are simulated. The time history of the waves is shown in Fig 4.9.

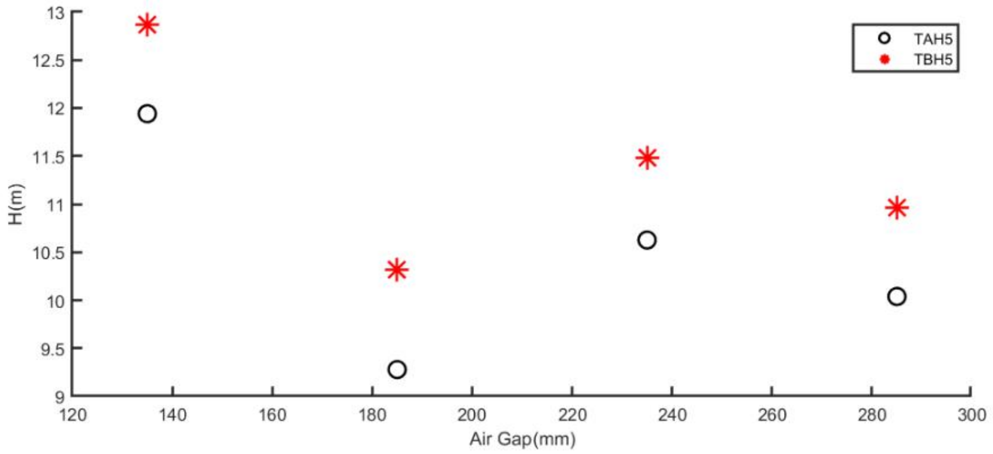

Fig 4.10. Comparison of focused wave crest height (at W1, under 2 wave types and 4 air gaps)

Fig 4.9 shows that when the waves are focused, the wave peak value is much greater than the significant wave height, and the energy of the waves is very concentrated. Studying the slamming force under the action of focused waves is of great significance to understanding the slamming force of structures under extreme sea conditions. The main goal of the experimental verification is to examine the impact of slamming force on the ocean platform under different air gaps. The experiment was conducted on four groups of focused waves with different air gap heights. The maximum wave height measured at W1 before the wave hit is shown in Fig 4.10.

It can be seen from Fig 4.10 that the maximum wave peak value of the focused wave in the TBH5 load condition is larger than that in the TAH5 load condition. This is because the wave frequency of TBH5 is 0.8s ~ 1.2s, which is more concentrated than the wave frequency (0.6s ~ 1.4s) of TAH5, and the wave energy is relatively concentrated, so the peaks generated are relatively large. The time history measured by the wave gauges at the three positions of the platform is shown in Fig 4.11.

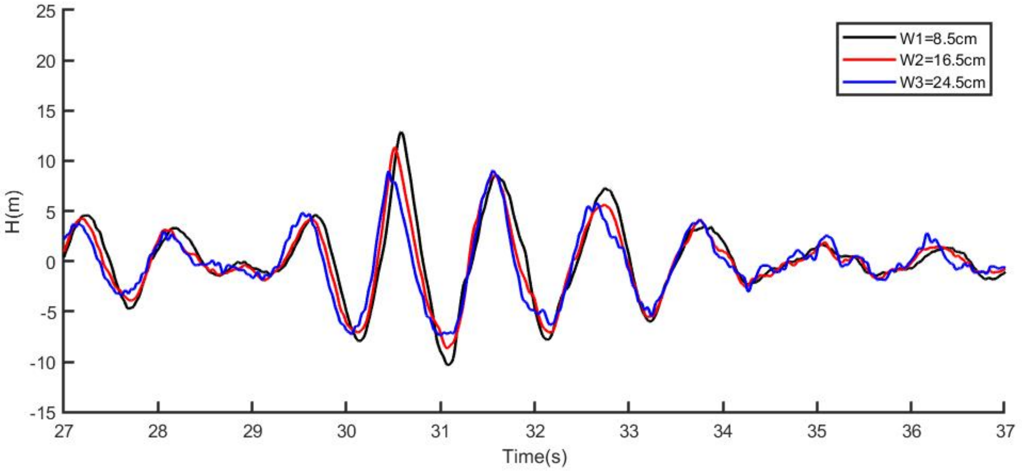

(a) TAH5 case, heading=180°, air gap=135mm

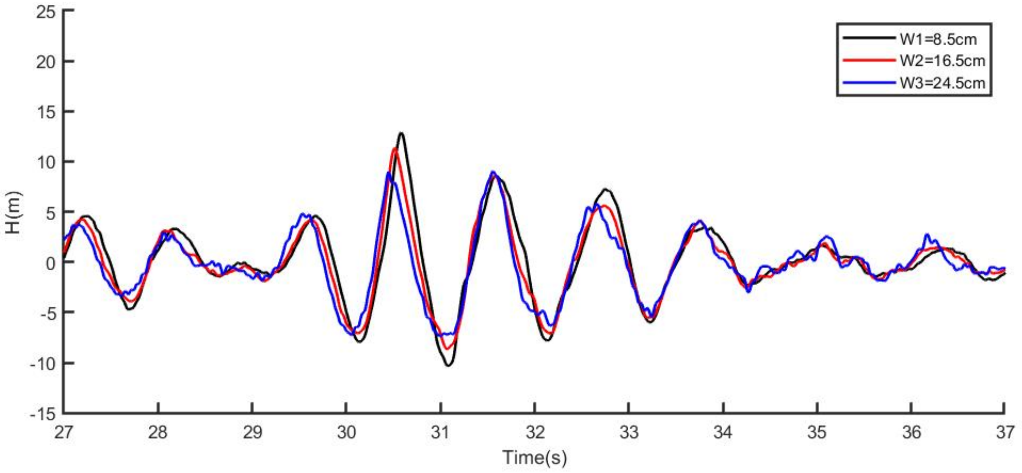

(b) TBH5 case, heading=180°, air gap=135mm

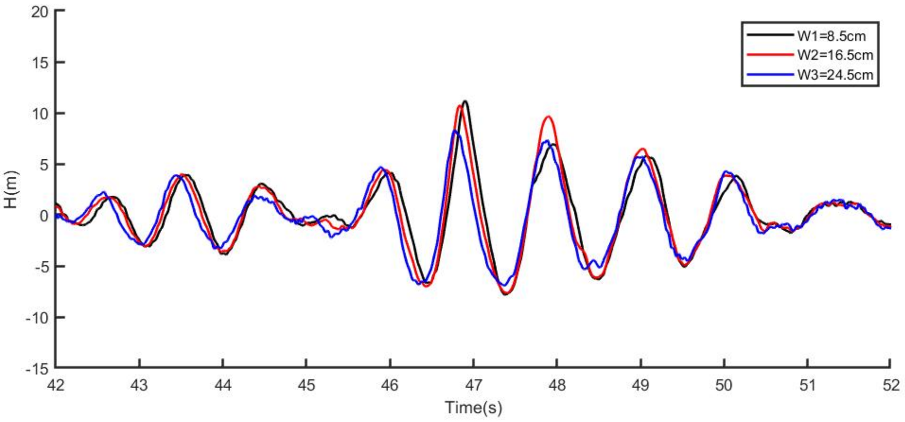

(c) TAH5 case, heading=135°, air gap=185mm

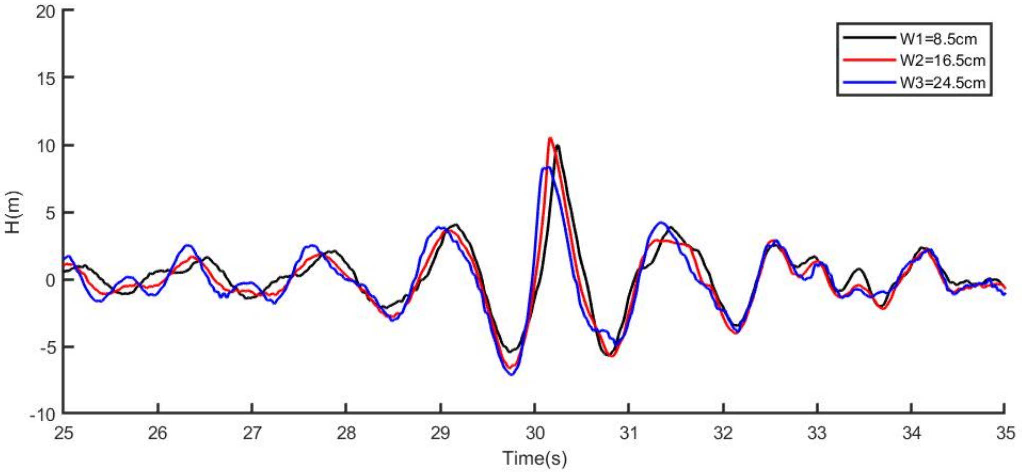

(d) TBH5 case, heading=135° , air gap=185mm

Fig 4.11. Wave time history measured by wave gauges with different distances from the platform (2 wave types, 2 wave directions, 2 air gaps)

From Fig 4.11 (a), (b), (c), it is observed that before–the maximum wave height occurs at W1, indicating that, prior to wave slamming on the platform, the wave height closer to the platform is greater than that farther away. This behaviour is consistent with the wave climbing phenomenon discussed in Chapter 1.. In Fig 4.11 (d), the maximum value of the wave height is generated at W2, but there is a little gap with the wave height at W1. This is because it has a certain impact on the formation of the focused waves after the direction of the platform changes, causing them to be broken before the slamming occurs. Waves have a climbing effect before crushing, and the height of the wave after crushing is reduced.

4.3.2 Distribution characteristics of horizontal wave slamming loads based on experimental results

Under the condition of a 180° wave heading, two focused waves, and four air gaps of 135 mm, 185 mm, 235 mm, and 285 mm, the following analyses are conducted: the time histories of wave forces on the column (two wave types, one wave heading, one air gap), the maximum wave forces (two wave types, one wave heading, four air gaps), the time histories of pressures at eight measurement points (F1–F8) on the column surface (two wave types, one wave heading, two air gaps), and the patterns of maximum pressures (two wave types, one wave heading, four air gaps). These are shown in Figs 4.12 to 4.16.

Fig 4.12 gives the joint force in the three coordinate directions of the space when a focused wave hits the platform. It is observed that the force of the direction of the waves (that is, the X direction) far exceeds that of the other two directions. This shows that the slamming force generates a large combination of power in the effect of wave power, and the amplitude of the shock is relatively large. Secondly, a significant value response was also generated due to the effect of waves in the Z direction. In addition, because the platform has a protruding deck, the position is subjected to a certain amount of wave slamming. It will also produce the force of the Z direction, which will cause the platform Z direction to show a strong non-linear state.

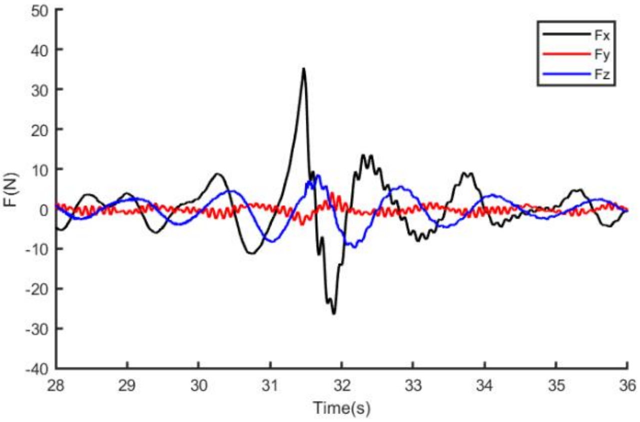

(a) TAH5 case

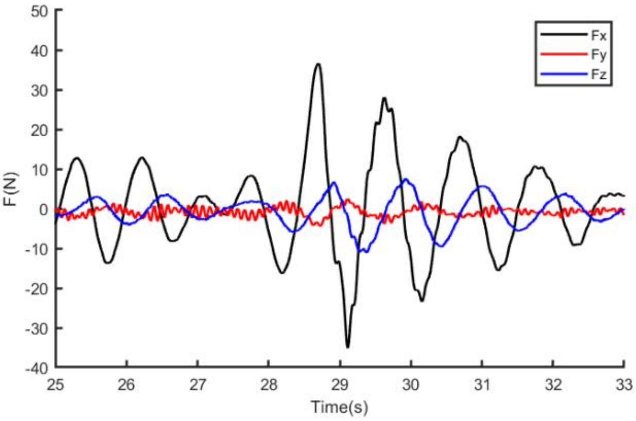

(b) TBH5 case

Fig 4.12. Time history of the wave slamming force on the platform(Heading=180°, Air Gap=185mm, 2 wave types）

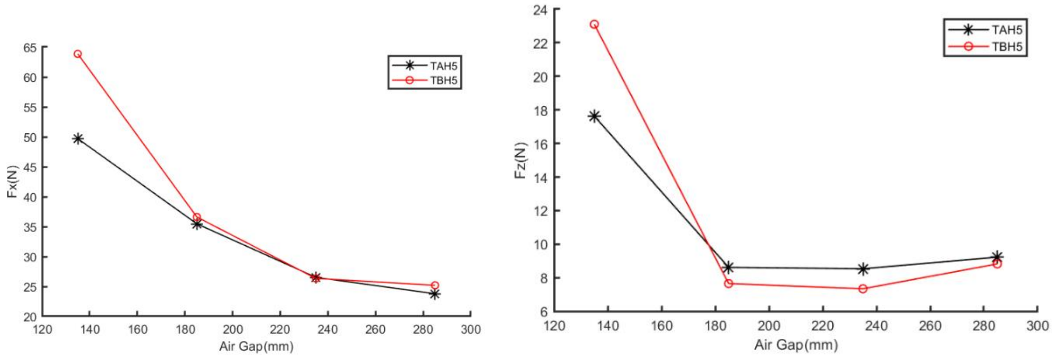

(a) Fx-Direction Force (b) Fz-Direction Force

Fig 4.13. Maximum force distribution of the platform under different air gaps (2 wave types, 4 air gaps, 180° wave heading)

In the experiment, due to the change of air gap, the change of the slamming force on the platform is shown in Fig 4.13. As the air gap continues to increase, the maximum value of the force in the X direction shows a significant decline, and the Fz direction is decreased first when the air gap increases and then slightly increases. This phenomenon shows that the air gap’s force on the waves’ formation has a more significant impact on the X direction. Experiments show that the larger the air gap, the smaller the horizontal slamming caused by the focused waves. However, with the further increase of the air gap, this trend shows a slowing trend, indicating that the impact of extending the deck is gradually decreasing.

In summary, the experiments show that as the air gap increases, the slamming force induced by focused waves decreases, and this decreasing trend becomes less pronounced with further increases in air gap, indicating that the influence of the deck overhang is gradually diminishing.

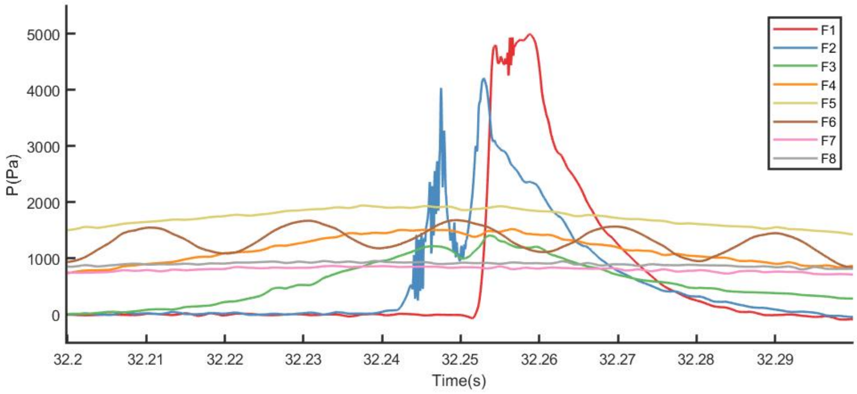

(a) TAH5, Heading=180° , Air Gap=135mm

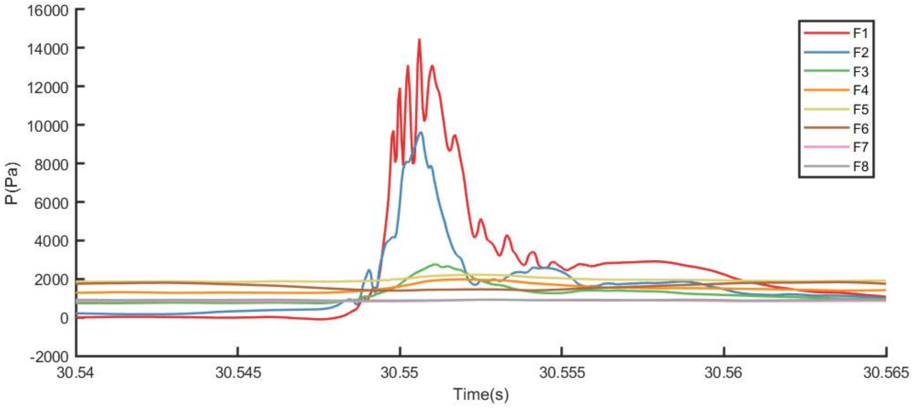

(b) TBH5, Heading=180° , Air Gap=135mm

Fig 4.14. Time history of pressure changes of each pressure transducer under focused waves (180° wave heading, 135 mm air gap)

Fig 4.14. describes the curve of the time history when the pressure measuring point is arranged on the platform. Fig 4.14 (a) shows that the F1 measuring point and F2 measuring point have had very strong non-linear changes, and the pressure increased from 0Pa to 4991Pa and 4039Pa within 0.01s. Moreover, the F2 measuring point appears at a second peak in 0.01s, 4161Pa, higher than the first peak. At the same time, it is also found that the peak of the pressure on the highest point F1 is different from the pressure peak of F2 for the first time, which is relatively close to that of the second pressure peak of F2. This is because the waves are broken at the top. After the broken waves, the waves are divided into two forces on the platform. The second peak is superimposed with the wave after the first attenuation, forming a greater force. The slamming load in Fig 4.14 (b) has a shorter action time and a higher peak value. The maximum value of F1 reaches 14490Pa, and the peak of F2 reaches 9656Pa. It shows that the narrower the frequency of the focused waves, the more concentrated the energy is, the larger the peak of the fluctuation, and the greater the slamming pressure produced.

In summary, the narrower the frequency band of the focused wave (TBH5, 0.8–1.2 s), the more concentrated the energy, resulting in larger wave amplitude peaks and higher slamming pressures than those produced by a wide frequency band (TAH5, 0.6–1.4 s) — for example, a peak of 14,490 Pa versus 4,991 Pa at point F1, 2.9 times greater. This concentration of energy leads to a significant increase in slamming intensity.

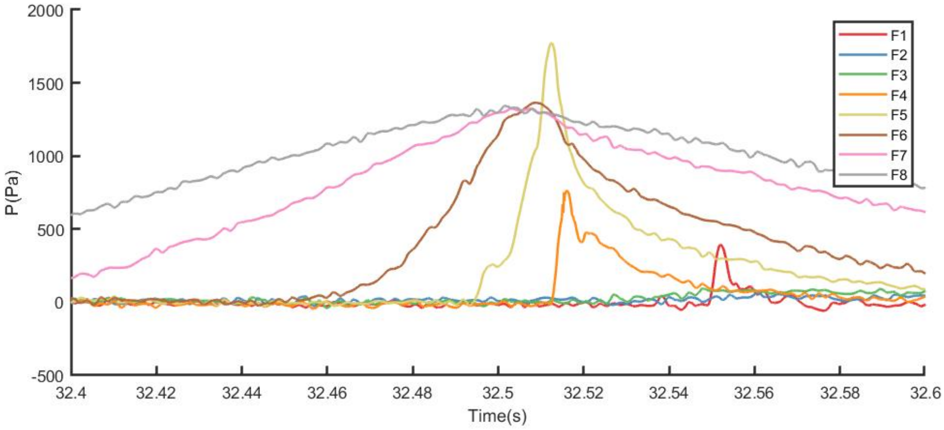

(a) TAH5, Heading=180° , Air Gap=235mm

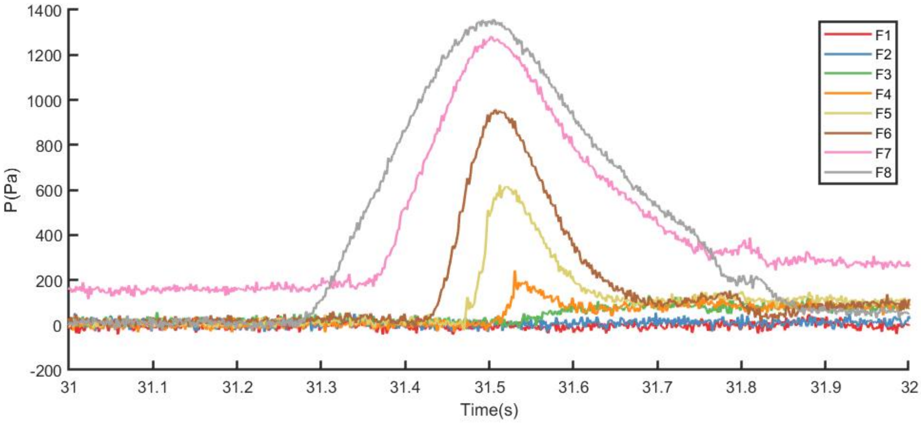

(b) TBH5, Heading=180° , Air Gap=235mm

Fig 4.15. Time history of pressure changes of each pressure transducer under focused waves (Heading=180° , Air Gap=235mm)

In Fig 4.15 (a), it can be found that although the pressure of the F6 to F8 transducer changes, the nonlinearity is not very severe, while the pressure change captured by the F5 transducer undergoes a strong nonlinear change and reaches the pressure peak 1758Pa at 32.5s. ;This indicates that, first, more pronounced slamming occurs at F5 and above, while the lower part is dominated mainly by linear wave forces; second, the severity of slamming at this location is much lower than that in the condition shown in Figure 4.14(a), and the intensity of the slamming has noticeably attenuated, which also proves the summary of the impact of the air gap on the slamming intensity in Fig 4.13. Based on the pressure–time history characteristics, the impact observed in Fig. 4.15(a) can be qualitatively associated with a Wagner-type slamming response, which is marked by a rapid pressure rise, a sharp peak, and a short impact duration, in contrast to the smooth and gradual pressure variations associated with linear wave loading. In comparison, the pressure signals shown in Fig. 4.15(b) correspond to a non-breaking wave impact without slamming. It can be found in Fig 4.15(b) that the wave pressure gradually decreases from the bottom to the top of the platform, and there is no strong non-linear change. This also indicates that, under this condition, the waves did not break and generate slamming; the pressure sensors merely captured the action of wave forces.

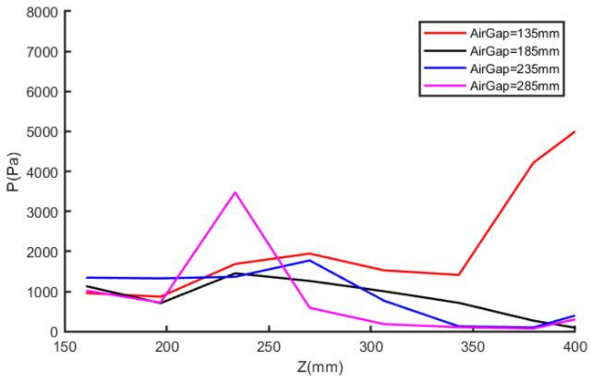

(a)TAH5, heading=180°

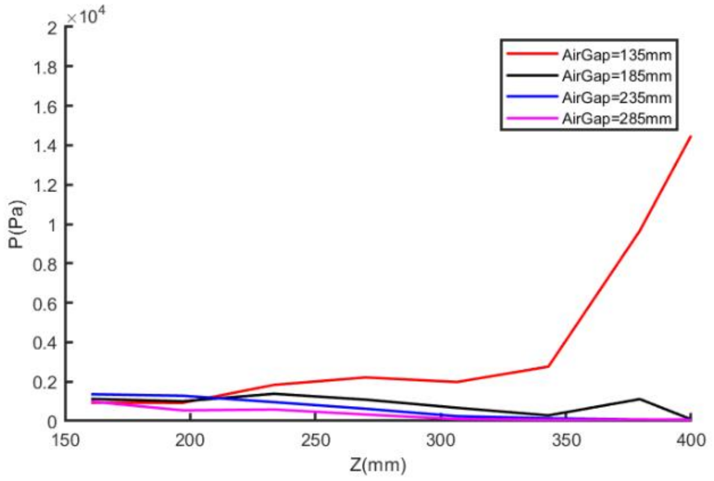

(b)TBH5 case, heading=180°

Fig 4.16. Maximum pressure value captured by the pressure transducer at different positions under the focused wave

Fig 4.16 shows the maximum value of the pressure transducer captured under different air gaps. It can be seen in Fig 4.16 (a) that the F6 transducer capture abnormally increased pressure under TAH5 wave conditions with a air gap of 285mm. This shows that the slamming pressure is mainly concentrated near the F6 transducer. The pressure peak at F5 in the load condition with a 235mm air gap is higher than that in other positions. This shows that the position of this slamming occurs at the F5 position, and the two comparisons of each other prove that the peak of the pressure is moved down from the platform with the increase of the air gap. Under the TBH5 wave conditions, in addition to the load condition with a gap of 135mm, a strong slamming load has been generated, and other load conditions have not increased significantly. The slamming effect is not obvious, and the discussion of the slamming load in Fig 4-16 (b) is confirmed.

4.4 Experimental results and characteristics of horizontal wave slamming under freak waves

4.4.1 Characteristics of freak wave and wave climbing effect

Two wave spectra were selected for the freak wave experiment, one is the S series wave spectrum and the other is the Jonswap spectrum. The significant wave height H and wave period of the S series spectrum gradually decrease. The average wave period in the Jonswap spectrum is the same. Two different values are used for the significant wave height in order to find the influence of different wave heights on slamming. Under the conditions of two freak waves, four air gaps (135 mm, 185 mm, 235 mm, and 285 mm), and two wave headings (180° and 135°), the following analyses are conducted: the time histories of waves (two wave types, one air gap, one wave heading), the wave crest heights (two wave types, four air gaps, one wave heading, at W1 and W3), and the characteristics of wave time histories at three measurement locations (two wave types, two air gaps, one wave heading). These are shown in Figs 4.17 to 4.20.

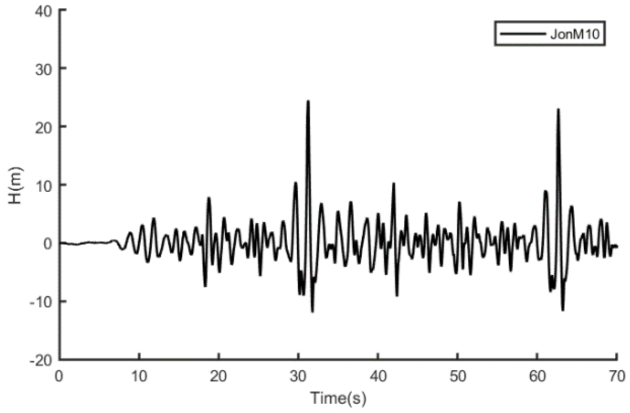

(a)JonM10, Period=1.46, Wave Height=0.258m

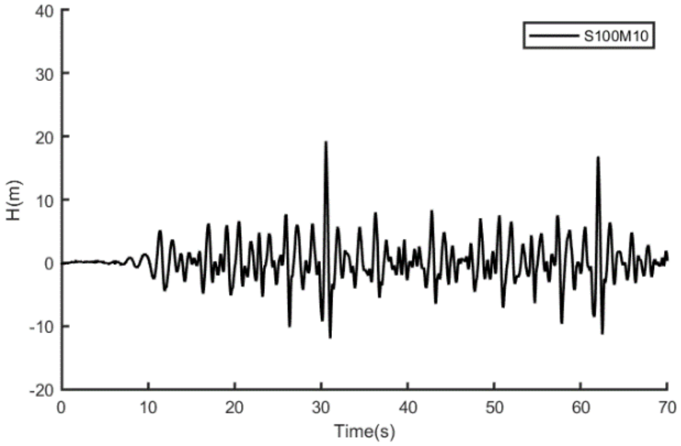

(b)S100M10, Period=1.15s, Wave Height=0.253m

Fig 4.17. Freak wave waveform time history

Fig 4.17 shows the wave S100M10 load condition and JonM10 load condition and the wave heights of these two are 0.253m and 0.258m respectively, which are similar. JonM10 has a relatively long period of 1.460s, and S100M101 has a wave period of 1.150s.

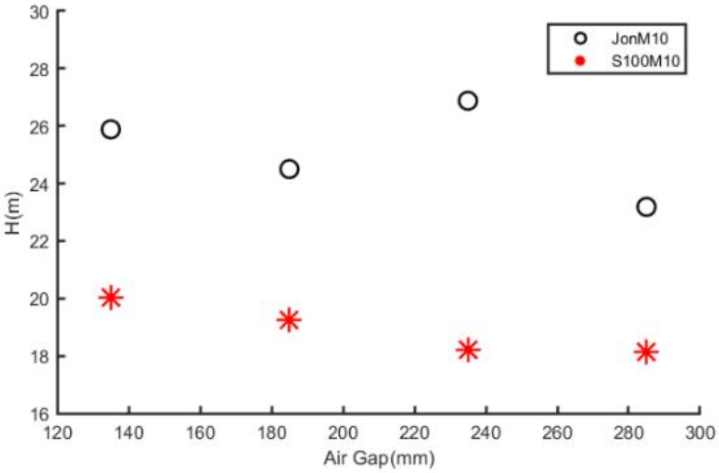

(a) Comparison of freak wave heights at wave gauge W1

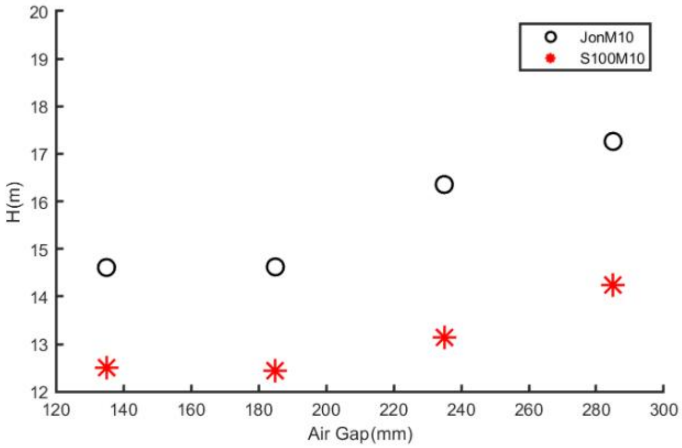

(b) Comparison of freak wave heights at wave gauge W3

Fig 4.18. Comparison of freak wave height (2 wave types, 4 air gaps, 180° wave heading)

In Fig 4.17, both waves produce two sets of higher wave heights within the time history range of 70s, and the formation moments are around 31S and 64S.

Comparison of these two groups of waves can reflect the impact of these two wave conditions on slamming. The maximum wave height generated by different air gaps under these two wave conditions is shown in Fig 4.18.

Fig 4.18 is a comparison of the maximum wave crest height values captured by W1 and W3 wave height gauges. The maximum value of the wave crest height of JonM10 is higher than that of S100M10, indicating that although the significant wave heights of the two wave spectra are similar, the waves in the Jonswap spectrum are more likely to be distorted, resulting in waves with higher relative significant wave heights after the waves are superimposed on each other. The waves of the S spectrum are relatively gentle, which has a certain weakening effect on the distortion caused by wave superposition, resulting in the maximum peak value of the wave being smaller than the maximum peak value of the wave produced by the Jonswap spectrum.

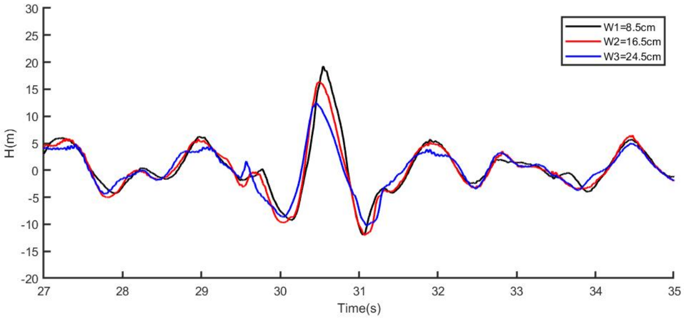

(a) JonM10 case, heading=180°, air gap=185mm

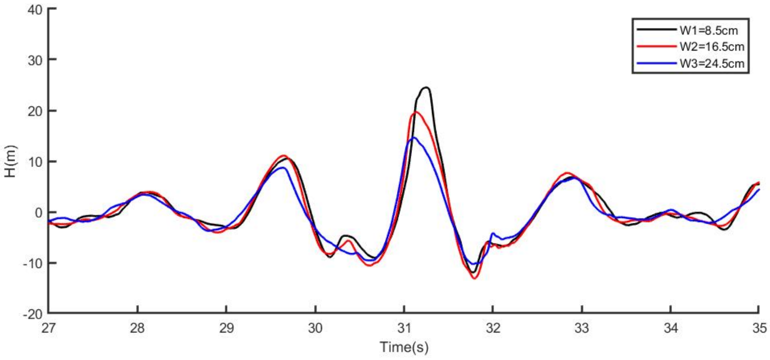

(b) S100M10 case, heading=180°, air gap=185mm

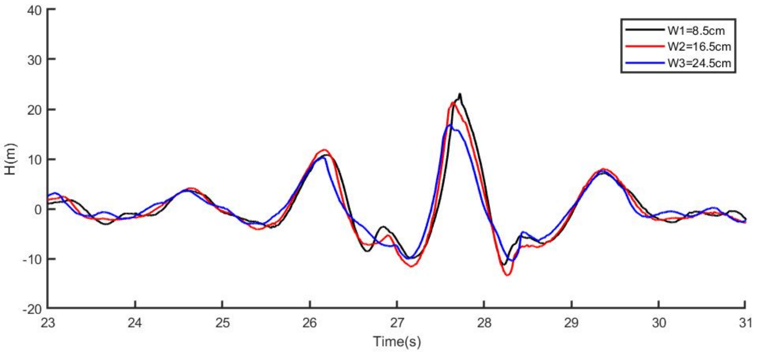

(c) JonM10 case, heading=180°, air gap=285mm

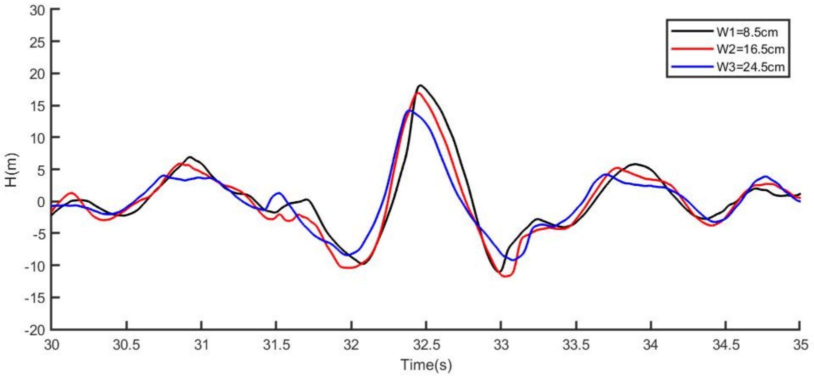

(d) S100M10 case, heading=180°, air gap=285mm

Fig 4.19. Wave time history of wave height gauges at different distances from the platform (2 wave types, 2 air gaps, 180°)

Under different air gap conditions, before the wave slamming occurs, the wave height time history obtained by the three measurement points of W1, W2, and W3 decreases in order, indicating that before the wave slamming occurs, the closer the waves are from the platform, the higher the wave height is, and this phenomenon reflects a local amplification of wave elevation adjacent to the column. Especially in Fig 4.19 (a), the measured height of W1 is significantly higher than that of W2 and W3, indicating a pronounced local increase in wave elevation near the column. As shown in Fig 4.20, when the air gap increases, the wave climbing ratio gradually decreases, indicating that the air gap has a significant effect on the climbing of the waves. When the air gap increases, this impact gradually weakens.

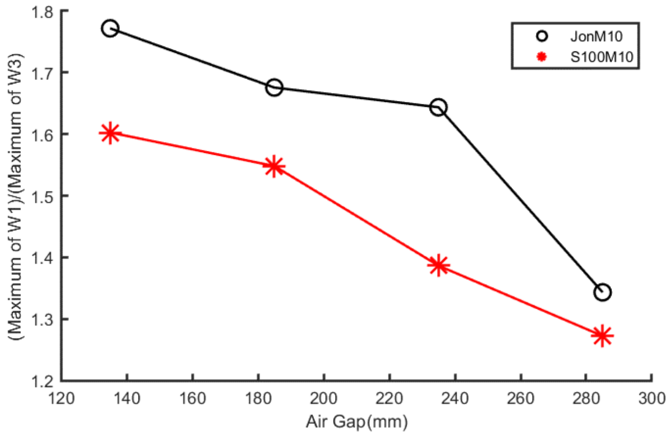

Fig 4.20. W1 and W3 wave peak ratio

4.4.2 Distribution characteristics of horizontal wave slamming loads based on experimental results

4.4.2.1 Wave slamming characteristics under 180° wave heading

Under the condition of a 180° wave heading, seven freak waves, and four air gaps (135 mm, 185 mm, 235 mm, and 285 mm), the following analyses are conducted: the time histories of wave forces on the column (two wave types, one wave heading, one air gap), the maximum wave forces (seven wave types, one wave heading, four air gaps), the time histories of pressures at eight measurement points (F1–F8) on the column surface (two wave types, one wave heading, one air gap), and the patterns of maximum pressures (six wave types, one wave heading, four air gaps). These are shown in Figures 4.21 to 4.24.

During the formation of extreme wave conditions under irregular seas, two key factors influence wave morphology and impact load responses: spectral characteristics (such as spectral peak sharpness and bandwidth) and phase randomness. Previous studies have shown that spectral parameters determine the energy distribution and affect the probability of extreme wave occurrence, while phase correlations govern the structure of wave groups and the formation mechanism of isolated large waves. Therefore, conducting only a single realization experiment makes it difficult to distinguish their respective effects and may lead to insufficient statistical robustness. To address this issue, the present study carried out 31 repeated experiments for the representative spectral case S100M10 and performed ensemble averaging and statistical dispersion analyses on the measured responses. The results show that, although noticeable scatter exists in the early stage due to stochastic variability, the cumulative mean of the maximum impact load gradually stabilises as the number of realisations increases.

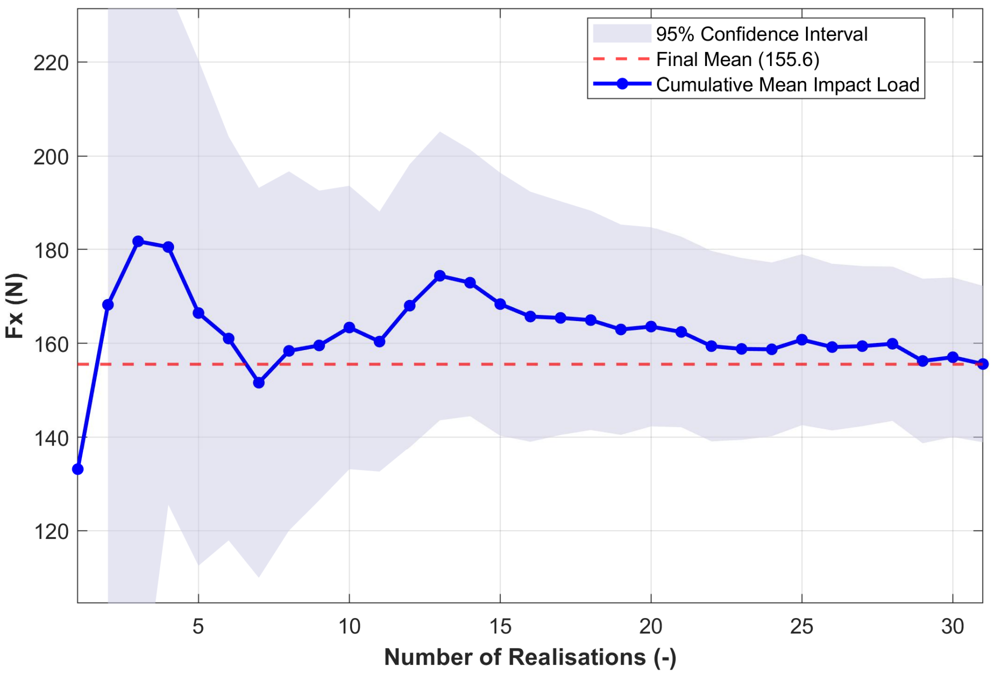

Fig 4.21 Convergence analysis of impact loads

To further assess the statistical robustness of the maximum impact load, a convergence analysis based on multiple realisations was performed. Figure 4.21 shows the evolution of the cumulative mean of the maximum horizontal impact force with respect to the number of realisations (N). At small sample sizes, noticeable fluctuations are observed due to the stochastic variability of individual extreme slamming events. As N increases, the cumulative mean progressively stabilises, accompanied by a clear narrowing of the 95% confidence interval. Statistical convergence is achieved when the number of realisations exceeds approximately 20, beyond which further increases have a negligible influence on the estimated mean maximum impact force. Therefore, the 31 realisations adopted in this study are sufficient to ensure the robustness of the reported extreme load statistics.

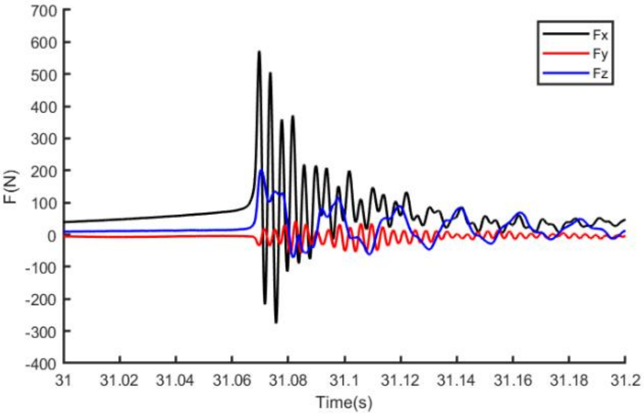

(a) JonM10 in detail

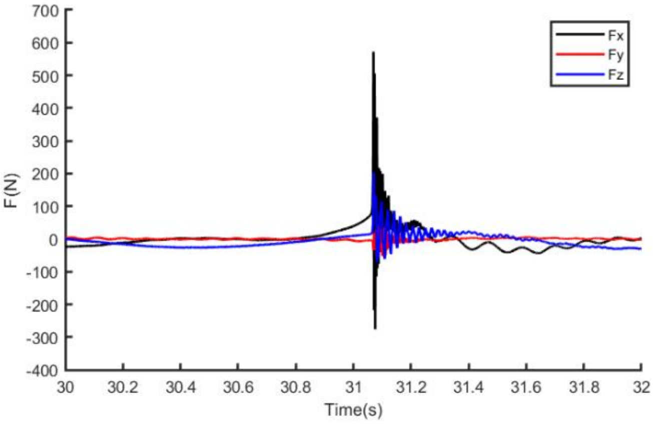

(b) JonM10

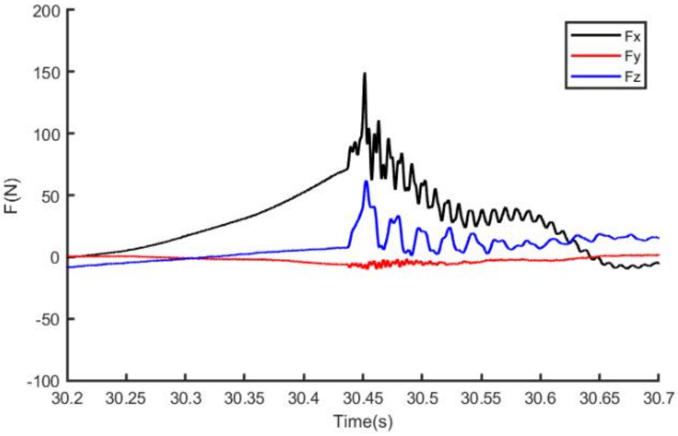

(c) S100M10 in detail

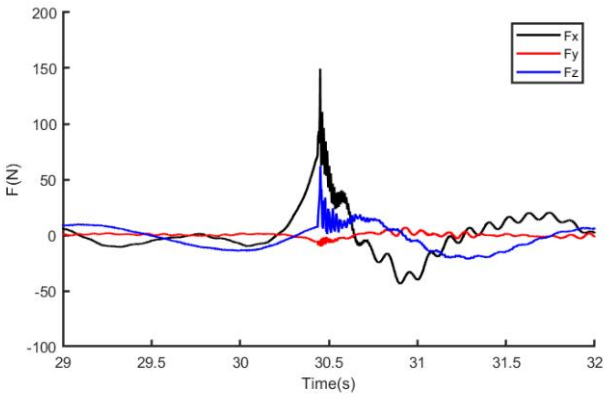

(d) S100M10

Fig 4.22. Time history of the wave slamming force on the platform(2 wave types, Heading=180°, Air Gap=185mm)

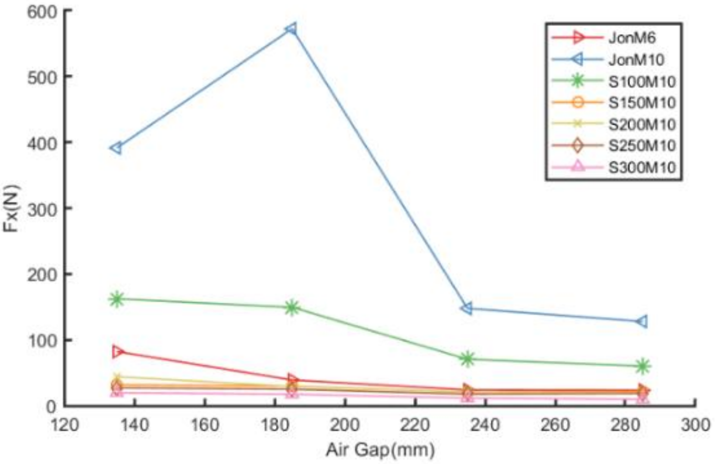

(a) Fx-Direction Force

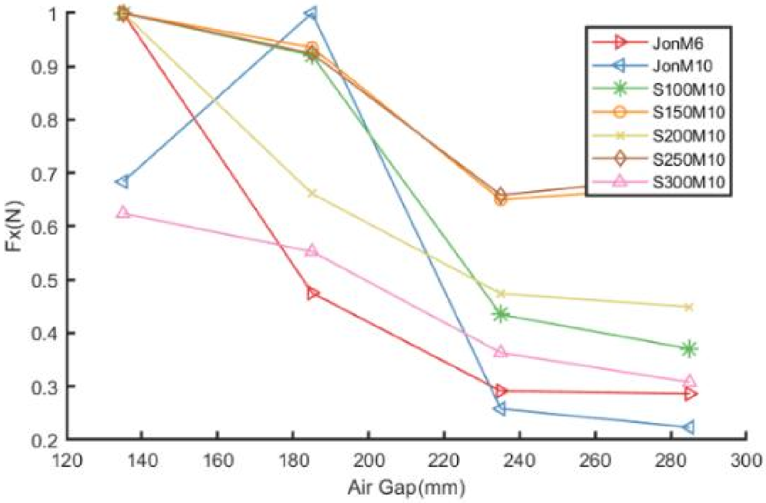

(b) Uniformization

Fig 4.23. Distribution of the maximum force on the platform under different air gaps (7 wave types, 4 air gaps, 180° wave heading)

Fig 4.22 shows the resultant force in each of the three coordinate directions of space when the platform is hit by the freak wave. The force in the direction of the wave (i.e., the *X* direction) is much larger than that in the other two directions. As the slamming force acts in the direction of the wave and a larger resultant force is produced, the amplitude of the oscillation is also relatively large. Then, due to the action of waves in the *Z* direction, a larger amplitude response is also produced. This is mainly due to the existence of a protruding deck on the platform, which is subject to a certain wave slamming effect and will also produce a force in the *Z* direction. Moreover, the climbing effect of the waves causes the wave force to increase relatively in the *Z* direction. The superposition of the two factors makes the *Z* directional force shows strong nonlinear changes. In the JonM10 load condition, the *X* direction force oscillates violently up and down, and a negative value occurs in that direction. While in the S100M10 working condition, this situation is relatively alleviated, but there is also a certain amount of oscillation. This is because after the platform receives the slamming force, the structure vibrates in response, thus forming the load fluctuations in the Fig 4.22.

From Fig 4.23(a), it can be found that relatively violent slamming occurred under JonM10 and S100M10 wave conditions, and the force in the *X* direction was much greater than that of other load conditions. In other wave conditions, wave slamming loads generated in the *X* direction are all below 100N. Fig 4.23(b) normalizes the force. It can be found that the overall slamming load shows a decreasing trend with the increase of the air gap, but the wave load of the JonM10 condition is the largest at the 185mm air gap, indicating that in some cases, the increase of the air gap will first increase and then decrease the slamming load. Similar situation has been analyzed in the regular wave section.

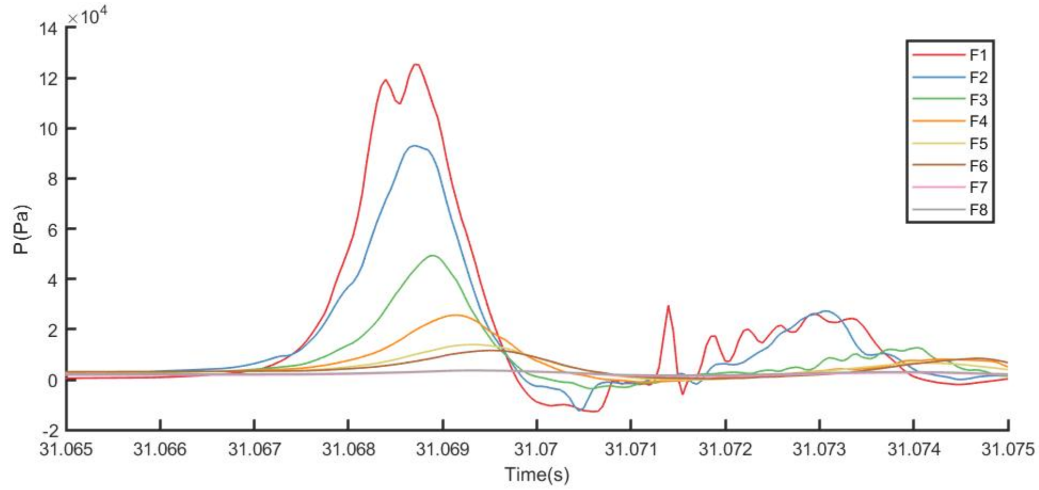

(a) JonM10, Heading=180°, Air Gap=185mm

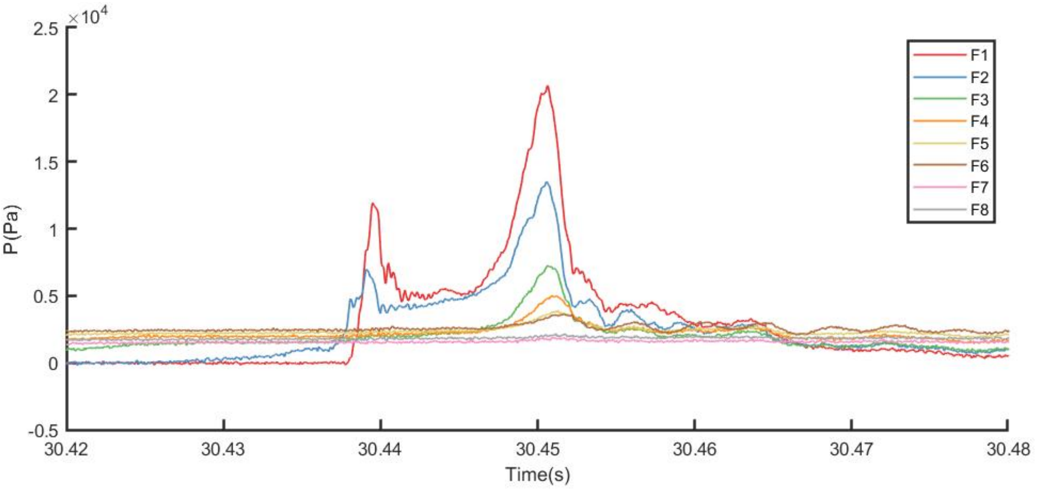

(b) S100M10, Heading=180°, Air Gap=185mm

Fig 4.24. Time history of pressure changes of each pressure transducer under freak wave (2 wave types, 1 air gap, 180° wave heading)

As shown in Fig 4.24, during the slamming process formed by the two wave spectra, the pressure transducer captured a very obvious pressure mutation time course, and the action duration was in the range of 0.01s~0.02s. It can be observed that as the position rises, the maximum pressure value captured by the pressure transducer also increases. The pressure value captured by the transducer extending from the top deck is the largest, reflecting that the impact of the slamming force in this area is relatively large. Although the significant wave heights of the two wave spectra are very close, the slamming force caused by the freak waves generated by the Jonswap spectrum is much greater than those generated by the S series wave spectrum.

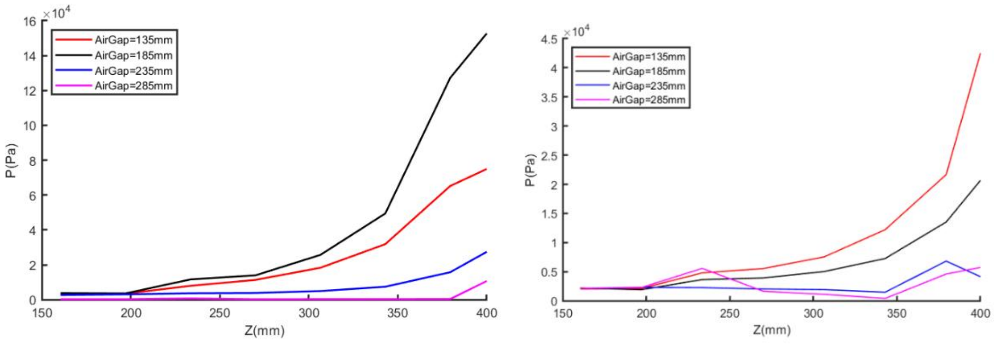

(a) JonM10 (b) S100M10

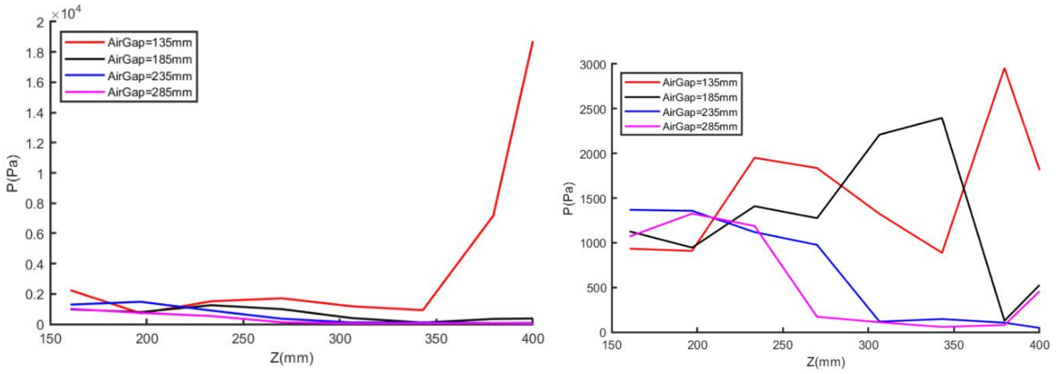

(c) JonM6 (d) S150M10

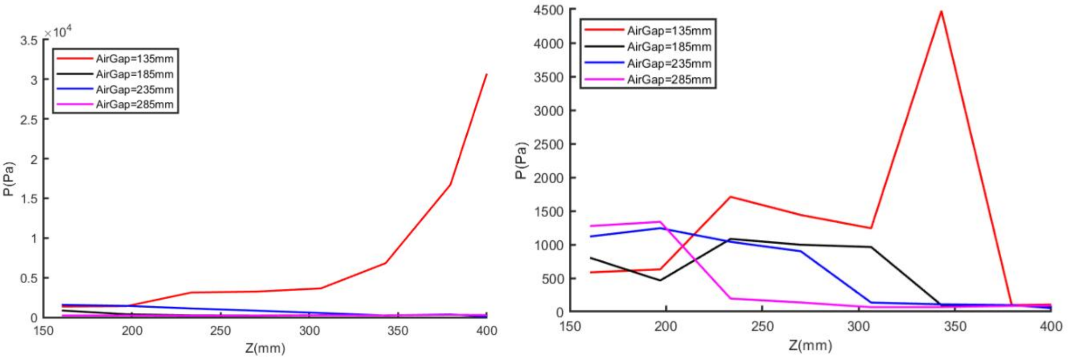

(e) S200M10 (f) S250M10

Fig 4.25. Maximum pressure value captured by the pressure transducer at each position under the action of freak waves (6 wave types, 180° wave heading)

The maximum slamming pressure generated by the Jonswap spectrum reaches 125.4kPa, and the slamming pressure generated by the S series wave spectrum is 20.65kPa. The former is 6.07 times the latter. Observing from the time history curve, it can be found that both JonM10 load condition and S100M10 load condition produced two slamming peaks, but there is a big difference in the size of the two peaks. During the slamming process of JonM10 load condition, the maximum slamming pressure reached 125.4kPa at 31.0688s, and reached the second smaller peak value of 29.59kPa at 31.0714s, which was equivalent to the maximum slamming force of S100M10 load condition. In S100M10, the slamming pressure reaches the first peak value of 11.7kPa at 30.44s, and the second peak value of 20.65kPa at 30.45s. Numerically, the second peak value is higher, which is opposite to the JonM10 load condition.In summary, as the measurement point height increases, the maximum pressure recorded by the sensors also increases; moreover, the slamming force caused by freak waves generated from the JONSWAP spectrum is more than six times greater than that produced by freak waves from the S-series spectrum.

As shown in Fig 4.25, the horizontal coordinate is the distance between the pressure transducer and the base surface in the Z direction, and the vertical coordinate is the maximum pressure value captured by the pressure transducer under this wave condition. In Fig 4.25 (a), (b), (c) and (e), the pressure transducer captured a considerable pressure value; these values exceeded 5000Pa and showed a relatively regular upward trend. In load conditions where the slamming pressure is small, the pressure value captured by the pressure transducer shows irregular ups and downs, which shows that the slamming pressure does not account for the main factor in the stress of the platform, and is affected by the linear wave force. As a result, the pressure curve cannot reasonably reflect the pressure field formed by the slamming force. Due to these smaller slamming pressures compared to the load conditions in which the slamming force is the main factor, the slamming force on the platform is smaller and the damage caused is smaller, which can be ignored when the experimental results are compared and analyzed. For load conditions that cause large slamming pressure, the relationship between slamming pressure and position can be clearly reflected, that is, as the position of the measuring point rises, the slamming pressure increases, making it easier to cause damage to the structure. Among all load conditions, the maximum slamming pressure was 152.7kPa generated under the conditions of JonM10, wave direction angle of 180°, and air gap of 185mm. In the design, it is necessary to focus on the ultimate force under such working conditions to prevent damage caused by slamming against the strength limit of the structure.

In summary, for conditions that produce relatively high slamming pressures, a clear relationship between slamming pressure and position can be observed: as the measurement point height increases, the slamming pressure increases, making structural damage more likely. In all conditions, the maximum slamming pressure occurs under the JonM10 spectrum, with a wave heading of 180° and an air gap of 185 mm, reaching 152.7 kPa. In design, special attention should be given to the extreme loading under this condition to prevent failure caused by exceeding the structural strength limit due to slamming.

4.4.2.2 Wave slamming characteristics under 180° wave heading

For two freak waves under the condition of a 135° wave heading and an air gap of 185 mm, the following analyses are conducted: the time histories of wave forces on the column (two wave types, one wave heading, one air gap), the maximum wave forces (two wave types, one wave heading, one air gap), the time histories of pressures at eight measurement points (F1–F8) on the column surface (two wave types, one wave heading, one air gap), and the patterns of maximum pressures (six wave types, one wave heading, four air gaps). These are shown in Figs 4.26 to 4.27.

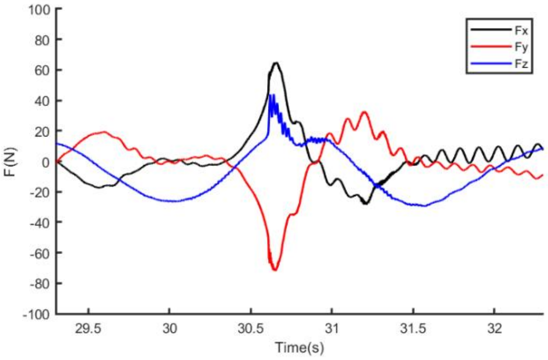

(a) JonM10 in detail

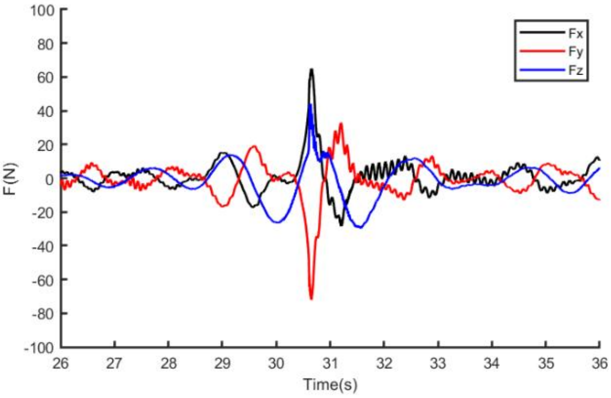

(b) JonM10

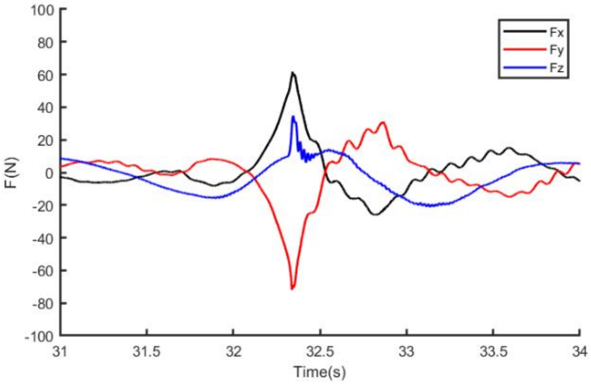

(c) S100M10 in detail

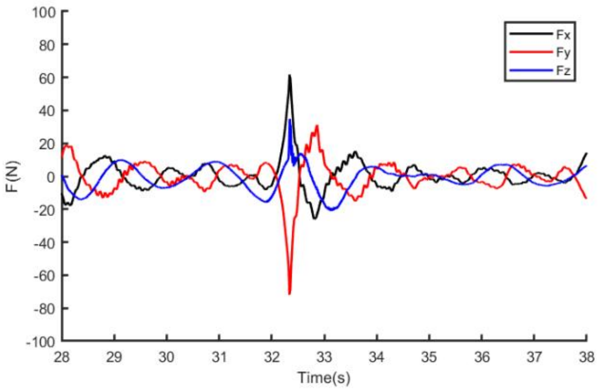

(d) S100M10

Fig 4.26. Time history of the wave slamming force on the platform (Heading=135°, Air Gap=185mm)

Table 4.1. Statistics on the maximum wave force on the platform (Heading=135°, Air Gap=185mm)

Value	JonM10(N)	S100M10(N)
Fx Maximum value (absolute value)	67.31	66.25
Fy Maximum value (absolute value)	75.43	74.42
Fz Maximum value (absolute value)	44.07	34.8
Fx-Fy The maximum value of the resultant force along the windward direction	100.932	99.468

Fig 4.26 describes the time history curve of the resultant force in three directions of the wave slamming force received by the platform when the wave direction angle is 135°. In this wave condition, the *Y* direction and the *X* direction together withstand the slamming of the waves, and are basically consistent in order of magnitude. From the maximum values of the resultant forces in the three directions in Table 4.1, it can be found that the maximum values of the forces in the JonM10 load condition and the S100M10 load condition are very close, and Fig 4.25 (a) and (c) also show that the force time history curves in the three directions of the platform are also very similar. As mentioned above, the wave height of JonM10 slamming is higher than that of S100M10, which shows that after the platform 1 is rotated at an angle of 45°,

the sensitivity to wave height and slamming force is weakened. Under wave conditions with a wave direction angle of 180°, the maximum forces in the wave direction (*X* direction) of the JonM10 load condition and the S100M10 load condition are 572.4N and 149.5N respectively. Compared with the wave direction angle of 135°, the forces in the direction of the waves (100.932N and 99.468N) are greater, which shows that after the wave direction angle changes, the sum of the slamming forces on the platform is relatively reduced.

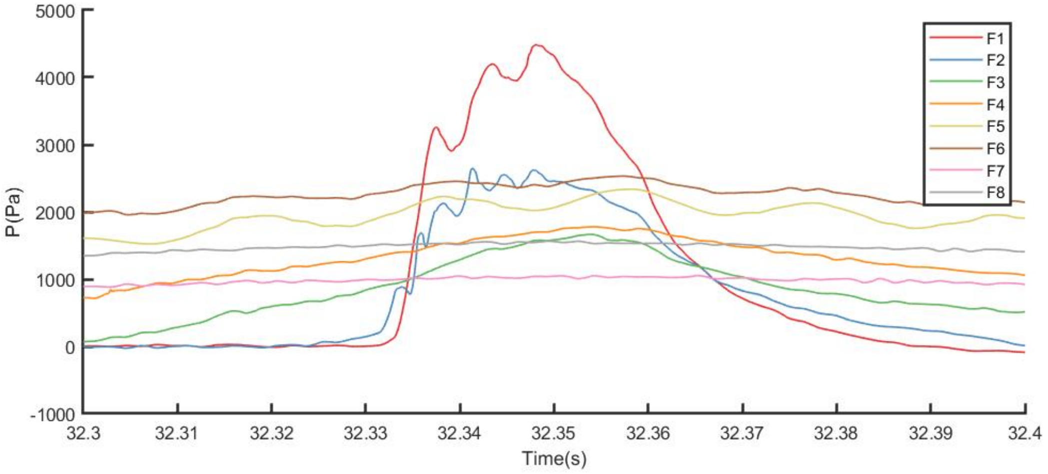

(a) JonM10

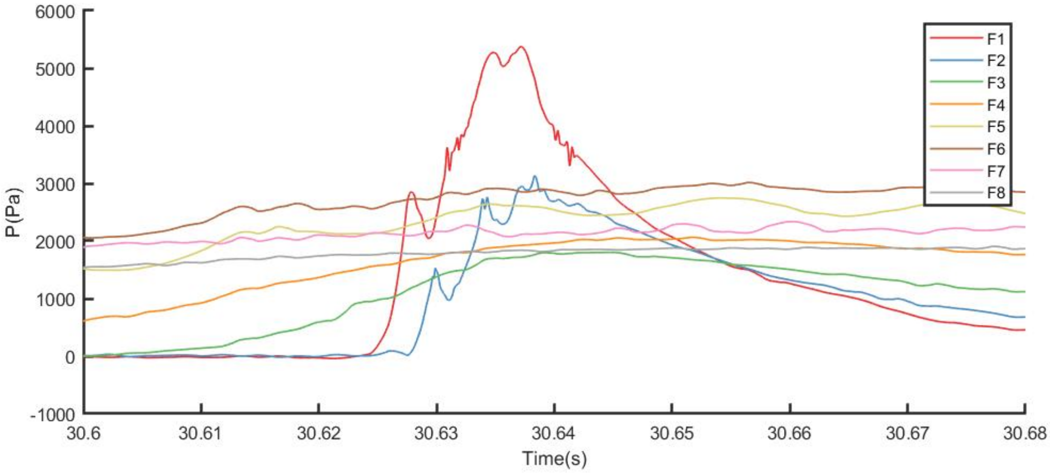

(b)S100M10

Fig 4.27. Pressure change time history of each pressure transducer under the freak waves (Wave heading 135°, 185 mm air gap)

As shown in Fig 4.27, under wave conditions with a wave direction angle of 135°, the pressure transducer at the F1 and F2 positions in the JonM10 and S100M10 load conditions experienced relatively strong nonlinear changes, while the nonlinear changes of other transducers were smaller. This phenomenon shows that the slamming mainly occurs on the upper part of the platform, and the slamming action time is very short. The slamming action time under the two wave spectrum conditions is only within the range of 0.05s. The slamming force is larger on the upper part of the platform and the extended deck, which is prone to cause damage. The pressure peaks captured by each pressure transducer under JonM10 and S100M10 wave conditions are 5376Pa and 6402Pa. Compared with the pressure peak captured by the pressure transducer under the wave direction angle of 180°, it is very small. This also reflects that changes in wave direction angle will have a great weakening effect on wave slamming, which is the same as the pattern reflected on the resultant force mentioned above.

4.5 Experimental results analysis

4.5.1 Air gap

Under the condition of a 180° wave heading, fourteen regular waves, and four air gaps (135 mm, 185 mm, 235 mm, and 285 mm), the variation of peak slamming pressures with air gap at four measurement points (F1–F4) on the column, where slamming is more pronounced, is analyzed. These are shown in Figures 4.28 to 4.30. The analysis in the previous section indicates that most wave slamming events occur at monitoring points F1 to F4 on the column. The slamming phenomenon is more prominent when the air gap values are 135mm, 185mm, and 235mm, and it can be more explored when the slamming phenomenon is more prominent. Therefore, this section analyzes the sensitivity relationship between the wave slamming pressure peak value and the air gap change under different wave conditions, starting from the load conditions where the slamming phenomenon is more pronounced.

Fig 4.28 presents a schematic diagram of the veriation in the slamming pressure peak at point F1 changing with the air gap. It can be seen from the Fig that the slamming value increases first and then decreases with the increase of the air gap under the wave parameters of R9 and R14. The slamming value is the largest when the value is 185mm. The change rate of the slamming value under the R9 and R14 wave parameters is 74.6%, -49.1%, -86.7%, 24.2%, -90.4%, -95.2% compared with the air gap value of 135mm. However, the slamming pressure under the other 12 wave parameters all showed a decreasing trend with the air gap increase.

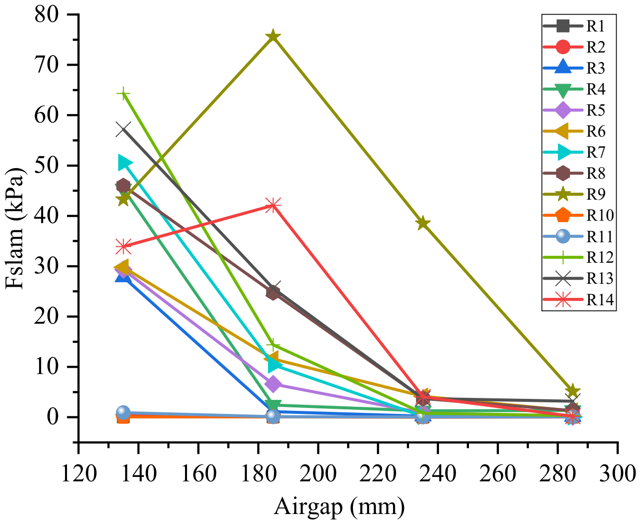

Fig 4.28. Schematic diagram of the variation of peak slamming pressure value changing with the air gap at point F1

Fig 4.29 is a schematic diagram of the variation of the peak slamming pressure at points F2 and F3 with the change of the air gap. It can be found that similar to point F1, the slamming peak value under the wave parameters of R9 and R14 shows a trend of first increasing and then decreasing as the air gap value increases. The slamming value is the largest when the air gap value is 185mm, and at point F2, R6 load condition also shows similar characteristics. At point F2, the change rate of the slamming force value is 6.6%, -75.5%, -92.4% under the wave parameter R6, 71.4%, -26.3%, -70.3% under the wave parameter R9 and 18.7%, - 79.9% and -93.5% under the wave parameter R14. At point F3, the change rates of slamming values under R9 and R14 wave parameters, compared with the air gap value of 135mm, are 71.0%,

-38.1%, -87.8% and 20.1%, -84.8%, -62.0%, while the slamming pressure under the other 12 wave parameters all show a decreasing trend with the increase of the air gap.

From the slamming pressure at points F1 to F3, it is observed that the smaller the air gap under most wave conditions, the higher the slamming value. The slamming value is the largest under the 135mm air gap. However, below the three wave conditions of R6, R9 and R14, there is an "inflexion point" when the slamming value changes with the air gap. That is, it shows that the slamming value is the highest under the air gap of 185mm. By analyzing the difference between these three wave load conditions and other conditions, it can be found that R6 and R9 have the highest wave steepness of 0.115 in waves with periods of 1s and 1.2s. In contrast, R14 has the longest period of 1.2s in a wave with a wave steepness of 0.12. It is worth noting that when the wave period is 0.8s, and the wave steepness is 0.115, the slamming pressure curve does not show the existence of an "inflexion point".

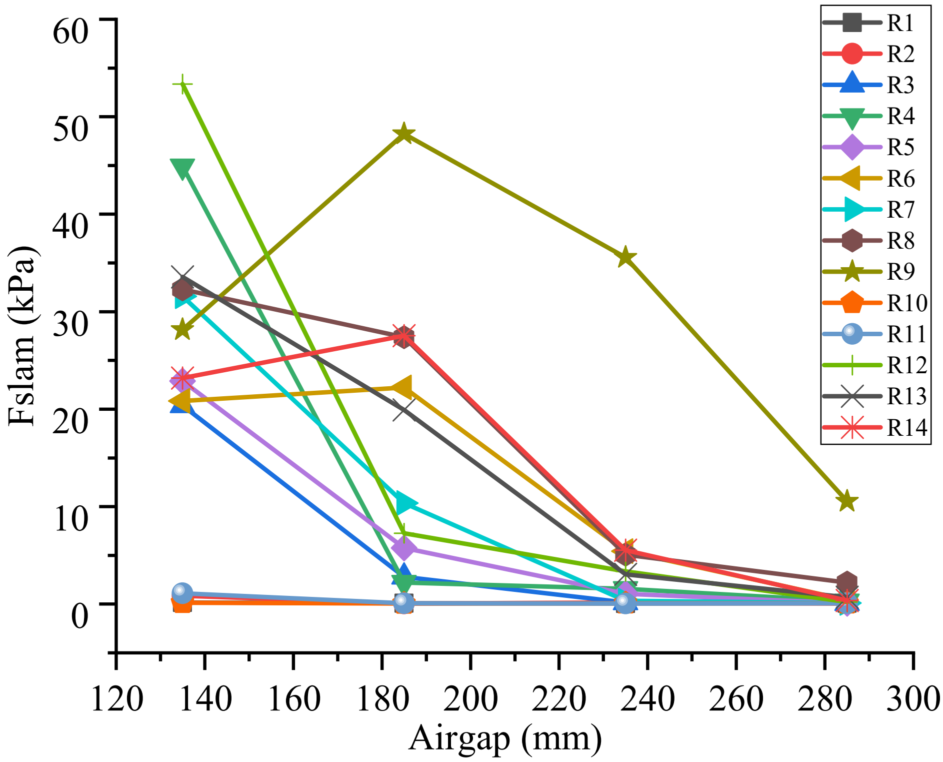

（a）At point F2

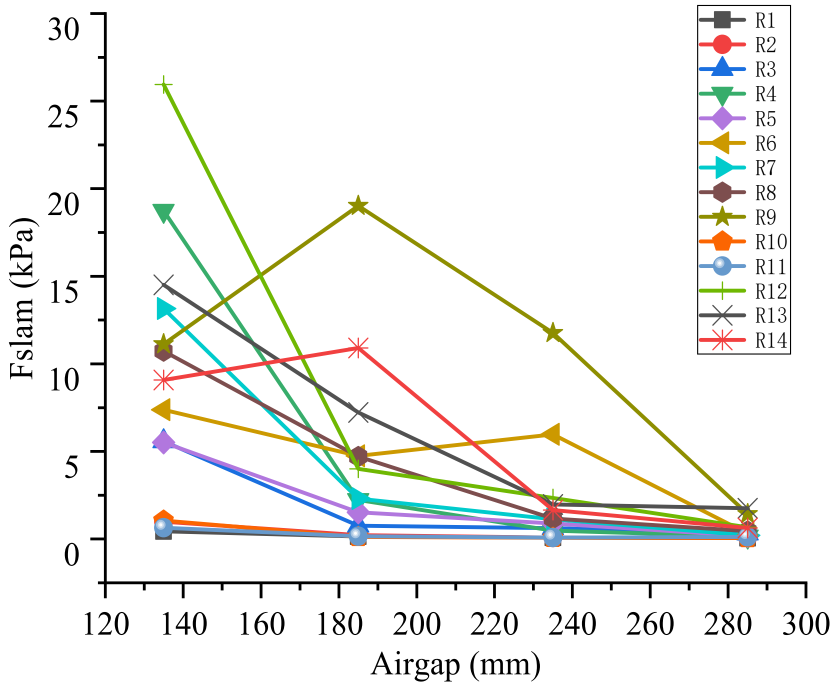

（a）At point F3

Fig 4.29. The variation of the peak slamming pressure value changing with the air gap at points F2 and F3

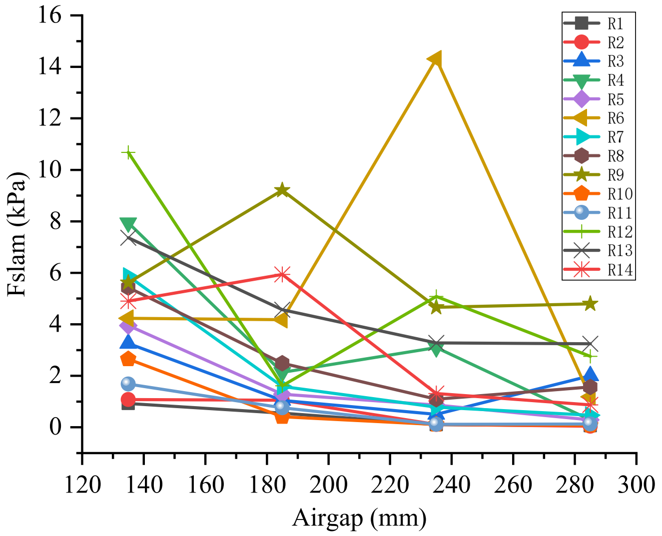

Fig 4.30. The variation of peak slamming pressure value changing with the air gap at point F4

By observing the changing pattern of slamming pressure at point F4 with the changing of the air gap value as shown in Fig 4.30, it is observed that the pressure under the load conditions of R9 and R14 maintains a similar changing pattern to that at points F1 to F3. That is, the slamming value increases first and then decreases with the increase of the air gap value and reaches the maximum value when the air gap value is 185mm.

Under the R6 load condition, the slamming values are almost the same when the air gap is 135mm and 185mm, but when the air gap is 235mm, the slamming value suddenly increases by 242.4%, with a maximum value of 14.3kPa, and then when the air gap is 285mm, the slamming value is reduced to 1.18kPa. The overall maximum slamming occurs when the air gap is 235mm. The maximum value is smaller than that of points F1 to F3. The reason may be that point F4 is farther away from the deck in the vertical direction, and the waves will climb along the column and slam on the top of the column, causing splashing and rolling. The farther away from the deck, the lower the probability of similar nonlinear superposition phenomena. In summary, apart from R6/9/14, most peak slamming pressures decrease as the air gap increases; in most wave conditions, the peak slamming pressure occurs at an air gap of 135 mm, while for R6/9/14 it occurs at an air gap of 185 mm.

4.5.2 Wave steepness

From the analysis results in the previous section, it is observed that the wave slamming phenomenon at points F1-F4 is more obvious, so points F1 to F4 were selected for analysis of the sensitivity to wave steepness. Under the condition of a 180° wave heading, three regular wave periods, and two air gaps (135 mm and 185 mm), an analysis is conducted to investigate the sensitivity of slamming intensity to wave steepness. In each regular wave condition, the average value of the first 1/3 pressure peaks within the simulation time is taken as the peak value of the slamming pressure.

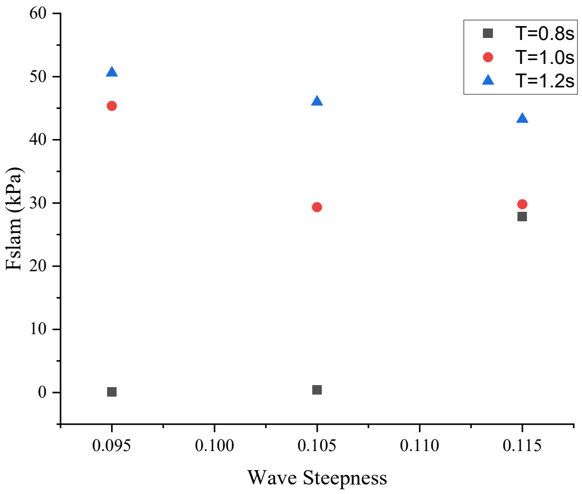

Fig 4.31. The variation of peak slamming pressure value changing with wave steepness at point F1 under an air gap of 135mm

It can be seen from Fig 4.31 that as the wave steepness increases, the wave slamming pressure at point F1 gradually decreases when T=1.0s. During the change of wave steepness, for every 0.01 increase, the peak pressure at point F1 changes by -16.0kPa and 0.5kPa. When T=1.2s, the slamming pressure at point F1 first decreases and then increases. During the change of the wave steepness, for every 0.01 increase, the peak pressure at point F1 changes by -4.6kPa and -2.7kPa. When T=0.8s, the slamming pressure at point F1 first fluctuates slightly and then increases rapidly. During the change of the wave steepness, for every 0.01 increase, the peak pressure at point F1 increases by 0.34kPa and 27.4kPa. It is observed that the slamming pressure is very sensitive to changes in wave steepness, and its rate of change is higher when the period is smaller. This is because the interval between the previous wave and the next wave is shorter when the period is smaller, and when the water surface is not yet calm, multiple waves will superimpose, resulting in a more obvious change in the slamming peak value.

By observing the sensitivity of pressure to wave steepness at point F2 in Fig 4.32, it can be found that the overall change pattern is slightly similar to that at point F1. With the increase of wave steepness, the wave slamming pressure at point F2 when

T=1.2s first increase and then decreases and fluctuates slightly around 30kPa. For every 0.01 increase during the process, the peak pressure at point F2 changes by -0.7kPa and -4.1kPa.

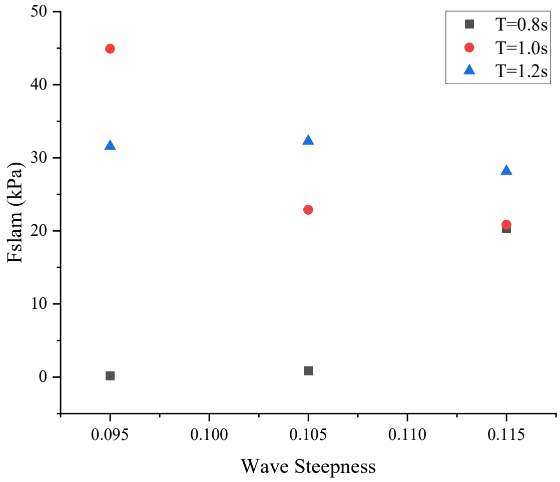

Fig 4.32. Schematic diagram of the variation of peak slamming pressure value changing with wave steepness at point F2 under an air gap of 135 mm

When T=1.0s, the slamming pressure at point F2 decreased rapidly and then fluctuated in a small range. When the wave steepness increased by 0.01, the peak pressure at point F2 changed by -22.0kPa and -2.0kPa. When T=0.8s, the slamming pressure at point F2 first fluctuated in a small range around 0kPa and then increased rapidly, and the peak pressure at point F2 increased by ~~0.34kPa and 27.4kPa~~ 0.69kPa and 19.52kPa for every 0.01 increase in the process of wave steepness change. It is observed that the slamming pressure is very sensitive to the change in wave steepness. The rate of change is higher when the period is small, which is the result of the short time interval between waves of short periods and the superposition of waves.

By observing the sensitivity of the pressure at point F3 to wave steepness in Fig 4.33, it can be found that with the increase of wave steepness, the wave slamming pressure at point F1 fluctuates between 10kPa and 14kPa at T=1.2s, and the range of change is small, presenting a trend of decreasing first and then increasing. When the wave steepness increases by 0.01, the peak pressure of point F3 changes by -2.4kPa and 0.4kPa.

When T=1.0s, the slamming pressure at point F3 decreased rapidly at first and then increased slightly. When the wave steepness increased by 0.01, the peak pressure at point F3 changed by -13.2kPa and -1.9kPa. When T=0.8s, the slamming pressure at point F3 first fluctuated in a small range around 0kPa and then increased rapidly, and the peak pressure at point F3 increased by 0.6kPa and 4.6kPa for every 0.01 increase in the wave steepness. It is observed that the slamming pressure is susceptible to the change in wave steepness. When the wave period is 1.0s and 1.2s, the slamming pressure decreases first and then increases with the increase of wave steepness, among which the decrease is even greater when T=1.0 s. When the period is 0.8s, the slamming pressure gradually increases with the rise of wave steepness and it increases significantly at the maximum wave steepness, which is also due to the short time interval between short-period waves and the superposition of front and rear waves.

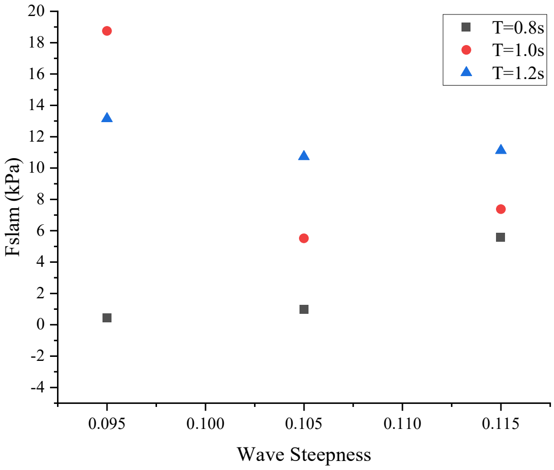

Fig 4.33. Schematic diagram of the variation of peak slamming pressure value changing with wave steepness at point F3 under an air gap of 135mm

In summary, under the 135 mm air gap condition, shorter wave periods (0.8 s and 1.0 s) show greater sensitivity of peak slamming pressure to wave steepness, with the 0.8 s period exhibiting a clear increase in peak pressure as wave steepness increases, while the 1.2 s period shows little variation. Overall, longer wave periods (1.2 s) produce higher peak slamming pressures than shorter ones, and higher measurement positions (F1/F2) display greater fluctuations in peak pressure across different wave steepness values.

When the air gap value is 185mm, the sensitivity of the slamming pressure at point F1 to wave steepness is shown in Fig 4.34. When the wave period is 0.8s, the slamming value at point F1 is minimal. When H/L is 0.095 and 0.105, the slamming value is both 0.09kPa, and the slamming value is only 1.1kPa when H/L=0.115.

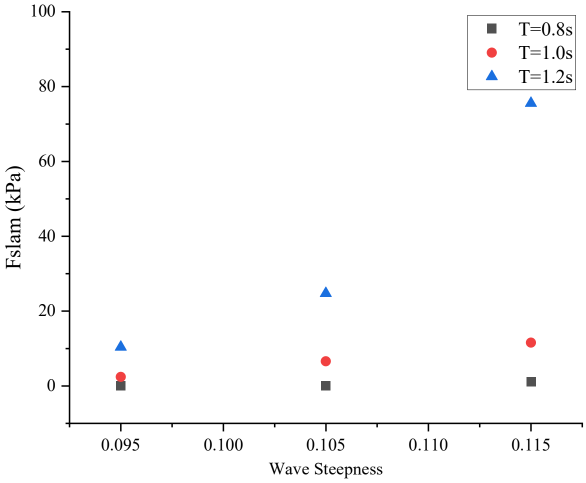

Fig 4.34. Schematic diagram of the variation of peak slamming pressure value changing with wave steepness at point F1 under an air gap of 185 mm

When T=1.0s, as the wave steepness increases, the slamming value shows a gradually increasing trend. Every time H/L increases by 0.01, the slamming value increases by 2.72 times and 1.75 times. When T=1.2s, as the wave steepness increases, the slamming value also shows a gradually increasing trend. Every time H/L increases by 0.01, the slamming value increases by 2.38 times and 3.05 times.

Overall, when the wave period is 1.2s, the slamming peak value is larger and the rate of change with the steepness increase of the wave is greater. However, when the wave period is 0.8s, the slamming phenomenon is very weak and does not reflect the change pattern.

The sensitivity of the slamming pressure at points F2 and F3 to wave steepness is shown in Fig 4.35 and Fig 4.36. They show a similar change pattern to the wave slamming at point F1. Overall, the slamming pressure increases with the increase of the wave steepness and it reaches the largest value when T=1.2s. When the wave period is 0.8s, the slamming values at points F2 and F3 are both very small. When H/L is 0.095 and 0.105, the slamming values are both below 0.2kPa. When H/L=0.115, the slamming values are also below 2kPa. Therefore, when T=0.8s, the wave slamming phenomenon is not obvious and is difficult to relate to the sensitivity of wave steepness.

When T=1.0s, as the wave steepness increases, points F2 and F3 show different trends: for every 0.01 increase in H/L at point F2, the slamming value increases by 2.63 times and 3.86 times; for every 0.01 increase in H/L at point F3, the slamming value changes by 0.69 times and 3.09 times. When T=1.2s, as the wave steepness increases, the slamming values at points F2 and F3 show a gradually increasing trend. For every 0.01 increase in H/L at point F2, the slamming value increases by 2.65 times and 1.76 times; for every 0.01 increase in H/L at point F3, the slamming value increases by 2.04 times and 4.04 times.Overall, at both points F2 and F3, the slamming peak value is larger when the wave period is 1.2s and the rate of change with the steepness increase of the wave is higher. However, when the wave period is 0.8s, the slamming phenomenon is very weak and does not reflect the changing pattern.

In summary, under the 185 mm air gap condition, longer wave periods (1.2 s) show greater sensitivity of peak slamming pressure to wave steepness, with the 0.8 s period exhibiting an increase in peak pressure as wave steepness increases, while the 1.2 s period shows little variation. Overall, peak slamming pressures for longer wave periods (1.2 s) are higher than those for shorter periods, and higher measurement positions (F1/F2) display greater fluctuations in peak pressure across different wave steepness values. The first two observations are opposite to those under the 135 mm air gap condition, while the latter two are consistent.

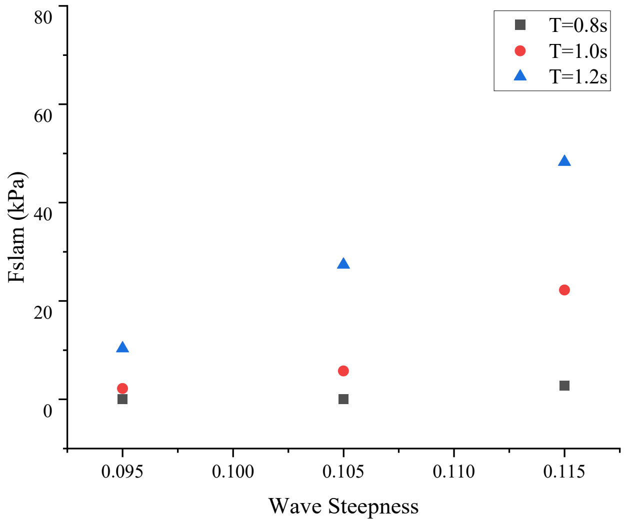

Fig 4.35. The variation of peak slamming pressure value with wave steepness at point F2 under an air gap of 185mm

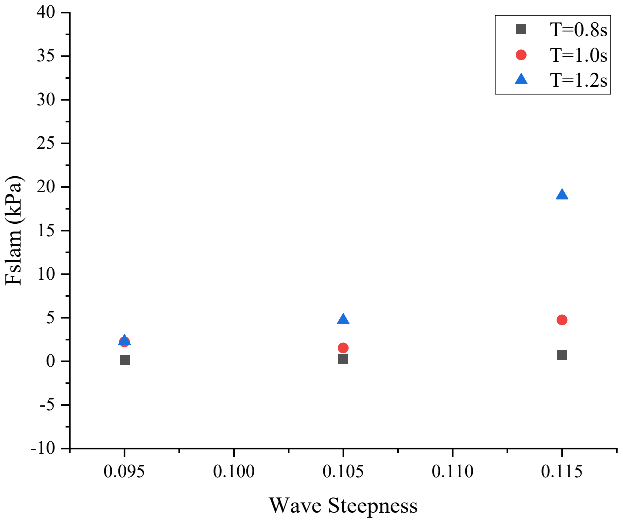

Fig 4.36. The variation of peak slamming pressure value changing with wave

steepness at point F3 under an air gap of 185 mm

4.5.3 Period

A regular wave steepness of H/L = 0.12 is selected, with five wave periods of 0.6 s, 0.8 s, 1.0 s, 1.1 s, and 1.2 s, four air gaps of 135 mm, 185 mm, 235 mm, and 285 mm, and measurement points F1 to F4 are analyzed to investigate the sensitivity of slamming peak values to wave period. In each regular wave load condition, the average value of the first 1/3 pressure peaks within the simulation time is taken as the peak value of the slamming pressure.

It can be seen from Fig 4.37 that as the wave period increases, the slamming pressure at point F1 under the 135mm air gap is almost zero at 0.6s and 0.8s; it reaches the maximum at 1.0s and then gradually decreases. When the period changes from 1.0s to 1.2s, the decrease rate of the pressure peak is 11.1% and 40.7% for every 0.1s increase. The slamming pressure at F1 point under the 185mm air gap shows a trend of gradually increasing with the increase of the period. When the period changes from 1.0s to 1.2s, the rising rate of the peak value for each additional 0.1s is 78.2% and 64.2%, which is observed that the slamming pressure is very sensitive to the change of period.

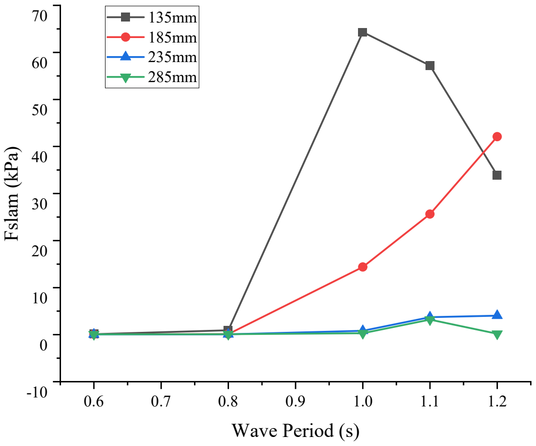

Fig 4.37. Schematic diagram of the variation of peak slamming pressure value changing with wave period at point F1

No matter what the air gap conditions are, the F1 point does not show obvious slamming phenomenon when the period is 0.6s and 0.8s. However, when the air gap is 135mm and 185mm, the slamming shows two completely different trends with the period.

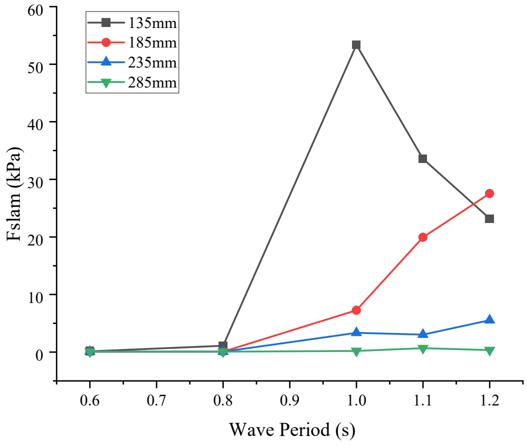

Fig 4.38. Schematic diagram of the variation of peak slamming pressure value changing with wave period at point F2

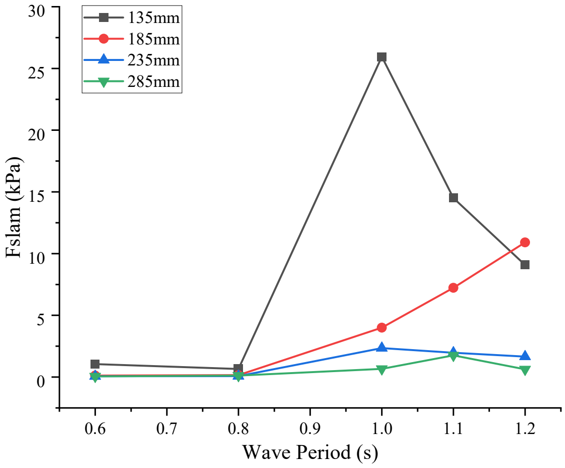

Fig 4.39. Schematic diagram of the change of peak slamming pressure value changing with wave period at point F3

Combining Fig 4.38 and Fig 4.39, it can be found that points F2 and F3 show a similar pattern to point F1: that is, the slamming is insensitive to periodic changes and the slamming value is small under a larger air gap. The slamming is very sensitive to periodic changes and the changing trends are very different under the air gap of 135mm and 185mm. The slamming value is the largest when the period is 1s under the 135mm air gap, and the slamming value is the largest when the period is 1.2s under the 185mm air gap.

Fig 4.40 shows the change of slamming with the period at point F4. It can be found that compared with points F1 to F3, the overall slamming value is smaller, and the changing trend is consistent under the air gap of 135mm and 185mm. At 235mm and 285mm, it shows a trend of first increasing and then decreasing as the period increases. However, as the slamming pressures remain below 6 kPa under this condition, their influence on the overall variation pattern is relatively minor.

In summary, considering points F1 to F4, the wave period producing the peak slamming pressure varies with air gap, but peaks mainly occur at 135 mm and 185 mm. For the 135 mm air gap, the slamming value at T = 1.0 s is significantly greater than for other waves, while for the 185 mm air gap, the maximum occurs at T = 1.2 s. Larger air gaps result in lower sensitivity of slamming to period changes and smaller slamming values, whereas smaller air gaps show high sensitivity, with markedly different trends between 135 mm and 185 mm. Regardless of air gap size, no obvious slamming is observed at F1 for periods of 0.6 s and 0.8 s, but at longer periods, the 135 mm and 185 mm air gaps exhibit two distinctly different patterns in peak slamming values.

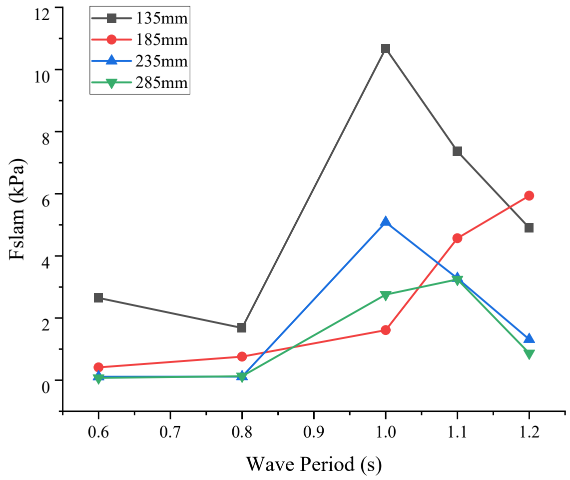

Fig 4.40. Schematic diagram of the variation of peak slamming pressure value changing with wave period at point F4

4.5.4 Wave direction

The incident angle of waves has a non-negligible influence on the movement of the platform and the slamming phenomenon. Under oblique wave conditions, there is a certain angle between the platform and the waves. The buoys and columns will form a blocking and shielding effect on the incoming waves, which will change the flow field relationship of the four columns and also the wave slamming phenomenon. In this experiment, an analysis and study on the slamming pressure of the column measuring points under wave incident angles of 185 degrees and 135 degrees has been conducted. Figs 4.41 to 4.42 show the slamming peak values of points F1 to F3 under waves R1 to R9. It is observed that the peak slamming pressure under oblique wave conditions is generally lower than the slamming pressure under windward wave conditions, and as the wave steepness increases, this gap shows an increasing trend.

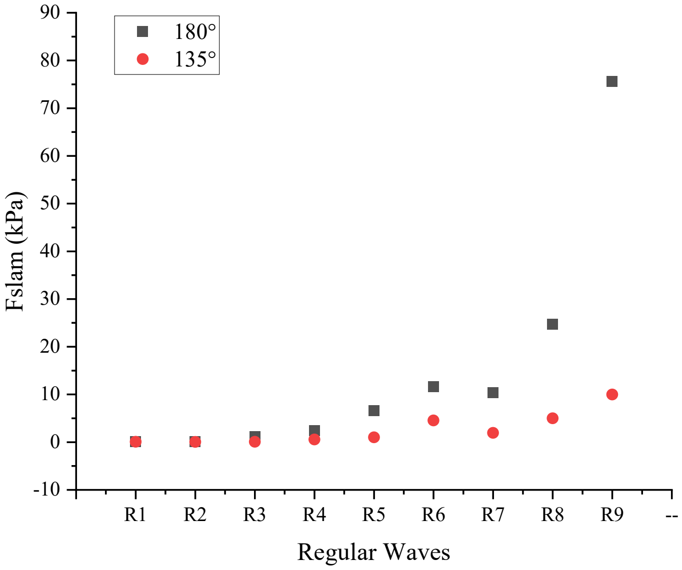

Fig 4.41. The change of slamming pressure

at point F1 under wave angles of 180° and 135°

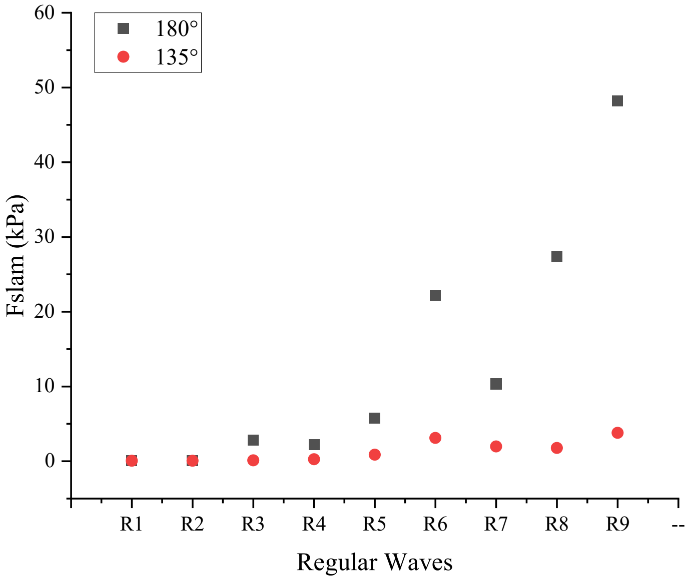

Fig 4.42. The change of slamming pressure

at point F2 under wave angles of 180° and 135°

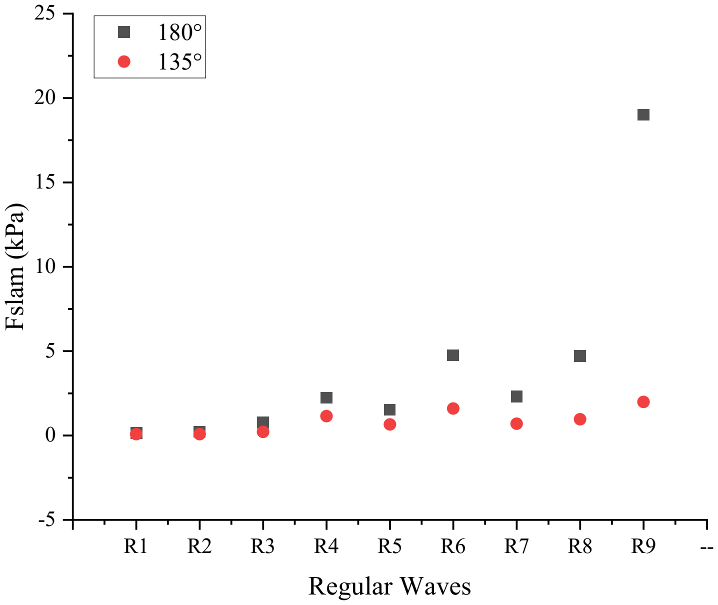

Fig 4.43. The change of slamming pressure

at point F3 under wave angles of 180° and 135°

In addition, by comparing the slamming pressure at points F2 and F3 under the higher wave steepness conditions of R3, R6, and R9, it was found that under the 180° wave heading, the slamming pressure variation of point F2 relative to F3 was 266.7%, 368.3%, and 153.7%, respectively; while under the 135° wave heading, the variation was −49.7%, 94.7%, and 90.1%. This indicates that under head-sea conditions, the slamming pressure at point F2 is significantly higher than that at F3; whereas under oblique-sea conditions, the difference between the two points decreases markedly, and in some cases (such as R3), the F2 value even becomes lower than F3. From a phenomenological perspective, since F2 is located at the upper part of the column near the deck edge, its increased peak value under head waves may be associated with momentum focusing caused by local wave crest convergence and geometric confinement. However, it should be noted that previous studies (Barcellona et al., 2003) have pointed out that during the formation of deck jetting, local shielding and ventilation effects may occur, which could weaken nearby pressure peaks. Taken together, the present results suggest that under head-sea conditions, momentum concentration effects at the deck edge appear to be more pronounced, resulting in higher peak pressures at F2.; while under oblique-sea conditions, the jet momentum tends to spread laterally and downstream, with the shielding and pressure-relief effects becoming more pronounced. In such cases, shielding and pressure-relief effects may become more significant, leading to a reduced pressure difference between F2 and F3, and occasionally a lower peak value at F2.. In summary: (1) The overall slamming pressure peaks under oblique-wave conditions are lower than those under head-wave conditions, and this difference tends to increase with wave steepness; (2) Under oblique-wave conditions, the slamming pressure peaks are less sensitive to measurement height compared to head-wave conditions—that is, the variation of peak slamming pressure with measurement height is much smaller under oblique waves.

4.6 Summary of this chapter

This chapter analyzes the slamming experiments of three types of waves: regular waves, focused waves and freak waves. First, a comparative study was conducted on the maximum value received by the pressure transducer in regular waves. The pressure distribution under regular waves was analyzed, and the characteristics of the time history curve were studied. Then, the wave climbing effect, air gap, incident angle and other factors under the focused waves and the freak waves were analyzed, and the changing trend of the slamming force relative to these factors was analyzed. Furthermore, the pressure time history curve captured by each pressure transducer was also analyzed, and the relationship between the time history curve and the slamming force was summarized. Finally, a comparative analysis was conducted on the relationship between the transducer peak value and the air gap change. The relevant conclusions are as follows:

1. Under regular wave conditions, when the air gap is small (135 mm and 185 mm), most wave cases exhibit significant and frequent slamming, with slamming intensity generally higher than in large air gap conditions. Under these low air gap conditions, slamming effects are more pronounced at measurement points F1–F4 (near the free surface), and in most cases, the slamming pressure decreases as the measurement point height increases. When the air gap increases to 235 mm and 285 mm, both the frequency and intensity of slamming are significantly reduced, and except for a few special cases, the relationship between slamming intensity and measurement point height no longer shows a clear pattern, with the response being dominated more by wave forces rather than typical slamming.

2. Under focused wave conditions, the weakening effect of air gap on slamming force is very evident: the larger the air gap, the smaller the slamming force, although this attenuation trend gradually slows as the air gap increases further, indicating that the amplifying effect of deck overhang on slamming is diminishing. At the same time, the frequency bandwidth has a significant impact on slamming intensity, with narrow-band focused

waves (TBH5, 0.8–1.2 s) having more concentrated energy, producing higher wave crests and greater slamming pressures (e.g., peak at F1 of 14,490 Pa vs. 4,991 Pa, about 2.9 times higher), thereby markedly enhancing slamming effects. In terms of wave run-up, at a 180° head sea, waves climb significantly along the platform columns (wave height at W1 greater than at W2/W3), whereas at a 135° oblique sea, run-up is reduced or even breaks earlier. Regarding directional forces, the X-direction slamming force decreases significantly with increasing air gap (notably from 185 mm to 235 mm), while the Z-direction force exhibits a nonlinear fluctuation pattern.

3. Under freak wave conditions, even with similar significant wave heights, the slamming loads generated by the JONSWAP spectrum remain significantly higher than those from the S spectrum, with the maximum reaching more than six times greater (e.g., 125.4 kPa for JonM10 vs. 20.65 kPa for S100M10). The slamming intensity increases with the elevation of the measurement point, and it is more likely to cause structural damage near the deck region. At the top measurement points (F1/F2), a double-peaked slamming phenomenon can be observed, where JonM10 produces a higher first peak, while S100M10 shows a higher second peak. When the wave heading is 135°, the resultant force in the X/Y directions is close to that at 180°, but the overall slamming intensity is significantly reduced (e.g., 5,376 Pa at F1 vs. 125.4 kPa). In terms of wave run-up, JonM10 exhibits a noticeably higher run-up ratio than S100M10, and this ratio decreases progressively with increasing air gap. Overall, slamming intensity increases with measurement point height, with locations closer to the deck being more prone to structural damage. Among all tested conditions, the extreme value occurs under the combination of JonM10, 180° wave heading, and a 185 mm air gap, reaching 152.7 kPa, which poses the greatest threat to structural

strength and should be a key focus in engineering design to prevent structural failure.

4. Under regular wave conditions, slamming intensity generally increases with measurement point height (F1 > F2 > F3 > F4), with point F1 (near the deck) sometimes exhibiting an abnormal increase under oblique waves due to the deck jet effect. Air gap, wave steepness, period, and wave heading are key factors influencing slamming, with air gap having the most direct impact—except for R6, R9, and R14, most cases show a decrease in peak slamming pressure with increasing air gap; however, R6, R9, and R14 reach their peaks at an air gap of 185 mm, reflecting the coupling effect of wave steepness (0.115–0.12) and period (1.0–1.2 s). At a 135 mm air gap, peak slamming pressure is most sensitive to wave steepness for shorter periods (0.8 s, 1.0 s), with a significant amplification when wave steepness increases, whereas at a 185 mm air gap, the highest sensitivity occurs at the longer period (1.2 s), showing an opposite trend to the 135 mm case. For both 135 mm and 185 mm air gaps, high measurement points (F1/F2) tend to show greater fluctuations in peak slamming values across different wave steepness levels. Regarding period effects, the period producing the maximum peak differs with air gap: T = 1.0 s for 135 mm and T = 1.2 s for 185 mm. Overall, larger air gaps result in smaller slamming values and lower sensitivity to period changes, whereas smaller air gaps lead to high sensitivity and distinctly different variation trends. In addition, the peak slamming pressure under oblique waves is generally lower than that under head seas, and this gap widens as wave steepness increases, with oblique waves also showing notably lower sensitivity of peak slamming pressure to changes in measurement point height compared with head seas.

5 NUMERICAL SIMULATION OF HORIZONTAL WAVE SLAMMING BASED ON CFD METHOD

To gain an in-depth understanding of the load evolution mechanisms during wave slamming on platform columns and to enable rapid and effective prediction of impact responses under extreme sea states, a reliable numerical simulation method is required. This study developed a CGNT-CFD numerical model based on a three-dimensional Cartesian-grid finite difference method. Under regular wave conditions, nine numerical simulations (wave parameter cases A1–A9) are conducted using the CGNT-CFD method, with a typical configuration of 185 mm air gap and 180° wave heading. By comparing the numerical results with experimental data, the model's prediction accuracy is validated in terms of wave generation, pressure time histories, and overall loads. Furthermore, a comparative analysis with STAR-CCM+ results is conducted to demonstrate the computational efficiency of the CGNT-CFD method. This chapter provides a solid foundation for the subsequent parameter sensitivity analysis.

5.1 Numerical wave tank simulation setup

This chapter presents a total of 16 simulation cases of wave slamming on a single platform column, all conducted with a unified air gap of 185 mm (with the still water level referenced in Fig. 4.1) and a wave heading of 180°. These cases are designed for grid convergence analysis, performance comparison between two CFD methods, and validation against experimental data. The complete set of cases is summarized in Table 5.1.

First, the high-wave case A9 (see Appendix A.3, Table 0.2) is selected for a grid density and time-step convergence study using the CGNT-CFD method. With the time step initially set to 0.0005 s, three different grid densities (approximately 1.4 million, 2.36 million, and 3.21 million cells) are tested. Based on the results, a grid of 2.36 million cells is adopted for subsequent simulations. On this basis, three time steps (0.01 s, 0.0005 s, and 0.0002 s) are evaluated for accuracy, and 0.0005 s is determined to be optimal. In total, six cases are used for the convergence analysis.

Subsequently, to validate the accuracy of the CGNT-CFD method, nine regular wave cases (A1–A9) are simulated and compared with experimental results presented in Chapter 4. The comparisons focus on wave profile generation, pressure time histories, and overall load predictions.

In addition, to compare the performance of the CGNT-CFD method with that of the commercial software STAR-CCM+, one high-wave case (A8) is simulated using STAR-CCM+, and the results are compared in terms of both simulation accuracy and computational efficiency.

Table 5.1 Simulation cases for numerical method comparison and validation.

Numerical method	Total Grid Cells (millions)	Time Step（s）	Wave No.	*H* (cm)	*T* (s)	*L* (m)	Wave Steepness
CGNT-CFD	1.4040	0.0005	A9	27.73	1.2	2.4106	0.115
	2.3562	0.0005	A9	27.73	1.2	2.4106	0.115
	3.2076	0.0005	A9	27.73	1.2	2.4106	0.115
	2.3562	0.01	A9	27.73	1.2	2.4106	0.115
	2.3562	0.0005	A9	27.73	1.2	2.4106	0.115
	2.3562	0.0002	A9	27.73	1.2	2.4106	0.115
STAR-CCM+	3.9200	0.0005	A8	24.95	1.2	2.3759	0.105
CGNT-CFD	2.3562	0.0005	A1	10.22	0.8	1.0754	0.095
			A2	11.48	0.8	1.0934	0.105
			A3	12.81	0.8	1.1135	0.115

			A4	15.81	1	1.6637	0.095
			A5	17.73	1	1.6882	0.105
			A6	19.74	1	1.7160	0.115
			A7	22.28	1.2	2.3456	0.095
			A8	24.95	1.2	2.3759	0.105
			A9	27.73	1.2	2.4106	0.115

5.2 Introduction of numerical simulation solutions based on general commercial CFD methods and CGNT-CFD method

5.2.1 Introduction to numerical simulation of wave slamming loads

The numerical water flume setup is developed based on the experiment framework, with the main parameters of the platform detailed in Chapter 3. To simulate the complex flow field induced by platform slamming and to minimize the impact of wall effects, the length of the computational domain for the simulation was set to three times the incident wavelength, ensuring a sufficiently large simulation space. The width and vertical height of the computational domain were set to 1m and 1.5m, respectively. The left boundary of the computational domain was defined as a velocity inlet boundary condition, with a uniform incoming flow velocity along the X-axis. The right boundary was set as a pressure outlet with zero pressure. The front and rear boundaries were set as symmetric surface boundary conditions, where all velocities and pressure gradients in directions other than their corresponding normal directions were zero. Fig 5.1 illustrates the specific boundary conditions:

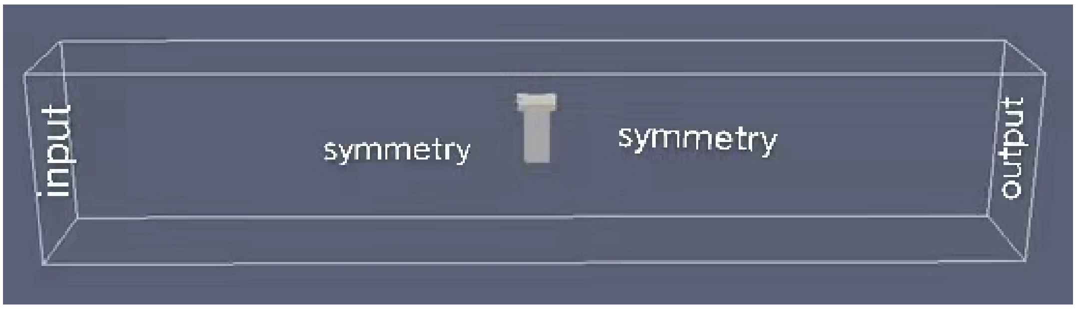

Fig 5.1. Setting of computational domain and boundary conditions for the numerical water flume

5.2.2 Convergence analysis of CGNT-CFD method

In CFD numerical simulations, grid discretization has a significant impact on the convergence and accuracy of the results. Different grid types can greatly affect computational efficiency and numerical precision. Therefore, before conducting numerical simulations, a convergence analysis should be performed on both the grid and the time step to verify the reliability of the numerical setup. Based on the load conditions of the model experiment, this convergence analysis uses load condition number A9 to conduct a numerical simulation of grid and time step convergence analysis and accuracy verification. To evaluate the impact of the grid and time step on the convergence results of the numerical water flume, three different numbers of grids and three different time steps were analyzed. The grid size in the x direction of the dense area was set to 1/160 of the target wavelength, while the z direction was set to 1/16 of the target wave height. The growth ratios are shown in Figs 5.2 to 5.4. This type of grid division uses a right-angle intersecting grid without a boundary layer grid division close to the platform. This simple and convenient grid division can improve computational efficiency. The total number of cells for the three grids were 1.404 million, 2.3562 million, and 3.2076 million, respectively. After completing the grid convergence analysis, a grid simulation with better results was selected as the baseline for the time step convergence analysis. Three different time steps were used in the time step convergence analysis: 0.01s, 0.0005s, and 0.0002s. Table 5.2 shows the relevant parameters used for grid convergence analysis; Table 5.3 shows the total number of grids corresponding to different grid sizes; Table 5.4 shows the location of pressure transducers.

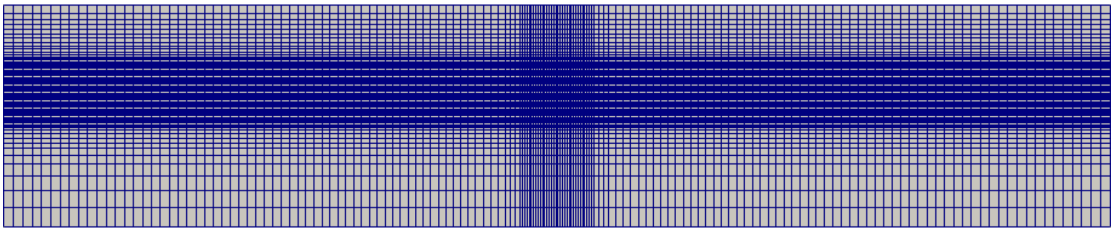

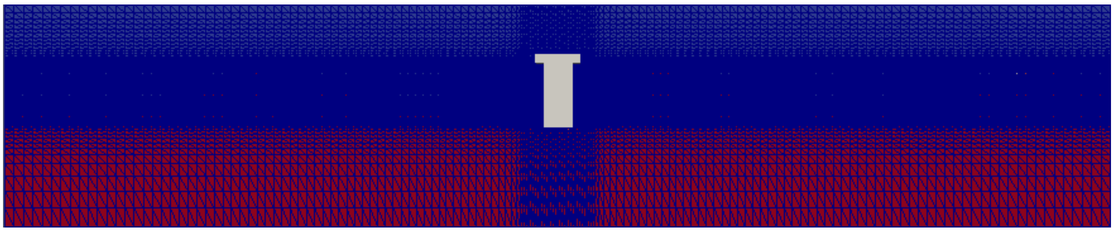

Fig 5.2. 1.404 million cells

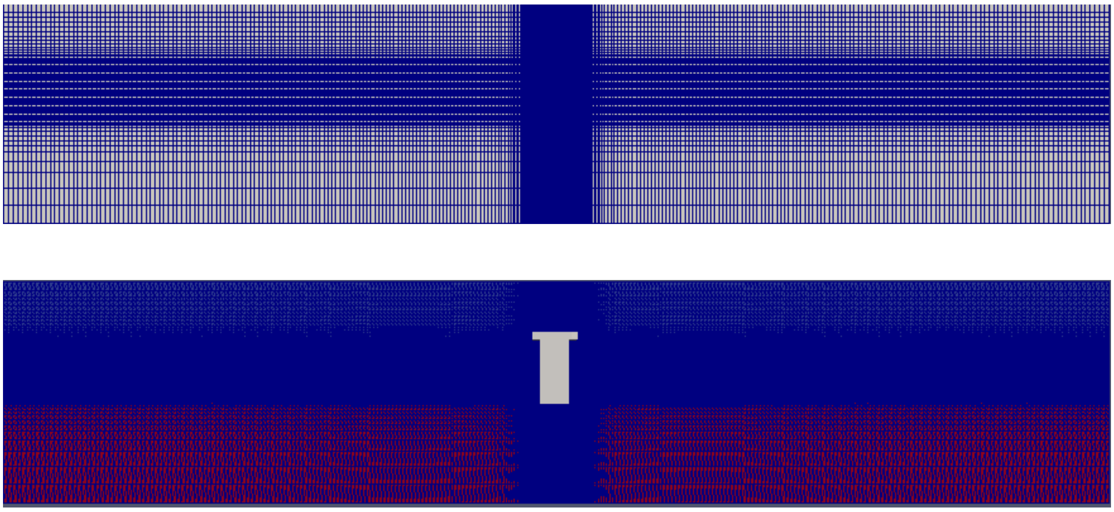

Fig 5.3. 2.356 million cells

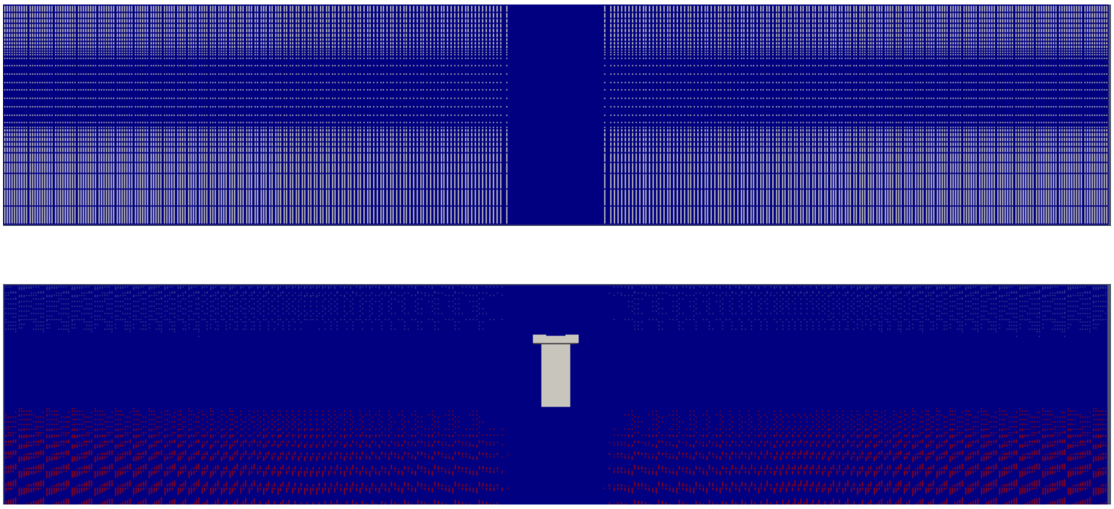

Fig 5.4. 3.208 million cells

Table 5.2. Relevant parameters

Parameters	Value
Wave height(cm)	27.73

Circumference(m)	2.4106
Period(s)	1.2
Air gap(mm)	185
air gap(mm)	215

Table 5.3.Grid density under different load conditions

Grid type	*Nx* × *Ny* × *Nz*	Total number of grids
Case1	520×36×75	1404000
Case2	561×56×75	2356200
Case3	594×72×75	3207600

Table 5.4. Location of pressure transducers

	X	*Y*	*Z*		*X*	*Y*	*Z*
F1	110.5	0	400	P1	0	110.5	400
F2	90	0	379.5	P2	0	90	379.5
F3	90	0	343	P3	0	90	343
F4	90	0	306.5	P4	0	90	306.5
F5	90	0	270	P5	0	90	270
F6	90	0	233.5	P6	0	90	233.5
F7	90	0	197	P7	0	90	197
F8	90	0	160.5	P8	0	90	160.5

Fig 5.5 shows the comparison of slamming pressures at the platform measurement points under different grid resolutions. From Fig 5.5 (a), it is observed that the slamming pressure at the measurement points under Case 2 and Case 3 grid densities are in good agreement. For a clearer observation, the pressure at measurement point F7 was taken and compared with the experimental value, as shown in Fig e. Through Fig 5.5 (e), it can be seen more clearly that the results under Case 2 and Case 3 grid densities are closer to the experimental values and are consistent with each other. Therefore, it can be concluded that the grid resolution used in Case 2 is sufficient to achieve grid convergence.. The subsequent relevant calculation grid size takes the size corresponding to Case 2.

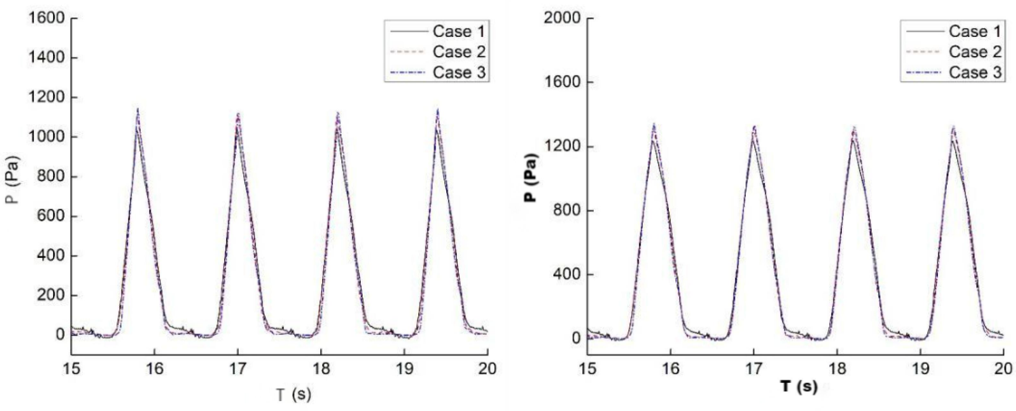

(a) Test point pressure at point F5 (b)Test point pressure at point F6

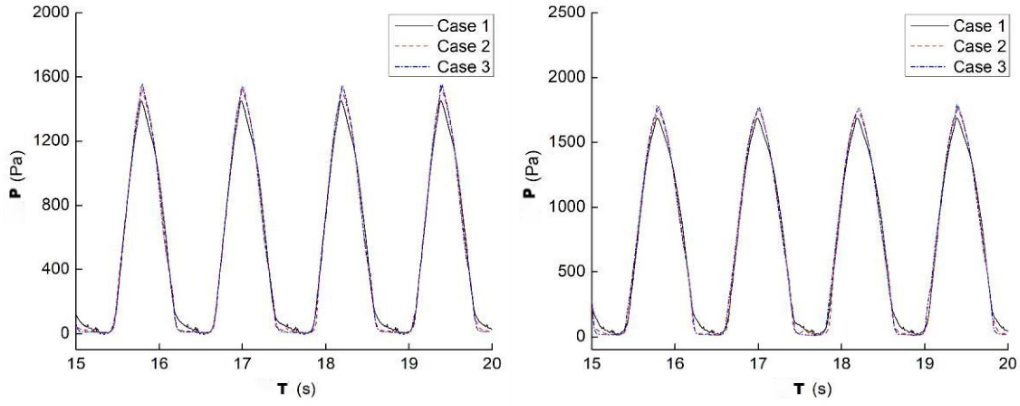

(c) Test point pressure at point F7 (d)Test point pressure at point F8

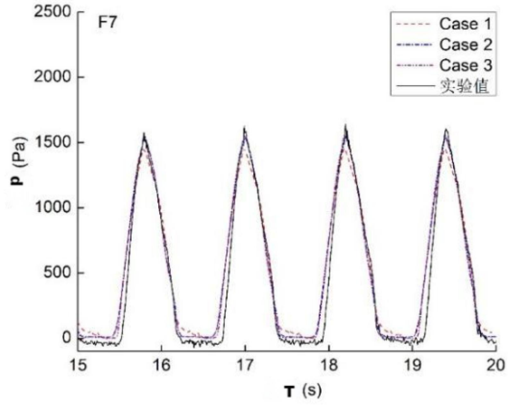

(e) Comparison between experimental and simulated values at point F8

Fig 5.5. Grid convergence analysis

As illustrated in Fig 5.5 (e) above: The error for Case 1 is 8.53%, the error for Case 2 is 5.29%, and the error for Case 3 is 3.67%. The errors satisfy the condition that the difference between Case 2 and Case 3 is less than the difference between Case 2 and Case 1, meeting the requirements of convergence analysis.

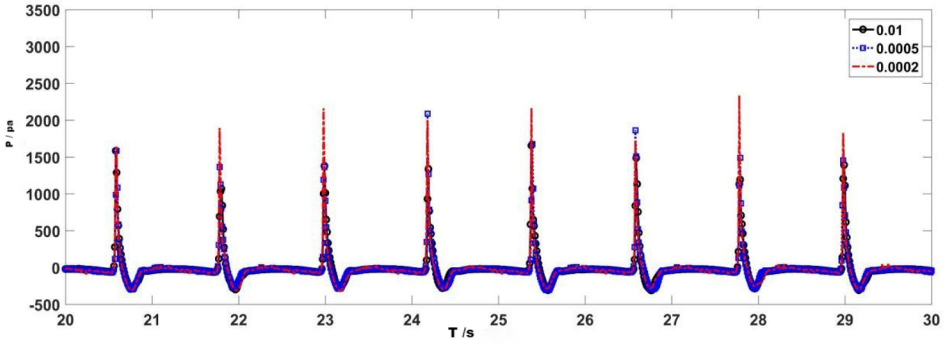

(a) Change in pressure at point F1 over time

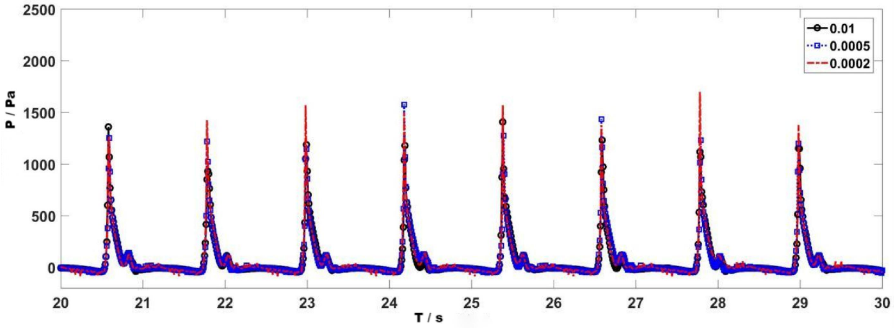

(b) Change in pressure at point F3 over time

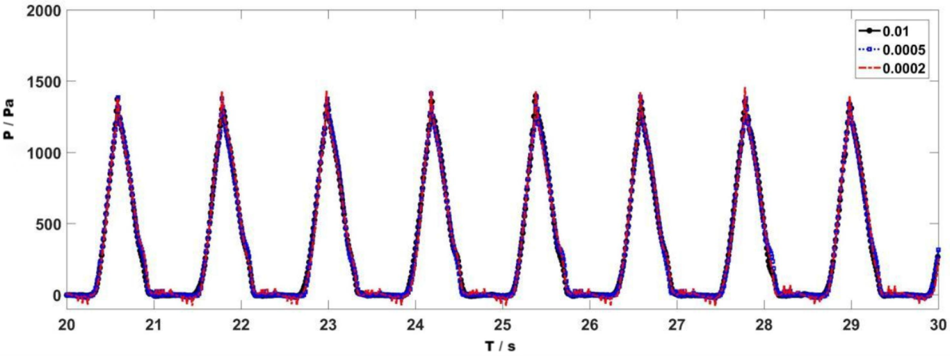

(c) Change in pressure at point F6 over time

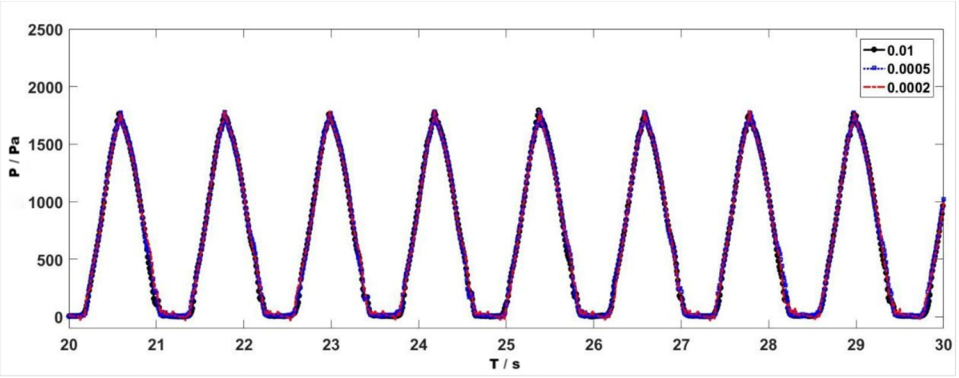

(d) Change in pressure at point F8 over time

Fig 5.6. Comparison of numerical results at different time steps

Figs 5.6 present a comparison of simulation results using different time steps. It is evident that the time step significantly impacts the pressure at the test point located on the platform's top, with smaller time steps resulting in higher peak pressures. For the pressure at the test point on the platform's top, the results using time steps of 0.0005s and 0.0002s are relatively close. As shown in Fig 5.6 (c) and 5.6 (d), the results under all three time steps are essentially consistent, primarily because the slover can automatically adjust the time step, reducing the difference between the result at a time step of 0.01s and those of smaller time steps. Through the analysis, it is determined that a time step of 0.0005s meets the requirements for the numerical simulations, striking a balance between computationl efficiency and solution accuracy.

To ensure that the time step satisfies the numerical stability requirements during the breaking wave and slamming stages, spatial and temporal convergence analyses were first conducted in this study. The final numerical model adopted a grid size of approximately 2.35×10^6 cells (minimum horizontal grid size $\Delta x\_min = \lambda/160 = 1.0754/160 \approx 0.0067$ m, and refined vertical grid size $\Delta z = 0.0173$ m) with a time step of $\Delta t = 0.0005$ s. Under a representative slamming condition, the local particle velocity near the free surface reached 1.24 m/s. According to the definition of the Courant number:

$$\mathrm{CFL} \approx \frac{u_{\max}\Delta t}{\Delta_{\min}} = \frac{1.24 \times 0.0005}{0.0067} \approx 0.093$$

CFL_max < 0.1, satisfying the stability requirement for breaking wave and interface capturing. The chosen time step adequately resolves high-frequency transients during slamming and post-slamming stages, avoiding numerical dissipation and aliasing errors.

5.3 Comparative analysis of general commercial CFD methods and CGNT-CFD method

STAR-CCM+ is a widely used computational fluid dynamics software. This section compares the results obtained from CGNT-CFD method, STAR-CCM+, and the experiment to verify the computational accuracy and relative efficiency of the numerical flume. Regular wave condition A8 is selected for tis comparison. The wave parameters are listed in Tables 5.5, while Table 5.6 presents the arrangement of the pressure transducers.

Table 5.5. Relevant parameters

Parameters	Numerical value
Wave height(cm)	24.95
Circumference(m)	2.3759
Period(s)	1.2
Air gap(mm)	185
air gap(mm)	215
Time step(s)	0.0006

Table 5.6. Location of pressure transducers

	X	*Y*	*Z*		*X*	*Y*	*Z*
F1	110.5	0	400	P1	0	110.5	400
F2	90	0	379.5	P2	0	90	379.5
F3	90	0	343	P3	0	90	343
F4	90	0	306.5	P4	0	90	306.5
F5	90	0	270	P5	0	90	270
F6	90	0	233.5	P6	0	90	233.5
F7	90	0	197	P7	0	90	197

F8	90	0	160.5	P8	0	90	160.5

Fig 5.7 illustrates a comparison between the total forces on the numerical simulation platform and the experimental measurements. It is evident that the numerical results align well with the experimental results, exhibiting similar waveforms, periods, and amplitudes. Additionally, as seen from the Figure, for simulating platform forces, the results from commercial software STAR-CCM+ are nearly identical to those obtained from CGNT-CFD method. CGNT-CFD method is more accurate than commercial software STAR-CCM+ in simulation. However, for the Z direction, there is a relatively pronounced "peak" in the flume's experimental results. Condition A8 has a relatively high wave height, and waves produce slamming on the column deck. From the Figure, it is observed that the slamming peak captured by the direct grid method consistently aligns more closely with the experimental value, while STAR-CCM+ slightly overestimates the slamming force in local time intervals due to its inability to accurately collect flow field information. Both the CGNT-CFD method and STAR-CCM+ meet expectations for simulating this highly nonlinear slamming process.

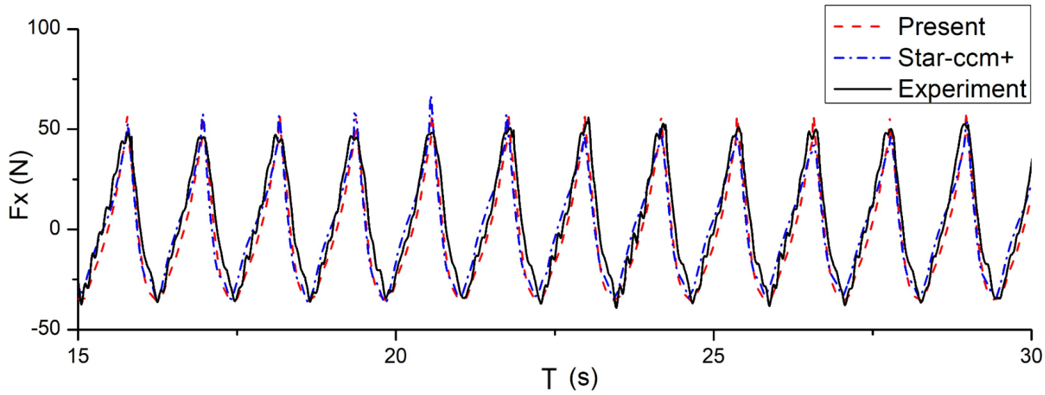

(a) Force on the platform in the x direction

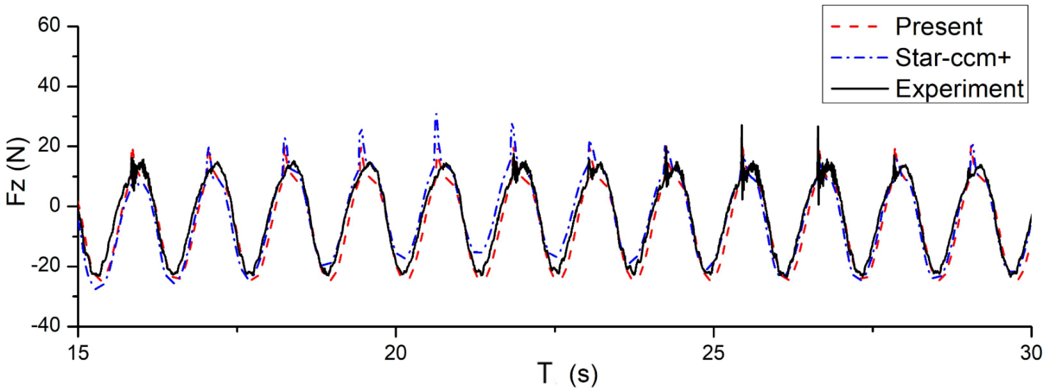

(b) Force on the platform in the z direction

Fig 5.7. Force on the platform

Fig 5.8 illustrates a comparison between the pressure at various measurement points on the platform and the experimental values. F6 to F8 are located below the still water level. It is evident that the simulated pressures at test points F3 and F5 align well with the experimental data, exhibiting similar waveforms, periods, and amplitudes. However, the pressure at test points F6-F8 has a larger deviations compared to the experimental values, with the error magitude increasing as the sensor location moves downward along the column. From Fig 5.8 (e) and (f), negative pressure observed in the exprimental results, while no obvious negative values are present in the simulated pressure. For all test points except for F3 and F8, The experimental results are greater than those of the two simulation methods; however, the pressure values simulated by the CGNT-CFD method consistently align closely with those from the commercial software STAR-CCM+, indicating that the CGNT-CFD method achieves comparable accuracy to STAR-CCM+ in predicting pressures at the measurement points. Over time, the discrepancy between simulation and experiment gradually decreases. The calculation results of the CGNT-CFD method remain stable within several periods.

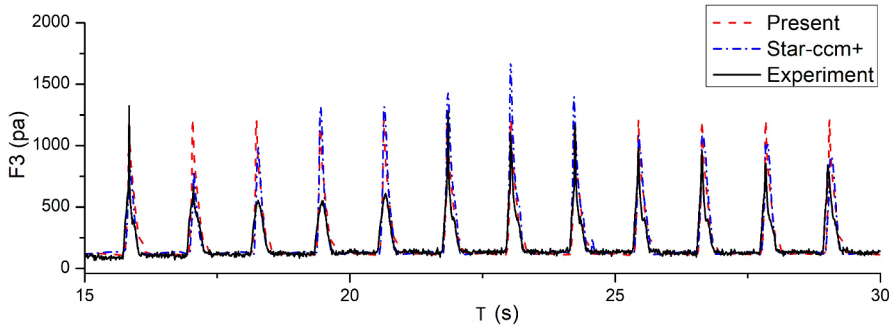

(a) Change in pressure at point F3 over time

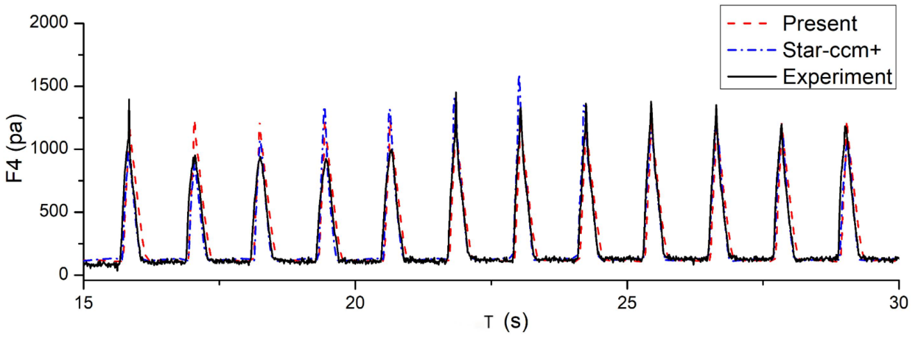

(b) Change in pressure at point F4 over time

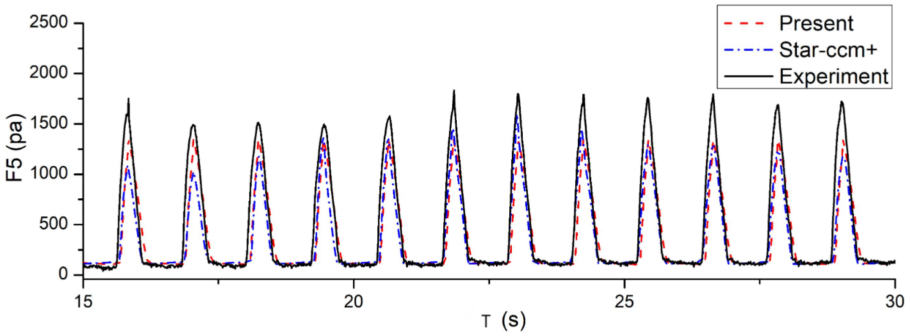

(c) Change in pressure at point F5 over time

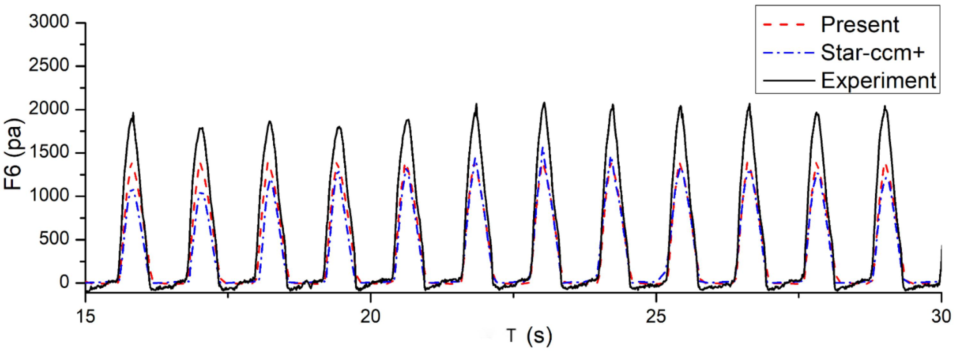

(d) Change in pressure at point F6 over time

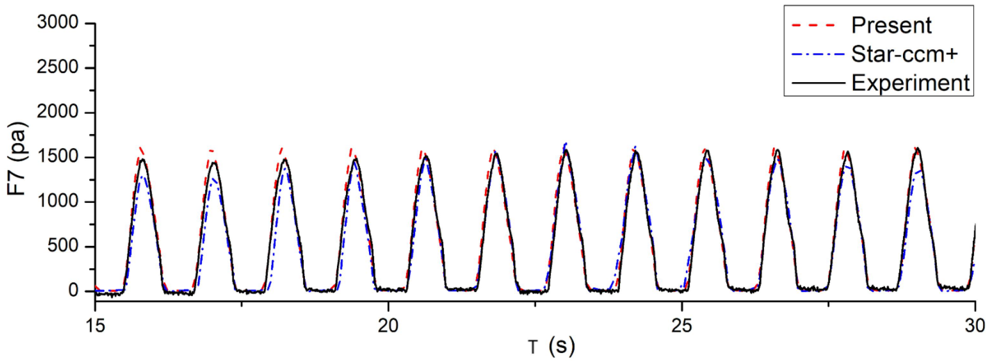

(e) Change in pressure at point F6 over time

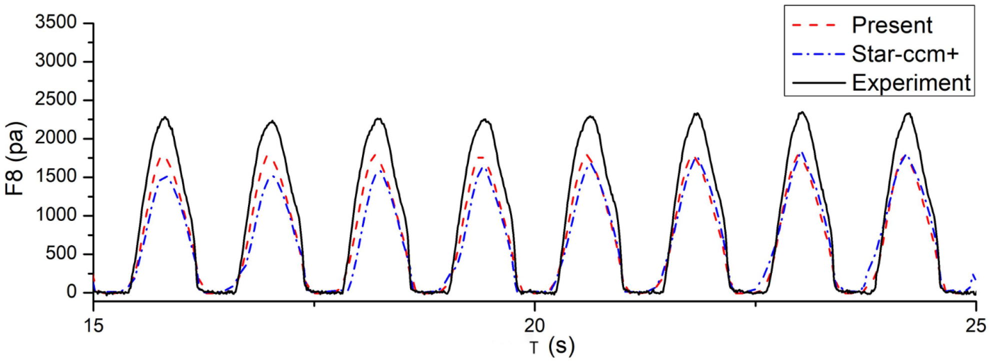

(f) Change in pressure at point F8 over time

Fig 5.8. Change in slamming pressure over time

As seen from the Fig 5.8, both STAR-CCM+ and CGNT-CFD method exhibit good simulation effects on wave slamming. The numerical simulation results from both align well with the experimental results in terms of waveform and period. For the peak pressure at the test points, except for F6 and F8, the simulated values of the other test points align well with the experimental values. The deviation at test point F8 primarily results from the sparse grid near the platform’s bottom. The grid size of the computational domain grid at the water surface position is 1/16 of the wave height. The grid size far from the water surface is larger than that at the water surface position, resulting in an error in the result. This can be accurately predicted by refining the grid according to engineering needs. Notably, at position F8, the mesh density of STAR-CCM+ is equivalent to that of the CGNT-CFD method, and the prediction accuracy of CGNT-CFD is comparable to that of the commercial software.

From the slamming pressure time histories at different sensor locations (F3 and F5) in Fig. 5.8(a – c), both numerical methods capture the periodicity and phase of the slamming events, but noticeable differences appear in peak magnitude and waveform shape. The pressure peaks computed by STAR-CCM+ are slightly lower than the experimental results, with rounder crests and faster decay, indicating stronger numerical dissipation (attenuation of high-frequency energy) and a slight underestimation of impact loads. In contrast, the CNT-CGCFD results exhibit peak amplitudes closer to the experiment and sharper crests, suggesting lower dissipation in interface compression and time-advancing processes, thus preserving more high-frequency transient components of the slamming load. After several propagation cycles, STAR-CCM+ shows greater peak attenuation, whereas CNT-CGCFD remains consistent with experimental trends, confirming that CNT-CGCFD experiences lower numerical dissipation and is better suited for simulating high-frequency nonlinear slamming phenomena.

It can be observed that the CGNT-CFD method yields simulation results for both the overall slamming force and the pressure responses at various measurement points that are in closer agreement with the experimental data, demonstrating good computational accuracy. By incorporating an improved wave breaking model with a three-dimensional Cartesian grid algorithm, the method achieves a level of accuracy comparable to that of the commercial software STAR-CCM+, with a maximum relative error of approximately 4%. This indicates that CGNT-CFD not only maintains high computational efficiency but also possesses predictive capabilities on par with high-accuracy commercial solvers.

Both CGNT-CFD method and STAR-CCM+ use Inter® Xeon® Platinum 8168@2.70GHz processors for serial calculation. Using 2.35 million grids and a time step of 0.0005s to simulate 30s physical time takes a total of 101 hours, while STAR-CCM+ uses 3.92 million grids and a time step of 0.0005s to simulate 30s takes 106 hours. Moreover, the CGNT-CFD method can achieve the required computational accuracy with significantly fewer grid cells. In large-scale simulations involving tens or hundreds of millions of cells for offshore platforms, the CGNT-CFD method offers a clear advantage in computational speed.

The CGNT-CFD method and the commercial software STAR-CCM+ both produce simulated waveforms, periods, and amplitudes of single slamming events on the platform that are generally consistent with the experimental results. Both simulations provide useful reference results and achieve reasonable accuracy. However, neither can accurately reproduce the small “spikes” in the overall slamming force response. In addition, for individual pressure sensors, both simulated values are lower than the experimental measurements, and the deviation increases progressively with decreasing sensor height. This is related to the coarser mesh near the platform bottom, indicating that mesh quality plays a decisive role in the accuracy of slamming simulations.

5.4 Simulation of horizontal wave slamming characteristics based on CGNT-CFD method

This section primarily focuses on verifying the reliability of simulating wave slamming on a single column using a CGNT-CFD method under regular waves. In this section, a total of 9 load conditions were simulated using the wave parameters shown in Table 5.7. The grid size near the platform column is 0.005m, approximately 1/16 of the wave height, with a total of about 2.35 million grids. The layout of the pressure transducers is illustrated in Table 5.8.

Table 5.7. Wave parameters

Wave No	*H* (cm)	*T* (s)	*L* (m)	Wave steepness
A1	10.22	0.8	1.0754	0.095
A2	11.48	0.8	1.0934	0.105

A3	12.81	0.8	1.1135	0.115
A4	15.81	1	1.6637	0.095
A5	17.73	1	1.6882	0.105
A6	19.74	1	1.7160	0.115
A7	22.28	1.2	2.3456	0.095
A8	24.95	1.2	2.3759	0.105
A9	27.73	1.2	2.4106	0.115

Table 5.8. Location of pressure transducers

	X	Y	Z		X	Y	Z
F1	110.5	0	400	P1	0	110.5	400
F2	90	0	379.5	P2	0	90	379.5
F3	90	0	343	P3	0	90	343
F4	90	0	306.5	P4	0	90	306.5
F5	90	0	270	P5	0	90	270
F6	90	0	233.5	P6	0	90	233.5
F7	90	0	197	P7	0	90	197
F8	90	0	160.5	P8	0	90	160.5

Initially, a load condition with a small wave height is selected as a representative case for comparing numerical simulations with numerical wave tank experiments. Fig 5.9 illustrates the comparison between the numerical solution and the experimental values of wave height under load condition A2.

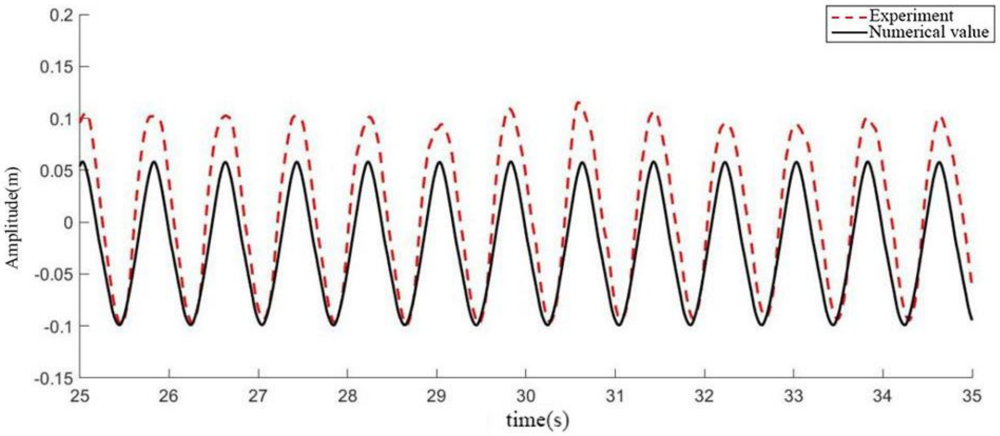

Fig 5.9. Comparison chart of numerical solution and experimental wave height under load condition A2

The simulation results of the CGNT-CFD method for waves closely match the experimental results in terms of waveform and period. However, the agreement between the amplitude of the experimental results and the simulation results of the CGNT-CFD method is not as good. The simulated values of both troughs are relatively close to the experimental values, but there is a significant difference between the simulated values of both peaks and the experimental values.

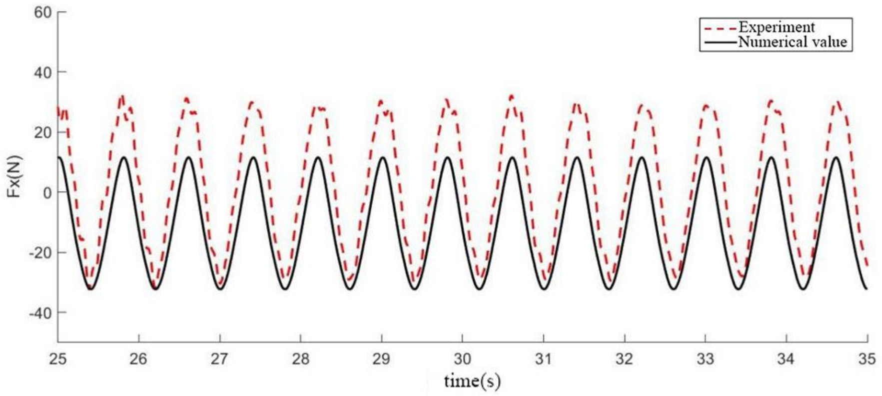

(a) Fx

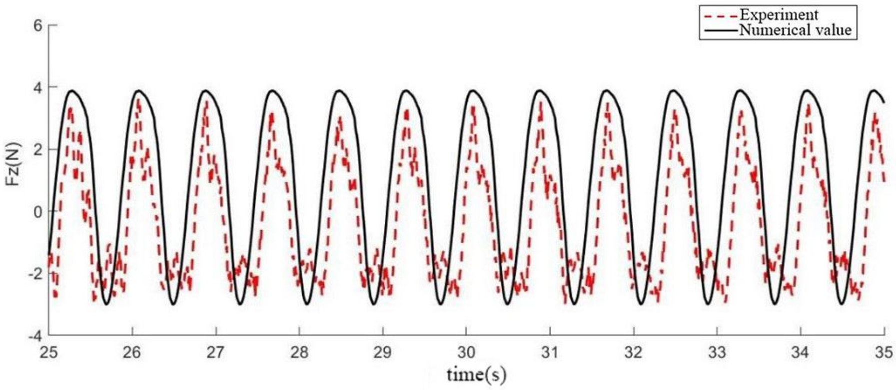

(b) Fz

Fig 5.10. Comparison chart of overall force between the numerical solution and experimental values under load condition A2

As shown in Fig 5.10, the simulation results of the overall force on the platform obtained form the CGNT-CFD method closely match the experimental results in terms of waveform and period. However, the agreement in the amplitude of the experimental results and the simulation results of the CGNT-CFD method is not as good. The experimental results capture distinct “spikes” in the overall force response, while the pressure curves of the pressure measurement points in the CGNT-CFD method are relatively smooth. Fig 5.10 (g) shows that the experimental values exhibit a secondary peak value in the overall force, while no secondary peak appears in the simulation results of the CGNT-CFD method. The experimental values display strong disorderliness, indicating that the pressure process is a highly nonlinear process. To simulate this process, the CGNT-CFD method may require a smaller grid size and a shorter time step. The “spike” phenomenon may be due to a mismatch between the grid and time used by the CGNT-CFD method or other factors. The absence of a secondary peak value in the simulation results may be because the peak values of both are relatively close and the CGNT-CFD method did not capture it accurately.

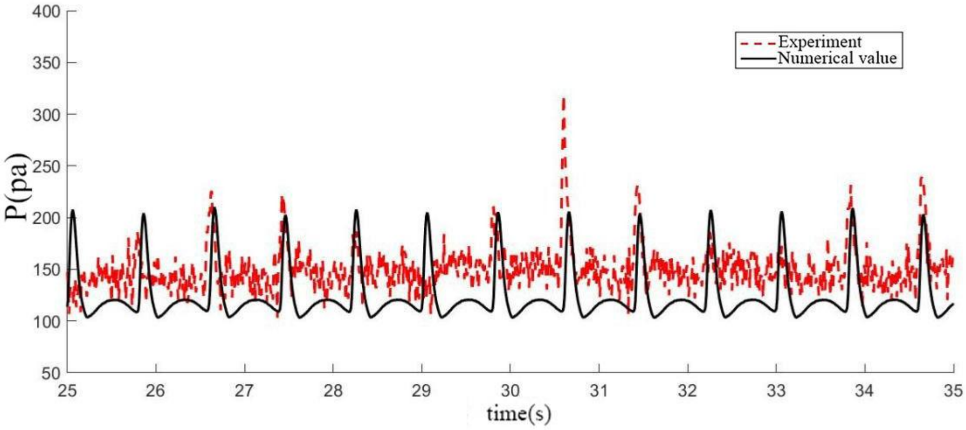

(a) Change in pressure over time at point F4

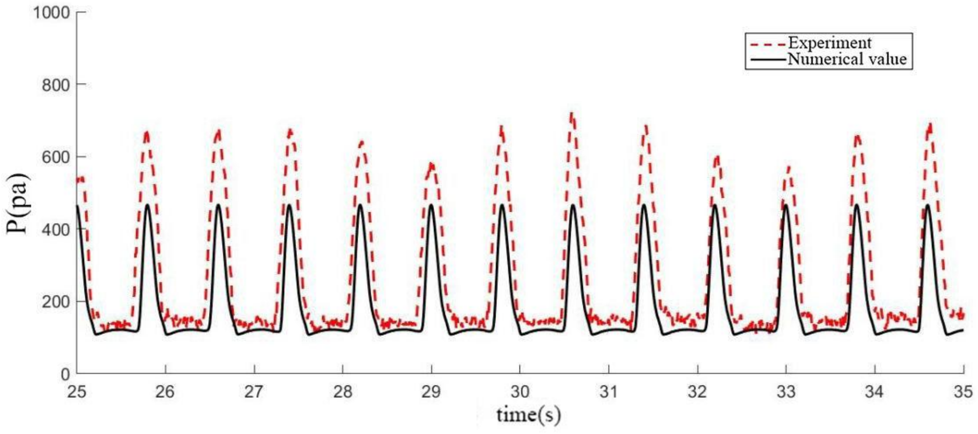

(b) Change in pressure over time at point F5

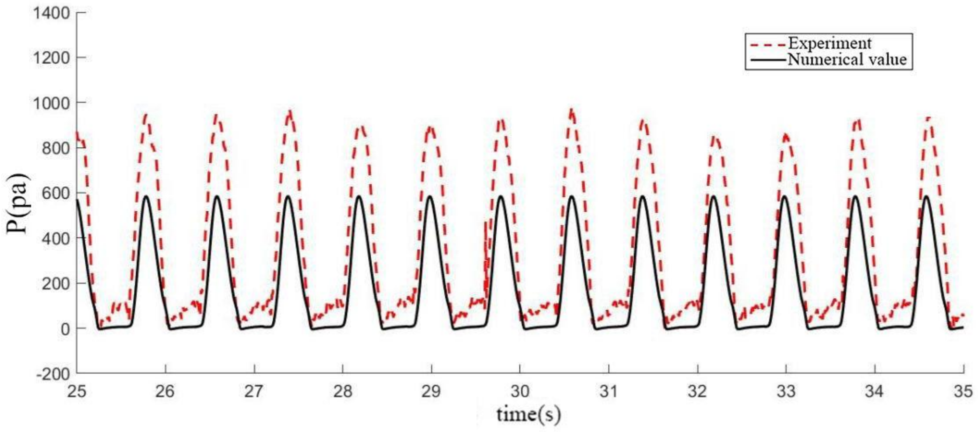

(c) Change in pressure over time at point F6

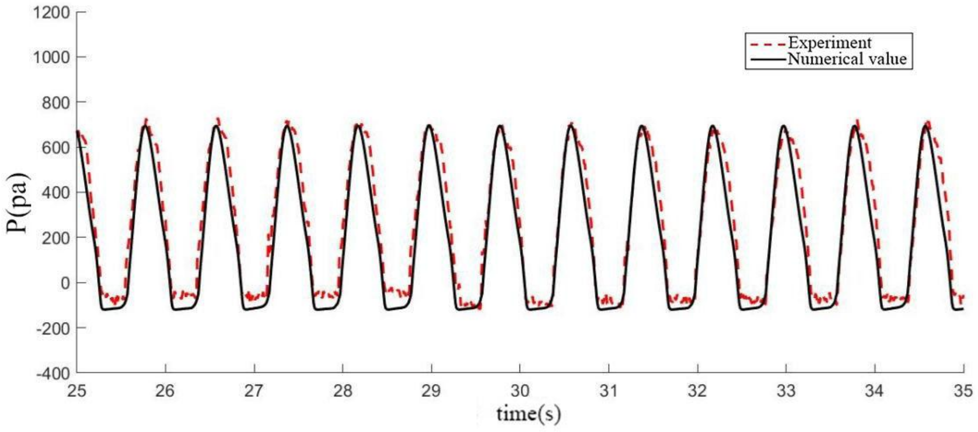

(d) Change in pressure over time at point F7

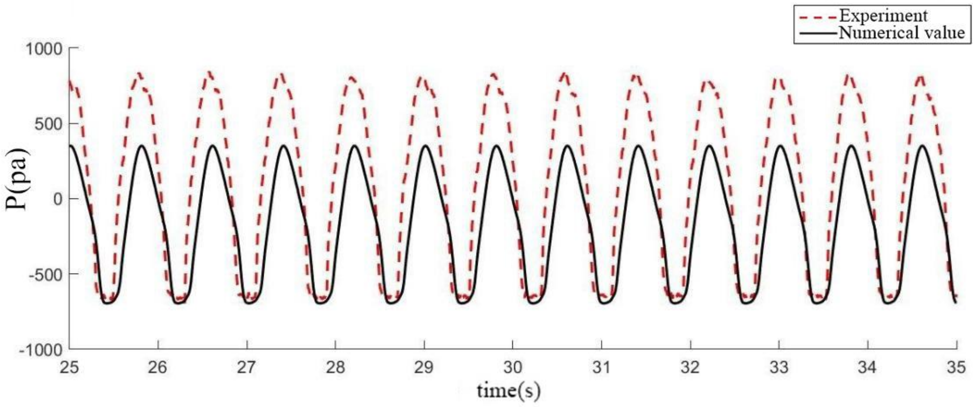

(e) Change in pressure over time at point F8

Fig 5.11. Comparison chart of pressure at measurement points between numerical solution and experimental values under load condition A2

From Fig 5.11, except for the F4 measurement point, the simulation results of the pressure measurement points in the CGNT-CFD method are in good agreement with the experimental results in terms of waveform and period. However, the amplitude of the experimental results is larger than that of the simulation results of the CGNT-CFD method. The experimental results capture “spikes” in the pressure at the pressure measurement points, while the pressure curves of the pressure measurement points in the CGNT-CFD method are relatively smooth. The experimental values at the F4 measurement point show strong disorderliness, which proves that the pressure process at this point is strongly nonlinear. The CGNT-CFD method may need a smaller grid size and a shorter time step to simulate this process. With this grid size and time step, the simulation of the F4 measurement point by the CGNT-CFD method is poor. For the “spike” phenomenon, it may be caused by instability in measurement during experimentation or by using a larger time step during numerical simulation, resulting in inaccurate capture of smooth information. It is more likely that the grid and time used by the CGNT-CFD method cannot accurately capture changes at measurement points. As the height of the measurement points decreases, the force on them also increases. The reason why the amplitude of the experimental results differs greatly from that of the simulation results of the CGNT-CFD method may be due to a smaller peak value of waves in numerical simulation compared to experiments.

Next, a load condition with a medium wave height is selected as a typical load condition for comparison between numerical simulation and numerical wave tank experiments. Fig 5.12 shows the comparison between the numerical solution and experimental wave height under load condition A5.

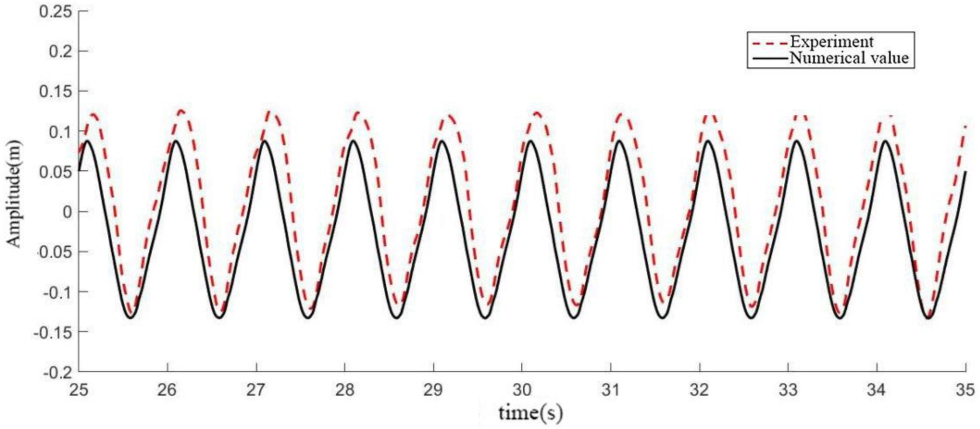

Fig 5.12. Comparison chart of numerical solution and experimental wave height under load condition A5

As shown in Fig 5.12, the simulation results of the CGNT-CFD method for waves closely match the experimental results in terms of waveform and period. However, the agreement between the amplitude of the experimental results and the simulation results of the CGNT-CFD method is not as good. The simulated values of both troughs are relatively close to the experimental values, but there is a significant difference between the simulated values of both peaks and the experimental values. During numerical simulation, the effect of the platform on the flow field results in a smaller peak value in the simulation process.

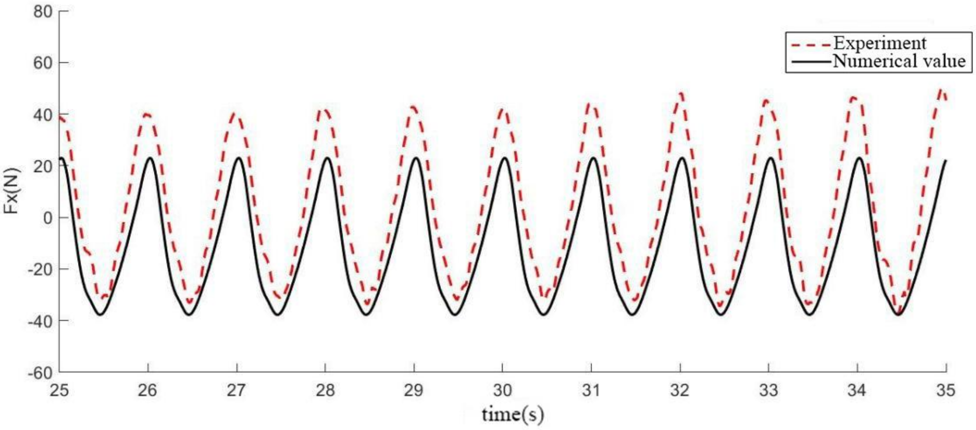

(a) Fx

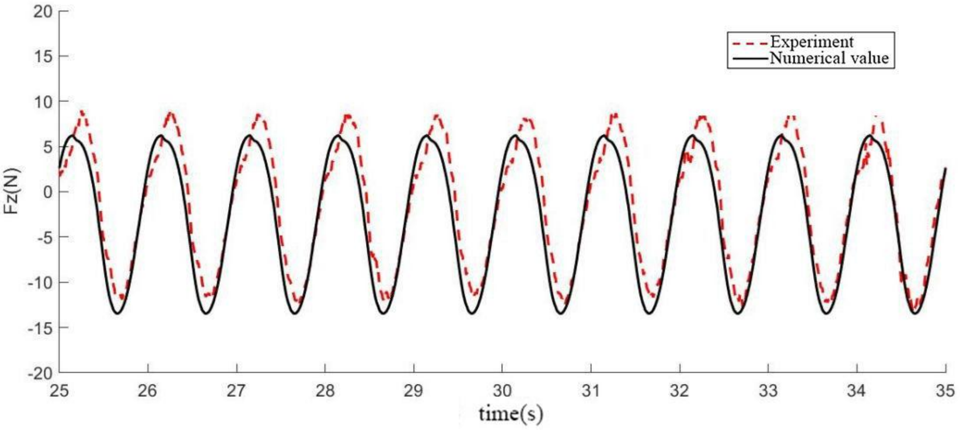

(b) Fz

Fig 5.13. Comparison chart of overall force between numerical solution and experimental values under load condition A5

As shown in the Fig 5.13, the simulation results of the overall force on the platform by the CGNT-CFD method closely match the experimental results in terms of waveform, period, and peak value. The significant difference between the amplitude of the experimental results and that of the simulation results of the CGNT-CFD method may be due to a smaller peak value of waves in numerical simulation compared to experiments.

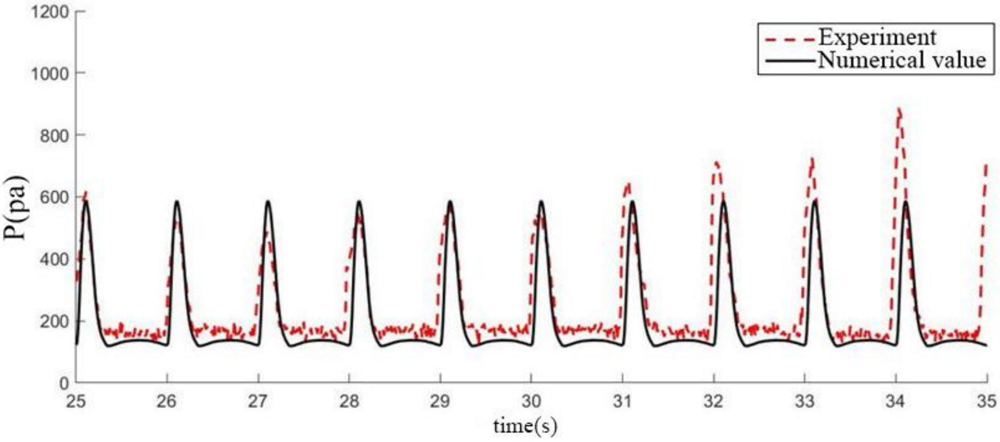

(a) Change in pressure over time at point F4

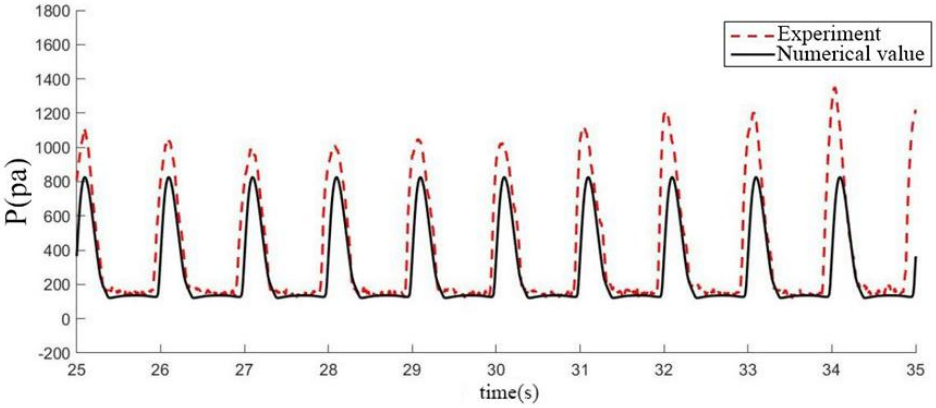

(b) Change in pressure over time at point F5

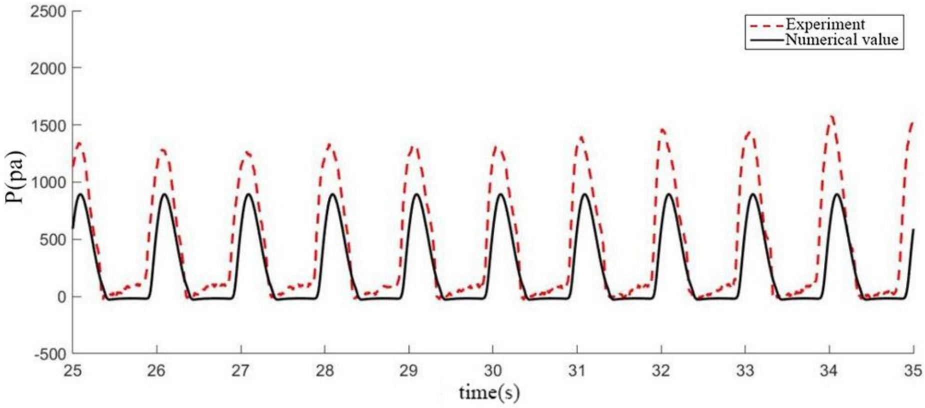

(c) Change in pressure over time at point F6

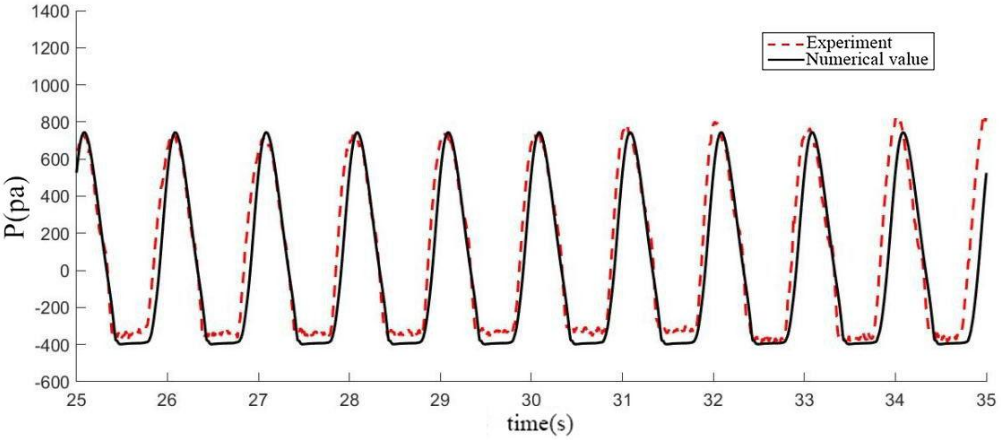

(d) Change in pressure over time at point F7

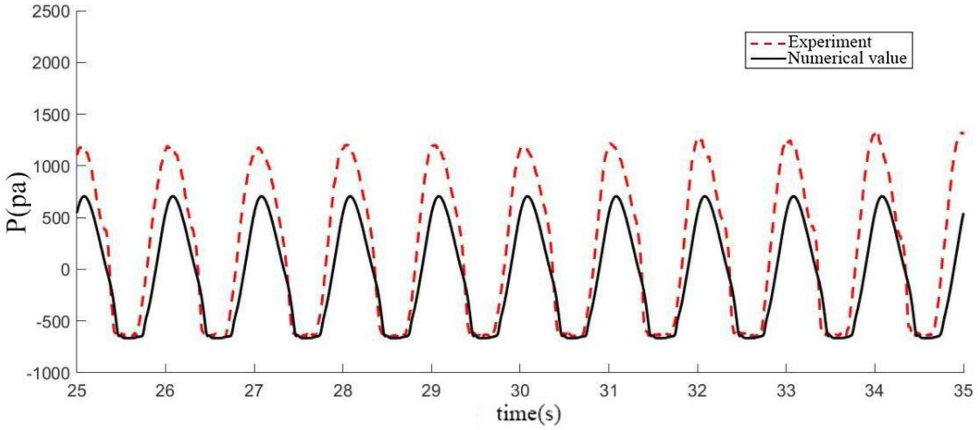

(e) Change in pressure over time at point F8

Fig 5.14. Comparison chart of pressure at measurement points between numerical solution and experimental values under load condition A5

From Fig 5.14, the simulation results of the pressure measurement point in the CGNT-CFD method closely match the experimental results in terms of waveform and period. However, the amplitude of the experimental results is larger than that of the simulation results of the CGNT-CFD method. The experimental results capture “burrs/noise” in the pressure at the pressure measurement points, while the pressure curves of the pressure measurement points in the CGNT-CFD method are relatively smooth. The significant difference between the amplitude of the experimental results and that of the simulation results of the CGNT-CFD method may be due to a smaller peak value of waves in numerical simulation compared to experiments. The reason for the “spike” phenomenon is consistent with the above reasons. Additionally, Fig 5.14 shows that as the height of the measurement points decreases, the force on them also increases.

Lastly, a load condition with a large wave height is selected as a representative case for comparing numerical simulations with numerical wave tank experiments. Fig 5-15 illustrates the comparison between the numerical solution and experimental wave height under load condition A8.

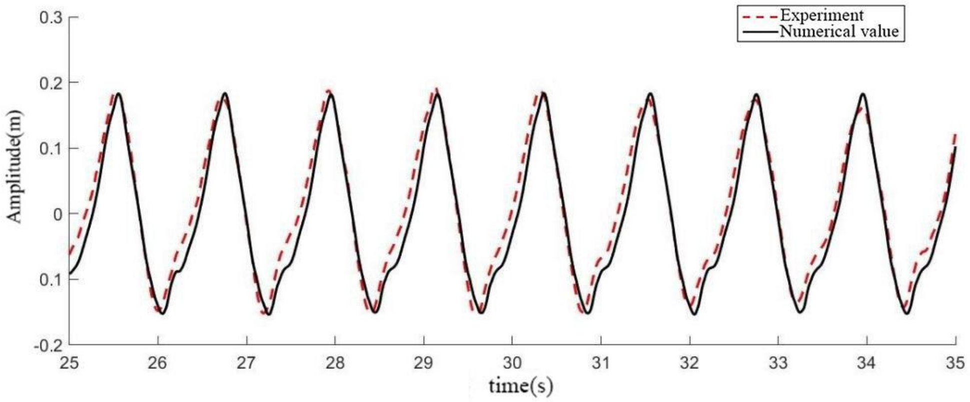

Fig 5.15. Comparison chart of numerical solution and experimental wave height under load condition A8

In the Fig 5.15 , the simulation results of the CGNT-CFD method for waves closely match the experimental results in terms of waveform and period. However, the agreement between the amplitude of the experimental results and the simulation results of the CGNT-CFD method is not as good. The simulated values of both troughs are relatively close to the experimental values, but there is a significant difference between the simulated values of both peaks and the experimental values. This discrepancy may be due to interference from the platform with the fluid during simulation, resulting in a lower amplitude of simulated waves.

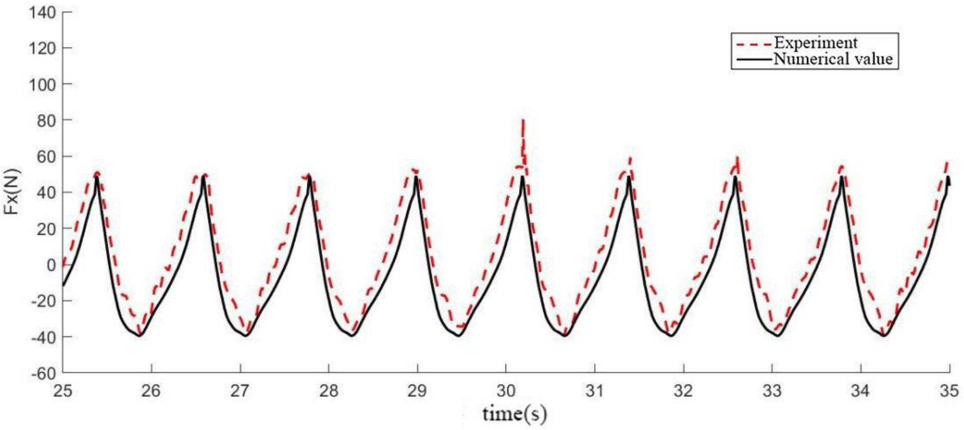

(f) Fx

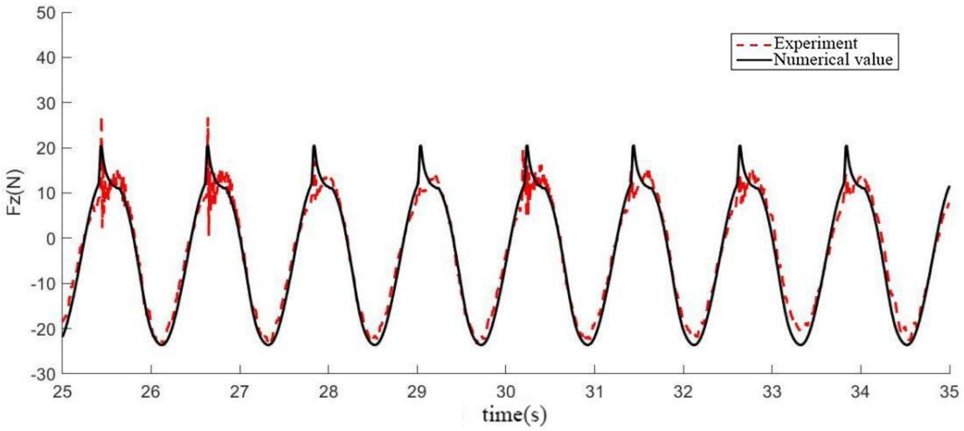

(g) Fz

Fig 5.16. Comparison chart of overall force between numerical solution and experimental value under A8 load condition

From Fig 5.16, it can be observed that the overall force simulation results of the numerical flume for the platform are consistent with the experimental results in terms of waveform and period. However, there is a significant difference between the amplitude of the experimental results and the simulation results of the numerical flume. The experimental results show “burrs/noise” in the overall force, while the pressure curve of the pressure measuring points in the numerical flume is relatively smooth. Fig 5.16 (g) shows that a secondary peak value appears in the Z direction in the experimental value, while no secondary peak appears in the simulation result of the numerical flume. The absence of a secondary peak value in the simulation result may be due to the proximity of the peak values, which prevents accurate capture by the numerical flume. The large difference between the amplitude of the experimental results and that of the simulation results of the numerical flume may be attributed to a smaller wave peak value in the numerical simulation compared to that of the experimental peak value.

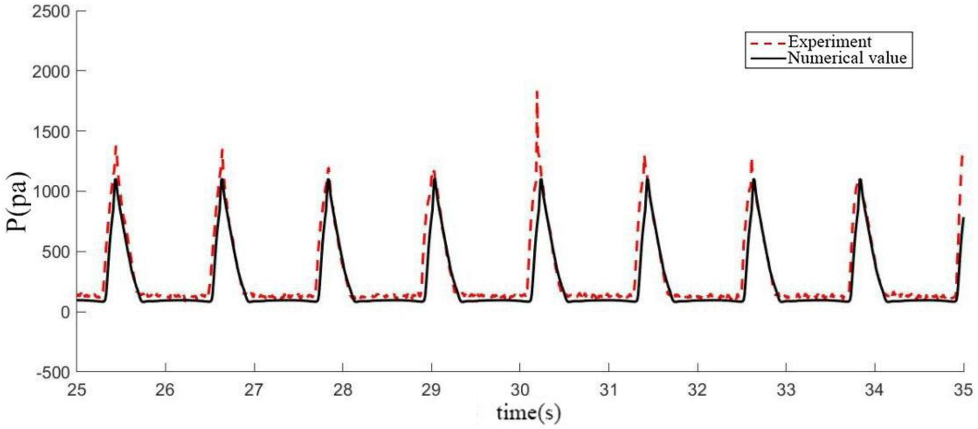

(a) Change in pressure at point F4 over time

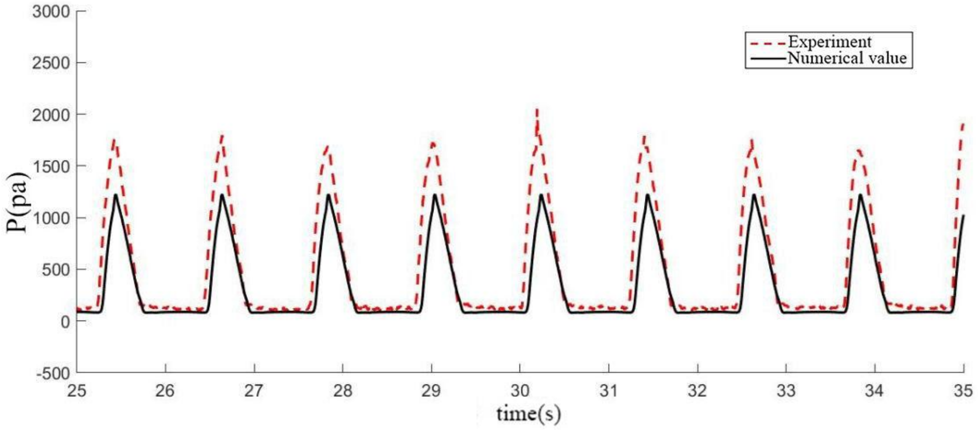

(b) Change in pressure over time at point F5

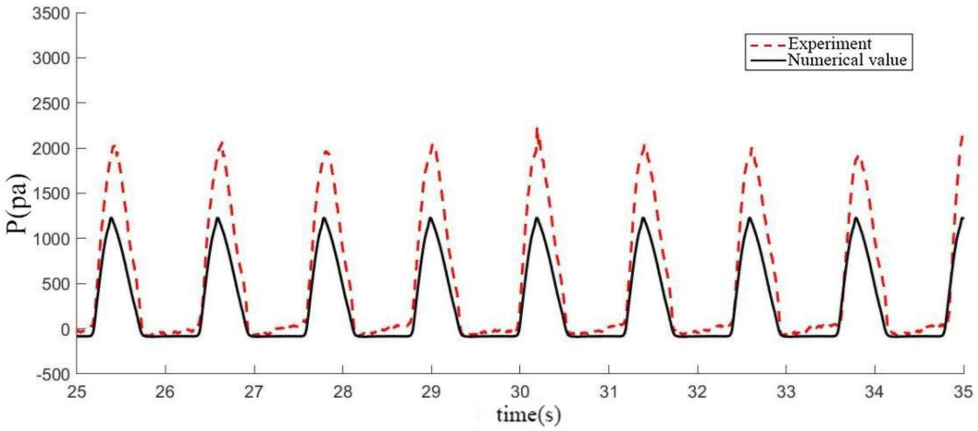

(c) Change in pressure over time at point F6

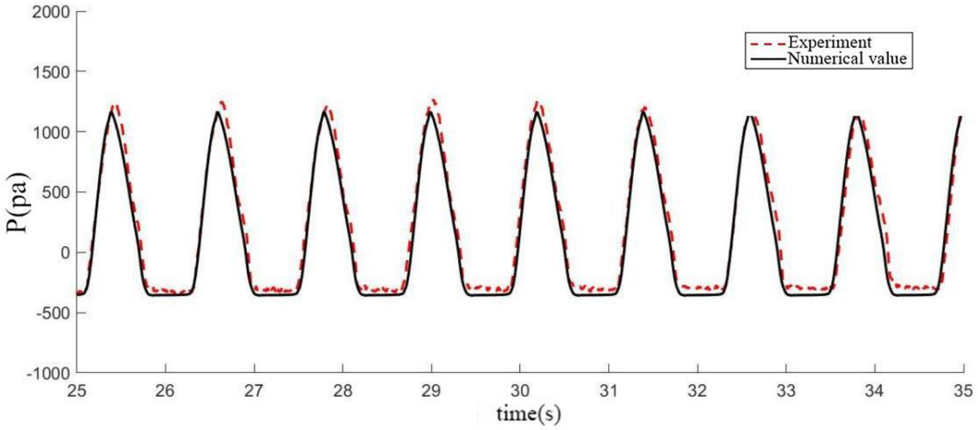

(d) Change in pressure over time at point F7

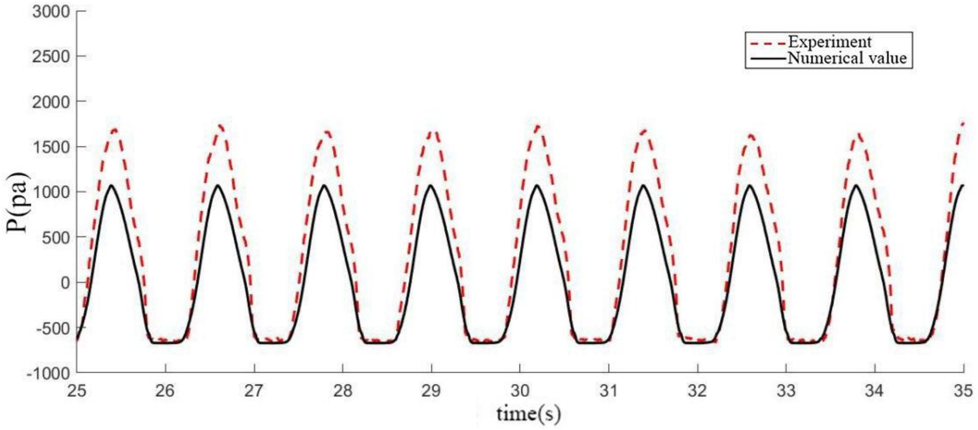

(e) Change in pressure over time at point F8

Fig 5.17. Comparison chart of pressure at measuring points between numerical solution and experimental value under load condition A8

From Fig 5.17, it can be observed that the simulation results of the pressure measuring points in the numerical flume are consistent with the experimental results in terms of waveform and period. However, the amplitude of the experimental results is larger than that of the simulation results of the numerical flume. The experimental results show “burrs/noise” in the pressure at the pressure measuring points, while the pressure curve of the pressure measuring points in the numerical wave tank is relatively smooth. The “burrs/noise” phenomenon may be due to the inability of the grid and time used by the numerical flume to accurately capture changes at the measuring points. As the height of the measuring points decreases, the force on them increases. The large difference between the amplitude of the experimental results and that of the simulation results of the numerical flume may be attributed to a smaller wave peak value in the numerical simulation compared to that of the experimental peak value.

For small wave height tank experiments A1, A2, and A3, the wave height simulated by the numerical flume is between 82.69%-86.22% of that of flume experiments. Due to wave height influence, its force on pressure measuring points is only between 78.68%-90.12%, and overall force is between 71.64%-87.22%. The wave height created by small wave height tank experiments is greater than expected value, causing feedback values on platform to be larger and making numerical simulation results about 20% smaller than tank results.

For medium wave height flume experiments A4, A5, and A6, wave height simulated by numerical flume is between 100.43%-108.38% of that of flume experiments. The simulation effect of wave height is good and its force on pressure measuring points is between 86.53%-103.16% of that in flume experiments. As height of measuring points decreases, accuracy of simulation improves and overall force is between

88.73%-100.75%. Numerical simulation for medium wave height flume experiments is significantly better than that for small wave height flume experiments.

For large wave height flume experiments A7, A8, and A9, results are similar to those for medium wave height flume experiments. Wave height simulated by numerical wave tank is between 101.25%-103.82% of that in flume experiments and simulation effect of wave height is good. Its force on pressure measuring points is between 79.91%-104.15% of that in flume experiments and as height of measuring points decreases, accuracy of simulation improves and overall force is between 102.46%-111.47% of that in flume experiments.

Numerical simulation for medium wave height flume experiments is better than that for large wave height flume experiments and both are significantly better than that for small wave height flume experiments.

In summary, the CGNT-CFD numerical wave tank demonstrates stable performance in reproducing wave periods and wave profiles, and it is capable of accurately simulating the load responses of floating platforms under various sea states. The model shows particularly high accuracy in predicting wave heights and localized pressures under moderate to high wave conditions. The numerically simulated wave heights generally align well with those observed in physical experiments, with overall discrepancies within ±10%. The total load responses of the platform also exhibit good agreement with experimental trends, especially at lower sensor positions, where pressure predictions closely match measured values.

However, under small wave height conditions, the CGNT-CFD method tends to underestimate wave heights compared to experimental results (by approximately 13%–17%), leading to lower predicted local pressures and total loads, with errors exceeding 20% in some cases. This discrepancy may stem from experimental wave amplitudes exceeding the target values, as well as limited accuracy in the numerical model's energy input and wave growth control under small wave conditions.

Additionally, while the numerically simulated pressure curves are relatively smooth, the experimental results often display “spikes” or high-frequency fluctuations. These features reflect the presence of local disturbances or transient pulses in the physical tests, which the current mesh resolution and time-step settings in the numerical model may not be sufficient to capture. As a result, local peak pressures may be filtered out in the simulation, leading to underestimation.

5.5 Summary of this chapter

Under regular wave conditions, a typical case with an air gap of 185 mm and a wave heading of 180° is selected for numerical analysis. The following conclusions are obtained:

1. This chapter uses a CGNT-CFD three-dimensional rectangular grid numerical flume to study the wave pressure and wave force characteristics of a single column under different regular waves. By comparing model experimental data, the accuracy of wave generation by the numerical flume solver is verified. The numerical flume can accurately predict the wave load and wave force of a single column with an error of less than 4%. In addition, the numerical flume can accurately capture nonlinear phenomena such as secondary wave peaks of wave force.

2. This chapter compares two methods (CGNT-CFD and STAR-CCM+) for simulating a single slamming event . The predicted wave slamming results closely match the experimental values.. The CGNT-CFD method is based on a Cartesian grid approach, which features simple mesh generation. This method enables accurate computations with fewer grid cells, resulting in a improvement in computational efficiency. This method solves N-S equations in single thread and can be simulated on ordinary computers with low computational cost.

3. The CGNT-CFD method demonstrates excellent free surface capturing capability. It is developed based on the Constrained Interpolation Profile (CIP) theory and incorporates the high-resolution THINC/SW interface reconstruction scheme,

enabling accurate representation of complex free surface evolution processes such as wave run-up and overturning while maintaining interface sharpness. Numerical simulations and comparative analyses of the complete wave run-up process validate the high accuracy and engineering applicability of this method in modeling free surface dynamics. In contrast, conventional CFD software typically employs the Volume of Fluid (VOF) approach with the High Resolution Interface Capturing (HRIC) scheme to track the free surface, which tends to suffer from interface diffusion and energy loss during severe surface deformation, thereby reducing local predictive accuracy. Overall, CGNT-CFD exhibits superior accuracy and numerical stability in handling free surface flows, making it well-suited for simulating nonlinear, strongly coupled problems such as wave-structure interactions.

4. For the application of the rectangular grid method to wave slamming calculations in the numerical flume, this chapter recommends the grid size and time step through convergence analysis. The rectangular grid strategy is used for the core area next to the floating body in the numerical simulation of wave slamming. 1/160 of the wavelength is chosen as the unit length in the X direction, 1/16 of the wave height is chosen as the unit length in the Z direction, and the unit length in the Y direction can be adjusted appropriately based on the X direction. However, it is particularly worth noting that wave height data has a great impact on accuracy of numerical simulation. After determining calculation conditions in engineering, it is recommended to refer to wave height to set grid refinement location. This can keep the target physical quantities (wave climbing height, slamming force, etc.) within a certain prediction accuracy range and capture nonlinear phenomena better.

6 SENSITIVITY ANALYSIS OF WAVE SLAMMING LOADS TO KEY PHYSICAL PARAMETERS

Building upon the previously established and validated numerical model, further analysis of the influence of platform structural parameters on wave slamming is a critical step toward achieving structural optimization. In this chapter, the developed CGNT-CFD method is employed to simulate a wide range of cases encompassing the geometric characteristics of the column-based platform (including column shape, size, and relative deck position), environmental variables (air gap height and wave heading angle), wave parameters (wave height, period, etc.), and multi-column arrangements (column spacing). The objective is to comprehensively investigate the influence of these factors on the spatial distribution of slamming loads, pressure time histories, and peak responses. Through sensitivity analysis and simulations of 153 cases, structural configurations prone to slamming load concentration are identified, and potential design strategies for mitigating impact risks are explored, thereby enhancing the platform's safety performance under extreme sea conditions.

6.1 Mechanisms of slamming load distribution induced by single-column platform geometry

6.1.1 Assessment of coupling effects between tank wall interference and wave slamming

6.1.1.1 Introduction of the load condition

For numerical simulations, choosing an appropriate calculation domain size can reduce the number of grids and provide computational efficiency. However, the calculation domain cannot be reduced infinitely. A too small calculation domain will result in poor wake capture and wave absorption effects. Additionally, wave reflection can interfere with the results. In this section, 18 wave slamming cases for a single column are analyzed. All cases share a unified air gap of 185 mm (with the still water level referenced in Fig. 4.1) and a wave heading angle of 180°. The column shape is square with characteristic dimensions of 180 mm × 180 mm. The characteristic widths of the platform tank walls are set to 1500 mm and 2000 mm, respectively. A total of nine wave conditions (R1–R9) are considered to assess the influence of finite tank boundaries on wave propagation and load response. Table 6.1 summarizes the case settings for tank wall width in the numerical wave tank.

Table 6.1 Numerical Wave Tank Wall Width Configuration

No.	Tank Wall Width	Wave No.	H (cm)	T (s)
Case1	1500mm	R1	10.22	0.8
Case2		R2	11.48	0.8
Case3		R3	12.81	0.8
Case4		R4	15.81	1
Case5		R5	17.73	1
Case6		R6	19.74	1
Case7		R7	22.28	1.2
Case8		R8	24.95	1.2
Case9		R9	27.73	1.2
Case10	2000mm	R1	10.22	0.8
Case11		R2	11.48	0.8
Case12		R3	12.81	0.8
Case13		R4	15.81	1
Case14		R5	17.73	1
Case15		R6	19.74	1

Case16		R7	22.28	1.2
Case17		R8	24.95	1.2
Case18		R9	27.73	1.2

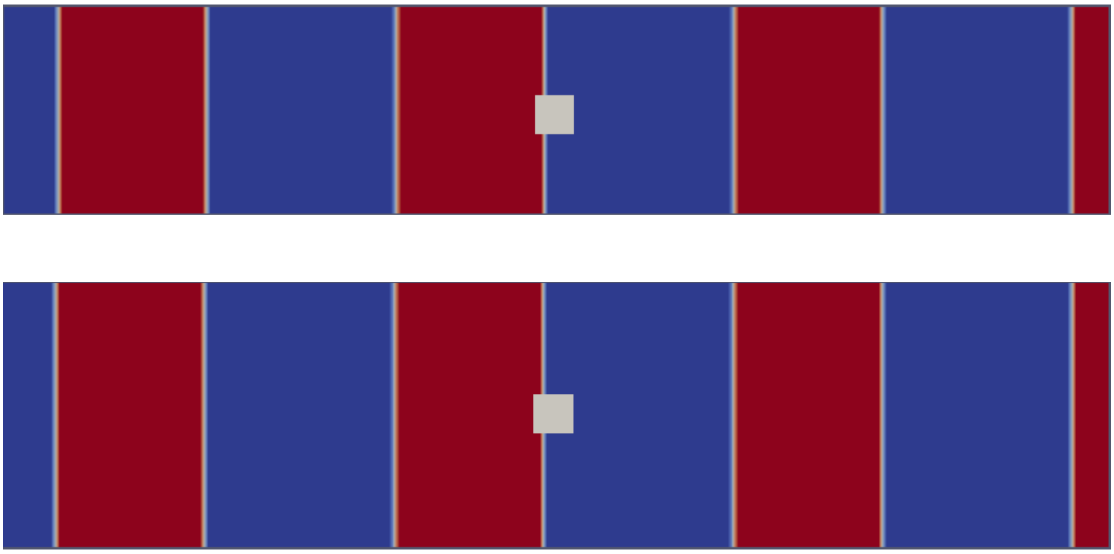

Fig 6.1. W_1.5m (top) W_2.0m (bottom)

6.1.1.2 Simulation results

As shown in Fig 6.2, the CGNT-CFD method simulates the wave environment with consistent wave periods and troughs under different flume wall widths. The wave period and trough amplitude remain consistent under all width conditions. At the wave crest, the tank with a width of 2000 mm exhibits a slightly higher peak compared to the 1500 mm case, indicating that the effect of tank width on wave propagation is minimal. The location of the virtual wave gauge is 245 mm away from the slamming face of the column, corresponding to the position of the outermost resistance-type wave gauge in the physical experiments.

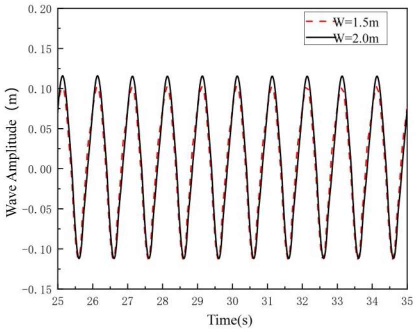

Fig 6.2. Comparison of wave height under regular wave R4 load condition (180° wave heading, 185 mm air gap, W3)

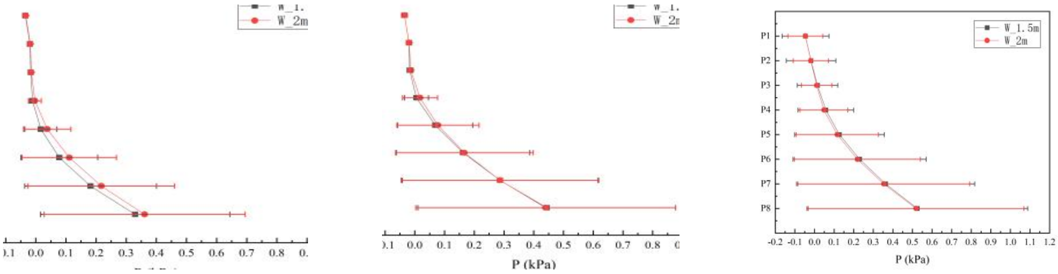

(a)R3 (b)R6 (c)R9

Fig 6.3. Comparison analysis chart of force on measuring points under different regular wave conditions（R3/R6/R9）

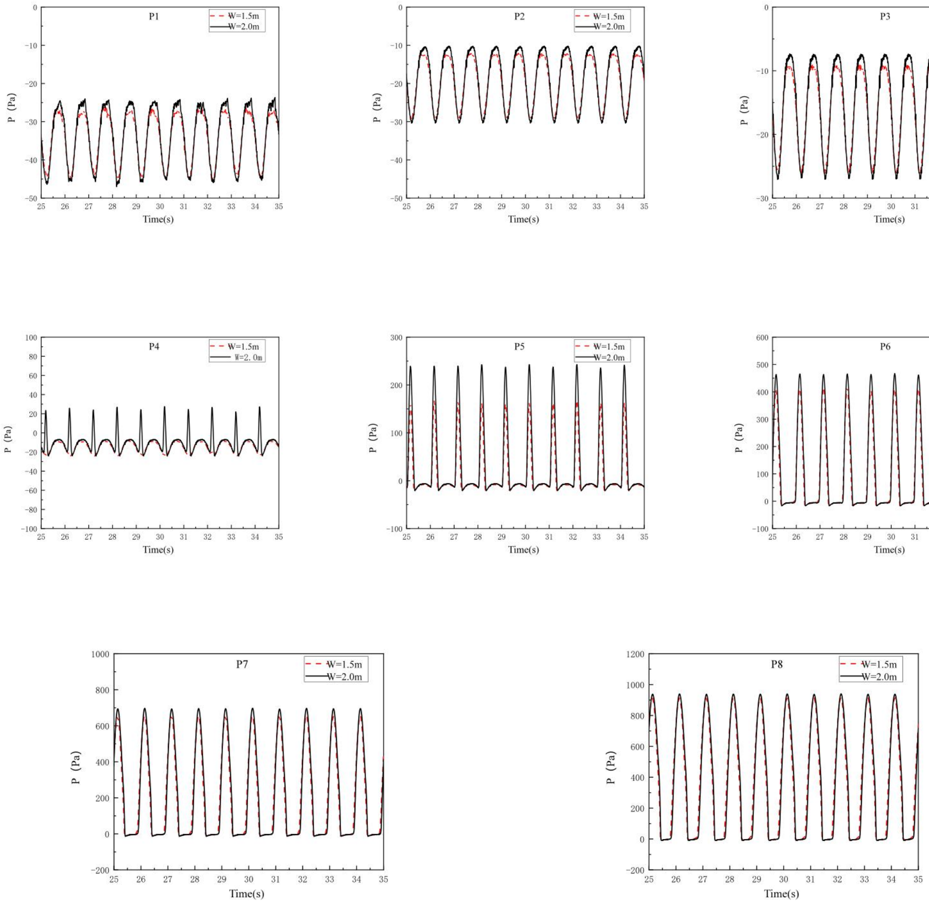

Fig 6.4. Comparison chart of force on measuring points (F1~F8) under regular wave R4 load condition

Fig 6.3 presents a comparative analysis of the pressures at each measuring point (F1~F8) under different regular wave conditions, with the specific locations of measuring points P1 – P8 given in Table 5.4. In the figure, each measuring point is subjected to periodic loading under the action of regular waves. The horizontal lines indicate the range of load fluctuations, while the colored solid dot in the middle represents the average load experienced by that point over the entire recording period.

Fig 6.4 shows the simulation results of different flume widths on the force of different measuring points on the platform. The force situation of different flume widths is more consistent in the waveform and the period of the results at the same measuring point. The pressure period is consistent with the wave period, and the impact load amplitude at the same wave condition and position measuring point differs very little between the two. As mentioned above, the wave height from the wave height gauge in the flume with a width of 1500mm is 20.83% lower than that in the flume with a width of 2000mm, so under the same wave conditions, the force at the same measuring point is greater in a water flume with a width of 2000mm than in the flume with a width of 1500mm. Regarding the negative pressure values observed at measurement points F1 to F4, the following explanation is provided. In the numerical simulation, the computed pressure values represent relative pressure, rather than absolute pressure. Specifically, the method involves calculating the average pressure of all computational grid points located in the air region above the free surface. The pressure at each point is then adjusted by subtracting this average value, yielding the relative pressure. As a result, in the air region, if a point's pressure is lower than the average, the corresponding relative pressure will appear as a negative value.

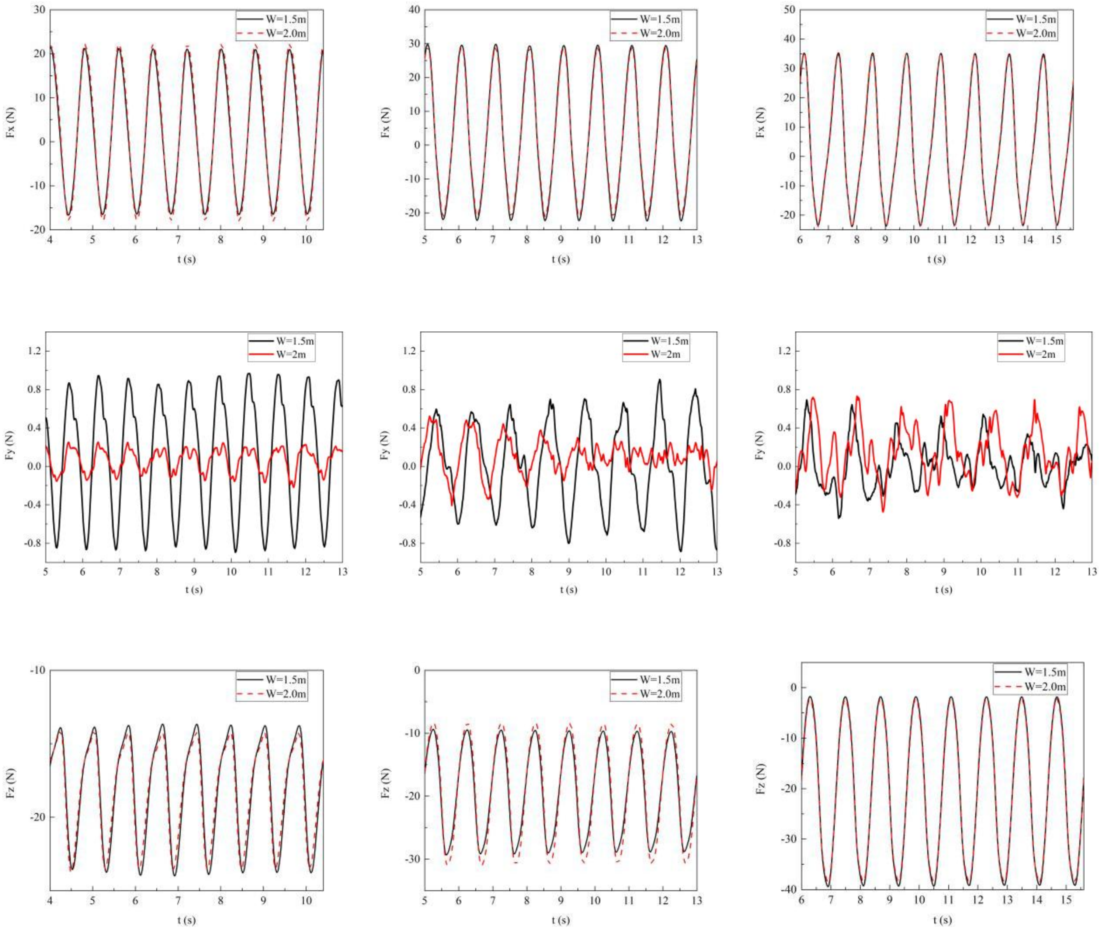

(a)R1 (b)R4 (c)R7

Fig 6.5. Overall force comparison chart

As shown in the Fig 6.5, the simulation results of the overall force of the platform by the numerical water flume are different for different flume widths. The results in the *X* and *Z* directions are relatively consistent, and the error between the two is less than 4%. The force in the *Y* direction is significantly different between the two, with a difference of 75.9% at one point, and there is a large fluctuation in the numerical value. With the increase of wave height, the amplitude of force on both will tend to be similar. In this study, the platform is primarily subjected to wave loads in the X-direction (wave-propagation direction) and Z-direction (vertical). The Y-direction, being transverse to the wave direction, theoretically does not bear significant direct wave-induced loads. As a result, the force response in the Y-direction is inherently small. However, despite the low magnitude of Y-direction forces, a certain degree of non-physical numerical fluctuation is observed, manifesting as minor oscillations. This fluctuation is not attributed to real physical phenomena (such as vortex shedding), but rather results from insufficient transverse recirculation space around the platform when the numerical wave tank has a limited width. This constraint causes disturbances near the side walls to reflect into the computational domain, thereby compromising the local pressure field stability. In summary,when the tank width is increased to 2000 mm, numerical fluctuations in the Y-direction are significantly reduced, and the overall numerical convergence and stability are notably improved. When calculating the overall force of the platform by numerical water flume force, it was found that the width of the water flume used in the CGNT-CFD numerical simulation has little effect on the overall force of the platform in the *XZ* direction and a greater impact on it in the *Y* direction.–The width of the wave flume was selected based on the characteristic length ratio of the column side length, with a value of 11.11 times (2000 mm / 180 mm), which meets the computational requirements.

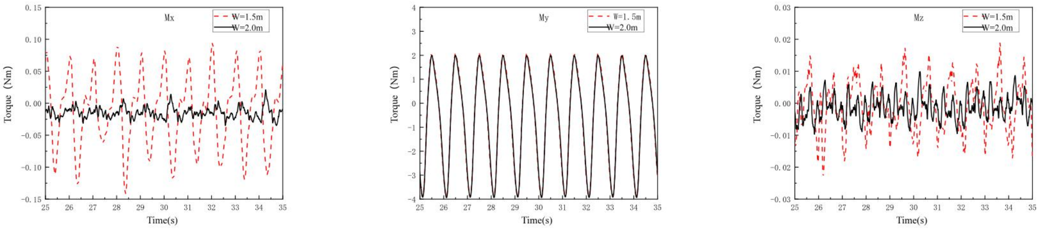

Fig 6.6. Overall force moment comparison chart under regular wave R4 load condition

Fig 6.6 shows that the numerical simulation results of the overall force of the platform under different flume widths are different for different measuring points. The width of the water flume used in this numerical simulation has a small effect on the overall force of the platform in the *XZ* direction. When calculating the force on the platform measuring points, the water flume width can be selected as 11.11 times of characteristic length to meet calculation requirements.

6.1.1.3 ~~Discussion of results~~ Conclusion

In summary, under different basin widths, the waveforms and periods of platform forces, moments, and slamming loads remain generally consistent, with these periods matching the wave periods. Basin width has little effect on the platform’s overall forces in the X and Z directions but has a greater impact in the Y direction. For the same wave conditions, the influence on a given measurement point is smaller when the basin width is 2000 mm compared with 1500 mm, and selecting a basin width equal to 11.11 times the characteristic length (column width) (2000/180) is sufficient to meet computational requirements. Since the force in the translational direction of the column is much greater than that in the rotational direction in the simulation, this thesis does not analyze the moment and force in the Y direction. The water flume width selected in this simulation is 2000mm.

6.1.2 Effect of column shape on wave run-up and pressure concentration

6.1.2.1 Introduction of the load condition

The column of the platform is always in a fluid environment and will be affected by waves no matter how small the wave height is. Usually, the column shape of the platform is in three states: circular, square, and square with chamfer. In this section, the sensitivity analysis of the column shape will be carried out. The length characteristic of the column selected for analysis in this section is 180mm. The square and cylinder column shapes are selected for numerical simulation in this section. Specifically, the side length of the square column section is 180mm and the cylinder column section has a diameter of 180mm, as shown in Fig 6.7.

In this section, 18 wave slamming cases for a single column are designed, all using a consistent air gap of 185 mm and a wave heading of 180°. Two typical column cross-sectional shapes—square and circular—are selected, both with a characteristic dimension of 180 mm to facilitate comparison of the effects of geometric shape on slamming response (as shown in Fig. 6.7). Wave conditions R1 to R9 are adopted, resulting in a total of 18 simulation cases. The specific case settings are listed in Table 6.2.

Table 6.2 Column Cross-section Simulation Cases

No.	Cross-sectional shape	Wave No.	*H* (cm)	*T* (s)
Case1	Square	R1	10.22	0.8
Case2		R2	11.48	0.8
Case3		R3	12.81	0.8
Case4		R4	15.81	1
Case5		R5	17.73	1
Case6		R6	19.74	1
Case7		R7	22.28	1.2
Case8		R8	24.95	1.2
Case9		R9	27.73	1.2
Case10	Circular	R1	10.22	0.8
Case11		R2	11.48	0.8
Case12		R3	12.81	0.8
Case13		R4	15.81	1
Case14		R5	17.73	1
Case15		R6	19.74	1
Case16		R7	22.28	1.2
Case17		R8	24.95	1.2
Case18		R9	27.73	1.2

(a)square column (b)cylinder

Fig 6.7. Schematic diagram of different column shapes

6.1.2.2 Simulation results

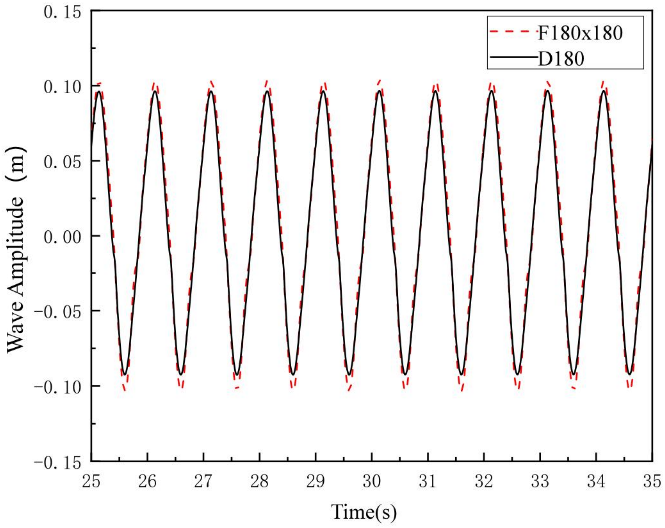

Fig 6.8. Comparison and analysis chart of wave simulationunder regular wave R4 load condition (180° wave heading, 185 mm air gap)

From Fig 6.8, it is observed that the numerical water flume has a wave environment that is basically the same for both the square and the cylinder columns. The slight differences in numerical values produced by different wave gauges are due to the fact that the column is in a flow field and its shape affects the propagation of flow field waves. To illustrate this difference, the average slamming load and its standard deviation of each regular wave sequence generated at different monitoring points of the structure and at different positions are also given in the Fig 6.8.

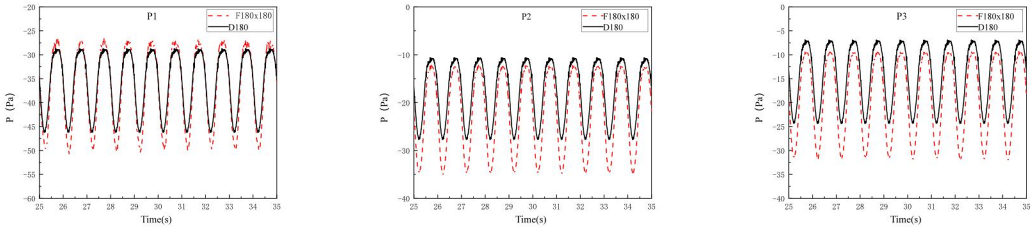

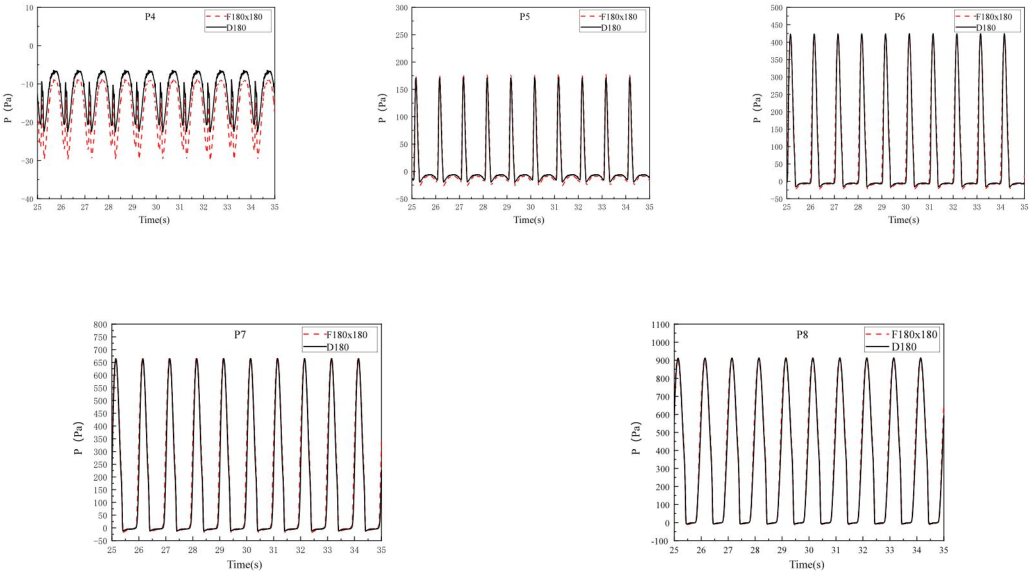

Fig 6.9. Comparison and analysis chart of load at measuring points under regular wave R4 load condition

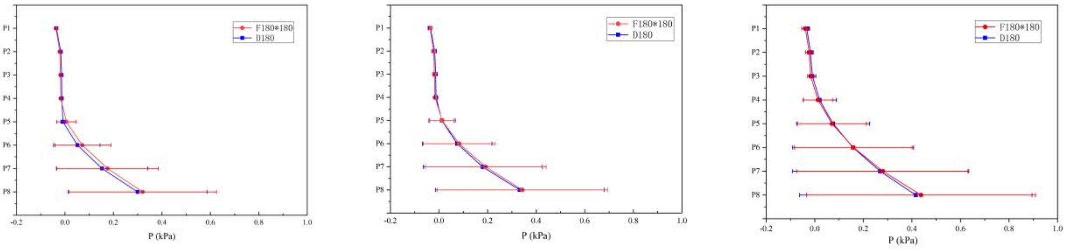

(a)R1 (b)R4 (c)R7

Fig 6.10. Comparison and analysis chart of force at measuring points under different regular wave conditions

Fig 6.10 shows the simulation results of the force on different measuring points of the platform in the numerical water flume. The locations of measurement points P1~P8 are shown in Table 5.4. The force situation of the square and cylindrical columns is more consistent with the waveform and period of the results at the same measuring point. The period is consistent with the wave period. At measuring points 1, 2, 3, and 4 above the column, the negative pressure of the square column is greater than that of the cylinder column by 30% to 50%. This is because compared with the square column, when waves hit the cylinder column, its surface structure is more conducive to the climbing water's descending, and the fluid velocity is faster, making it difficult to form a vacuum and cause negative pressure.

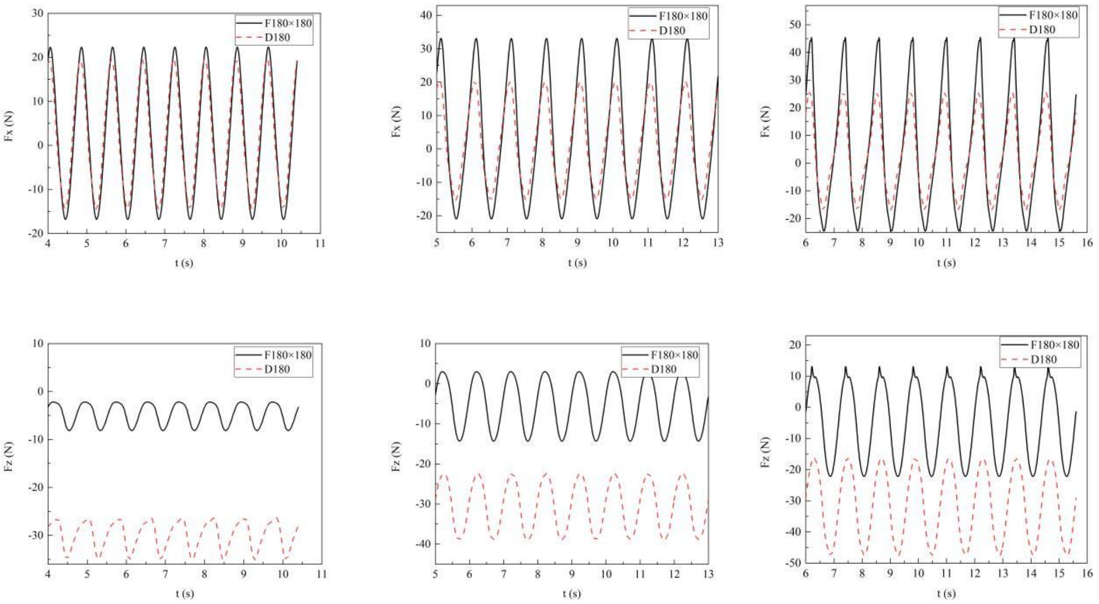

(a)R1 (b)R4 (c)R7

Fig 6.11. Comparison chart of overall force in time domain

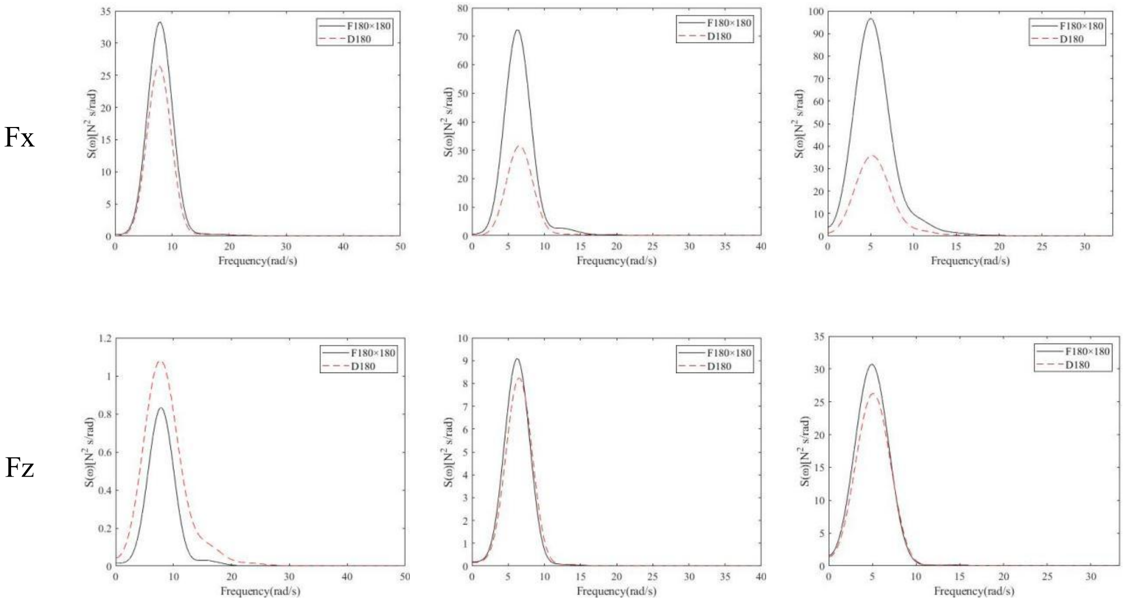

(a)R1 (b)R4 (c)R7

Fig 6.12. Comparison chart of overall force in frequency domain

At monitoring points 6, 7, and 8, the slamming load amplitude of the square column is 2% to 5% higher than that of the cylinder column measuring point. This may be due to the fact that the square structure causes more water to stay on the windward side.

According to the time-domain graph Fig 6.11, the simulation results show that the force on the square and cylindrical columns is more consistent with the waveform and wave period of the results at the same measuring point in the X and Z directions. In the X direction, the force on the square column is 15.79% to 80% greater than that on the cylinder column, while in the Z direction, the negative peak pressure on the cylinder column is 150% to 337.5% greater than that on the square column.

According to the frequency-domain graph Fig 6.12, there is a great correlation between slamming load and wave characteristics for both X and Z directions. The peak frequency of the spectrum is equal to that of the incident wave frequency, indicating that its force is mainly caused by wave slamming.

A horizontal comparison among the R1, R4, and R7 cases with different wave heights shows that as the wave height and period increase, the wave-induced kinetic energy and nonlinear characteristics become more pronounced. Consequently, the interaction between waves and the platform intensifies, and the influence of wave tank boundary reflections or disturbances on the force response becomes more significant. Therefore, under conditions of large wave height and long period, a greater wave tank width is required to ensure the accuracy and stability of the numerical simulation results.

By comparing the overall force situation of different shapes of platforms, it is found that the force on square columns is greater than that on cylinder columns. This is because under the same wave conditions, square columns with the same characteristic size have a larger wave climb than cylinder columns. When an incident wave encounters a platform column, water will be divided into three parts. One part of water will continue to climb along the column upwardly, while the other two parts of water will flow away along both sides of the column. The two sides of square columns are less smooth than those of cylinder columns, so more water stays on their windward surface and less water flows away from both sides. Therefore, square columns have higher wave climb on their windward surface than cylinder columns. On the other hand, due to its smooth surface structure, more water flows away from both sides of cylinder columns and less water stays on their windward surface. This leads to lower wave climb on their windward surface than square columns.

6.1.2.3 Conclusion

Overall, the comparison shows that square-section columns and cylindrical columns (with a diameter equal to the side length of the square column section) exhibit similar waveforms and periods for pressures at each measurement point as well as for the overall slamming loads in the X and Z directions, with these periods matching the incident wave period. However, pressures on the square column are higher than those on the cylindrical column: in the upper part of the column, values are 30%–50% greater, while in the lower part, slamming amplitudes are 2%–5% higher. The overall X-direction force on the platform follows the same pattern as wave run-up, with the square column platform experiencing greater wave action than the cylindrical column platform. In both the X and Z directions, the peak frequencies of the slamming load spectra match the incident wave frequency, indicating that the slamming loads are primarily induced by the incident waves.

6.1.3 Effect of column size on impact response magnitude

6.1.3.1 Introduction of the load condition

The shape and size of the columns of the three-sized platforms are important parameters that affect the force on the platform. In this section, a sensitivity analysis on column size is conducted. Square cross-section columns are uniformly used, and wave conditions R1 to R9 are selected. The characteristic dimensions are set to 150 mm × 150 mm, 180 mm × 180 mm, and 210 mm × 210 mm to evaluate the impact of scale variation on slamming response. All cases adopt a consistent air gap of 185 mm and a wave heading of 180° to ensure comparability. A total of 27 numerical cases are defined, as detailed in Table 6.3.

Table 6.3 Column Size Simulation Cases

No.	Column Size	Wave No.	H (cm)	T (s)
Case1	150mmx150 mm	R1	10.22	0.8
Case2		R2	11.48	0.8
Case3		R3	12.81	0.8
Case4		R4	15.81	1
Case5		R5	17.73	1
Case6		R6	19.74	1
Case7		R7	22.28	1.2
Case8		R8	24.95	1.2
Case9		R9	27.73	1.2
Case10	180mmx180 mm	R1	10.22	0.8
Case11		R2	11.48	0.8
Case12		R3	12.81	0.8
Case13		R4	15.81	1
Case14		R5	17.73	1
Case15		R6	19.74	1
Case16		R7	22.28	1.2
Case17		R8	24.95	1.2
Case18		R9	27.73	1.2
Case19	210mmx210 mm	R1	10.22	0.8
Case20		R2	11.48	0.8
Case21		R3	12.81	0.8
Case22		R4	15.81	1
Case23		R5	17.73	1
Case24		R6	19.74	1
Case25		R7	22.28	1.2
Case26		R8	24.95	1.2
Case27		R9	27.73	1.2

6.1.3.2 Simulation results

Taking the regular wave R4 with medium wave height as an example, the wave simulation results are as follows.

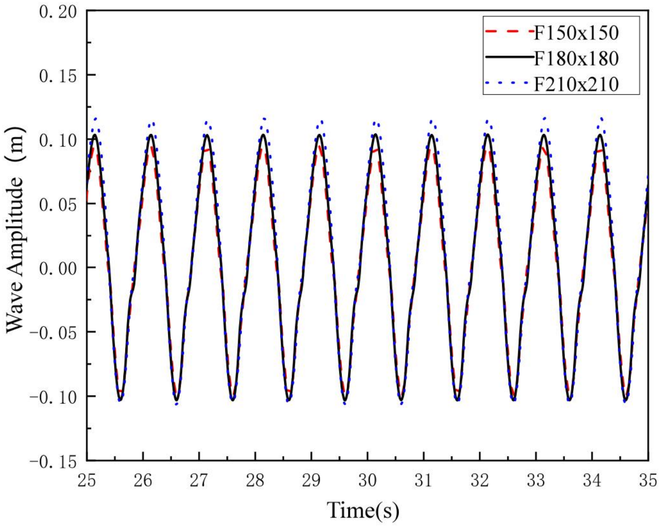

Fig 6.13. Comparison chart of wave height under regular wave R4 load condition

Based on the Fig 6.13, it can be observed that the CGNT-CFD method provides a consistent wave environment for wave simulation across all three cases. For instance, when taking the regular wave R4 with medium wave height as an example, the measured impact load results are as follows.

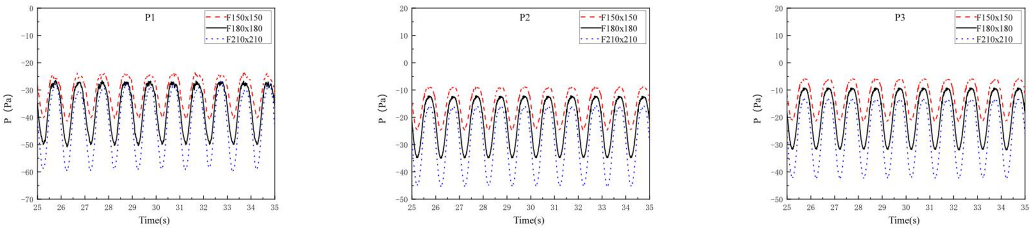

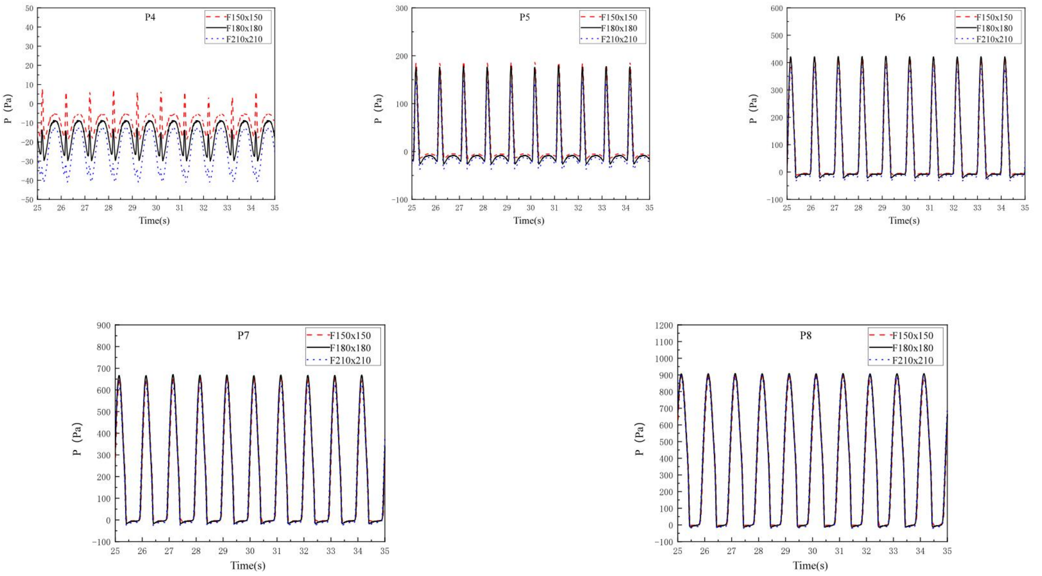

Fig 6.14. Comparison chart of force at measuring points

under regular wave R4 load condition

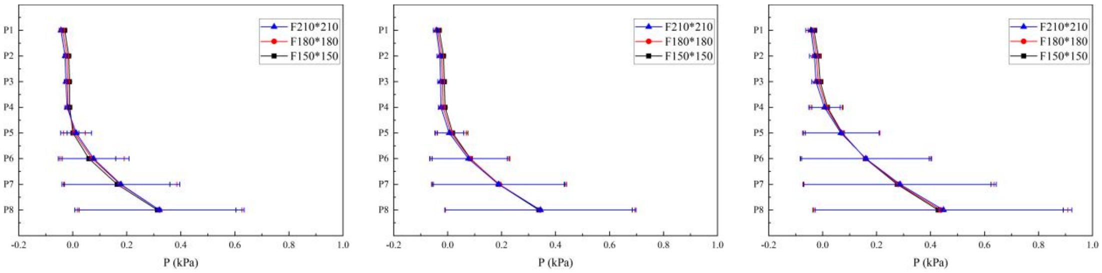

(a)R1 (b)R4 (c)R7

Fig 6.15. Comparison chart of force at measuring points under different regular wave conditions

From Fig 6.15, the CGNT-CFD method provides consistent waveforms for pressure simulation at the platform’s measuring points. The periods of the pressure in three cases are consistent with the wave period. At monitoring points 1-4 on the upper part of the column, the negative pressure on the column decreases from 210mmx210mm to 180mmx180mm and then to 150mmx150mm. This means that the larger the cross-sectional size of the platform, the greater the force on the measuring point. The negative pressure on 210mmx210mm is 52.5%~166.7% greater than that on

150mmx150mm. At the lower part of the square column, the difference in impact load is 4.12%~10.9%. The reason for this is that the larger the cross-sectional area of a column, the larger its interaction area with waves and platforms, and thus, its retention effect on waves is more significant. When incident waves encounter platform columns and move forward, water is divided into three parts: one part will continue to climb along columns; while two other parts flow along both sides of columns. The water in the middle of larger columns is less likely to flow away, resulting in more water staying on windward surfaces and generating greater negative pressure when it leaves.

As shown in Fig 6.16, measuring points experience a secondary increase in force. This is because when waves reach platform columns, they climb up and then fall due to gravity after reaching their maximum position. Since larger platforms have greater resistance to waves, they cause greater wave climbing and generate a second “slamming” when they fall due to gravity near water surface measuring points, resulting in greater slamming pressure.

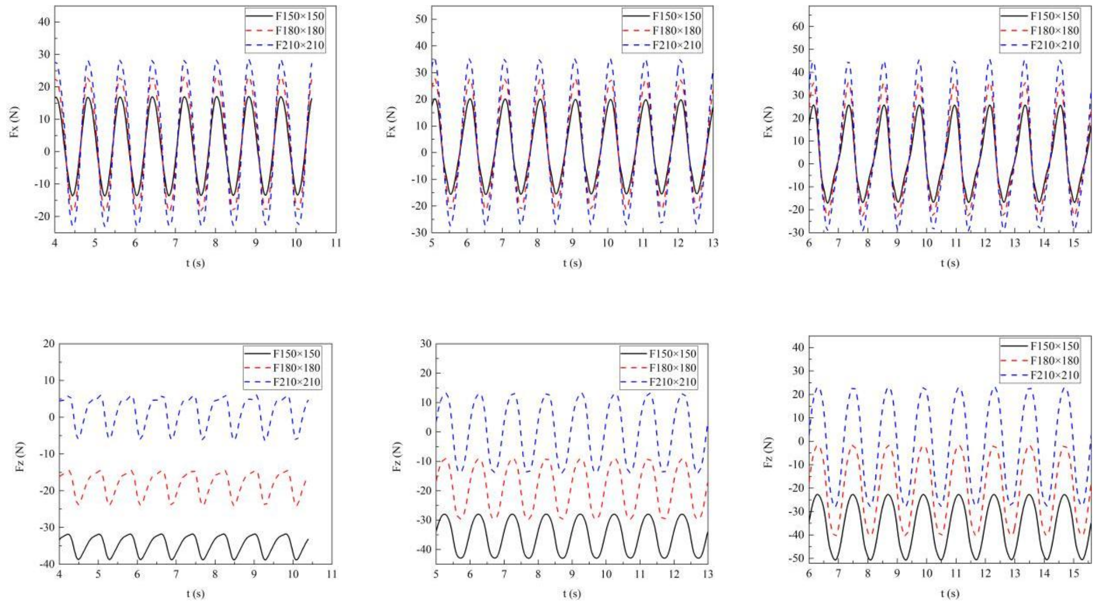

(a)R1 (b)R4 (c)R7

Fig 6.16. Comparison chart of force at measuring points under different sea conditions

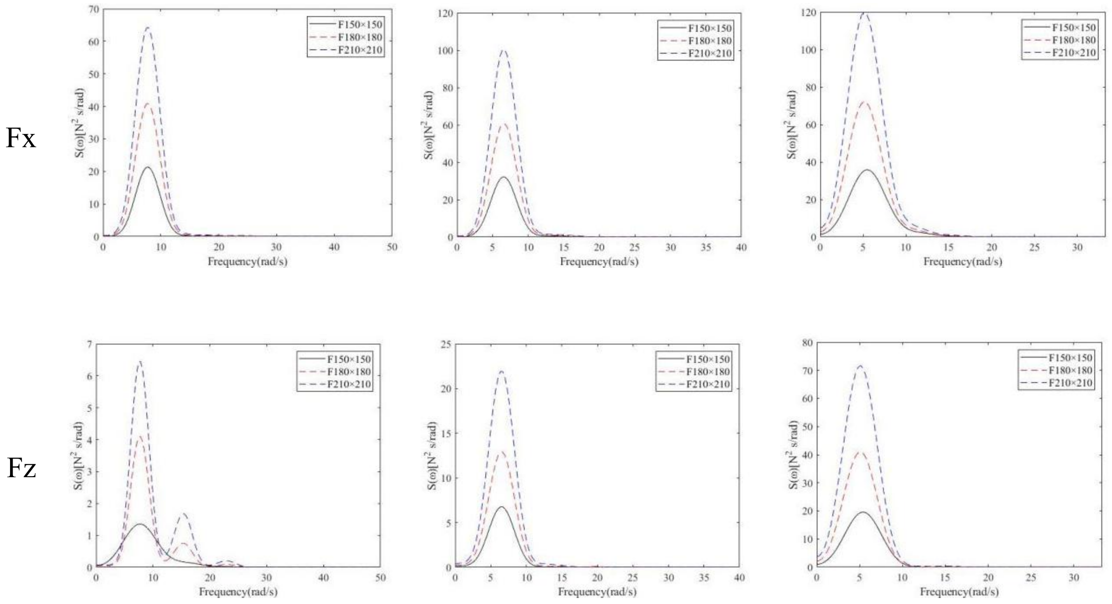

(a)R1 (b)R4 (c)R7

Fig 6.17. Comparison chart of force in frequency domain for the whole structure

From the time-domain graph, it is evident that the waveforms and periods of the X and Z directions of the squares with different sizes in the simulation results of the overall force of the platform in the numerical flume are relatively consistent, and the period is consistent with the wave period. In the X direction, the force decreases from 210mmx210mm to 180mmx180mm and then to 150mmx150mm. This means that the larger the cross-sectional size of the platform, the greater the force on the measuring point. The negative pressure on 210mmx210mm is 52.5%~166.7% greater than that on 150mmx150mm. In the Z direction, the negative forces from large to small are 150mmx150mm, 180mmx180mm, and 210mmx210mm. The negative force of 150mmx150mm is 234.9%~698.6% greater than that of 210mmx210mm. The reason for this is similar to that of slamming load mentioned earlier.

From the frequency-domain graph, it is observed that the peak frequency of force spectrum in X and Z directions is consistent with the incident wave frequency, indicating that its force is mainly caused by slamming from incident waves. In load condition R1, a secondary peak appears in Fz frequency spectrum analysis, and its peak frequency is twice that of wave frequency, indicating that at this time, waves have an effect on Z direction when they are superimposed. However, there was no obvious secondary peak phenomenon in other load conditions.

6.1.3.3 Conclusion

In summary, the pressure distribution across different measurement points, as well as the overall slamming loads on columns in the X and Z directions, exhibit similar waveforms and periods, with those periods matching the incident wave periods. Larger horizontal cross-sectional dimensions of the columns correspond to higher slamming pressure amplitudes at all measurement points, and also result in greater overall slamming loads on the platform in the X direction. The peak frequencies of the slamming load spectra in both X and Z directions align with the incident wave frequencies, indicating that the slamming loads are predominantly caused by the incident waves.

6.1.4 Effect of deck-column arrangement on local wave focusing and load superposition

6.1.4.1 Introduction of the load condition

For platforms subjected to large wave heights, slamming may occur on the underside of the deck. The relative position between the column and the deck plate can influence the wave slamming behavior. In this section, a sensitivity analysis is conducted on the relative position between the deck plate and the column. Square cross-section columns with characteristic dimensions of 180 mm × 180 mm are uniformly used. Three typical configurations are considered: the column located at the middle point of the side, at the vertex;, and at the center of the plate, as illustrated in Fig. 6.18. To eliminate the influence of other variables and highlight the effect of structural arrangement on wave slamming response, all cases adopt a consistent air gap of 185 mm and a wave heading of 180°, with wave conditions set from R1 to R9. A total of 27 simulation cases are defined in this section, as detailed in Table 6.4.

Table 6.4 CasesSettings for the Relative Position between Deck Plate and Column

No.	Deck-Column Arrangement	Wave No.	*H* (cm)	*T* (s)	*L* (m)
Case1	At the middle point of the side	R1	10.22	0.8	1.0754
Case2		R2	11.48	0.8	1.0934
Case3		R3	12.81	0.8	1.1135
Case4		R4	15.81	1	1.6637
Case5		R5	17.73	1	1.6882
Case6		R6	19.74	1	1.7160
Case7		R7	22.28	1.2	2.3456
Case8		R8	24.95	1.2	2.3759
Case9		R9	27.73	1.2	2.4106
Case10	At the vertex;	R1	10.22	0.8	1.0754
Case11		R2	11.48	0.8	1.0934
Case12		R3	12.81	0.8	1.1135
Case13		R4	15.81	1	1.6637
Case14		R5	17.73	1	1.6882
Case15		R6	19.74	1	1.7160
Case16		R7	22.28	1.2	2.3456
Case17		R8	24.95	1.2	2.3759
Case18		R9	27.73	1.2	2.4106
Case19	At the center.	R1	10.22	0.8	1.0754
Case20		R2	11.48	0.8	1.0934
Case21		R3	12.81	0.8	1.1135
Case22		R4	15.81	1	1.6637
Case23		R5	17.73	1	1.6882
Case24		R6	19.74	1	1.7160
Case25		R7	22.28	1.2	2.3456
Case26		R8	24.95	1.2	2.3759

Case27		R9	27.73	1.2	2.4106

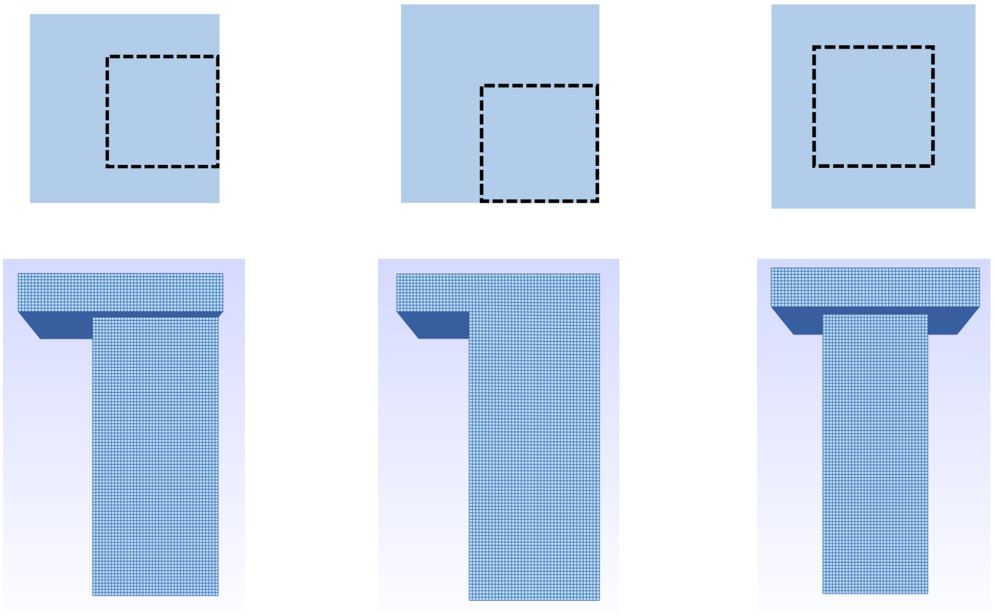

(a) (b) (c)

Fig 6.18. Relative position diagram of the plate and the column. The column is located (a) at the middle point of the side; (b) at the vertex;(c) at the center.of the plate.

6.1.4.2 Simulation results

Taking regular wave R4 as an example, the measurement point load results are as follows.

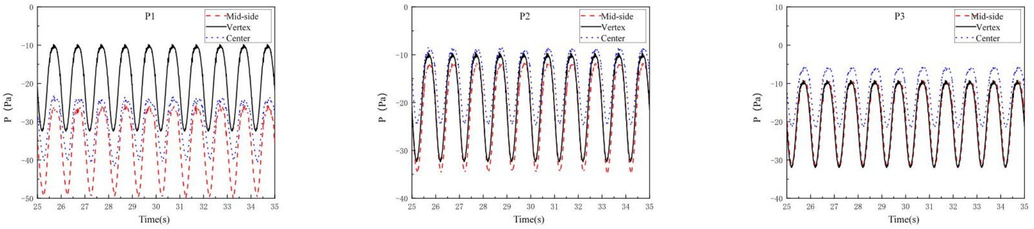

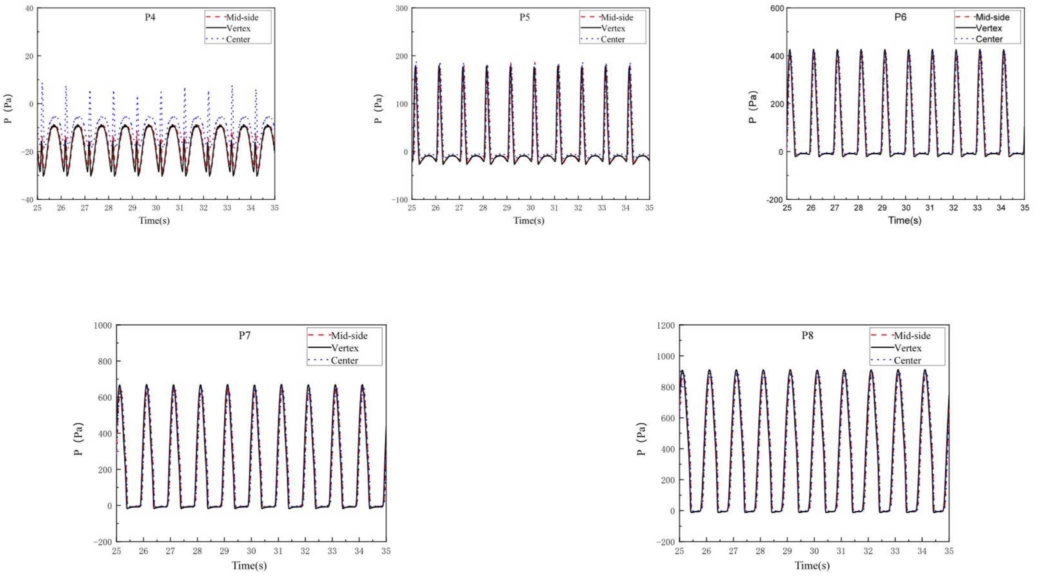

Fig 6.19 Comparison chart of measured load at measuring points under regular wave R4 load conditions

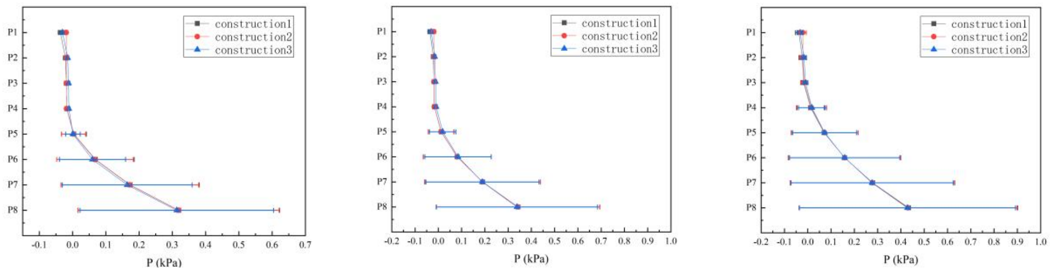

(a)R1 (b)R4 (c)R7

Fig 6.20. Comparison chart of measured loads at measuring points under different regular wave conditions

From Fig 6.20, it is observed that under different wave environments, there are slight differences in the relative positions of different columns at measuring points 1 to 4 on the platform. However, the forces at different measuring points on the platform with different columns at measuring points 5 to 8 are the same. The difference in shape between platforms lies in the relative position of the flat plate on top of the platform and the platform itself. The positions of measuring points 1 to 4 are relatively high and are more affected. This is particularly evident at monitoring point 1, where Construction1 is subjected to a slamming load greater than Construction 2 by 22.3% and greater than Construction 3 by 55.6%. At measuring points 2 to 4, Construction 1 and Construction 2 have similar slamming load values, with a difference of 2.3% to 6.25%, but both are greater than Construction 3's load by 22.6% to 51.3%. The positions of measuring points 5 to 8 are relatively low and are less affected, with differences ranging from 3.56% to 7.62%, but Construction 1 is greater than Construction 2 and greater than Construction 3.

The overall force simulation results are as follows.

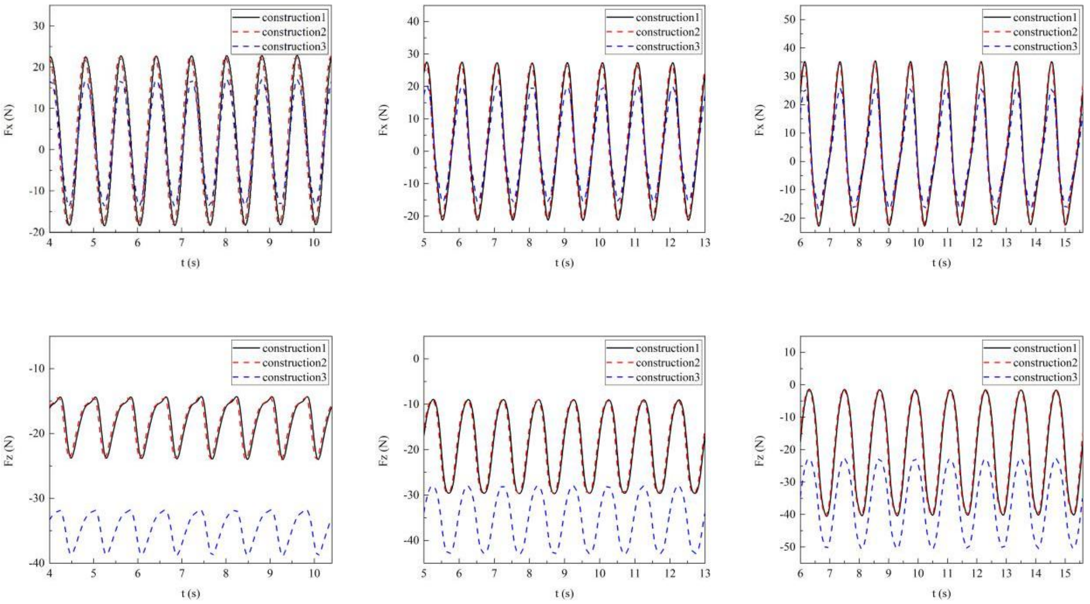

(a)R1 (b)R4 (c)R7

Fig 6.21. Comparison chart of time domain of overall force under different regular wave conditions

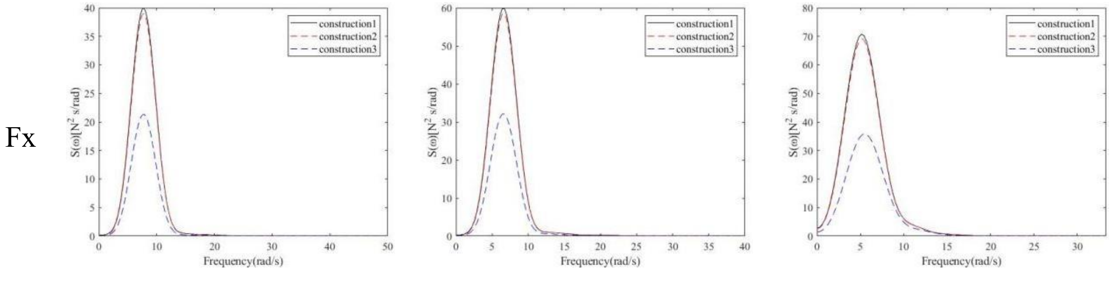

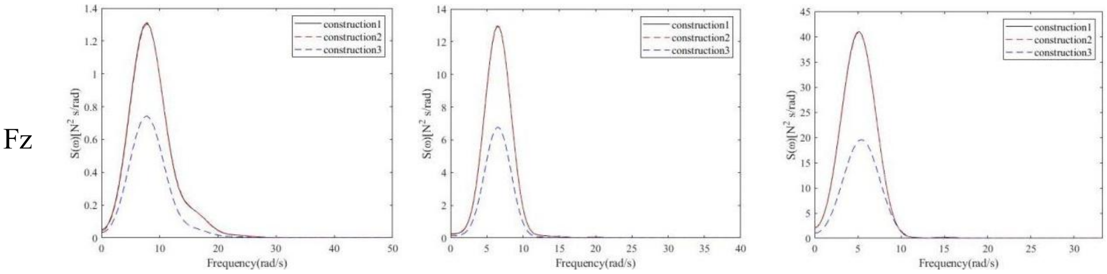

(a)R1 (b)R4 (c)R7

Fig 6.22. Comparison chart of frequency domain of overall force

From the time-domain graph Fig 6.21, it is observed that in the X direction, Construction 1 experiences a force greater than Construction 2 by 1.56% to 3.45%, and greater than Construction 3 by 40.2% to 46.7%. In the Z direction, Construction 3 experiences a negative force greater than Construction1 and Construction 2 by 24.7% to 60.8%. This may be due to the fact that when waves climb to the top, although a lot of kinetic energy is consumed, there is more water climbing on, which has a greater negative effect on the columns when falling down. According to the frequency-domain graph Fig 6.22, the peak frequency of the force spectrum in both X and Z directions is the same as that of the incident wave frequency, indicating that its force is mainly caused by slamming from incident waves.

6.1.4.3 Conclusion

In summary, for columns located at different relative positions to the top deck, the pressure distributions at each measurement point and the overall slamming loads in the X and Z directions exhibit a high degree of consistency in waveform and period, with the period matching that of the incident waves. Larger column dimensions result in higher slamming pressure amplitudes at all measurement points. In terms of the platform’s overall load in the X direction, Scheme 1 is greater than Scheme 2, and Scheme 2 is greater than Scheme 3. Moreover, the peak frequencies in the X- and Z-direction slamming load spectra are consistent with the incident wave frequency, indicating that the slamming loads are primarily induced by the incident waves.

6.2 Slamming response under environmental variations

6.2.1 Effect of air gap on column slamming load magnitude

6.2.1.1 Introduction of the load condition

The important basis for judging the occurrence of slamming phenomenon on the lower deck of the platform is whether there is a negative air gap. In this section, a sensitivity analysis of the air gap around the column is conducted. All simulations use square columns with characteristic dimensions of 180 mm × 180 mm and a wave heading of 180°. The air gap values selected for the analysis are 135 mm, 185 mm, 235 mm, and 285 mm, with wave conditions ranging from R1 to R9. Table 6.5 presents the configuration of the different air gap cases, totaling 36 in all. Under varying air gap settings, the slamming pressure monitoring points located below the water surface differ accordingly. The air gap depths used in this section are consistent with the experimental conditions described in Chapter 3, and the spatial distribution of the monitoring points relative to the free surface is shown in Fig. 4.1 of Chapter 4.

Table 6.5 Simulation Case Settings for Different Air Gaps

No.	Air Gap （mm）	Wave No.	*H* (cm)	*T* (s)
Case1	135	R1	10.22	0.8
Case2		R2	11.48	0.8
Case3		R3	12.81	0.8
Case4		R4	15.81	1
Case5		R5	17.73	1
Case6		R6	19.74	1
Case7		R7	22.28	1.2
Case8		R8	24.95	1.2
Case9		R9	27.73	1.2
Case10	185	R1	10.22	0.8
Case11		R2	11.48	0.8
Case12		R3	12.81	0.8
Case13		R4	15.81	1
Case14		R5	17.73	1

Case15		R6	19.74	1
Case16		R7	22.28	1.2
Case17		R8	24.95	1.2
Case18		R9	27.73	1.2
Case19	235	R1	10.22	0.8
Case20		R2	11.48	0.8
Case21		R3	12.81	0.8
Case22		R4	15.81	1
Case23		R5	17.73	1
Case24		R6	19.74	1
Case25		R7	22.28	1.2
Case26		R8	24.95	1.2
Case27		R9	27.73	1.2
Case28	285	R1	10.22	0.8
Case29		R2	11.48	0.8
Case30		R3	12.81	0.8
Case31		R4	15.81	1
Case32		R5	17.73	1
Case33		R6	19.74	1
Case34		R7	22.28	1.2
Case35		R8	24.95	1.2
Case36		R9	27.73	1.2

6.2.1.2 Simulation results

Taking the regular wave R4 with medium wave height as an example, the wave simulation results are as follows.

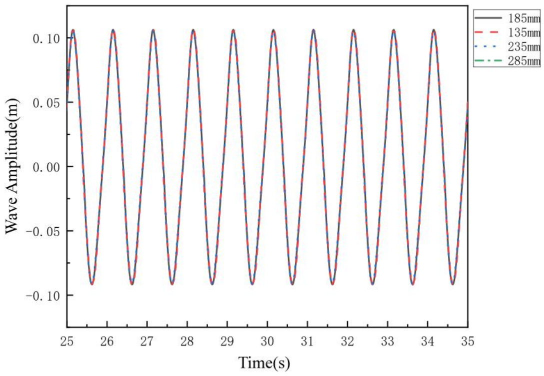

Fig 6.23. Comparison chart of wave height under regular wave R4 conditions

From Fig 6.23, the wave environment of the four numerical flume is basically the same for the simulation of waves. The different air gaps have different effects on the propagation of waves in the flow field. When the air gap is small, negative air gap phenomenon will occur on the platform. This phenomenon will cause slamming on the lower surface of the platform and affect the free water surface.

Taking the regular wave R4 with medium wave height as an example, the force simulation results of the measuring points are as follows.

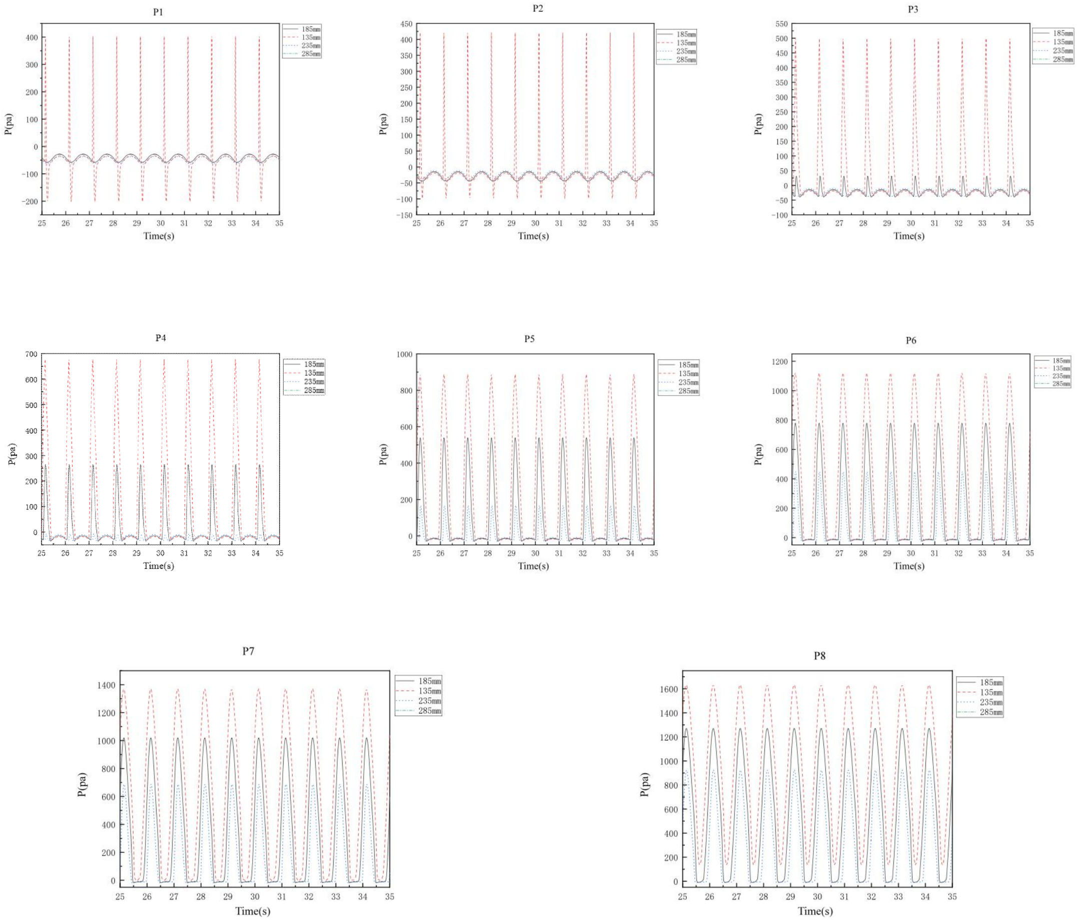

Fig 6.24. Comparison chart of measured force at measuring points under regular wave R4 load condition

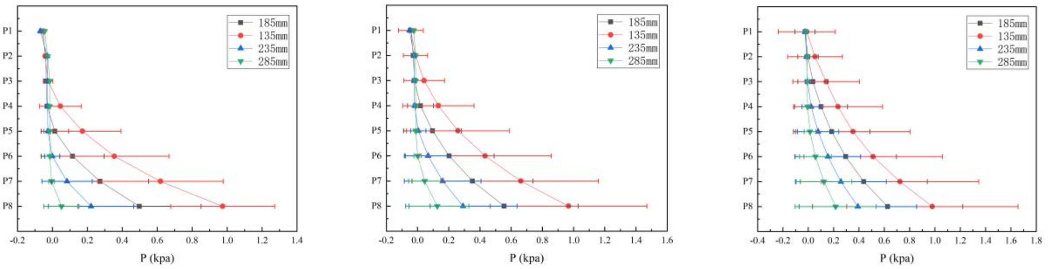

(a)R1 (b)R4 (c)R7

Fig 6.25. Comparison chart of loads on measuring points under different regular wave conditions

From Fig 6.24 the pressure simulation results of the numerical flume for the measuring points on the platform are consistent in waveform, and the pressure period is consistent with the wave period. The simulated column shapes used above is also consistent, and the position of the wave and platform interaction surface is also consistent. The slamming loads on the measuring point decrease as air gap increases. At the upper part of the column (measuring point), 135mm air gap receives 172.4%~735.6% more slamming load than 285mm air gap. At the lower part of the column, 135mm air gap receives more slamming load than 285mm air gap. When the initial air gap is large (285mm and 235mm), wave crest does not directly reach the connection between column and the deck. The wave will only act on the top of the column and the bottom of deck after climbing. The larger the initial air gap, the more energy loss during the wave climbing process, and the smaller wave-induced load generated at the top of the column and the bottom of the deck. When the initial air gap is of 185mm, the wave crest just reaches the deck height. At this time, water particle velocity near the wave crest is large and generates maximum slamming load on the column and the deck. When the initial air gap decreases to 135mm, the wave crest has exceeded the deck height. The column and the deck are located in the area below the wave crest although free water surface rises rapidly at this time.

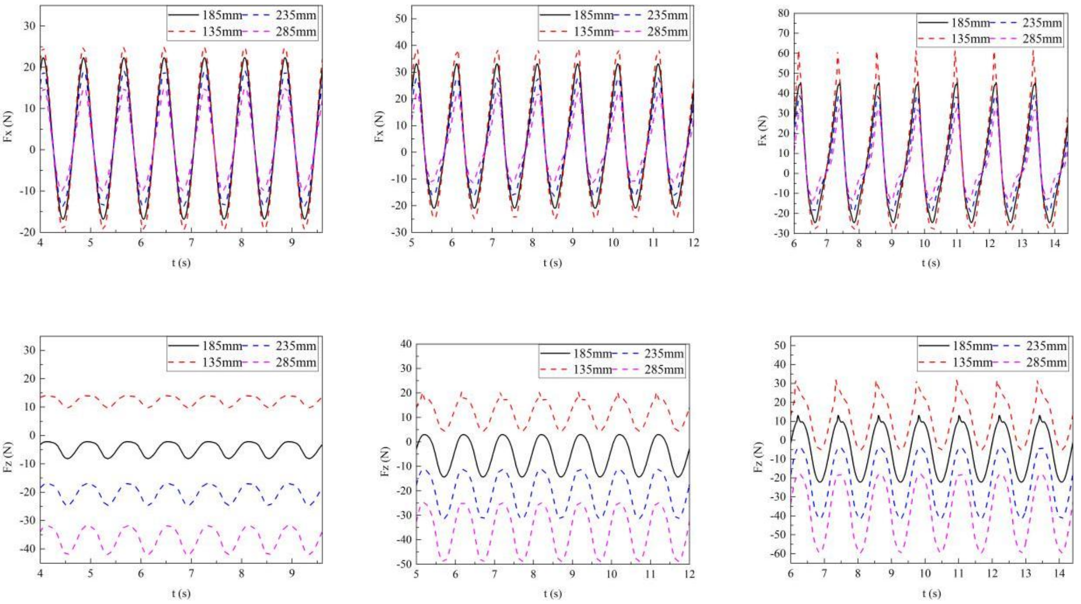

(a)R1 (b)R4 (c)R7

Fig 6.26. Comparison chart of time domain of overall force under different regular wave load conditions

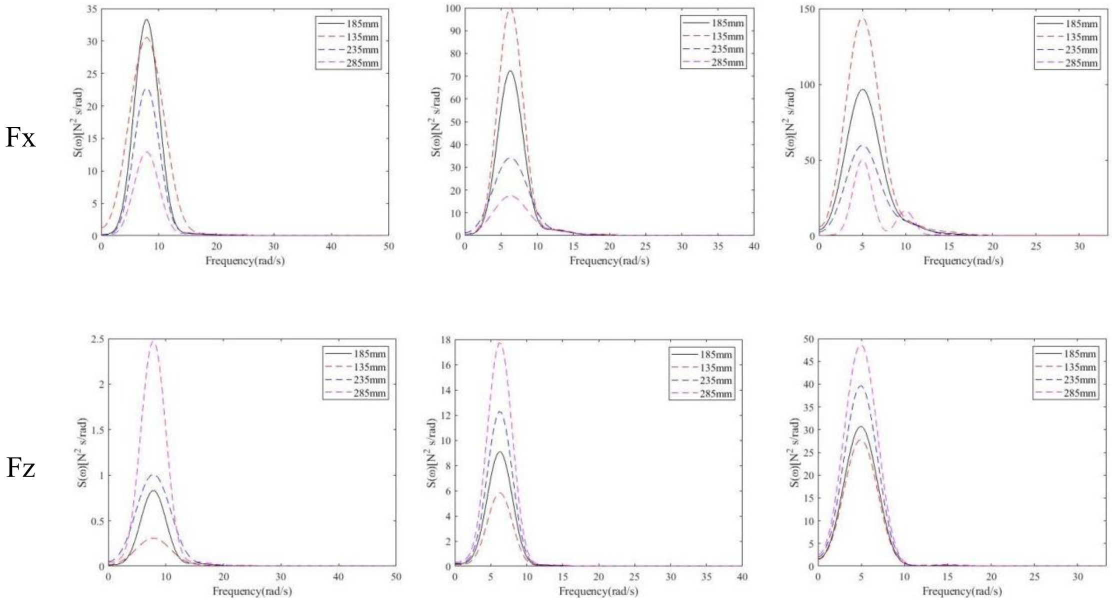

(a)R1 (b)R4 (c)R7

Fig 6.27. Comparison chart of frequency domain of overall force

From the above Fig 6.27, the overall force simulation results of the numerical flume for the platform under different air gaps are basically consistent in terms of waveform, period and force in the X and Z directions. For the force conditions in the X and Z directions, it can be analyzed that the slamming load conditions of the two are closely related to the wave characteristics. In the X direction, the overall force from large to small is obtained sequentially under 135mm air gap, 185mm air gap, 235mm air gap, and 285mm air gap. The overall force under 135mm air gap is 68.5%~102.5% larger than that under 185mm air gap. In the Z direction, 135mm air gap is affected by positive force, while other air gaps are affected by negative force. From the magnitude of the force amplitude, it is from large to small for 285mm air gap, 235mm air gap, 135mm air gap, and 185mm air gap. This is because the larger the platform’s air gap is, the greater its buoyancy is. The greater its buoyancy is, the greater its force in the Z direction is. The difference in force it receives is equal to that in static water. As can be seen from the frequency domain diagram, the peak frequency of X and Z direction force spectrum is the same as that of incident wave frequency, indicating that its force is mainly caused by incident wave slamming.

6.2.1.3 Conclusion

In summary, variations in air gap size have a significant impact on the load characteristics experienced by the columns. Under different air gap conditions, the pressure distribution at each measurement point on the column, as well as the overall slamming loads in the X and Z directions, exhibit highly consistent waveforms and periods, which match the incident wave period. In terms of pressure magnitude, larger air gaps correspond to lower pressures at the measurement points, with this trend being particularly evident at the upper column points (F1–F4). From the perspective of the platform’s overall loading in the X direction, increasing the air gap markedly reduces the magnitude of slamming loads, indicating a strong sensitivity of these loads to air gap size.

The sensitivity analysis of column air gap is conducted using a uniform square column shape with characteristic dimensions of 180 mm × 180 mm and a wave heading of 180°. The slamming load received by the measuring point decreases as the air gap increases. The slamming load decreases from the largest to the smallest as the air gap increases in the order of 135mm, 185mm, 235mm, and 285mm. The slamming load received by the measuring point under 135mm air gap is 78.6%~735.6% larger than that received under 285mm air gap. This difference is particularly evident in measuring points 1, 2, 3, and 4 at the upper part of the column. In the X direction, the overall force decreases from largest to smallest as the air gap increases in the order of 135mm air gap, 185mm air gap, 235mm air gap, and 285mm air gap. The slamming load received by the measuring point under 135mm air gap is 68.5%~102.5% larger than that received under 185mm air gap. In the Z direction, when under 135mm air gap, the slamming on the measuring point under is positive while it is negative under other air gaps. The magnitude of force received decreases from largest to smallest as the air gap changes in order of 285mm, 235mm, 135mm, and 185mm.

When the initial air gap is relatively large (285mm and 235mm), the wave peak height does not directly reach the connection between the column and deck. The wave only has an effect on the top of the column and the bottom of the deck after climbing. The larger the initial air gap, the more energy loss during the wave climbing process and the smaller wave-induced load generated on the top of the column and the bottom of the deck. When the initial air gap is reduced to 135mm, the wave peak height has exceeded the deck height and the column and deck are located in an area below the wave peak although at this time free water surface rises rapidly. The simulation results of the overall force of the platform in the numerical flume are relatively consistent in the waveforms and periods of the X and Z directions under different air gaps.

6.2.2 Effect of wave heading on spatial distribution and peak slamming loads

6.2.2.1 Introduction of the load condition

Wave direction is an important parameter in wave environments. Although wave direction is 360° without dead angles in real sea conditions, waves also have a statistical value of wave direction. Choosing an appropriate wave direction according to sea conditions is a correct choice. In this section, a sensitivity analysis of wave heading on column slamming response is conducted. Square cross-section columns with characteristic dimensions of 180 mm × 180 mm are uniformly used, and the air gap is set to 185 mm. Two typical wave heading angles—180° and 135°—are considered to compare the effects of different wave incidence directions on slamming response. A total of 18 cases are simulated, with the specific configurations listed in Table 6.6.

Table 6.6 Wave Heading Simulation Case Settings

No.	Wave Heading	Wave No.	*H* (cm)	*T* (s)
Case1	180°	R1	10.22	0.8
Case2		R2	11.48	0.8
Case3		R3	12.81	0.8
Case4		R4	15.81	1
Case5		R5	17.73	1
Case6		R6	19.74	1
Case7		R7	22.28	1.2
Case8		R8	24.95	1.2
Case9		R9	27.73	1.2
Case10	135°	R1	10.22	0.8
Case11		R2	11.48	0.8
Case12		R3	12.81	0.8
Case13		R4	15.81	1
Case14		R5	17.73	1
Case15		R6	19.74	1
Case16		R7	22.28	1.2
Case17		R8	24.95	1.2
Case18		R9	27.73	1.2

6.2.2.2 Simulation results

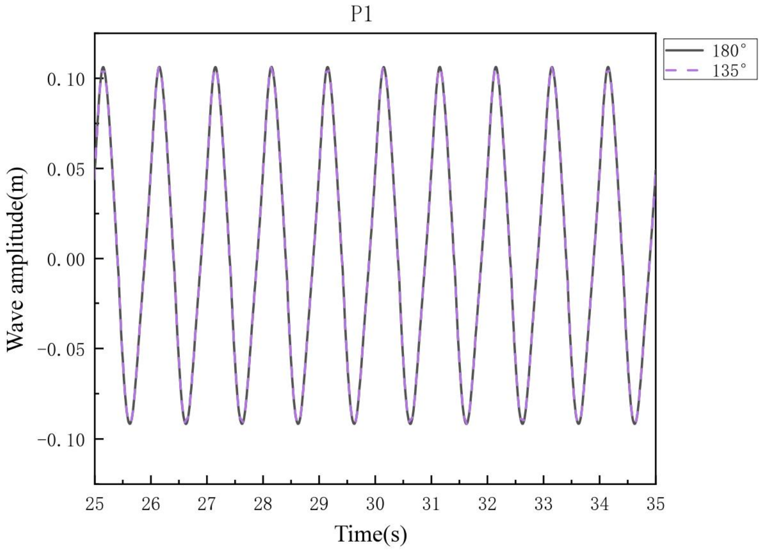

Fig 6.28. Comparison chart of wave height under regular wave R4 load condition

The wave simulation results can be seen from Fig 6.28. For simulating waves, the CGNT-CFD method provides a similar environment for different wave direction angles. However, due to different wave directions, wave reflection and structural interference, each wave in the regular wave sequence will not be exactly the same, and the resulting wave-induced loads will also differ.

Taking the regular wave R4 with medium wave height as an example, we can see the simulation results of force on measuring points.

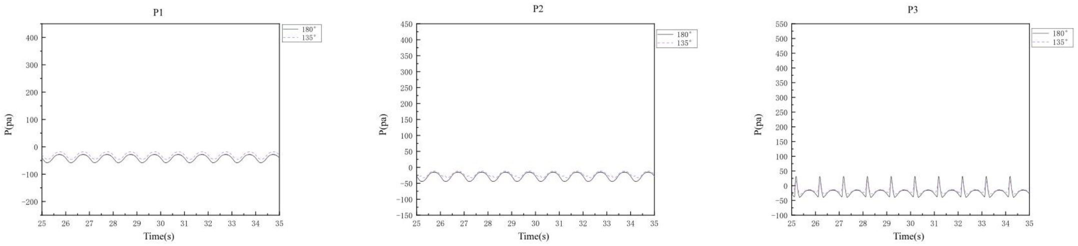

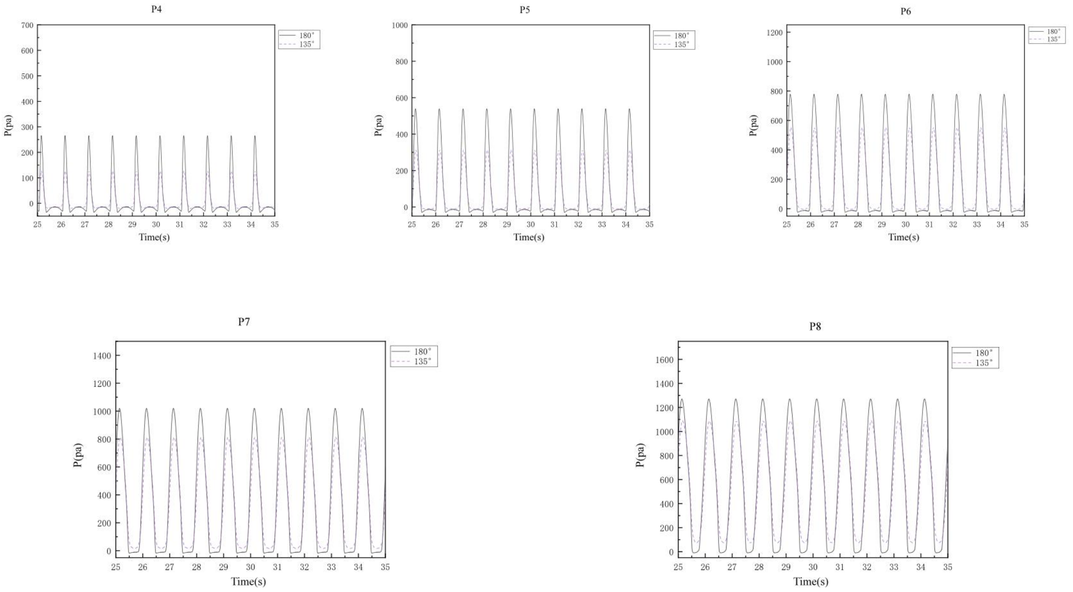

Fig 6.29. Comparison chart of loads on measuring points under regular wave R4 load condition

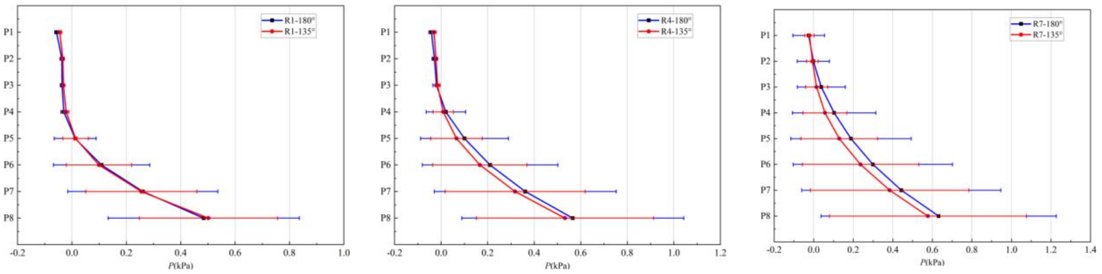

(a)R1 (b)R4 (c)R7

Fig 6.30. Comparison chart of load on measuring points under different regular wave conditions

The CGNT-CFD method's pressure simulation results for the measuring points on the platform are consistent with each other in waveform and have the same period as the wave period. Both have greater slamming loads on the measuring points in the 180° wave direction than in the 135° wave direction due to wave reflection and structural interference. At measuring points 1, 2, and 3 on the upper part of the column, the difference in slamming loads between the two is small. However, below the column, the slamming load on the 180° wave direction measuring point is 11.3% to 98.6% greater than that on the 135° wave direction. The reason for this is that when water flows down at 180°, it directly hits the surface of the column, causing higher wave climbing and more severe load on the measuring point; while at 135°, water flows along the surface of the column and can dissipate more quickly, resulting in lower wave climbing and weaker load on the measuring point.

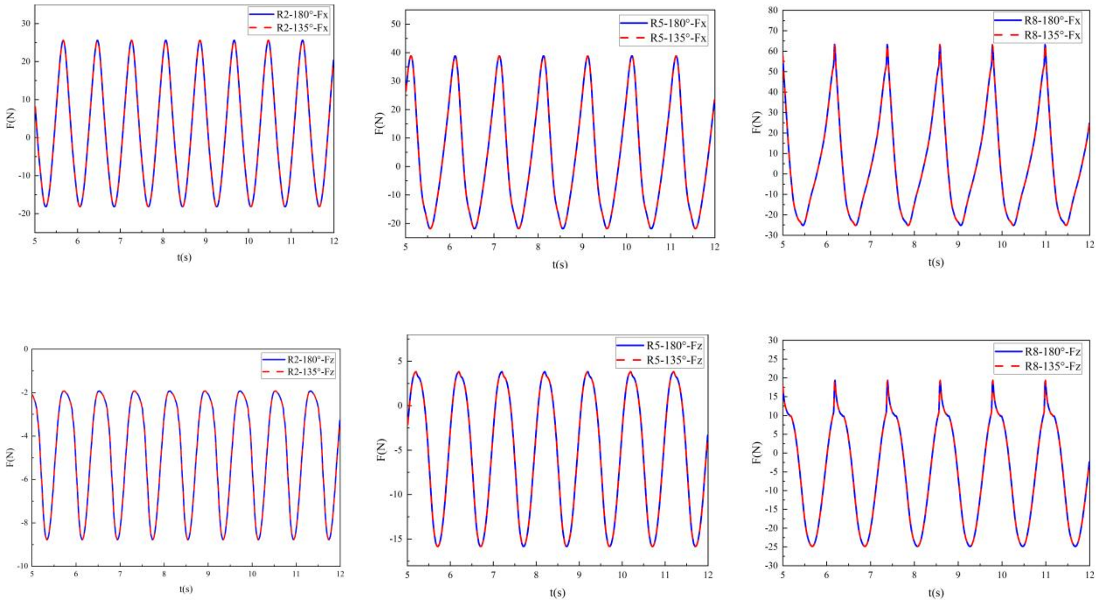

(a)R2 (b)R5 (c)R8

Fig 6.31. Comparison chart of overall force time domain

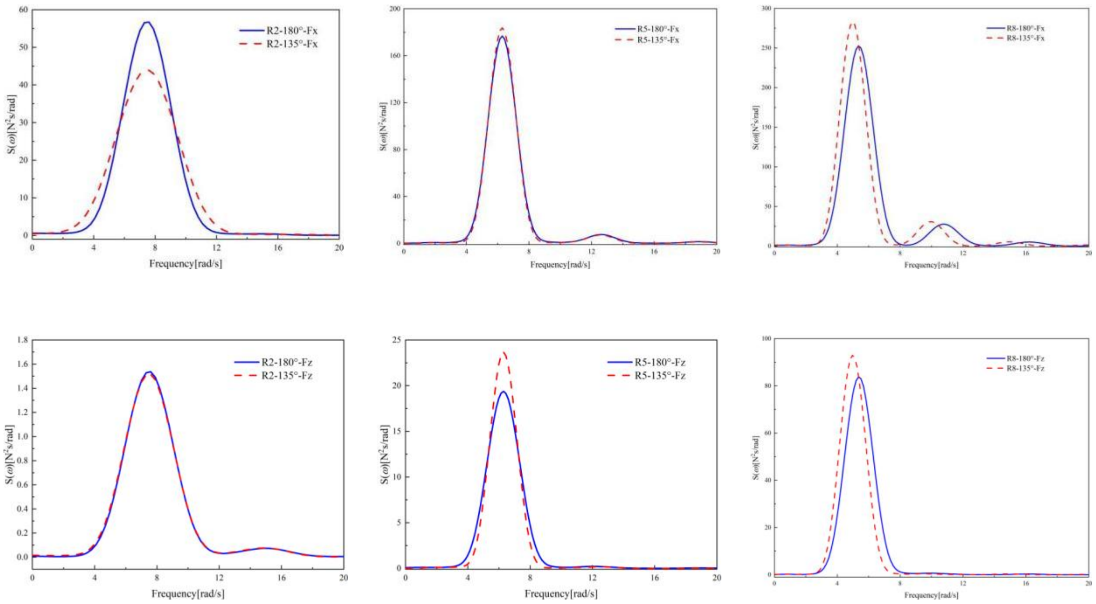

(a)R2 (b)R5 (c)R8

Fig 6.32. Comparison charts of overall force frequency domain

From the time-domain graph, it is observed that the CGNT-CFD method's simulation results for the overall force on the platform in the 135° and 180° directions are consistent in waveform and period in the X and Z directions. Both have similar forces in the X and Z directions.

For the single-peak spectrum in Fig 6.32 (a) and (b), the peak frequency is the same as the incident wave frequency, indicating that the main force comes from regular waves. There are noticeably two peaks. The first peak frequency is $\omega=2\pi/T$, which is the same as the wave frequency and is a first-order main frequency component. The second peak is at 2ω, with a peak value corresponding to a second-order nonlinear component, which means that the force in the X and Z directions under medium sea conditions exhibits second-order nonlinear characteristics. In Fig 6.32 (c), there is a spectral peak shift phenomenon for the 135° incident wave, and the main peak frequency is less than the wave frequency. At the same time, there are also third-order main frequency components.

The reason for the appearance of a secondary peak in force spectral analysis may be that as waves propagate to columns, waves propagating along both sides of the column superimpose on the back of the column and rise to their highest point. Some waves will move back along the side of the column. As the incident waves continue to move towards the column, wave energy also gradually propagates forward, and water quality points around the column increase continuously. Moreover, edge waves resonating along both sides of the column will continue to move until near their windward surface and superimpose. The influence of wave superposition and disturbance may cause strong nonlinear phenomena such as large-scale deformation and fragmentation of waves on the back of columns, which further affect column forces. In addition, for spectral peak shift phenomenon under 135° direction, waves can propagate faster along both sides of columns on surfaces, with less intense backflow movement, making forces caused by waves being of lower-frequency in frequency domain but not significantly affecting overall forces on columns.

6.2.2.3 Discussion of results

In summary, under different wave directions, the pressure distribution at each measurement point on the column and the overall slamming loads in the X and Z directions exhibit a high degree of consistency in waveform and period, with the period matching that of the incident waves. In terms of pressure magnitude, the 180° wave direction generally produces higher pressures than the 135° wave direction, a difference particularly pronounced at the lower measurement points on the column. The overall loads on the platform in the X and Z directions remain largely consistent. Furthermore, the peak frequencies of the slamming load spectra in the X and Z directions match the incident wave frequency, indicating that the slamming loads are primarily generated by the action of the incident waves.

6.3 Impact of multi-column geometry on wave slamming

6.3.1 Grid independence verification

The quality of the grid significantly affects the accuracy of numerical basin simulations. This section analyzes the impact of different grid schemes on the convergence of the numerical basin results. Observations and comparisons will be conducted on the time history of the free surface within the numerical basin using five distinct grid configurations. A regular wave with a wave height of 0.1022 m and a wavelength of 1.0754 m will be selected as the target wave, with a computational time step of 0.01 s.

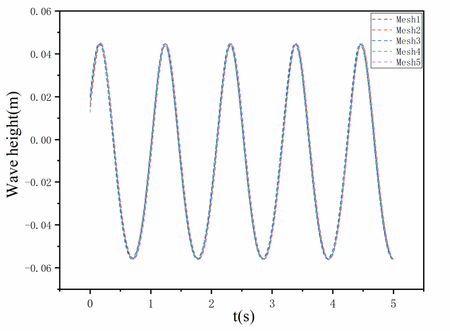

Fig 6.33. Time history curve of force in the x-direction

Table 6.7. Total mesh counts for different meshing schemes

No.	1	2	3	4	5
Mesh Counts	13.818	50.82	68.145	164.01	321.09
Peak Value/m	0.4377	0.4482	0.4478	0.4482	0.4478

The Fig 6.33 displays the time-history curves of free surface elevation at a monitoring point under five different grid schemes. The table shows the total grid numbers corresponding to each scheme. Observing the Fig 6.33, it is observed that the five curves largely overlap, with similar time-history variations, though differences appear at peak values. Initially, the peak values of the free surface under each grid scheme are extracted to analyze the relationship between peak values and grid numbers.

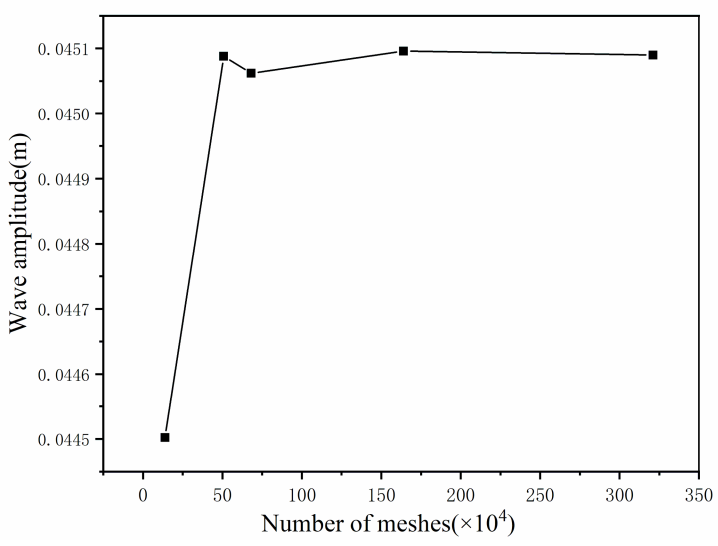

Fig 6.34. Comparison of peak values under different mesh counts

It is evident that when the grid number is below 508,200, the free surface peak increases with the number of grids. When the grid number exceeds 508,200, convergence begins, and the free surface peak stabilizes, with the discrepancy among grid schemes remaining below 1%. At this point, the effect of grid number on the computational results is minimal. Considering factors like grid quality and computational efficiency, this study selects the grid scheme with 508,200 grids within the allowable error range.

Although the present study focuses on regular wave conditions, the selected grid resolution ($\lambda/\Delta x = 1.0754/0.01 \approx 107 > 50$) was verified to be sufficiently fine for resolving key flow features and turbulence structures in the breaking region. For freak or highly nonlinear waves, the required spatial resolution may be more stringent due to steeper gradients and enhanced turbulence generation. Since the present work does not include freak-wave simulations, the grid convergence and TKE spectrum validation for such cases are not assessed herein. Nevertheless, based on the existing grid sensitivity analysis and published benchmarks, the adopted 0.508 million-cell mesh can be considered adequate for the current regular and moderately breaking wave cases. Further verification under extreme or freak wave conditions will be addressed in future studies.

6.3.2 Model description

The complete semi-submersible platform comprises multiple components, such as columns and the deck, making it significantly more complex than a single square column with a deck. For a semi-submersible platform, various hydrodynamic interactions occur between different components (such as the forward columns, aft columns, and deck), including wave run-up along the columns and near-field interference between columns. These phenomena critically impact wave slamming on the semi-submersible platform, adding complexity to the system.

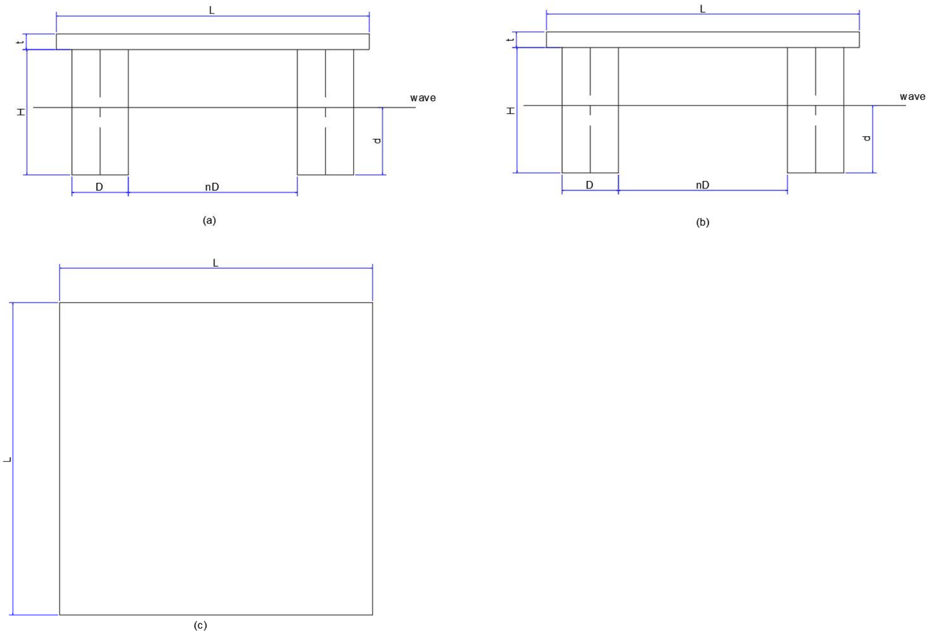

(a)

(b)

(c)

Fig 6.35. Sketch of the semi-submersible platform: (a) side view, (b) front view, (c) top view.

Through a series of simulations in a numerical basin, this study examines the local wave slamming loads on different components of a typical semi-submersible platform, including the forward columns, aft columns, bottom of the deck, and side walls of the box-type deck. Based on the simulation results, a comprehensive analysis of wave slamming loads on this semi-submersible platform was conducted, focusing on the impact of severe sea conditions, differences in wave slamming loads among components, and the spatial distribution of horizontal and vertical slamming loads.

The semi-submersible platform used in the simulations consists of four rectangular columns and a box-type deck, as shown in the Fig 6.35. The table provides the platform's main dimensions and weight parameters.

Table 6.8. Main dimensions and weight parameters of the semi-submersible platform

Name	Symbol	Value	Unit
Deck dimensions	$L\times L\times t$	\	m
Column size	$D\times H$	0.18×0.4	m

Column spacing	*nD*	\	m
Platform thickness	*t*	0.05	m
Air gap	*d*	185	m

This study conducts a sensitivity analysis on column spacing in multi-column configurations. Three typical spacings — 1D, 2D, and 3D (where D is the characteristic width of the square column)—are selected to evaluate the effect of spacing on the slamming response of the rear column. All simulations use square columns (180 mm × 180 mm), with a uniform air gap of 185 mm and a wave heading of 180°. Three representative regular wave conditions are chosen, resulting in a total of 9 simulation cases. The detailed configurations are provided in Table 6.9.

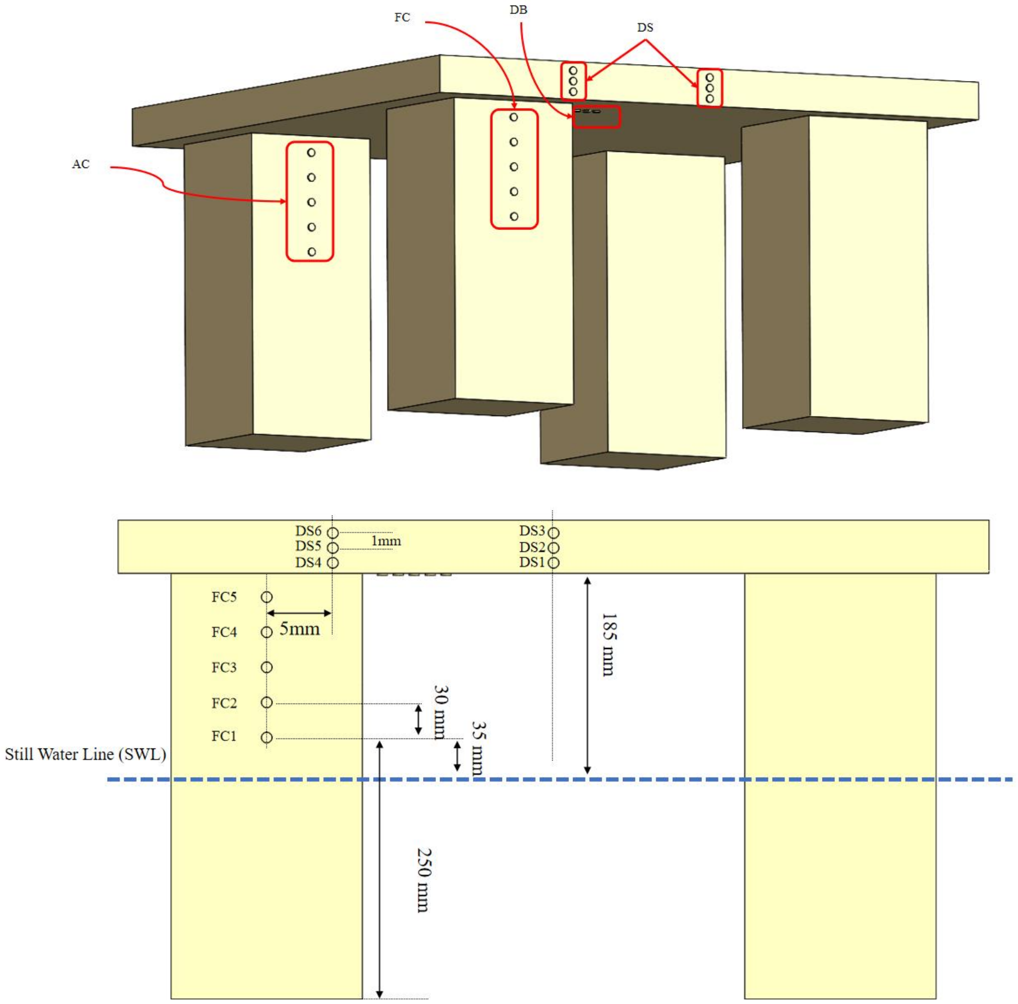

(a)

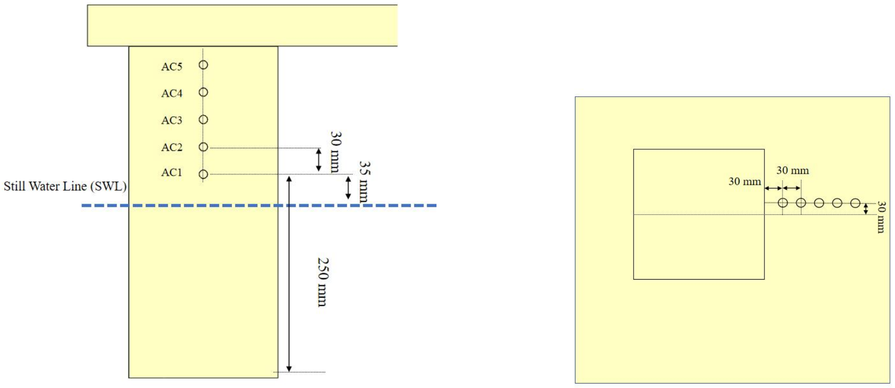

(b) (c)

Fig 6.36. Configuration of the slam panel locations (full-scale, unit, m): (a) the fore column and deck side, (b) the aft column, (c) the deck bottom in the vicinity of the aft column.

Table 6.9. Column Spacing and Wave Environment Parameters

Working Condition	Spacing
1	1D
2	2D
3	3D

(a)

Working Condition	Wave Heights H(cm)	Period T(s)
1	10.22	0.8
2	11.48	0.8
3	12.81	0.8

(b)

To measure wave slamming loads, a total of 23 slamming units were selected on the semi-submersible platform model. These units are distributed across the forward columns, aft columns, deck bottom, and deck sidewalls. For the convenience of subsequent analysis, these structural parts are respectively referred to as FC, AC, DB, and DS. Fig 6.36 shows their detailed locations and numbering. All slamming units are positioned above the Still Water Line (SWL). Five slamming units are arranged vertically along each of the forward and aft columns. Specifically, three slamming units are installed at the mid-height of the forward columns to analyze the horizontal variation of wave slamming loads on the forward columns.

Additionally, one row of slamming units was installed along both the left edge and the center of the deck sidewall, with each row containing three evenly spaced units.

To measure slamming loads on the deck bottom, caused by waves overtopping the freeboard or climbing along the aft columns, five slamming units were installed along the deck length. The spacing between adjacent slamming units on the columns and deck sidewalls is 30 mm, and the spacing between units on the deck bottom is also 3 mm.

6.3.3 Impact of column spacing on platform slam load characteristics

As demonstrated in the previous research, the shape of the columns, air gaps, relative position of the deck, and wave direction significantly influence the slam loads on the columns and the deck. Column spacing is a crucial parameter when considering both the safety and economic aspects of platform structures. This section analyzes and compares the effects of three different column spacings1D, 2D, and 3D (where D is the column diameter) on the slam load characteristics of the platform, with wave parameters set to R3. In multi-column structures, the front column often creates a shielding effect for the rear column, affecting the wave climbing or slam load on the rear column. Additionally, the waves between multiple columns may interfere with each other, either amplifying or weakening the wave, which can also affect the magnitude of the slam load.

In this study, numerical simulations are conducted with an air gap of 185 mm and a wave heading of 180 ° to systematically evaluate the spatial distribution and variation trends of slamming loads on key regions of the platform—such as the front column, rear column, underside of the deck, and side walls—under different column spacing conditions. The results provide a reference for structural layout and impact-resistant design of the platform.

(1) column spacing has a small impact on slam loads on the front column

For the R3 wave condition with wave height H=0.1281m, H = 0.1281, H=0.1281m and wavelength L=1.1135m, L=1.1135, L=1.1135m, we analyzed the time-history diagrams of the slam loads at FC3 and FC6 points on the front column, as shown in

Fig 6.37 (a). At the FC3 point, the maximum slam loads corresponding to the 1D, 2D, and 3D column spacings are very close, with values of 1767 kPa, 1736 kPa, and 1686 kPa, respectively, with a difference of no more than 5%. Similarly, the slam load amplitudes at these three spacings are also very close, at 1184 kPa, 1113 kPa, and 1064 kPa, differing by about 10%. Additionally, the load periods at different column spacings coincide with the wave period (T = 1.11s), and the load curves resemble smooth sinusoidal functions, meaning that the small differences in loads have little impact on structural safety and fatigue analysis. Therefore, the column spacing has a minimal impact on the slam load experienced by the front column.

The main cause of the wave load difference on the front column is the interference effect between the front columns. When waves encounter the columns during propagation, part of the water will climb along the front-facing side of the column, while another portion will split into two and propagate along the two sides of the column. When waves interact with the front column, the wave surface will scatter outward along the column, and the diffused water will combine between the two front columns and generate waves, causing an interference effect. When the column spacing is 1D, this interference effect is most prominent, resulting in the largest slam load on the column. As the column spacing increases, the interference between the inner edge waves gradually weakens, causing the wave field around the front column to resemble that of a single column, thus reducing the slam load.

(2) Large column spacing leads to a significant increase in slam loads on the rear column

Fig 6.38 (b) compares the impact of column spacing on the slam load on the rear column. The slam loads at 1D and 2D column spacings are very similar. At these spacings, the slam loads at points AC4 and AC5 on the rear column are around 1150 kPa, which is 46% – 53% lower than the maximum slam load on the front column. This is likely because, at these spacings, the rear column is shielded by the front column, and the wave energy has been significantly dissipated before reaching the rear column.

When the column spacing increases to 3D, the slam loads on the rear column increase significantly, with the measured values at points AC1 to AC5 increasing by nearly an order of magnitude (about 20 times) compared to the 1D and 2D cases. Moreover, for the 3D column spacing, the load gradually increases from AC1 to AC5. This suggests that at larger column spacings, the interference effects between the columns become stronger, causing a sharp wave surge at the rear column, which amplifies the wave energy locally, leading to a larger slam load. This numerical analysis only considers regular wave conditions, which are relatively common in real sea state wave spectra. Semi-submersible platforms typically operate under such conditions for extended periods. Therefore, it is important to optimize column spacing to minimize or avoid the sharp increase in wave loads on the rear column. Even though most sixth-generation and later deep-water semi-submersible platforms are designed with directional capabilities, front and rear column positions may frequently switch under complex sea conditions. Thus, while optimizing column spacing, it is also necessary to reinforce the structural strength around the platform's inner side, particularly near the AC series monitoring points.

(3) As column spacing increases, the wave slamming load on the deck wall and bottom decreases; maximum slam load near the deck bottom-column interface decreases with increased column spacing

Fig 6.38 (c) and (d) show the time-history changes at DS2/DS5 and DB1/DB5 load monitoring points. These Figs provide insights into how column spacing affects the wave slam loads on the deck wall and bottom. The load on both the deck wall and bottom is caused by the wave surge. In the different column spacing models, the wave period on the deck wall is approximately 0.44 s (about 40% of the wave period), and the wave period on the deck bottom is around 0.90 s, indicating that column spacing has little effect on the wave period at the deck.

From the perspective of wave slam impact load, both on the deck sidewall and bottom, as the column spacing increases, the slam load tends to decrease. The maximum impact load is primarily considered, particularly at the DS2 monitoring point. For the deck side, the maximum wave slam load decreases by about 2.0% from the 1D to the 2D column spacing. From the 2D to the 3D spacing, the maximum slam load increases by about 3.5%. For the deck bottom, when the column spacing increases from 1D to 2D, the maximum wave slam load increases by about 12.2%, and when it changes from 2D to 3D, the maximum slam load increases by about 2.2%. This may be because larger column spacings reduce the interference between columns and weaken the wave climbing effect on the deck wall, thereby decreasing the intensity of the wave surge.

For the wave slam load at the deck bottom-column interface, the impact load decreases along the direction away from the column. As the column spacing increases, both the average and maximum slam loads at this point increase slightly. When the column spacing is 2D or 3D, the average load at the five DB monitoring points is approximately 320 kPa, compared to 340 kPa when the spacing is 1D, a difference of only 6%. When the column spacing is small, wave interference between the columns is more likely to occur, enhancing the wave surge and slam effect at the interface. As the column spacing increases to 3D, the mutual influence between columns weakens, reducing the wave climbing effect and consequently decreasing the wave slam pressure on the deck bottom.

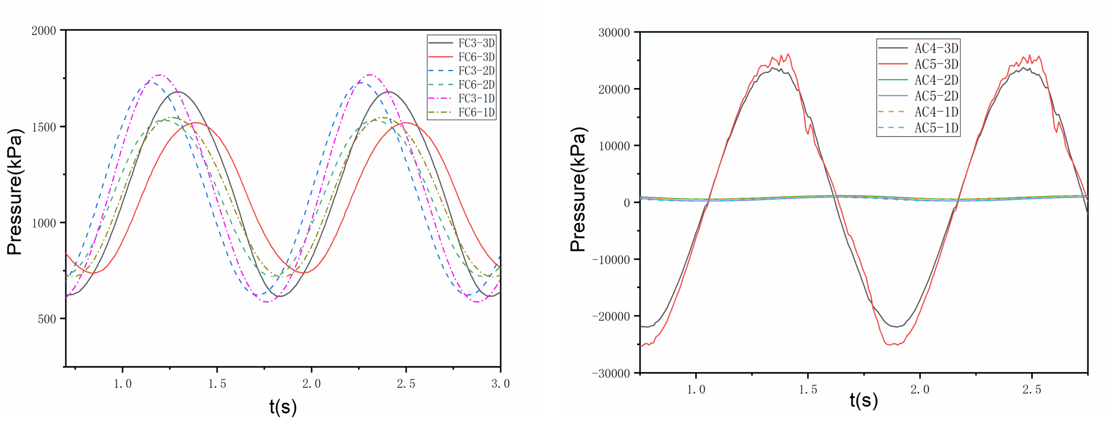

(a) Forward Columns (b)Aft Columns

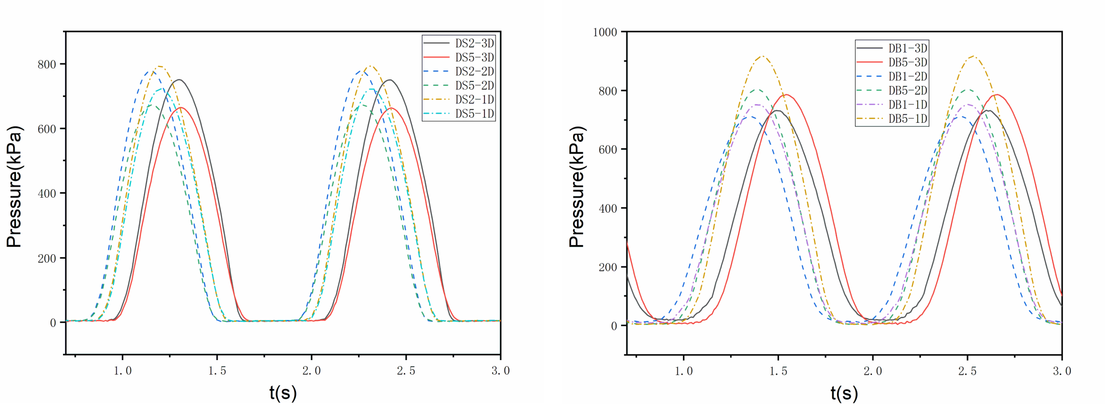

(c)Deck Wall (d)Deck Bottom

Fig 6.37. Time history curves of wave slamming pressure on the forward columns, aft column, deck wall, and deck bottom under different column spacings(H=0.1281m, L=1.1135m)

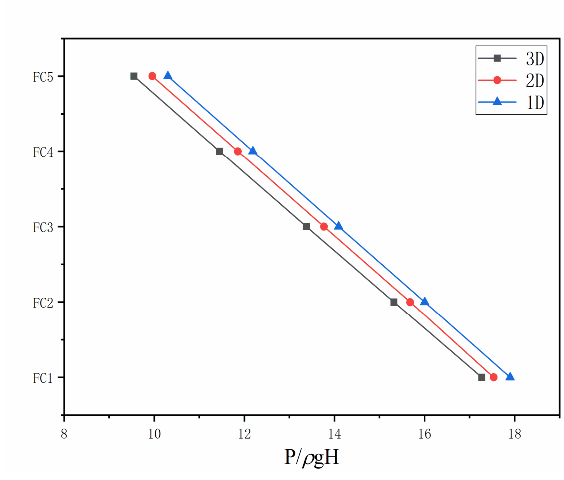

(a) Forward Columns

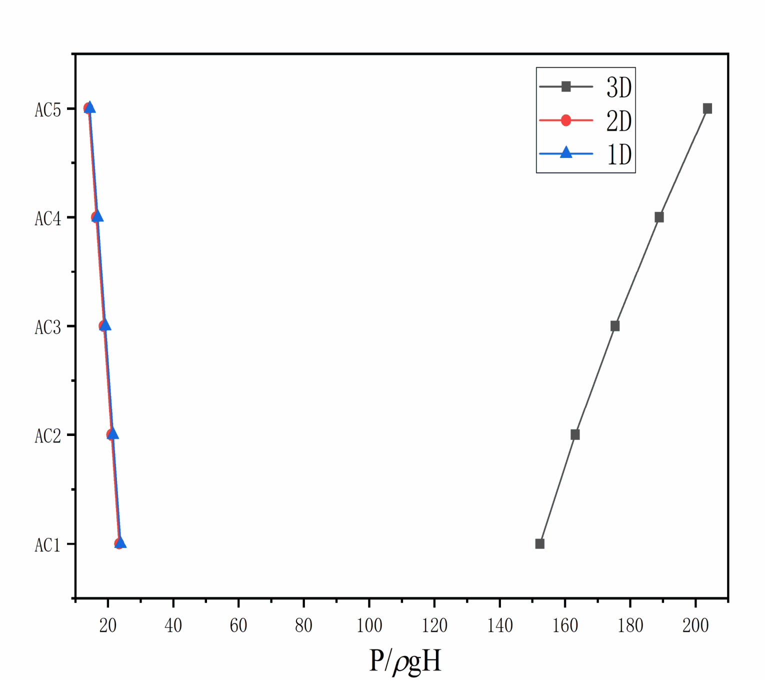

(b) Aft Columns

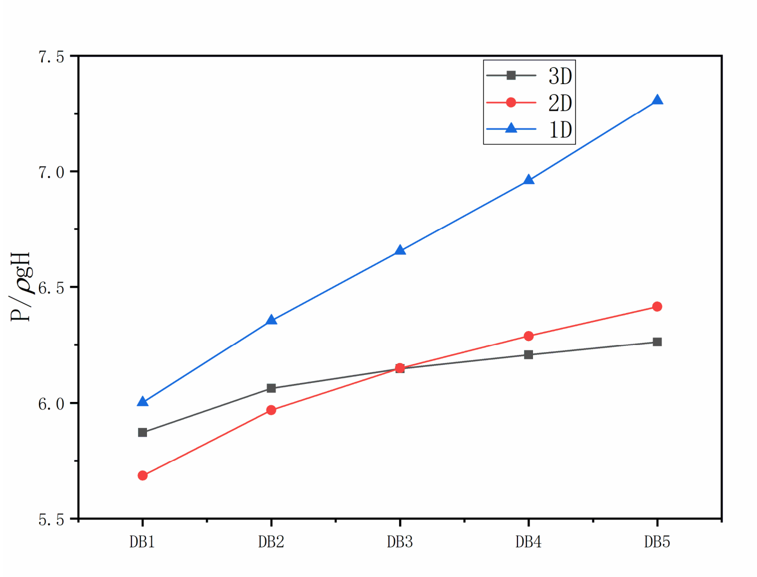

(c) Deck Bottom

Fig 6.38. Slamming load profile for different column spacings

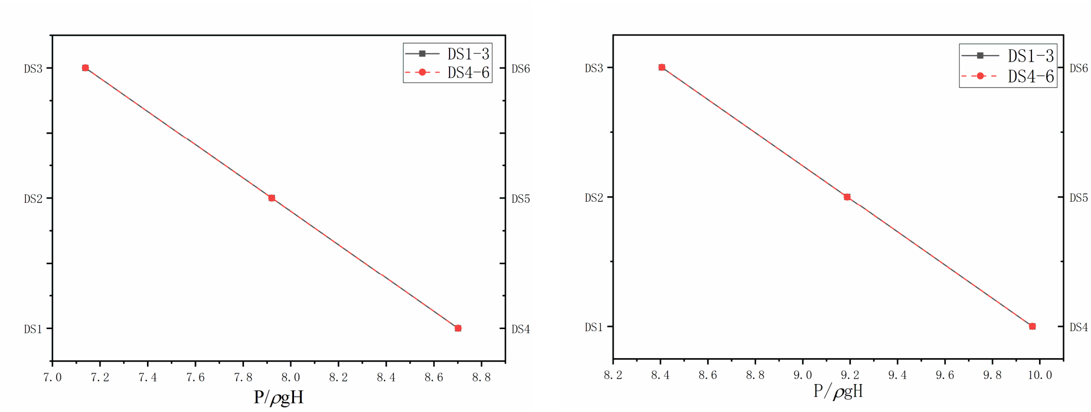

1D

(b)2D

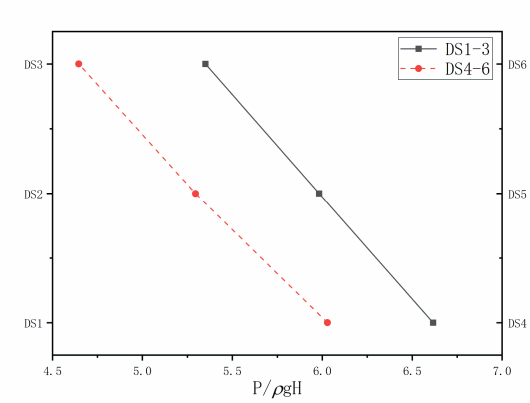

(c)3D

Fig 6.39. Slamming load profile on deck wall

The relationships between column spacing and wave run-up or slamming loads derived under regular wave conditions remain valid under irregular waves. However, the absolute magnitude of slamming loads must be re-evaluated by considering the spectral bandwidth, wave height probability distribution, and extreme value statistics of irregular waves. For extreme wave events such as focused or freak waves, a single highest wave method can be used for rapid prediction—using the equivalent regular wave corresponding to the maximum wave height and its associated period within the irregular wave sequence as input conditions. For general irregular waves, a probability distribution approach is recommended, as follows: individual wave groups satisfying the Rayleigh distribution are first identified and separated from the wave time history, then the slamming responses of these individual waves are weighted and superimposed according to their probabilities, thereby obtaining the statistical estimation of slamming loads under irregular wave conditions.

$$p(H) = \frac{2H}{H_{1/3}^2} \exp\left[-\left(\frac{H}{H_{1/3}}\right)^2\right] \tag{6.1}$$

$$\bar{F} = \int_0^\infty F(H) \cdot p(H) dH \tag{6.2}$$

In addition, according to API-RP-2MET (2021), directional spreading effects significantly reduce wave energy concentration, leading to smaller extreme responses in multidirectional irregular waves compared with those predicted under regular or long-crested wave conditions. Therefore, results obtained under regular waves can be regarded as conservative upper bounds, while responses under irregular waves better reflect realistic sea states. It is thus recommended that final engineering evaluations be performed using numerical simulations or experiments based on both frequency and directional spectra.

6.4 Optimization recommendations of engineering design

Through the above research, qualitative suggestions are given on how to use these factors in engineering design to optimize the design of slamming.

(1) During numerical simulation, more than 11.11 times the characteristic scale of the platform is selected as the width of the virtual flume. Its boundary conditions can be treated with wall surfaces, and the influence of wall effects can be ignored.

By comparing the force on the platform when the flume wall width is 1.5m and 2m, it can be found that the flume width of 1.5m has a greater impact on the force on the platform, especially in the Y direction. During numerical simulation, the influence of the flume wall effect can be ignored if the width of the simulated flume is 11.11 times the characteristic length.

(2) Regarding the shape of the platform columns, square columns have a greater blocking effect on water, a more obvious wave climbing effect, and a greater effect on the column. It is recommended that cylinders be actually used for the project.

By comparing the force conditions of different platform column shapes, it can be found that under the same characteristic size and wave conditions, the wave force, moment and local measuring point force values of the cylinder column are smaller than those of the square column. In the calculation simulation, it can be observed that when the incident wave travels forward and encounters the platform column, the water body will be divided into three parts. One part of the water body continues to climb up the column, and the other two parts of the water body flow along both sides of the column. The reason why the force of the cylinder column is smaller than that of the square column is that due to its smoothness, more water flows away from both sides of the cylinder column and less water stays on the windward side, causing the wave climb on the windward side to be lower than that of the square column and the wave force on it to be smaller than that of a square column. In engineering applications, it is recommended to use cylinder platform columns, so that the overall force of the platform column and the load value of local measuring points are smaller.

(3) Under the condition of ensuring strength, the smaller the column size, the better.

By comparing the force conditions of different platform column sizes, it can be found that under the same column shape and wave conditions, the larger the column size, the greater the wave force, moment and local measuring point force value of the column. The reason is that larger columns have a larger force-bearing area, causing more water to stay on the windward surface and causing larger wave climbs. Therefore, the smaller the platform column size, the smaller the slamming load it will receive, but it will lead to insufficient platform structural strength. In engineering applications, it is recommended to use smaller-sized platform columns, but at the same time, the structural strength of the platform must be ensured.

(4) For the wave slamming of the platform, the relative position of the flat plate has little influence on the slamming. Regarding the moment in the Z direction, the force on the platform is smaller when the column is in the middle. By comparing the forces on the relative positions of different platform plates and columns, it can be found that the forces on different relative positions are relatively small under the same wave conditions. This shows that the relative positions of different platforms' flat plates and columns have little impact on the wave slamming of the platforms.

(5) Regarding the air gap of the platform, under the same column height, the greater the air gap, the greater the probability of waves slamming on the lower surface of the platform plate. It is recommended to appropriately reduce the air gap according to the wave environment.

By comparing the force conditions of different platform air gaps, it can be found that the wave crest height does not directly reach the connection between the column and the deck. The wave will only have an effect on the top of the column and the bottom of the deck after climbing. The larger the initial air gap, the higher the wave climbs. The greater the energy loss, the smaller the wave loads generated at the top of the columns and the bottom of the deck. The wave crest is just close to the height of the deck. At this time, the water particle speed near the wave crest is high, and the wave slamming load on the columns and deck reaches the maximum. The initial air gap is reduced to the point where the wave crest height has exceeded the deck, and the column and deck are located in the area below the wave crest. At this time, the free liquid level rises faster and the slamming is larger. In engineering applications, it is recommended to investigate the working water area of the platform in the early stage of designing the platform, and select the platform freeboard that is greater than the simulated wave climb as the design value.

(6) Regarding the wave heading of the platform column, a 180° wave heading has a greater obstruction effect on the water, the wave climbing effect is more obvious, and

its effect on the column is greater. It is recommended that the project set the column placement direction based on the actual wave heading of 135°.

By comparing the force on the platform under different waves, it can be found that the overall force on the platform is basically the same under the action of different wave directions on columns of the same shape. The force on the local measuring point where the 180° wave is downward is greater than that at 135°. The reason is that when the wave direction is 180°, the wave directly hits the surface of the column, causing the wave to climb higher and the force value of the measuring point to be greater. However, as the height of the measuring point decreases, the pressure difference on platforms with different wave directions gradually decreases.

6.5 Summary of this chapter

This chapter examines the wave slamming load of a typical structure (square column and the deck attached above it) of a semi-submersible platform using the three-dimensional rectangular grid CGNT-CFD method method. It explores the distribution of slamming load under regular waves on the column, pressure-time history curve, wave force characteristics and changes in column shape and wave parameters. It provides information on the impact of different model parameters and other factors on slamming. Under regular wave conditions, considering variations in wave heading, air gap height, column shape, and scale, the main research conclusions are as follows::

1. Under different basin width conditions, the platform’s forces, moments, and slamming loads exhibit high consistency in waveform and period, with the period matching that of the incident waves. Basin width has little effect on the platform’s overall loads in the X and Z directions but has a more significant impact in the Y direction. Under identical wave conditions, the influence on the same measurement point is smaller when the basin width is 2000 mm compared to 1500 mm. Therefore, selecting a basin width equal to 11.11 times the column’s characteristic length (180 mm), i.e., 2000/180, is sufficient to meet the calculation requirements.

2. At an air gap of 185 mm and a wave direction of 180°, square-section and circular columns (with the circular diameter equal to the square column width) exhibit high consistency in the pressure distribution at each measurement point and in the waveform and period of overall slamming loads in the X and Z directions, with the period matching that of the incident waves. However, the square column generally experiences larger slamming load amplitudes: at upper measurement points, the square column is 30%~50% higher than the circular one; at lower measurement points, it is 2%~5% higher. For the platform's overall load in the X direction, the square column consistently exceeds the circular column, in line with the wave run-up trend, with X-direction loads 15.79%~80% higher. In addition, the peak frequencies of the slamming load spectra in both X and Z directions match the incident wave frequency, indicating that the slamming loads are mainly induced by the incident waves.

3. At an air gap of 185 mm and a wave direction of 180°, columns of different sizes show high consistency in the pressure distribution at each measurement point and in the waveform and period of overall slamming loads in the X and Z directions, with the period matching that of the incident waves. As the horizontal cross-sectional size of the column increases, the slamming pressure amplitude at each measurement point generally increases, and the platform's overall load in the X direction also rises; for example, the X-direction negative pressure of a 210 mm×210 mm column is 52.5%~166.7% higher than that of a 150 mm×150 mm column. In addition, the peak frequencies of the slamming load spectra in both the X and Z directions match the incident wave frequency, indicating that the slamming loads are mainly induced by the incident waves.

4. At an air gap of 185 mm and a wave direction of 180°, columns with different relative positions to the top deck exhibit high consistency in pressure distribution at each measurement point, as well as in the waveform and period of overall slamming loads in the X and Z directions, with the period matching that of the incident waves. Larger horizontal cross-sections result in higher slamming

pressure amplitudes at each measurement point, and the platform's overall load in the X direction follows the order: "column at side center" > "column at corner" > "column at center." Slamming loads at upper measurement points are highly sensitive to structural geometric changes, with differences reaching 30.5%–166.7% when the shape, size, and relative position between the platform column and deck are altered. In contrast, slamming load variations at lower measurement points are relatively small, typically within 10%, indicating that the upper structure is the primary sensitive region to wave slamming. In addition, the peak frequencies of slamming load spectra in the X and Z directions match the incident wave frequency, suggesting that the slamming loads are mainly induced by the incident waves.

5. With a column size of 180 mm × 180 mm and a wave direction of 180°, the pressure distribution at each measurement point and the overall slamming loads in the X and Z directions under different air gap conditions show high consistency in waveform and period, with the period matching that of the incident waves. Overall, larger air gaps result in lower pressures at each measurement point, a trend particularly evident at upper points (F1–F4). The platform's overall load in the X direction also decreases as the air gap increases. The air gap has a significant influence on slamming loads—especially for smaller air gaps—where pressures at both upper and lower points increase markedly. For example, under a 135 mm air gap, slamming loads are 78.6%–735.6% higher than those at a 285 mm air gap. This trend indicates that air gap size directly affects energy transfer during the wave run-up process and is a key factor influencing slamming intensity.

6. In the wave-direction sensitivity analysis, a square column with a characteristic size of 180 mm and an air gap of 185 mm was used. The results indicate that, under different wave directions, the pressure distribution at each measurement point and the overall slamming loads in the X and Z directions exhibit high consistency in waveform and period, with the period matching that of the

incident waves. Overall, the 180° wave direction—due to stronger wave blocking and more pronounced wave run-up—produces pressures 11.3%–98.6% higher than those at 135°. The overall loads in the X and Z directions change little between wave directions, indicating that while local wave run-up is enhanced, the overall loading pattern remains stable. The peak frequencies of the slamming load spectra in both the X and Z directions match the incident wave frequency, confirming that they are mainly caused by incident wave action.

7. Under regular wave conditions with an air gap of 185 mm and a wave incident angle of 180°, the influence of column spacing on wave load distribution exhibits clear spatial asymmetry. The front-row columns experience relatively stable slamming loads, with minimal sensitivity to spacing variations. In contrast, the response of the rear-row columns is highly sensitive and displays pronounced nonlinear behavior. Specifically, as the spacing increases from 1D to 2D, shielding effects dominate, leading to a significant reduction in slamming loads on the rear columns. However, when the spacing increases to 3D, enhanced wave interference and diffraction cause a sharp rise in local slamming loads, with peak values reaching up to 20 times those observed in the 1D configuration—marking a distinct "critical amplification range" of column spacing. As the spacing further increases to 4D and beyond, mutual interference between structures weakens, and wave run-up is mitigated accordingly, resulting in a gradual decrease in slamming loads on the rear columns. These findings highlight that rear columns—especially the inner wave-facing surfaces near the structural center—should receive particular attention in layout design and impact-resistant reinforcement. Avoiding typical high-load spacing ranges is essential to ensure structural safety.

7 CONCLUSION

This thesis focuses on the characteristics of wave slamming load on platform columns. It investigates the experimental equipment for measuring wave slamming load and high-frequency long-term data processing and analysis technology, comprehensively examining the wave slamming process of columns with decks. A new CGNT-CFD method method for predicting wave slamming load is introduced and its computational efficiency and prediction accuracy are verified by comparing it with experimental results. The rectangular grid numerical flume is used to systematically reveal the influence of key structural parameters on slamming load. The main findings are briefly summarized and the possibilities for future research are outlined as follows.

7.1 Main research conclusions

The conclusions of this thesis are summarized in the following three aspects:

7.1.1 Research on model experiment measurement technology and characteristics of wave slamming load on platform columns

This thesis proposes a wave slamming load measurement method and a set of experimental result processing methods. The study uses a slamming load measurement device combining pressure transducers and force plates to measure the wave slamming load on the column’s windward surface and upper deck, verifying the performance and reliability of the wave slamming load measurement device. Unlike traditional pressure transducers, this experimental wave slamming load measurement device can be used for large-area slamming load measurement. In processing noise components and dynamic amplification interference in load data, this thesis adopts wavelet denoising and frequency transfer function. The results suggest that the wavelet analysis method can be used to adopt the same parameters to denoise different intensity wave slamming events with high quality without changing peak values. The frequency transfer function (FRF) method is further used to reduce dynamic amplification interference in slamming load measurement signals.

While conventional slamming studies typically employ solitary or focused wave forms to isolate extreme impact mechanisms, this thesis extends the investigation to include regular wave conditions as well. This approach enables a systematic comparison of slamming behaviors across different wave regimes and contributes to a more complete understanding of platform response in both extreme and operational sea states. It should be noted that the present study considers a fixed-platform configuration. Therefore, the findings are not directly applicable to moored floating platforms, where structural motions and mooring compliance may significantly modify wave slamming characteristics. The main conclusions are summarised as follows:

1. Under regular wave conditions, slamming loads exhibit a clear dependence on air gap. With smaller air gaps (135 mm, 185 mm), more wave cases experience frequent slamming events, and the intensity during these events is generally higher than under larger air gap conditions. At low air gaps, higher measurement points tend to register greater slamming intensity, though the frequency of occurrence decreases—particularly evident at points F4 to F1. Under larger air gaps (235 mm, 285 mm), except for a few specific cases, the relationship between slamming intensity and measurement point height is not significant; only a small number of regular wave cases show a distinct increasing or decreasing trend with height, while most cases reflect wave loading without pronounced slamming. Based on these patterns, this study focuses on measurement points, wave conditions, and air gaps

that are more sensitive to variations in slamming pressure to further analyze the relationship between wave slamming and wave parameters.

2. Under focused wave conditions, the air gap has a significant weakening effect on slamming force: the larger the air gap, the smaller the slamming force. However, as the air gap increases further, this attenuation trend gradually slows, indicating that the amplifying effect of deck overhang on slamming is progressively diminishing. The frequency bandwidth also has a notable influence on slamming intensity: narrow-banded focused waves (TBH5, 0.8 – 1.2 s) concentrate energy more effectively, generating higher wave crests and producing much greater slamming pressures (e.g., F1 peak value 14,490 Pa vs. 4,991 Pa, about 2.9 times higher), thereby significantly intensifying slamming effects. In terms of wave run-up, the 180° head-sea condition results in markedly greater run-up along the platform columns (wave height at W1 exceeding W2/W3), whereas under the 135° oblique-sea condition, run-up is reduced and may even break earlier. Force responses differ by direction: in the X direction, slamming forces decrease significantly with increasing air gap (with especially notable attenuation from 185 mm to 235 mm), while in the Z direction, the loads exhibit a nonlinear fluctuation pattern.

3. Under freak wave conditions, even with similar significant wave heights, the slamming loads generated by the JONSWAP spectrum remain markedly higher than those from the S spectrum, with maximum values exceeding the latter by more than six times (e.g., 125.4 kPa for JonM10 vs. 20.65 kPa for S100M10). In cases producing higher slamming pressures, there is a clear correlation between slamming pressure and measurement point height — the higher the point, the greater the pressure, and the higher the risk of structural damage. The extreme case occurs under the combination of JonM10, 180° wave heading, and a 185 mm air gap, reaching 152.7 kPa. This scenario poses the greatest threat to structural integrity and should be a priority in engineering design to prevent failure. At 135° wave heading, the resultant load in the X/Y directions is close to that of the 180° heading, but the overall slamming intensity is significantly reduced (e.g., 5.376 kPa at F1 vs. 125.4

kPa). In terms of wave run-up, JonM10 shows a significantly higher run-up ratio than S100M10, which decreases progressively with increasing air gap. Overall, slamming intensity increases with measurement point height, with positions near the deck being most susceptible to damage. Double-peaked impact processes are often observed at top measurement points, with peak magnitudes varying depending on wave type. Under oblique wave conditions, although the resultant force direction is similar to that in head seas, the overall slamming intensity decreases substantially. Compared with the two typical freak wave spectra, J-type waves also outperform S-type waves in run-up capability, while increased air gap generally suppresses run-up behavior.

4. Under regular wave conditions, slamming intensity generally increases with measurement point height (F1 > F2 > F3 > F4), with F1 (near the deck) showing abnormal amplification under oblique waves due to deck jet effects. Air gap, wave steepness, wave period, and wave heading are the primary influencing factors, among which the air gap effect is the most direct—except for R6, R9, and R14, most cases exhibit a decrease in slamming peak with increasing air gap. For R6, R9, and R14, the peaks occur at an air gap of 185 mm, reflecting the coupling effect of wave steepness (0.115–0.12) and period (1.0–1.2 s). At a 135 mm air gap, short periods (0.8 s, 1.0 s) are most sensitive to changes in wave steepness, with increased steepness significantly amplifying slamming; at a 185 mm air gap, long periods (1.2 s) are most sensitive, with trends opposite to those at 135 mm. Regardless of air gap size, high measurement points (F1/F2) generally show greater variability in slamming peaks across different steepness values. Regarding period effects, the period producing the maximum peak varies with air gap: T = 1.0 s for 135 mm, and T = 1.2 s for 185 mm. Overall, large air gaps yield smaller slamming values with low sensitivity to period changes, while small air gaps are highly sensitive and show distinct variation trends. Additionally, slamming peaks under oblique waves are generally lower than under head seas, with the difference increasing as steepness grows, and sensitivity to measurement point height is notably weaker under oblique waves than in head seas.

7.1.2 Research on numerical flume simulation technology for wave slamming load

This thesis innovatively proposes a CGNT-CFD method to study the wave pressure and wave force characteristics of platform columns under different regular waves. By comparing model experimental data, the accuracy of wave generation by the numerical flume solver is verified. The numerical flume can accurately predict the wave-induced load and wave force of a single column and analyze the influence of regular wave steepness and period on wave slamming load. Moreover, its computational efficiency is significantly higher than that of conventional commercial viscous CFD software such as STAR-CCM+. Based on regular wave scenarios, a representative simulation case with an air gap of 185 mm and a wave heading angle of 180° is selected. The following analysis results are obtained:

1. The maximum prediction error of wave-induced load by the numerical flume is less than 4%, demonstrating predictive accuracy comparable to that of STAR-CCM+. This fully validates the method’s predictive accuracy and reliability in wave slamming problems.

2. The CGNT-CFD method is based on a three-dimensional Cartesian grid finite difference scheme, offering advantages such as structured mesh configuration and simplified grid generation, which significantly reduce both mesh preparation and computational costs. Validated against experimental data, the method maintains high simulation accuracy while requiring fewer computational cells. Its computational efficiency surpasses that of STAR-CCM+, demonstrating strong potential for practical engineering applications.

3. The numerical flume method is based on CIP theory. Compared with VOF HRIC theory used by traditional fluid mechanics software for describing free water surface, this method captures free water surface more accurately.

4. By comparing the force on platform under flume wall widths of 1.5m and 2m, it can be found that the width of 1.5m flume has a greater impact on platform force,

especially in the Y direction. When simulating numerically, the width of the simulation flume can be 11.11 times the characteristic length without considering the impact of flume wall effect.

7.1.3 Research on the influence of key control parameters on wave slamming load of platform columns

This thesis uses numerical flume methods to study the main factors affecting platform slamming loads, including wave characteristics such as waveform, wave height, and wave period, and platform characteristics such as geometric parameters. The focus is on the process and load characteristics of regular wave slamming and the influence of wave period, different column parameters, and wave direction on wave slamming loads. The distribution of column slamming loads under regular waves, pressure-time curves, and the relationship between wave force characteristics and column shape and wave parameters are explored. An in-depth analysis of the influence mechanism of column spacing on the wave slamming load characteristics of a semi-submersible platform is conducted. It focused on the effects of different column spacings (1D, 2D, 3D) on the load characteristics of the front column, rear column, and deck structure. The research provides a reference for future platform column design, construction, and optimization. The conclusions are as follows:

1. Effects of Cross-Section Shape, Size, and Relative Position to the Deck
   Under the conditions of an air gap of 185 mm and a wave heading of 180°, square columns (compared with circular columns of equal width) generally experience higher slamming loads: 30%–50% higher at upper measurement points and 2%–5% higher at lower points. The overall platform load in the X direction follows the same trend as wave run-up, with square-column platforms subjected to greater wave action than circular-column platforms. As the cross-sectional size increases, both slamming pressure and overall X-direction load increase accordingly; for example, the X-direction negative load of a 210 mm × 210 mm column is 52.5%–166.7% higher than that of a 150 mm × 150

mm column. The magnitude of slamming pressure at each measurement point and the overall X-direction load follow the pattern: “column at mid-side” > “column at corner” > “column at center.” Moreover, regardless of changes in column size, cross-sectional shape, or relative position to the deck, the pressure at all measurement points and the overall slamming load in the X and Z directions exhibit waveforms and periods consistent with those of the incident waves, and the peak frequencies of the slamming load spectra in both directions always match the incident wave frequency.

2. Air Gap Effect

   With a column size of 180 mm × 180 mm and a wave heading of 180°, a larger air gap results in lower slamming pressure and overall X-direction load, with the reduction being more pronounced at the upper measurement points. Under small air gaps, slamming is significantly intensified, with the load at a 135 mm air gap exceeding that at a 285 mm air gap by 78.6%–735.6%. This trend indicates that the air gap directly affects wave run-up energy transfer and is a key controlling factor for slamming intensity.

3. Wave Heading Effect

   For a square column with a characteristic size of 180 mm and an air gap of 185 mm, the 180° wave heading, due to stronger wave blocking and more pronounced wave run-up, produces pressures at each measurement point that are 11.3%–98.6% higher than those under the 135° heading. Despite the significant increase in local loads, the overall X- and Z-direction load patterns remain stable across different wave headings.

4. Spacing Effect of Columns

   Under regular wave conditions with an air gap of 185 mm and a wave heading of 180°, column spacing has minimal impact on the wave loads experienced by the front-row columns but significantly affects the slamming response of the rear-row columns, exhibiting a distinctly nonlinear trend. As the spacing increases from 1D to 2D, slamming loads on the rear columns decrease markedly due to shielding effects. However, when the spacing expands to 3D, wave interference becomes more pronounced, leading to a sharp surge in slamming loads on the rear columns—peaking at nearly 20 times the value observed in the 1D case—defining a locally intensified “characteristic spacing scale.” If the spacing continues to increase, structural interference and localized wave run-up effects gradually weaken, which helps reduce slamming loads on the rear columns. These findings indicate that rear columns—particularly the inner wave-facing surfaces—should receive special attention in structural safety assessments and slamming-resistant reinforcement design to avoid falling into typical high-load spacing ranges.

7.2 Prospects for future research

Researching the mechanism of wave slamming and predicting slamming loads can provide important references for the design of marine structures and help avoid wave slamming accidents. This thesis combines model experiments and numerical flume to study the wave slamming load characteristics of platform columns and analyze the influence of key design parameters on column slamming loads. The results have engineering application value. However, there are still many issues worth further study on wave slamming of marine structures, including:

1. Wave slamming involves two-way coupling between flow field and structure This thesis focuses on studying wave slamming from the perspective of load, assuming that solids are rigid under the action of slamming loads. In reality, marine structures will vibrate and deform, which will affect the wave slamming process. Future research should explore the material and mechanical properties of marine structures and carry out solid-liquid coupling simulation analysis to make structural design safer.

2. The CGNT-CFD numerical flume does not take into consideration of the motion response or mooring effect of platform columns. In actual engineering, platforms

will have full-degree-of-freedom motion responses such as heave, pitch, and roll when subjected to waves. Floating platforms are moored to the sea bed using moooring chains. In the present study, a fixed-platform assumption is adopted; consequently, the influence of platform motions and mooring compliance on wave slamming loads is not explicitly considered and should be addressed in future investigations.

3. Although the CGNT-CFD method, with its structured three-dimensional Cartesian grid system and high-accuracy free surface capturing technique, has demonstrated excellent computational accuracy and engineering applicability in simulating wave slamming on floating platforms, it currently relies primarily on a serial computing framework. A dedicated parallel computing module for such problems has yet to be developed. In future work, a parallelized CGNT-CFD solver architecture should be established to enable efficient scheduling of multi-core computing resources and load balancing, thereby further unlocking the performance potential of Cartesian grid methods in wave slamming simulations.

4. The model experiments lack flow field velocity measurement data and the mechanism research is mainly based on CFD methods. The model experiment constructed in this article does not add flow field velocity measurement devices such as particle velocimeters. The three-dimensional velocity field data can provide a more in-depth mechanism study for the wave slamming load phenomenon of platform columns. It can also optimize the calculation methods related to numerical flume and help the right-angle network. The grid numerical flume is updated iteratively to establish a more efficient and accurate prediction method for wave slamming loads on marine structures.

5. Based on the findings of this study, existing simplified algorithms for wave slamming loads (e.g., OTG13/14) should be refined, and a more accurate and

efficient rapid assessment method suitable for engineering design should be proposed—balancing both computational efficiency and predictive accuracy.

6. It should be noted that the 1:100 scale model used in this study may overestimate the air gap when extrapolated to full scale due to scale effects. According to industry practice, platform design air gaps are typically controlled within the range of 8–12 m. However, under extreme sea states or in designs requiring higher safety margins, the air gap may reach 15–20 m. In this context, the extrapolated results of 13.5–28.5 m obtained in this study are intended for illustrative purposes only. These results should be interpreted as indicative of the sensitivity of air-gap behaviour under extreme wave conditions, rather than as direct or final design guidance. Future work should incorporate semi-empirical approaches and industry standards to refine and constrain these results, enhancing their engineering applicability.

7. Future research should further explore the quantitative relationships between wave slamming loads and the geometric parameters of platform columns. A slamming response model will be developed that incorporates key wave inputs and sea state parameters. On this basis, a parametric design methodology for platform column geometry should be established, providing both theoretical support and practical tools for structural optimization and rapid engineering iteration under various operating conditions.

8. The transient peak and spatial distribution of wave slamming loads are highly sensitive to local cavitation and entrained-air effects. Air-entrainment modelling is prioritised because the present measurements indicate that peak slamming pressures are highly sensitive to local two-phase processes. Specifically, the pressure records show sharp peaks and noticeable case-to-case variability under highly nonlinear impacts, suggesting that unresolved air-entrainment or local cavitation effects may modulate the peak pressure levels and the temporal evolution of the load. Air entrainment can reduce or redistribute peak pressures

through cushioning, ventilation, and pressure-relief mechanisms, while also affecting the spatial distribution of impact loads near the deck edge. Future research should, based on the CGNT-CFD method, focus on modeling and experimental validation of air–water interaction effects, aiming to develop an efficient numerical tool capable of accurately capturing the evolution of slamming loads under cavitation conditions, thereby providing more reliable theoretical and engineering support for impact-resistant platform design.

REFERENCE

Abdussamie, N., Y. Drobyshevski, R. Ojeda, G. Thomas and W. Amin, 2017. Experimental investigation of wave-in-deck impact events on a TLP model. Ocean Engineering 142, 541-562.

Ariyarathne, K., K.-A. Chang and R. Mercier, 2012. Green water impact pressure on a three-dimensional model structure. Experiments in Fluids 53(6), 1879-1894.

Baarholm, R., 2005. A Simple Numerical Method for Evaluation of Water Impact Loads on Decks of Large-Volume Offshore Platforms. ASME 2005 24th International Conference on Offshore Mechanics and Arctic Engineering.

Barcellona, M., Simos, M., Greco, M., & Faltinsen, O. M, 2003. An experimental investigation on bow water shipping. Journal of ship research 47(04), 327-346.

Bilandi, R. N., Jamei, S., Roshan, F., & Azizi, M., 2018. Numerical simulation of vertical water impact of asymmetric wedges by using a finite volume method combined with a volume-of-fluid technique. Ocean Engineering 160, 119-131.

Bihs, H., Kamath, A., Alagan Chella, M., Aggarwal, A., & Arntsen, Ø. A., 2016. A new level set numerical wave tank with improved density interpolation for complex wave hydrodynamics. Computers & Fluids 140, 191-208.

Bredmose, H., D. H. Peregrine and G. N. Bullock, 2009. Violent breaking wave slammings. Part 2: modelling the effect of air. Journal of Fluid Mechanics 641, 389-430.

Brodtkorb, B., 2008. Prediction of Wave-in-Deck Forces on Fixed Jacket-Type Structures Based on CFD Calculations. ASME 2008 27th International Conference on Offshore Mechanics and Arctic Engineering.

Chen, H. C., & Yu, K., 2009. CFD simulations of wave–current-body interactions including greenwater and wet deck slamming. Computers & fluids, 38(5), 970-980.

Chen, Z. W., Jiao, J. L., Jiang, C. X., Si, H. L., & Chen, S., 2024. Scale effects on wave loads and slamming loads in ship hydroelasticity simulation by CFD - FEM method. Ocean Engineering 314(Part 1), 119718.

Choi, S. -J., Lee, K. -H., & Gudmestad, O. T., 2015. The effect of dynamic amplification due to a structure's vibration on breaking wave impact. Ocean Engineering 96, 8-20.

Chuang, W.-L., K.-A. Chang and R. Mercier, 2017. "Impact pressure and void fraction due to plunging breaking wave slamming on a 2D TLP structure." Experiments in Fluids 58(6), 68.

Cui, W.-h., 2018. Numerical Simulation of the Interaction between a Large-Scale Floating Platform and a Mooring Chain System Doctor, Shanghai Jiao Tong University.

Dalane, E., 2011. Estimation of ALS wave-column impact loads for a semi-submersible and a simplified assessment of the associated structural response.(Master's thesis, Norges teknisk-naturvitenskapelige universitet, Fakultet for ingeniørvitenskap og teknologi, Institutt for marin teknikk).

Datta, T. K. and A. K. Jain, 1988. "Nonlinear surge response of a tension leg platform to random wave forces." Engineering Structures 10(3), 204-210.

de Sonneville, B., B. Hofland, A. Mowinckel and B. T. Paulsen, 2015. wave slamming Loads on Offshore Gravity Based Structure. ASME 2015 34th International Conference on Ocean, Offshore and Arctic Engineering.

Ding, H.-y. and X.-q. Liu, 2012. "Test Research on Impact of Towing Speed on Towing of Ocean Platform with Four Bucket Foundations." Journal of Tianjin University(Science and Technology 45(01), 43-49.

Dong, Y.-q., 2005. Wave Loads and Response of the Oil-Extraction Platform in Deep Ocean, Tianjin University Press.

Du, Z. and Y.-g. Liu, 2014. "Towing Resistance Evaluation for Self-Elevating Platform." Ship Engineering 36(S1), 181-183+201.

Engle, A. and R. Lewis, 2003. A comparison of hydrodynamic impacts prediction methods with two dimensional drop test data. Marine Structures 16(2), 175-182.

Entezam, S. and S. Kazemi, 2015. Numerical modeling of wave run-up along columns of semi-submersible platforms. International Journal of Marine Science and Environment 5(2), 77-86.

Facci, A. L., Panciroli, R., Ubertini, S., & Porfiri, M., 2015. Assessment of PIV - based analysis of water entry problems through synthetic numerical datasets. Journal of Fluids and Structures 55, 484-500.

Facci, A. L., Porfiri, M., & Ubertini, S, 2016. Three - dimensional water entry of a solid body: A computational study. Journal of Fluids and Structures 66, 36 - 53.

Faltinsen, O.M, 2001. Hydroelastic slamming. Journal of Marine Science and Technology. Technol 5, 49 – 65.

Fu, L., 2020. Research on the Prediction of Slamming Loads and Structural Strength Assessment Method for Semi-Submersible Platforms, Harbin Engineering University.

Gie, T. S. and W. de Boom, 1981. The Wave Induced Motions of a Tension Leg Platform in Deep Water. Offshore Technology Conference.

Gingold, R. A. and J. J. Monaghan, 1977. Smoothed particle hydrodynamics: theory and application to non-spherical stars. Monthly Notices of the Royal Astronomical Society 181(3), 375-389.

Gu, G., 2008. An overview on research and development of Spar platform. Ship Science and Technology(03), 167-170.

Gu, J. Y. and J. M. Yang, 2015. Characteristics of tendon vortex induced vibrations influenced by platform motion. Chuan Bo Li Xue/Journal of Ship Mechanics 19, 677-689.

Haver, S. K., 2013. Prediction of characteristic response for design purposes. Preliminary Revision 5, 54.

Hayat, M. M., 2012. Study on Structural Analysis Techniques of TLP Master, Harbin Engineering University.

Huo, F. L..and H.-X. Zhang, 2015. Sensitivity Analysis of Wave Slamming Load with Respect to Wind Load for Semi-Submersible Platform Design. Journal of Shanghai Jiaotong University(Science) 20(04), 385-394.

Huo, F. L., Y. Nie, D. Q. Yang, G. Dong and J. Cui, 2016. Sensitivity analysis of air gap motion with respect to wind load and mooring system for semi-submersible platform design. China Ocean Engineering.

Huo, F. L.., Zhao, Y., Zhang, J., Zhang, M., & Yuan, Z.-M., 2021. Study on slamming pressure characteristics of a floating platform under freak waves. Journal of Marine Science and Engineering, 9(12), 1266.

Huo, F. L.., Zhao, Y., Zhang, J., Zhang, M., & Yuan, Z.-M., 2023. Study on wave slamming characteristics of a typical floating wind turbine under freak waves. Ocean Engineering 269, 113464.

Huo, F. L., Ye, Z., Nie, Y., Yuan, Z.-M., & Xu, Y., 2025. Experimental investigation of wave slamming responses of a moored semi-submersible platform under extreme seas. China Ocean Engineering, 39, 1 – 16

Iwanowski, B., M. Lefranc and R. Wemmenhove, 2009. CFD Simulation of Wave Run-Up on a Semi-Submersible and Comparison With Experiment. ASME 2009 28th International Conference on Ocean, Offshore and Arctic Engineering.

Jiang, Z.-y. and J. Cui, 2014. On Numerical Investigation of Air Gap for Semi-submersible Platform in Irregular Waves. China Offshore Platform 29(01), 13-27.

Kaiser, M. J., Y. Yu and C. J. Jablonowski, 2009. Modeling lost production from destroyed platforms in the 2004–2005 Gulf of Mexico hurricane seasons. Energy 34(9), 1156-1171.

Kamath, A., Alagan Chella, M., Bihs, H., & Arntsen, Ø. A., 2016. Breaking wave interaction with a vertical cylinder and the effect of breaker location. Ocean Engineering128, 105-115.

Kaplan, P. and M. N. Silbert, 1976. Impact Forces on Platform Horizontal Members in the Splash Zone. Offshore Technology Conference.

Kapsenberg GK, 2011. Slamming of ships: where are we now? Philos Trans A Math Phys Eng Sci. 369(1947):2892-919.

Kazemi, S. and A. Incecik, 2005. Numerical Prediction of Air Gap Response of Floating Offshore Structures Using Direct Boundary Element Method. ASME 2005 24th International Conference on Offshore Mechanics and Arctic Engineering.

Kazemi, S. and A. Incecik, 2006. Experimental Study of Air Gap Response and wave slamming Forces of a Semi-Submersible Drilling Unit. 25th International Conference on Offshore Mechanics and Arctic Engineering.

Kim, J.-W., A. Magee and K. Y. H. Guan , 2011. CFD Simulation of Flow-Induced Motions of a Multi-Column Floating Platform. ASME 2011 30th International Conference on Ocean, Offshore and Arctic Engineering.

Kim, M. S., H. S. Park, K. H. Jung and H. H. Chun, 2016. Air-gap effect on life boat arrangement for a semi-submersible FPU. International Journal of Naval Architecture and Ocean Engineering 8(5), 487-495.

Krastev, V. K., Facci, A. L., & Ubertini, S., 2018. Asymmetric water impact of a two dimensional wedge: A systematic numerical study with transition to ventilating flow conditions. Ocean Engineering147, 386-398.

Li, J., Z. Huang and S. K. Tan, 2010. Extreme Air-Gap Response below Deck of Floating Structures. The International Journal of Ocean and Climate Systems 1(1), 15-26.

Liang, X., J. Yang, L. Xiao, X. Li and J. Li, 2010. Numerical Study of Air Gap Response and wave slamming Load on a Moored Semi-Submersible Platform in Predetermined Irregular Wave Train. Asme International Conference on Ocean.

Lin, Z., Liu, X., & Lotfian, S., 2021. Impacts of water depth increase on offshore floating wind turbine dynamics. Ocean Engineering, 224, 108697.

Lind, S. J., Stansby, P. K., Rogers, B. D., & Lloyd, P. M., 2015. Numerical predictions of water–air wave slam using incompressible–compressible smoothed particle hydrodynamics. Applied Ocean Research 49, 57-71.

Liu, J.-c. and Y.-h. Guo, 2018. An Experimental Study of wave slamming Loads on a Drilling Semi-submersible Platform. Ocean Engineering Equipment and Technology 5(S1), 234-237.

Liu Jianyu, 2024. Research on nonlinear motion and slamming characteristics of the connecting bridge of trimaran. [Doctoral dissertation, Harbin Engineering University], 44-46.

Lucy, L. B., 1977. A numerical approach to the testing of the fission hypothesis. Astronomical Journal, vol. 82, 1013-1024.

Lugni, C., M. Brocchini and O. M. Faltinsen, 2006. wave slamming loads: The role of the flip-through. Physics of Fluids 18(12).

Marine Public, 2020. Offshore Environmental Conditions for Marine Projects. Marine Public.

Martínez-Ferrer, P. J., Qian, L., Ma, Z., Causon, D. M., & Mingham, C. G., 2018. Improved numerical wave generation for modelling ocean and coastal engineering problems. Ocean Engineering152, 257-272.

Matsumoto, F. T., R. A. Watai, A. N. Simos and M. D. A. S. Ferreira, 2013. Wave Run-Up and Air Gap Prediction for a Large-Volume Semi-Submersible Platform. Journal of Offshore Mechanics and Arctic Engineering 135(1).

McIver, D. B., 1981. The Static Offset In Waves Of Tension Leg Platforms. Offshore Technology Conference.

M. S. Longuet-Higgins, E. D. Cokelet, 1976.The Deformation of Steep Surface Waves on Water A Numerical Method of Computation. Proceedings of the Royal Society of London A Mathematical and Physical Sciences.350(1660), 1-26.

Naess, A., C. T. Stansberg, O. Gaidai and R. J. Baarholm, 2008. Statistics of Extreme Events in Airgap Measurements. ASME 2008 27th International Conference on Offshore Mechanics and Arctic Engineering.

Nielsen, F. G., 2003. Comparative study on airgap under floating platforms and run-up along platform columns. Marine Structures 16(2), 97-134.

Oger, G., M. Doring, B. Alessandrini and P. Ferrant, 2006. Two-dimensional SPH simulations of wedge water entries. Journal of Computational Physics 213(2), 803-822.

Oran, C., 1983. Overall Dynamic Characteristics of Tension Leg Platforms. Offshore Technology Conference.

PC, S., 2001. Prediction of bow door loads in extreme wave conditions. Proceedings of the RINA Conference on Design and Operation for Abnormal Conditions, London.

Petroleum Safety Authority Norway (PSA), 2016. Investigation of an incident with fatal consequences on COSLInnovator, 30 December 2015 Investigation report, Activity number 418005005, approved 6 July 2016.

Qiang, L., 2013. The Research on Mooring System for 981 Semi-submersible Drilling Unit Master, Yangtze University.

Qin, H., Tang, W. Y., Xue, H. X., & Hu, Z. , 2017. Numerical study of nonlinear freak wave impact underneath a fixed horizontal deck in 2-D space. Applied Ocean Research 64, 155-168.

Ren, B., Z. Ding, Y. Wang and X. Ren, 2007. Experimental Study of Regular wave slamming On the Three-dimensional Structure In the Splash Zone. The Seventeenth International Offshore and Polar Engineering Conference.

Roos, J., C. Swan, S. Haver and O. T. Gudmestad, 2009. An Experimental Investigation of wave slammings on the Deck of a Gravity Based Structure. ASME 2009 28th International Conference on Ocean, Offshore and Arctic Engineering.

Shaanxi United Mechanical Co., Ltd., 2024. China Oilfield Services takes the lead in using Intelligent Monitoring System for Key Equipment of Offshore Drilling Platforms, 2 July 2024.

Shan, T.-B., X. Li, G. Chen, L.-f. Xiao, H.-n. Lu and J. Li, 2012. Leg Spacing Effect On Wave Run-Up And Non-Linear Wave Disturbance Along Semi-Submersible

Columns. The Twenty-second International Offshore and Polar Engineering Conference.

Shan, T.-B. and J. Yang, 2014. Current Effects on Wave Run-up Characteristics Around Column. Journal of Shanghai Jiaotong University 48(01), 116-124+131.

Simos, A. N., J. o. V. Sparano, J. A. P. Aranha and V. c. L. F. Matos, 2008. 2nd Order Hydrodynamic Effects on Resonant Heave, Pitch and Roll Motions of a Large-Volume Semi-Submersible Platform. ASME 2008 27th International Conference on Offshore Mechanics and Arctic Engineering.

Simos, A. N., J. V. Sparano, J. A. P. Aranha and V. L. F. Matos, 2008. 2nd Order Hydrodynamic Effects on Resonant Heave, Pitch and Roll Motions of a Large-Volume Semi-Submersible Platform. ASME 2008 27th International Conference on Offshore Mechanics and Arctic Engineering.

Stansberg, C. T., R. Baarholm, T. Fokk, O. T. Gudmestad and S. Haver, 2004. Wave Amplification and Possible Deck Impact on Gravity Based Structure in 10-4 Probability Extreme Crest Heights. ASME 2004 23rd International Conference on Offshore Mechanics and Arctic Engineering.

Sun, H. and C.-h. Lu, 2003. Experimental research on the fluid-structure interaction in water entry of2D elastic wedge Chinese Journal of Hydrodynamics(01), 104-109.

Suyuthi, A. and S. K. Haver, 2009. Extreme Loads Due to Wave Breaking Against Platform Column. The Nineteenth International Offshore and Polar Engineering Conference.

Sweetman, B. and S. R. Winterstein, 2003. Non-Gaussian Air Gap Response Models for Floating Structures. Journal of Engineering Mechanics 129(3), 302-309.

Sweetman, B., S. R. Winterstein, T. S. Meling, J. Birknes and D. N. V. Høvik, 2001. Airgap Prediction: Use of Second-Order Diffraction and Multicolumn Models. Proceedings Isope

Teigen, P. and J. M. Niedzwecki, 2003. Wave Diffraction Effects And Runup Around Multicolumn Structure. The Thirteenth International Offshore and Polar Engineering Conference.

Terziev, M., Tezdogan, T., & Incecik, A, 2020. A posteriori error and uncertainty estimation in computational ship hydrodynamics. Ocean Engineering, 208, 107434.

The Sun, 2020. I swam for my life in freezing seas as hundreds died in MS Estonia disaster, The Sun, 13 October 2020.

Veldman, A. E. P., R. Luppes,et al., 2011. Extreme wave slamming on Offshore Platforms and Coastal Constructions. ASME 2011 30th International Conference on Ocean, Offshore and Arctic Engineering.

Wagner, H., 2006. Über Stoß- und Gleitvogänge an der Oberfläche von Flüssigkeiten. ZAMM - Journal of Applied Mathematics and Mechanics / Zeitschrift für Angewandte Mathematik und Mechanik 12, 193-215.

Wu, J., 2014. Main structural features and technical characteristics of different types of tension leg platforms. Marine Science, 38(04), 101-108.

Wang, X., Zhou, J. -F., Wang, Z., & You, Y. -X., 2018. A numerical and experimental study of internal solitary wave loads on semi - submersible platforms. Ocean Engineering 150, 298 - 308.

Wang, Y.-y., 2011. Research on Computation of Hydrodynamic Performance for Oceanic Floating Platform in Deepwater." Journal of Dalian University of Technology 51(06), 837-845.

Wang, Z.-d. and M.-y. liu, 2015. Air gap prediction of a semi-submersible platform. The Ocean Engineering 33(05), 10-15.

Webb, G., 2009. Providing Real-time Biofeedback for Amputee Gait Re-training. NI Days Worldwide Graphical Systems Design Conference.

Xie, Z., Stoesser, T., Yan, S., Ma, Q., & Lin, P. (2020). A Cartesian cut-cell based multiphase flow model for large-eddy simulation of three-dimensional wave-structure interaction. Computers & Fluids, 213, 104747.

Yan, G.-w. and J.-p. Ou, 2012. The Conceptual Design of New Type Separating Self-balance Minimum-offshore-surface Extended Mooring TLP (SSME TLP). Science Technology and Engineering 12(08), 1724-1732.

Yang, B. and A.-g. Shi, 2015. Simulation of ship's non-linear roll motion. Journal of Ship Mechanics 19(05), 509-517.

Yang, S., X.-f. Kuang and Q.-m. Miao, 2009. The Stability Analysis of New Concept TLP in deep water. Proceedings of the 9th National Conference on Hydrodynamics and the 22nd National Symposium on Hydrodynamics, Chengdu, Sichuan, China.

Zeng, Z. and J. Yang, 2009. Air gap prediction of a semi-submersible platform." The Ocean Engineering 27(03), 14-22.

Zhao, G.-x. , 2006. FPSO Design Technology. China Offshore Platform(01), 1-5.

Zhao, X.-z., 2009. Experimental and Numerical Study of Freak Wave Doctor, Dalian University of Technology.

Zheng, K. and Z.-c. Sun, 2009. On methods of processing solid boundary condition in SPH simulation. Port & Waterway Engineering(08) 23-27.

Zheng, X.-l. and S. Huang, 2014. Study of ship resistance prediction method based on CFD. Journal of Jiangsu University of Science and Technology(Natural Science Edition) 28(02), 109-113.

Zhu, R.-c. and H.-q. Guo, 2009. A Computational Method for Evaluation of Added Mass and Damping of Ship Based on CFD Theory. Journal of Shanghai Jiaotong University 43(02), 198-203.

APPENDIX A

The appendix A details the wave slamming model experiment based on water flume.

A.1 Objectives of the experiment

A refined slamming experiment is conducted on a semi-submersible platform to investigate the characteristics and mechanisms of wave slamming loads under different wave conditions, providing validation data for numerical simulations. The following aspects are studied:

Fig 0.1. numerical wave tank (20 m×1.0 m×1.2m)

1. Under regular wave conditions, wave slamming loads on the square columns,considering the influence of different wave parameters such as wave height and period.
2. Under irregular wave conditions, wave slamming loads on the square columns

3. Under breaking wave conditions, wave slamming loads on the square columns

4. The effect of air gaps on wave slamming loads

5. The influence of the air gap of the pontoon on wave slamming

A.2 Experiment model

The experimental research objects include two types of structural models: square columns with decks and deck boxes, as shown in Fig 0.2. The dimensions of the experimental models are based on actual semi-submersible offshore platforms. The main dimensions and their comparison with the two types of semi-submersible platforms are presented in Table 1. The dimensions of the square columns are shown in Fig 0.2, and the dimensions of the deck boxes are shown in Fig 0.3.

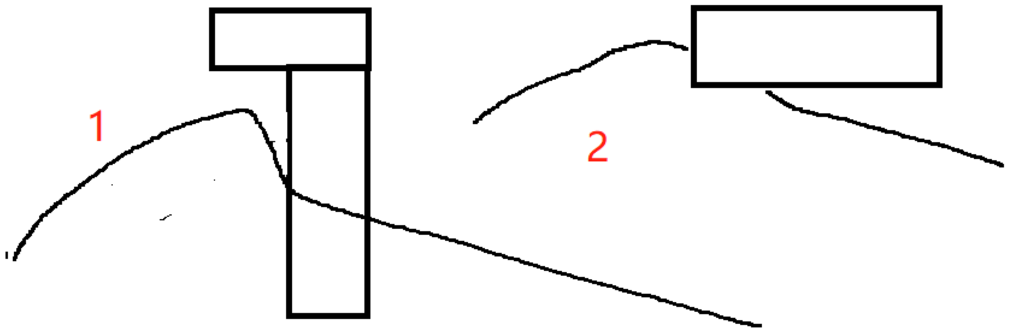

Fig 0.2. Experimental research objects

Table 0.1. Model dimension (1:100)

Parameter	Letter	CM-SD1000	7th semi	Column model
Column length	*Lc*	16000	19250	180
Column width	*Bc*	15000	18500	180
Survival draft	*D*	18000	19500	224.5
Distance from water plane to main deck upper surface	*Ha*	22500	25800	227.5
Distance from baseline to main deck upper surface	*Ht*	40500	45300	452

Height of deckbox	*Hd*	8500	8800	52
Distance from baseline to main deck lower surface	*Ht-Hd*	32000	36500	400
Distance from water plane to main deck lower surface	*Ht-Hd-D*	14000	17000	175.5
Proportion of draft to column height	*D/(Ht-Hd)*	0.56	0.53	0.56
Proportion of column height above water to column height	*(Ht-Hd-D)/(Ht-Hd)*	0.44	0.47	0.44
Proportion of column width to height	*Bc/(Ht-Hd)*	0.47	0.51	0.45
Proportion of column width to height above water	*Bc/(Ht-Hd-D)*	1.07	1.09	1.03

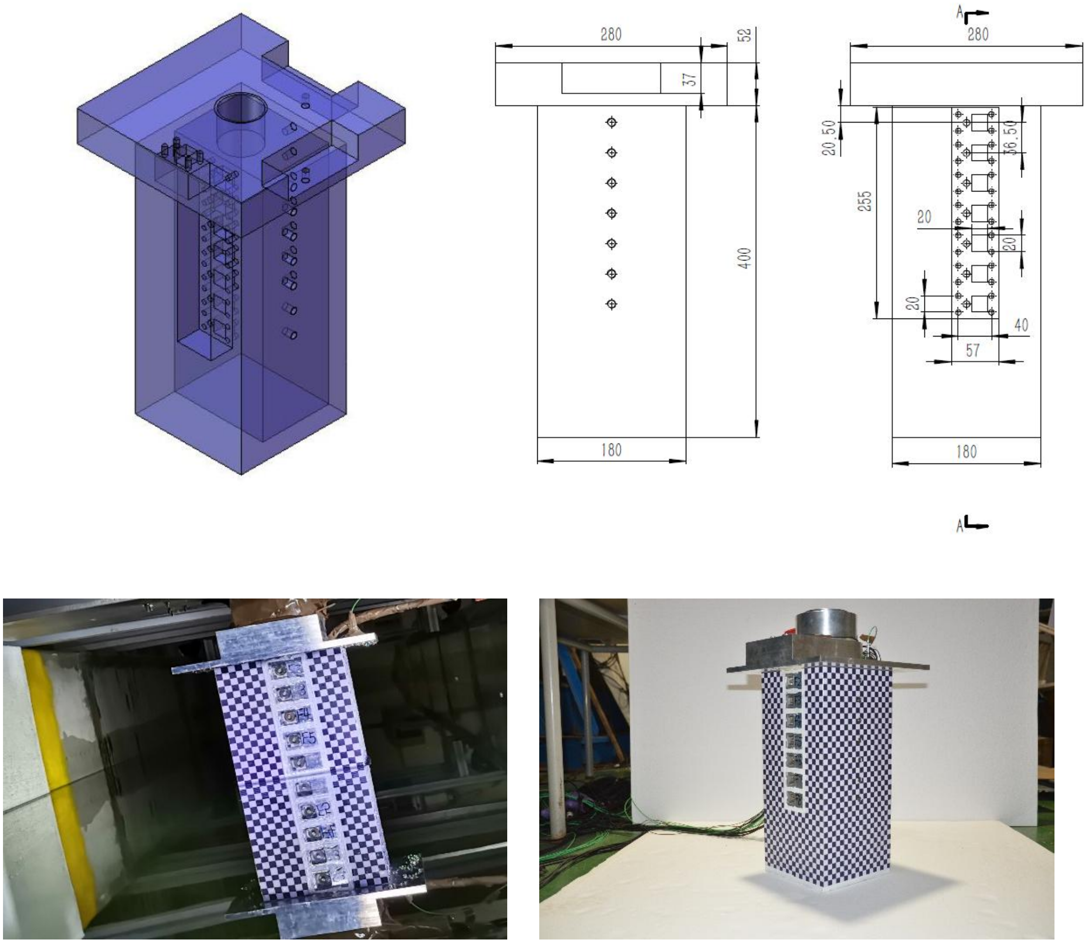

Fig 0.3. Dimension and model of column and deckbox

A.3 Modal and Resonance Analysis of the Single-Column Model

This study investigates the natural frequencies of the single-column platform. Modal analysis results indicate that the first few natural frequencies are as illustrated in Fig. 0.4. The first-mode period is approximately 1.77 ms (≈565 Hz), while the second and third modes have periods of about 1.14 ms and 0.88 ms, respectively. These results indicate that the structure has high overall stiffness, with natural frequencies in the several-hundred-hertz range.

According to the criterion proposed by Faltinsen (1996, 2000)—the ratio between the impact duration and the structure's natural period (FSP)—the structure in this study has FSP = 5.6, clearly within the quasi-static regime (FSP > 1.5). This suggests that hydroelastic effects have only a limited influence on load amplification. Kapsenberg (2011) also pointed out that when the impact duration is much shorter than the structural natural period, or when there is a significant frequency mismatch between them, resonance is unlikely to occur; thus, the rigid-body assumption is generally valid and even slightly conservative.

Furthermore, as shown in Fig. 4.15, the typical slamming pressure pulse lasts about 10–25 ms, corresponding to a dominant frequency of 40–100 Hz, which is an order of magnitude lower than the structural natural frequency (≈500–1000 Hz). Such a significant frequency mismatch further confirms that the slamming loads cannot excite the main vibration modes of the structure, and the resulting load amplification due to structural vibration is minimal.

It is also acknowledged that, although Froude scaling is adopted as the primary similarity criterion in the present study, viscous and surface tension effects, as represented by the Reynolds and Weber numbers, cannot be simultaneously preserved and may have a secondary influence on local flow features and pressure fluctuations.

In summary, both the modal analysis results and literature evidence demonstrate that adopting the rigid-body assumption for analyzing slamming loads in this study is reasonable and engineeringly valid.

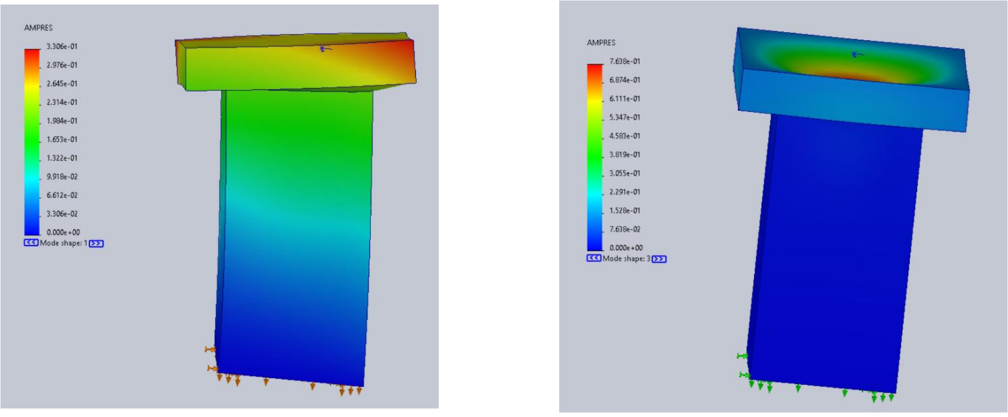

(a) P = 1.77 ms (b) 3rd mode P = 1.14 ms

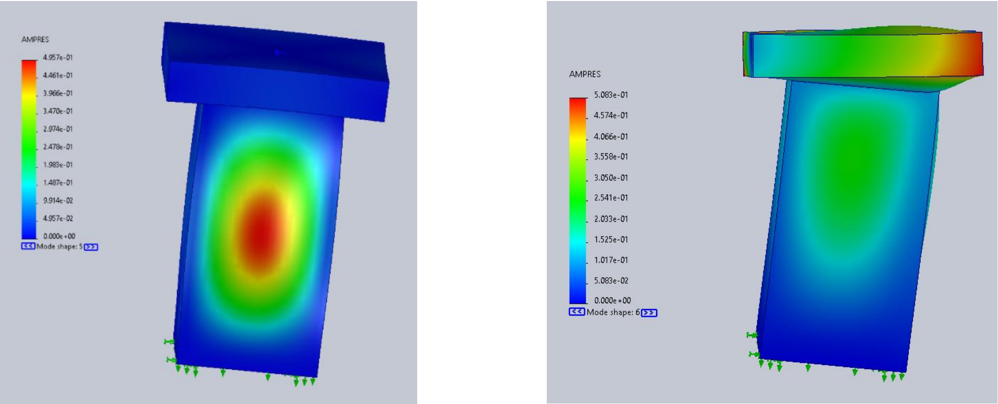

(e) 5th modeP = 0.88 ms (f) 6th mode P = 0.87 ms

Fig. 0.4 Modal characteristics of the single-column platform structure

A.4 Experimental case setup

Table 0.2 Experimental Case Parameter Setup

Note: The F group cases are repeated tests

Case NO.	Air Gap (mm)	Wave Heading(°)	Wave Type	*H* (cm)	*T* (s)	*L* (m)	wave steepness
A1	185	180	R1	10.22	0.8	1.0754	0.095
A2			R2	11.48	0.8	1.0934	0.105
A3			R3	12.81	0.8	1.1135	0.115
A4			R4	15.81	1	1.6637	0.095
A5			R5	17.73	1	1.6882	0.105

A6			R6	19.74	1	1.716	0.115
A7			R7	22.28	1.2	2.3456	0.095
A8			R8	24.95	1.2	2.3759	0.105
A9			R9	27.73	1.2	2.4106	0.115
A34			TAH5	0.1	0.6～1.4	NA	NA
A35			TBH5	0.1	0.8～1.2	NA	NA
A36			JonM06	1.46	0.258	NA	NA
A37			JonM10	1.46	0.155	NA	NA
A38			S100M10	1.150	0.253	NA	NA
A39			S150M10	0.939	0.169	NA	NA
A40			S200M10	0.813	0.126	NA	NA
A41			S250M10	0.727	0.101	NA	NA
A42			S300M10	0.664	0.084	NA	NA
A43			R10	7	0.6	0.56	0.125
A44			R11	12	0.8	1	0.120
A45			R12	19	1	1.56	0.122
A46			R13	23	1.1	1.89	0.122
A47			R14	27	1.2	2.25	0.120
B1	135	180	R1	10.22	0.8	1.0754	0.095
B2			R2	11.48	0.8	1.0934	0.105
B3			R3	12.81	0.8	1.1135	0.115
B4			R4	15.81	1	1.6637	0.095
B5			R5	17.73	1	1.6882	0.105
B6			R6	19.74	1	1.716	0.115
B7			R7	22.28	1.2	2.3456	0.095
B8			R8	24.95	1.2	2.3759	0.105
B9			R9	27.73	1.2	2.4106	0.115
B27			TAH5	0.1	0.6～1.4	NA	NA
B28			TBH5	0.1	0.8～1.2	NA	NA
B29			JonM06	1.46	0.258	NA	NA
B30			JonM10	1.46	0.155	NA	NA
B31			S100M10	1.150	0.253	NA	NA
B32			S150M10	0.939	0.169	NA	NA
B33			S200M10	0.813	0.126	NA	NA

B34			S250M10	0.727	0.101	NA	NA
B35			S300M10	0.664	0.084	NA	NA
B106			R10	7	0.6	0.56	0.125
B107			R11	12	0.8	1	0.120
B108			R12	19	1	1.56	0.122
B109			R13	23	1.1	1.89	0.122
B110			R14	27	1.2	2.25	0.120
B36	235	180	R1	10.22	0.8	1.0754	0.095
B37			R2	11.48	0.8	1.0934	0.105
B38			R3	12.81	0.8	1.1135	0.115
B39			R4	15.81	1	1.6637	0.095
B40			R5	17.73	1	1.6882	0.105
B41			R6	19.74	1	1.716	0.115
B42			R7	22.28	1.2	2.3456	0.095
B43			R8	24.95	1.2	2.3759	0.105
B44			R9	27.73	1.2	2.4106	0.115
B62			TAH5	0.1	0.6～1.4	NA	NA
B63			TBH5	0.1	0.8～1.2	NA	NA
B64			JonM06	1.46	0.258	NA	NA
B65			JonM10	1.46	0.155	NA	NA
B66			S100M10	1.150	0.253	NA	NA
B67			S150M10	0.939	0.169	NA	NA
B68			S200M10	0.813	0.126	NA	NA
B69			S250M10	0.727	0.101	NA	NA
B70			S300M10	0.664	0.084	NA	NA
B111			R10	7	0.6	0.56	0.125
B112			R11	12	0.8	1	0.120
B113			R12	19	1	1.56	0.122
B114			R13	23	1.1	1.89	0.122
B115			R14	27	1.2	2.25	0.120
B71	285	180	R1	10.22	0.8	1.0754	0.095
B72			R2	11.48	0.8	1.0934	0.105
B73			R3	12.81	0.8	1.1135	0.115
B74			R4	15.81	1	1.6637	0.095

B75			R5	17.73	1	1.6882	0.105
B76			R6	19.74	1	1.716	0.115
B77			R7	22.28	1.2	2.3456	0.095
B78			R8	24.95	1.2	2.3759	0.105
B79			R9	27.73	1.2	2.4106	0.115
B97			TAH5	0.1	0.6～1.4	NA	NA
B98			TBH5	0.1	0.8～1.2	NA	NA
B99			JonM06	1.46	0.258	NA	NA
B100			JonM10	1.46	0.155	NA	NA
B101			S100M10	1.150	0.253	NA	NA
B102			S150M10	0.939	0.169	NA	NA
B103			S200M10	0.813	0.126	NA	NA
B104			S250M10	0.727	0.101	NA	NA
B105			S300M10	0.664	0.084	NA	NA
B116			R10	7	0.6	0.56	0.125
B117			R11	12	0.8	1	0.120
B118			R12	19	1	1.56	0.122
B119			R13	23	1.1	1.89	0.122
B120			R14	27	1.2	2.25	0.120
D1	185	135	R1	10.22	0.8	1.0754	0.095
D2			R2	11.48	0.8	1.0934	0.105
D3			R3	12.81	0.8	1.1135	0.115
D4			R4	15.81	1	1.6637	0.095
D5			R5	17.73	1	1.6882	0.105
D6			R6	19.74	1	1.716	0.115
D7			R7	22.28	1.2	2.3456	0.095
D8			R8	24.95	1.2	2.3759	0.105
D9			R9	27.73	1.2	2.4106	0.115
D34			TAH5	0.1	0.6～1.4	NA	NA
D35			TBH5	0.1	0.8～1.2	NA	NA
D36			JonM06	1.46	0.258	NA	NA
D37			JonM10	1.46	0.155	NA	NA
D38			S100M10	1.150	0.253	NA	NA
D39			S150M10	0.939	0.169	NA	NA

D40			S200M10	0.813	0.126	NA	NA
D41			S250M10	0.727	0.101	NA	NA
D42			S300M10	0.664	0.084	NA	NA
D43			R10	7	0.6	0.56	0.125
D44			R11	12	0.8	1	0.120
D45			R12	19	1	1.56	0.122
D46			R13	23	1.1	1.89	0.122
D47			R14	27	1.2	2.25	0.120
D1			R1	10.22	0.8	1.0754	0.095
D2			R2	11.48	0.8	1.0934	0.105
F1	185	180	S100M10	1.150	0.253	NA	NA
F2			S100M10	1.150	0.253	NA	NA
F3			S100M10	1.150	0.253	NA	NA
F4			S100M10	1.150	0.253	NA	NA
F5			S100M10	1.150	0.253	NA	NA
F6			S100M10	1.150	0.253	NA	NA
F7			S100M10	1.150	0.253	NA	NA
F8			S100M10	1.150	0.253	NA	NA
F9			S100M10	1.150	0.253	NA	NA
F10			S100M10	1.150	0.253	NA	NA
F11			S100M10	1.150	0.253	NA	NA
F12			S100M10	1.150	0.253	NA	NA
F13			S100M10	1.150	0.253	NA	NA
F14			S100M10	1.150	0.253	NA	NA
F15			S100M10	1.150	0.253	NA	NA
F1			S100M10	1.150	0.253	NA	NA
F2			S100M10	1.150	0.253	NA	NA
F3			S100M10	1.150	0.253	NA	NA
F4			S100M10	1.150	0.253	NA	NA
F5			S100M10	1.150	0.253	NA	NA
F6			S100M10	1.150	0.253	NA	NA
F7			S100M10	1.150	0.253	NA	NA
F8			S100M10	1.150	0.253	NA	NA
F1			S100M10	1.150	0.253	NA	NA

F2			S100M10	1.150	0.253	NA	NA
F3			S100M10	1.150	0.253	NA	NA
F4			S100M10	1.150	0.253	NA	NA
F5			S100M10	1.150	0.253	NA	NA
F6			S100M10	1.150	0.253	NA	NA
F7			S100M10	1.150	0.253	NA	NA
F8			S100M10	1.150	0.253	NA	NA